

University of Nottingham
UK | CHINA | MALAYSIA

Whole-brain imaging in rodents using MRI and 3D microscopy: A cross-scale, multi-modal approach

Jenna Mary Hanmer

Thesis submitted to the University of Nottingham
for the degree of Doctor of Philosophy

September 2024

Abstract

Magnetic Resonance Imaging (MRI) has transformed neuroscience by enabling the measurement of brain structure, function, physiology, chemical composition, and connectivity. Yet, despite its sensitivity to microscopic biophysical tissue changes (e.g., from development, ageing, plasticity, or pathology), MRI's macroscopic (millimetre-scale) resolution and indirect nature limit specificity and pose challenges to interpretation. To address this, prior studies have combined MRI with histology, which has microscopic resolution and higher specificity. However, classical histology is inherently two-dimensional and tissue sectioning introduces distortions, making data fusion with MRI challenging. In contrast, advanced 3D techniques like light sheet microscopy preserve the full complexity of brain architecture but are typically restricted to small optically transparent samples, such as the cleared mouse brain.

This thesis introduces a novel multiscale imaging framework for the larger rat brain, integrating whole-brain 3D light-sheet microscopy (10μm isotropic) with 3D *ex-vivo* anatomical and diffusion MRI (100-200μm). Due to the larger size and higher lipid content of the rat brain, new tissue processing techniques were developed, including advanced tissue clearing protocols and electric field-enhanced immunolabelling. These innovations enable high-resolution 3D imaging of cellular structures that would otherwise be compromised in histology. Furthermore, by preserving the 3D anatomy of the tissue, alignment of microscopy images with MRI becomes less challenging, enabling detailed characterisation of white and grey matter across scales and modalities.

The methods introduced in this thesis advance multiscale brain imaging, offering enhanced insights into neuroanatomy at the cellular level. This work also lays the foundation for improving the specificity of the MRI contrasts and developing novel *in vivo* imaging techniques to explore brain connectivity and microstructure.

Acknowledgements

This multimodal, cross-resolution, interdisciplinary project has relied on many friends, colleagues and collaborators, to whom I'm extremely thankful for their contributions.

First and foremost, I would like to sincerely thank Dr Matteo Bastiani for believing in me and encouraging me to apply for this project. His training and support provided me with a strong foundation in dMRI techniques and image analysis methods, as well as confidence in my abilities, both of which were instrumental in securing the MRC funding for this project.

I would also like to express my gratitude to the IMPACT Doctoral Training Programme, particularly Dr Karen Robinson and Miss Vikki Harrison, for providing me with countless opportunities to grow both academically and personally. Through this programme, I have not only developed invaluable skills but also built friendships that I know will last a lifetime.

I am forever indebted to my supervisors for their unwavering support, guidance, patience, reassurances, and understanding throughout my PhD journey. Stam, you have assembled an outstanding research group in just a few years, and I feel truly privileged to have been one of your PhD students. Learning from you has been an incredibly rewarding experience, and I sincerely appreciate the time and energy you've dedicated to my project. Paul, I am grateful for your continued interest in my progress, and your advice before my viva truly made a significant difference. Tracy, you were always there to guide me back on course whenever I was struggling. I sincerely hope that your time in Edinburgh is proving to be as fulfilling as you hoped and that your colleagues have given you a warm welcome - you are greatly missed.

I would like to extend my gratitude to Dr Rebeccan Trueman for generously allowing me to work under her project licence for the duration of my PhD and to Dr Maxine Fowler for her moral support and assistance with all

lab-related matters. A special thank you also to Clare Spicer and Dr David Watson for their invaluable help with perfusions and tissue collection.

I am grateful to Dr Malcolm Prior for his ongoing support with MRI protocol development, acquisitions, and data processing. I would also like to extend a special thank you to Dr. Martin Craig for his invaluable assistance in resolving numerous computational challenges, as well as his patient and clear explanations.

I would like to acknowledge the Imaging Suite at the University of Birmingham for providing access and support on their Ultramicroscope II. These imaging facilities are funded by COMPARE (Centre of Membrane Proteins and Receptors). A special thanks to Dr Joao Correia for sharing his expertise in light sheet microscopy and introducing me to key contacts. I would also like to acknowledge the School of Life Sciences imaging facility (SLIM) in Nottingham and its staff for their support and generously sharing their lab space.

At Oxford University, I am grateful to Prof Jason Lerch, and Drs Mohamed Tachrount, Cristiana Tisca, Aurea Martins-Bach and Frederik Lange for granting me access to the preclinical imaging facility, providing the diffusion MRI acquisition sequences, and sharing their expertise in image registration. It has been a pleasure working with you all.

At Vanderbilt University, I would like to extend my appreciation to Dr Kurt Schilling, Prof Bennett Landman and the MASI (Medical-image Analysis and Statistical Interpretation) lab for hosting me during my second year and for their keen interest in my project. I am also incredibly thankful to Dr Michelle Badenbaugh at the Simerly lab for taking the time during a busy period to introduce me to active clearing and labelling approaches and for demonstrating the advantages of the SmartSPIM light sheet microscope.

I would like to sincerely thank Dr Kim Chisholm for supporting my career development through her excellent advice and for providing me with

numerous opportunities to extend my technical skills to new scales.

To all my friends in Sir Peter Mansfield Imaging Centre, thank you for your kindness, the comic relief, and much-needed sanity checks.

Last but not least, I want to express my deepest gratitude for the love and unwavering support of Sam, my parents, Jeffrey, Kerry, Kevin, and Aunty Cheryl. None of this would be possible without you.

To Sam, we're finally going to have that long-overdue adventure. To Gabriel, Veronica, and Eleanor, I can't wait to hear all about your experiments and discoveries.

Contents

Abstract i

Acknowledgements ii

Research Outputs 1

Chapter 1 Introduction 3

1.1 Organisation of Thesis 8

Chapter 2 Background 12

2.1 Exploring the Multiple Scales of Brain Organisation 13

2.2 Magnetic Resonance Imaging (MRI) 14

2.2.1 MRI as a Tool for Pre-clinical Research 15

2.2.2 Diffusion MRI for Probing Brain Microstructure . . . 18

2.3 Optical Imaging and Microscopy 27

2.3.1 Conventional 2D Approaches 29

2.3.2 Modern 3D Approaches 33

2.3.3 Tissue Clearing 35

2.3.4 Light Sheet Fluorescence Microscopy 39

2.4 Cross-resolution, Cross-modal Imaging 42

2.4.1 Existing Frameworks 43

2.4.2 Thesis Aims 46

Chapter 3 *Ex vivo* MRI of the Rat Brain 49

3.1 Introduction 49

3.2 Theory & Methods 52

3.2.1 *Ex-vivo* MRI for the Rat Brain 52

3.2.2 Anatomical MRI Processing Pipeline 64

3.2.3 Diffusion MRI Processing Pipeline 71
3.3 Results 74
3.3.1 Optimising Data Acquisition 74
3.3.2 Data Conversion and Image Pre-processing 80
3.3.3 Anatomical MRI Pipeline 83
3.3.4 Diffusion MRI Pipeline 91
3.4 Discussion 94
3.4.1 Limitations and Future Extensions 97
3.4.2 Contributions 99
Chapter 4 Passive Clearing and 3D Microscopy of the Rat Brain 100
4.1 Introduction 100
4.2 Methods 104
4.2.1 Tissue Clearing 106
4.2.2 Light Sheet Fluorescence Microscopy 112
4.2.3 Data Conversion and Image Processing 115
4.2.4 Registration of Microscopy Imaging to MRI 116
4.3 Results 117
4.3.1 Optimisation of Tissue Clearing 118
4.3.2 Registration of Microscopy Imaging to MRI 129
4.4 Discussion 134
4.4.1 Limitations and Future Extensions 136
4.4.2 Contributions 137
Chapter 5 Active Clearing and Staining in the Intact Rat Brain 139
5.1 Introduction 139
5.2 Methods 144
5.2.1 Sample Preparation 144
5.2.2 Pre-treatment 145

5.2.3 Tissue Preservation 145
5.2.4 Electrophoretic-driven Clearing and Staining 149
5.2.5 Refractive Index Matching 155
5.2.6 Light Sheet Fluorescence Microscopy 156
5.2.7 Data Conversion and Image Processing 159
5.2.8 Structure Tensor Analysis 159
5.2.9 Registration of Microscopy to MRI 162
5.3 Results 162
5.3.1 Optimisation of Sample Preparation 163
5.3.2 Tissue Preservation and Processing 164
5.3.3 Optimising Active Delipidation 166
5.3.4 Optimising Active Immunolabelling 167
5.3.5 Structure Tensor Analysis and Comparison to MRI . 171
5.4 Discussion 174
5.4.1 Limitations and Future Extensions 177
5.4.2 Contributions 180
Chapter 6 Conclusions & Future Directions 181
6.1 Main Contributions 181
6.2 Future Directions 185
6.2.1 Specific MRI contrasts 186
6.2.2 Mapping cellular and molecular mechanisms 188
6.2.3 Neural connectivity mapping 190
6.2.4 Data fusion and joint modelling 191
References 192

List of Tables

2.1 Techniques used to explore tissue microstructure 28

2.2 Commonly used methods for tissue clearing 35

3.1 Time between sample fixation and MRI scanning 55

3.2 Acquisition parameters for anatomical scans 59

3.3 Acquisition parameters for multi-shell dMRI 60

3.4 Summary of MRI data acquired across sites 61

3.5 Standard templates used in rat MRI 66

3.6 Data quality for 2D-EPI dMRI in Nottingham 78

3.7 Data quality for 2D/3D-EPI dMRI in Oxford 79

3.8 Correcting diffusion gradient vectors 82

4.1 Microscopy and MRI data used to test registration 116

4.2 Performance of hydrophobic tissue clearing protocols 118

5.1 Electrophoresis accelerates immunolabelling 155

5.2 Summary of samples imaged across different microscopes . . 158

5.3 Microscopy and MRI data used to test registration 162

List of Figures

1.1 The multiple scales of brain organisation 6

2.1 *Ex vivo* MRI achieves higher spatial resolution 17
2.2 Diffusion in white matter 19
2.3 Diffusion in multi-compartment models 23
2.4 Ambiguities in mapping diffusion to axon geometry 25
2.5 Microscopy and dMRI can be used to study microstructure . 26
2.6 Comparing label-free approaches with tissue staining 30
2.7 Challenges with tissue sectioning and 2D microscopy 32
2.8 Combining tissue clearing with light sheet microscopy 34
2.9 The principles of light sheet microscopy 40
2.10 Advances in light-sheet microscopy 42
2.11 Whole-brain imaging: a multimodal cross-resolution approach 43

3.1 Preparing a sample for *ex vivo* MRI 56
3.2 Standardising image orientation 62
3.3 Organisation of pre-processing pipelines 64
3.4 Anatomical and diffusion MRI across two sites 75
3.5 Perfusing samples with gadolinium reduces T_1 75
3.6 Perfusing samples with gadolinium allows for shorter scans . 76
3.7 Perfusing samples with gadolinium boosts image contrast . . 77
3.8 Mapping contrast-to-noise for dMRI with 2D/3D-EPI . . . 79
3.9 Validating image orientation 81
3.10 Validating direction of diffusion encoding gradients 82

3.11 Performance of tools for brain extraction 84
3.12 Estimating the bias field 86
3.13 Correcting for the bias field 87
3.14 Anatomical alignment of T2-scan to the template 88
3.15 Comparison of tissue segmentation 89
3.16 Generalisation of pipeline across scanners 90
3.17 Generalisation of pipeline across species 91
3.18 Differences in bias field across scanners 92
3.19 2D-EPI dMRI acquisitions across scanners 93
3.20 Differences between 2D-EPI and 3D-EPI readout for dMRI . 95

4.1 Key steps of hydrophobic clearing protocol 107
4.2 Imaging cleared samples using the UltraMicroscope II 113
4.3 Clearing of rat brain requires gradual delipidation 119
4.4 3D-Microscopy of rat brain section after clearing 120
4.5 Tissue clearing of rat brain hemisphere 121
4.6 Refractive index matching for rat brain section 121
4.7 Volumetric imaging of the rat brain hemisphere 122
4.8 Autofluorescence of rat brain hemisphere after clearing . . . 123
4.9 Correcting intensity non-uniformity in 3D microscopy. 124
4.10 Passive clearing in samples perfused with gadolinium 125
4.11 Only superficial staining is seen with AdipoClear+ 126
4.12 Increasing antibody concentration does not improve penetration 127
4.13 Comparing tissue contrast in 3D microscopy and MRI 128
4.14 A linear transformation can align 3D microscopy to MRI . . 130
4.15 Finding the optimal parameters for image registration 131
4.16 Direct comparison across modalities and resolutions 132
4.17 Direct comparison between 3D microscopy and MRI 133

5.1 Interactions between key variables in tissue staining 142

5.2 The principles of tissue preservation in active clearing 147
5.3 SmartBatch+ device for active clearing/labelling 150
5.4 Imaging cleared samples using the BLAZE microscope . . . 157
5.5 Active clearing in gadolinium-enhanced brains 163
5.6 Pre-treatment reduces vessel autofluorescence 164
5.7 Active clearing in the rodent brain 165
5.8 Image contrast after active clearing 166
5.9 Active delipidation with SDS impacts sample integrity . . . 167
5.10 Electrotransport accelerates antibody penetration 168
5.11 Active labelling of cortical myelination 169
5.12 Myelin staining in the cerebellum is uniform 170
5.13 Individual fibres are visible with active labelling 171
5.14 SDS-based delipidation enhances transparency and staining . 172
5.15 Estimating fibre orientation from myelin staining 172
5.16 Estimating fibre orientation in cleared tissue 173
5.17 Alignment between the diffusion orientation and autofluorescence signal in the same sample 174

6.1 Whole-brain 3D microscopy of glial cells 187
6.2 Whole-brain mapping of neuroinflammation 189

Research Outputs

Presentations and Publications

- "Whole-brain imaging in rats using MRI and 3D microscopy: A cross-scale, multi-modal approach", **J. Hanmer**, M. Craig, M. Prior, J. Correia, M. Tachrount, J. Lerch, R.C. Trueman, P.S. Morgan, T.D. Farr, S.N. Sotiropoulos. **BIC-ISMRM Annual Meeting**, Oral, Nottingham, United Kingdom, September 2024.

- "A pipeline for concurrent whole-brain light-sheet microscopy and MRI in the rat", **J. Hanmer**, M. Craig, M. Prior, J. Correia, C. Tisca, A. Martins-Bach, M. Tachrount, M. Bastiani, K. Schilling, J. Lerch, P.S. Morgan, T.D. Farr, and S.N. Sotiropoulos. Light-sheet in Action Symposium, Oral, **Francis Crick Institute**, London, United Kingdom, April 2024.

- "A pipeline for concurrent whole-brain 3D microscopy and MRI in the rat", **J. Hanmer**, M. Craig, M. Prior, J. Correia, C. Tisca, A. Martins-Bach, M. Tachrount, M. Bastiani, K. Schilling, J. Lerch, P.S. Morgan, T.D. Farr, and S.N. Sotiropoulos. **OHBM Annual Meeting**, Poster, Montreal, Canada, June 2023. doi: 10.5281/zenodo.10719609

Software

- Modified version of Brkraw that is correctly configured for Rodent Diffusion MRI
- Pre-processing pipeline for Rodent Structural MRI
- Pre-processing pipeline for Rodent Diffusion MRI

Knowledge Transfer

- Trained BBSRC PhD candidate and two Senior Research Technicians on active clearing techniques.

Public Engagement

- 2024: Soapbox Science in Nottingham City Centre
- 2023: Science in the Park at Wollaton Hall
- 2022: Scholars Programme with Hillside Primary School (14hrs), Specialist STEM tutoring with Friern Barnet Secondary School (30hrs), British Science Week event at Welbeck Primary School (2hrs)

Chapter 1

Introduction

Santiago Ramón y Cajal, who pioneered modern neuroscience, recognised that our understanding of all things, including the human brain, is shaped by the scientific techniques at our disposal. Since his time, the landscape of neuroscience has changed considerably, as advances in technology and research methodologies have allowed us to explore new frontiers. These advancements have not only refined our maps of brain organisation but have also deepened our appreciation for how the brain's complex architecture is moulded by a myriad of factors, including genetics, ageing, disease, and environmental influences. Nonetheless, despite these strides, fully comprehending the biological basis of phenomena that emerge from the brain's highly interconnected web of networks and govern behaviour, remains a formidable challenge (Thiebaut de Schotten and Forkel, 2022).

Indeed, the scale of this challenge becomes apparent when considering the vast continuum of brain organisation, which spans many orders of magnitude. At the nanoscale, lies the synapse, where the strength of individual connections is modulated. Ascending to the microscale, we encounter individual neurons and glia, with their unique morphology, patterns of connectivity

and signalling mechanisms. Finally, expanding our perspective to the meso- and macroscopic scales, white matter tracts emerge as the highways which facilitate neural communication between anatomical regions. Yet, our exploration of neuronal structures across these scales is inherently constrained by the resolution and modalities of the techniques that we use. Thus, the challenge of unravelling the multi-scale organisation of the brain persists for the neuroscience community (D'Angelo and Jirsa, 2022; Walhovd et al., 2014).

On a macroscopic scale, the advent of modern neuroimaging methods has transformed our understanding of the human brain. Amongst these techniques, magnetic resonance imaging (MRI) was the first non-invasive means of visualising the living brain, without exposure to ionising radiation. This powerful form of three-dimensional (3D) imaging allows researchers to explore the complex anatomy of brain (Lerch et al., 2017) and reveal patterns of regional activation (Morita et al., 2016).

Moreover, specific MRI modalities, such as diffusion MRI (dMRI), provide insights across multiple scales, shedding light on areas that were previously challenging to study. By facilitating the tracing of macroscopic trajectories of white matter tracts *in vivo*, dMRI unveils the complex interconnections that facilitate signalling between regions (Assaf et al., 2019). This information can be used to reveal networks of connectivity across the whole brain (Sotiropoulos and Zalesky, 2019). Additionally, dMRI has provided novel insights on a microscopic scale, as it is sensitive to the biophysical properties of axonal bundles and other neural structures in the brain (Alexander et al., 2019). As such, dMRI can be used to better understand how microstructure and connectivity change in the brain of an individual over their lifespan (Vogel et al., 2023; Raghavan et al., 2021). However, despite the promise of MRI, it is crucial to acknowledge its inherent limitations.

Although MRI measurements are sensitive, they are not specific in what they represent (Yendiki et al., 2022). Tissue parameters are inferred indirectly from the magnetic resonance (MR) signal, which measures properties of water molecules and how they are influenced by the various micro-environments. Multiple micro-environment patterns can give rise to the same signal (Jelescu et al., 2020), and this signal is noisy. Furthermore, the resolution of MRI is limited to the macroscale *in vivo* ($\geq$millimetre resolution). This presents a particular challenge as the volume of brain tissue represented by an imaging voxel contains tens of thousands of microscopic processes, that all contribute to an average measured signal. Combining information from more than one MRI contrast takes advantage of overlapping and complementary information about tissue properties (Cercignani and Bouyagoub, 2018; Sotiropoulos et al., 2016), but does not address these limitations. Another approach is therefore required.

One way of better understanding which features we can accurately measure with MRI-based methods is to combine them with complementary 'gold standard' techniques that allow us to directly observe the microstructural 'ground truth'. This provides a means for making comparisons for the purposes of understanding and validating macroscopically measured parameters (Axer et al., 2016; Leuze et al., 2014; Mollink et al., 2017; Schilling et al., 2018; Wang et al., 2015) or advancing modelling efforts (Howard et al., 2019; Jelescu et al., 2020). By using different imaging techniques, with distinct and complementary spatial resolutions, fields of view, mechanisms of contrast, and specificities, it also becomes possible to probe multiple scales of neural structure and brain connectivity (Roebroeck et al., 2019), as demonstrated in Figure 1.1. This is important because it provides a more holistic appreciation of the brain, where the whole is more than the sum of its parts.

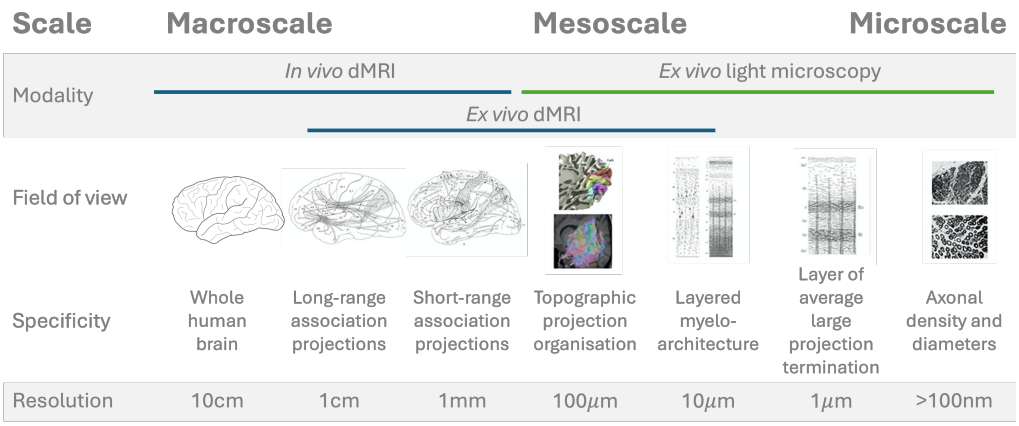


Figure 1.1: The multiple scales of brain organisation, with the imaging techniques used to map connections and investigate anatomy. The spatial resolution and field of view for each modality limits which features can be characterised. *Ex vivo* dMRI has an important role in mapping brain architecture because it has a mesoscopic resoltion ($\sim$100μm), and therefore bridges the gap between *in vivo* dMRI and light microscopy. Adapted from Roebroeck et al. (2019).

In the case of structural imaging, optical techniques, such as light microscopy (Zhu et al., 2017), allow for the direct study of brain tissue at the microscopic scale ($\sim$micron resolution). When combined with labelling techniques, it is possible to quantify specific tissue properties, such as axonal density, myelination or fibre orientation (Schilling et al., 2018). However, these techniques are usually only possible *ex vivo*. Furthermore, they are typically 2-dimensional (2D) and limited to relatively small tissue samples ($\leq$1cm^3) that need to be sectioned, thereby losing valuable information about the whole structure and potentially missing critical findings (e.g., by providing false negatives) due to poor sampling. The process of preparing tissue for microscopy is also labour-intensive and time consuming. Together, these factors render comparisons with MRI challenging and sub-optimal (Lazari and Lipp, 2021; Yendiki et al., 2022), especially if such comparisons are required for the whole-brain.

More recently, the combination of novel tissue clearing techniques (Chung et al., 2013; Ertürk et al., 2012; Renier et al., 2014; Costantini et al., 2019;

Susaki et al., 2015; Tian et al., 2021) and light sheet microscopy (Dodt et al., 2007; Huisken, 2004) has allowed for detailed study of the microstructure of intact brain tissue in 3D. Although these methods still require further development, it is currently possible to stain, clear, and image large samples (particularly the relatively small mouse brain), without sectioning, thereby preserving the tissue's microstructure and spatial organisation (Pawłowska et al., 2019). Methods for integrating data from optically cleared tissue, imaged *ex vivo* in 3D, with relevant MRI modalities, are also improving (Goubran et al., 2019; Johnson et al., 2023; Chang et al., 2017; Stolp et al., 2018; Foxley et al., 2021).

This project has capitalised on these new opportunities by developing a multi-modal and cross-resolution imaging framework, based on high resolution structural and diffusion MRI, combined with 3D light sheet microscopy for the rodent brain. By directly fusing measures derived from MRI and microscopy in the same brain, it is possible to bridge the scales of spatial resolution and unify cross-scale information. This can provide a better understanding of the specificity of existing contrasts that can be obtained using MRI *in vivo*, as well as approaches to develop and optimise new ones.

Contrary to the majority of previous approaches that have focused on the mouse brain, this thesis provides novel solutions for the rat brain. The rat is also widely used in neuroscience research (El-Ayache and Galligan, 2020), but its brain is at least 400% larger (Welniak–Kaminska et al., 2019; Kovačević et al., 2005). This creates extra challenges in obtaining 3D microscopy data, as tissue clearing protocols have been optimised for the mouse brain and do not easily translate to the rat. Also, most light sheet microscopes can only image samples that are relatively small ($\sim$1cm^3) due to limits in their working distance and field of view. In this work, these challenges are addressed and we showcase the potential value of combining

3D MRI with 3D microscopy for the optically-cleared rat brain. The scope of the project spans methods development, data acquisition and image processing. It will enable further studies to explore MRI contrasts and determine what biophysical information they convey, in the context of healthy tissue or in rodent models of disease.

1.1 Organisation of Thesis

This thesis describes the development of a novel end-to-end framework for obtaining and integrating whole-brain 3D microscopy and MRI in the rat. It is split into 6 chapters, which demonstrate how this approach bridges microscopic information to a macroscopic resolution. This introductory chapter is followed by a background chapter and three research chapters. We describe the contents of each chapter in more detail below.

In **Chapter 2**, we provide an overview of MRI and diffusion MRI, which has allowed researchers to investigate the brain across different scales. We highlight the significance of MRI in translating preclinical research while also acknowledging its inherent limitations. Furthermore, we explore how MRI's specificity can be improved through comparison with optical imaging techniques, which complement MRI by allowing for direct observation of tissue microstructure at superior resolution. After describing the challenges of validating MRI contrasts with histology, we introduce tissue clearing as a next generation approach, which has pushed the boundaries of optical imaging by facilitating 3D microscopy. Finally, we conclude with a more detailed description of the aims of this work and a discussion of how it compares with what has been previously done.

Chapter 3 is the first chapter containing original research. It aims to

tackle long-standing challenges in the field of rodent MRI, focusing on image acquisition and data processing. This has not been not trivial, as rodent brain imaging lacks standardisation and scientific consensus, and existing tools are suboptimal with limited generalisability. To address this, we optimised and validated protocols for *ex vivo* rodent MRI by acquiring data across multiple sites and scanners, showing that gadolinium perfusion and alternative imaging sequences can boost image contrast and shorten acquisition time. We also introduce methods for automatic processing and analysis of the multi-modal images acquired, ensuring generalisability by testing on data with different architectures and levels of signal, noise and contrast. To maximise impact, we demonstrate that these pipelines are flexible and robust enough to handle mouse brain data with minimal modification. Finally, we outline what we found to be best practice, and describe how to fully leverage our MRI dataset and processing pipelines.

In the following chapter, **Chapter 4**, we present tissue clearing and light-sheet (3D) microscopy as a crucial departure from traditional histology, enabling the characterisation of structures that would otherwise span tissue sections. We describe the fundamental challenge of clearing the rat brain, given it's large size and that existing methods were developed for the mouse brain, where the lipid content and overall volume are lower. We then demonstrate how we have overcome these challenges by establishing a passive solvent-based tissue clearing protocol that is extended for further delipidation and permeabilisation. We proceed to describe the methods we developed for 3D microscopy of the intact rat brain hemisphere at cellular resolution. This allowed us to verify that using gadolinium contrast in sample preparation (as required for some MRI protocols) did not negatively impact tissue clearing or autofluorescence. Furthermore, the passive clearing method presented in this chapter do not require any specialised equipment,

rendering it accessible to a broader scientific community. We conclude the chapter by demonstrating that a simple registration approach can anatomically align the 3D microscopy images with corresponding MRI volumes.

Chapter 5 explores the challenge of visualising specific cellular targets in the intact rodent brain, which arises from the mismatch between slow molecular diffusion and rapid antibody binding. To address this, we adapted state-of-the-art techniques that actively transport antibodies and modulate their binding affinity, scaling them up from the mouse to the much larger rat brain. This active approach, which is compatible with tissue clearing and light sheet microscopy, improved antibody penetration and provided high-contrast, specific labelling of myelin and neuorofilament without the shrinkage observed with the passive solvent-based method. Although active labelling requires a specialised device, automation halved the processing time and improved reproducibility. Finally, we demonstrate how structure tensor analysis of microscopy images of white matter staining provided estimates of fibre orientation, and discuss how integrating these measures with MRI could advance microstructural studies and offer new insights into brain architecture.

Finally, **Chapter 6** concludes the thesis by discussing the potential of expanding our cross-resolution multimodal framework for whole-brain imaging to new applications. One promising direction is its use in studying neuroinflammation as a potential cause, rather than just a consequence, of conditions like multiple sclerosis and neurodegeneration. Innovative imaging solutions for detecting neuroinflammation are urgently needed as the only method currently available, positron emission tomography, suffers from low resolution, poor specificity, and a reliance on ionising radiation. These limitations hinder our ability to measure and understand neuroinflammation.

By expanding our framework to this area, we could address these gaps and create new opportunities to translate scientific insights into real-world impact.

Chapter 2

Background

This chapter begins with an overview of how magnetic resonance imaging (MRI) has allowed researchers to explore brain architecture and anatomical connections across multiple scales. We discuss the versatility and limitations of this non-invasive imaging technique, emphasising the importance of determining which specific tissue properties are captured by imaging contrasts. Then, we explain how the specificity of MRI can be improved through comparison with complementary techniques that directly observe tissue architecture with better resolution. After describing the challenges of validating MRI contrasts with histology, we advocate for the adoption of next-generation approaches, exemplified by tissue clearing and light sheet (3D) microscopy. Finally, the chapter concludes with a more detailed description of our proposal and discussion of how this project compares with and augments what has previously been done.

2.1 Exploring the Multiple Scales of Brain Organisation

The human brain's complex organisation and connectivity profoundly influences how it processes, stores, and responds to information. Experiences across an individual's lifespan lead to changes in neural architecture, shaping how signals propagate and further constraining brain function (Power and Schlaggar, 2017). Yet despite advancements, comprehensive mapping of brain organisation and connectivity eludes us, presenting a fundamental challenge to understanding the basic mechanisms underlying memory, thought, and consciousness (Zupanc, 2017). Furthermore, the complicated relationships between brain structure, function, and dynamics remain unresolved (D'Angelo and Jirsa, 2022).

Investigating the brain's complex organisation entails studying the cells which transmit signals across the brain; neurons. Neurons can have axons up to a metre in length, but synapses are less than 40 nanometres in diameter. As such, understanding brain organisation requires imaging across multiple scales (Betzel and Bassett, 2017). However, our ability to simultaneously access and integrate information across these scales remains limited, further hindering our efforts to discern how change at one level affects another. Integrating data from diverse modalities and sources can reveal the multiscale organisation of the brain, albeit with inherent challenges (Axer and Amunts, 2022).

The development of comprehensive multiscale maps of neural organisation represents a significant step forward in enhancing our understanding of brain development, evolution, and pathology. For example, by integrating features across various resolutions, such as the accumulation of microstructural pro-

tein aggregates across macroscale brain networks, researchers have gained valuable insights into the mechanisms underlying neurodegenerative diseases and their clinical presentation (Vogel et al., 2023). Similarly, investigations spanning micro to mesoscopic scales have shed light on how dysfunction in astrocytes contributes to alterations in the morphology, activity, and connectivity of neurons in epilepsy and neurodevelopmental disorders (Kumamoto and Tsurugizawa, 2021). On a more fundamental level, understanding the principles governing brain organisation across micro, meso, and macroscopic levels has helped explain how localised events, such as stroke, impact on the configuration of other brain structures and networks (Latifi and Carmichael, 2024), potentially opening avenues for novel therapeutic interventions that improve neuropsychological outcomes. In the future, the multiscale approach to understanding brain organisation could lead to personalised brain networks (Pines et al., 2022) and more precise predictions of brain function and behaviour, heralding a new era in neuroscience research and clinical practice. Notably, many of these breakthroughs owe their realisation to the emergence of MRI.

2.2 Magnetic Resonance Imaging (MRI)

Medical diagnostics and neuroscience research were transformed by the advent of MRI, as it does not require ionising radiation and the soft tissue contrast it provides is unmatched (Lerch et al., 2017). Multiple tissue properties, such as brain morphology, organisation, function, structural/-chemical composition, and connectivity, can be investigated in a single session by using different imaging protocols (Cercignani and Bouyagoub, 2018). The large field of view (FOV) also means that the whole brain can be non-invasively imaged at a relatively high resolution (i.e., 1-2mm). All

of these advantages have helped to establish MRI as an indispensable tool in advancing our understanding of the brain.

Technical advances in hardware, acquisition, reconstruction, and data processing are significantly improving the quality of MRI data. Scanners are becoming more accessible, and data acquisition is relatively fast and can be automated. This has allowed scientists to conduct large-scale population-based studies (>10'000 subjects), with repeated measures (for example, Miller et al. (2016)). In these studies multimodal MRI is used to non-invasively investigate brain anatomy and function *in vivo*, alongside testing of cognition, genetics, and health, so that we can better understand how all these factors interact and account for inter-individual differences. In addition, these powerful imaging studies are providing a rich, multi-faceted description of how an individual's brain deviates from population norms over time, which is leading to insights into the causes or mechanisms of brain disease, and aiding in the discovery of early indicators or predispositions to disease (Smith et al., 2021). This would be impossible without modern neuroimaging techniques. Nevertheless, experimental research using animal models remains crucial for identifying the molecular and cellular mechanisms associated with disease, as well as for testing novel therapies and treatments.

2.2.1 MRI as a Tool for Pre-clinical Research

Animal models offer a unique opportunity to investigate how various manipulations — genetic, environmental, surgical, and/or pharmacological — impact on brain development, structure, and function (Wang et al., 2020b; Wu and Zhang, 2016). Pre-clinical MRI scanners extend upon this by allowing researchers to acquire measures in experimental animals, particularly rodents, that are comparable to those taken in human studies. This

capability plays a crucial role in bridging the translational gap between novel discoveries in animal models and their clinical application (Hoyer et al., 2014), and has led to valuable insights into multiple domains (Benveniste and Blackband, 2002). For instance, pre-clinical MRI has allowed detailed imaging of cerebral blood flow, infarct size, and tissue viability in animal models of stroke (Sokolowski et al., 2023). This has enhanced our knowledge of stroke pathophysiology and the efficacy of potential treatments. MRI has also facilitated the assessment of structural damage, blood-brain barrier disruption, and the dynamics of injury progression and recovery in pre-clinical models of traumatic brain injury. This is leading to promising developments in diagnostic and therapeutic approaches (Kaijzel et al., 2017). These examples underscore the versatility and impact of pre-clinical MRI in advancing our understanding of brain organisation, neurological processes and diseases.

Pre-clinical scanner hardware and acquisition methods differ from those used clinically as they have been customised to account for the small size of the rodent brain (Hoyer et al., 2014). Whilst the volume of the human brain is ∼950–1800 cm^3, that of the mouse and rat are ∼0.32–0.52 cm^3 and ∼1.81–2.00 cm^3 respectively (Wang et al., 2020a; Goerzen et al., 2020). To obtain meaningful measures of individual structures, such as the hippocampus, the voxel size in rodent neuroimaging should be ∼0.1% of that used in human studies (Hoyer et al., 2014). However, reducing voxel size decreases the signal. To maintain a comparable signal-to-noise ratio (SNR), longer scans (i.e., for signal averaging), reduced noise levels, and higher field strengths are necessary. Although pre-clincal scanning sessions can be longer than possible in clinical settings (>1hr), limitations arise when using anaesthesia (Jelescu et al., 2022), and ethical considerations remain. As such, SNR gains are typically achieved by using higher field strengths (>3T), with much

stronger and/or faster switching magnetic field gradients (∼140–1500mT/m), and specialised radiofrequency coils (Jelescu et al., 2022). These advances in hardware and acquisition methods have allowed pre-clinical imaging to access the mesoscopic scale.

It is further possible to probe mesoscopic features of brain anatomy in fixed tissue *ex vivo*, as a higher spatial resolution (100-200μm) and SNR can be achieved if scanning sessions are longer (i.e., over days instead of hours) and free of motion and physiological noise (Oguz et al., 2013; Maranzano et al., 2020). The contrast-to-noise ratio (CNR) can also be higher *ex vivo* due to the chemical changes caused by fixation (Benveniste and Blackband, 2002) and the optional use of contrast agents (e.g., gadolinium, Sharief and Johnson (2006)). *Ex vivo* MRI can be performed with human tissue post mortem, clinical samples (e.g., biopsies), or experimental animals, as shown in Figure 2.1.

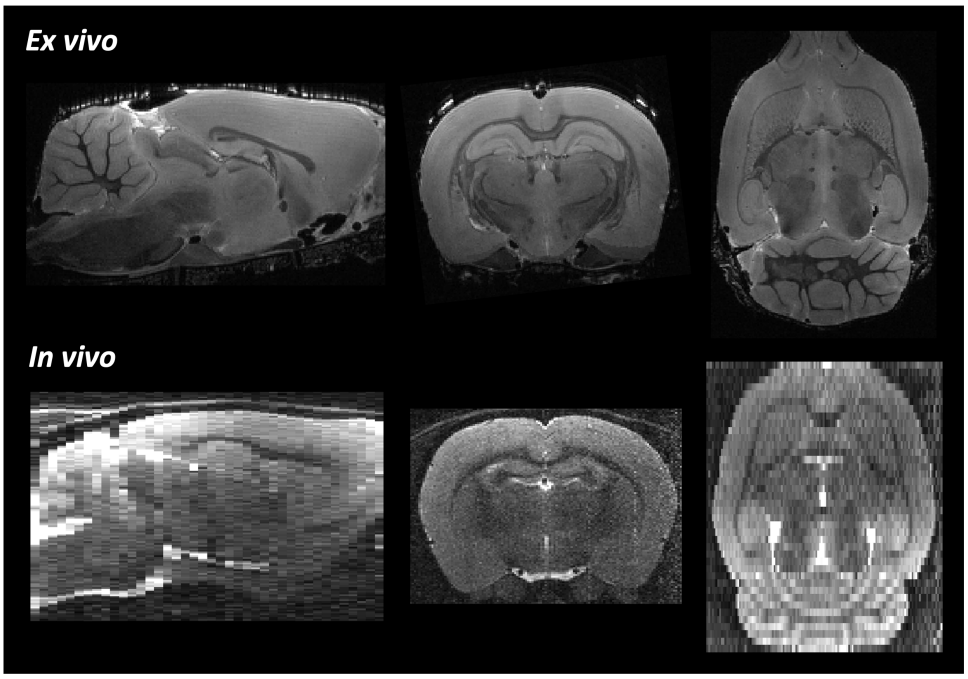


Figure 2.1: Comparison of rat MRI acquired *ex vivo* (above, 100μm isotropic) versus *in vivo* (below, 125x100x500μm) using a T2-weighted RARE sequence. Although the voxel size for the two datasets are roughly similar, the spatial resolution of the *ex vivo* sample is higher than that of the *in vivo* acquisition (dataset provided by Dr Tracy Farr).

Despite the numerous advantages and versatility of MRI, an important limitation remains; many modalities only provide indirect estimates of brain features. Conventional MRI measures the signal emitted by hydrogen atoms (e.g., in water molecules) within tissue after the application of a sequence of electromagnetic pulses and spatially varying magnetic field gradients. As the signal associated with each imaging voxel varies with the local density of protons and the tissue micro-environment, researchers can infer various features of brain anatomy, such as the size, shape, and biophysical properties of different structures (Weiskopf et al., 2021). However, this estimation/inference process can vary in terms of complexity and indirectness depending on the modality used. As a result, MRI can provide sensitive markers of tissue change, which are however not necessarily specific.

For example, in diffusion magnetic resonance imaging (dMRI), the modality of choice for probing microstructure and connectivity in the brain (Assaf et al., 2019), many different approaches have been developed to decode the measurements obtained into biologically meaningful features of brain structure (Alexander et al., 2019). Such inference processes can pose challenges in interpreting imaging contrasts and the changes detected with them (Jelescu et al., 2020). As such, it is important that we keep these challenges in mind when considering microstructural MRI in more detail.

2.2.2 Diffusion MRI for Probing Brain Microstructure

Diffusion MRI is a powerful technique which provides detailed insight into brain microstructure *in vivo* (Bastiani and Roebroeck, 2015). The benefit of conducting this form of non-invasive 'virtual histology' is that the entire brain can be imaged *in situ*. Non-invasive imaging of brain microstructure is possible as dMRI is sensitive to the random (i.e., thermally driven)

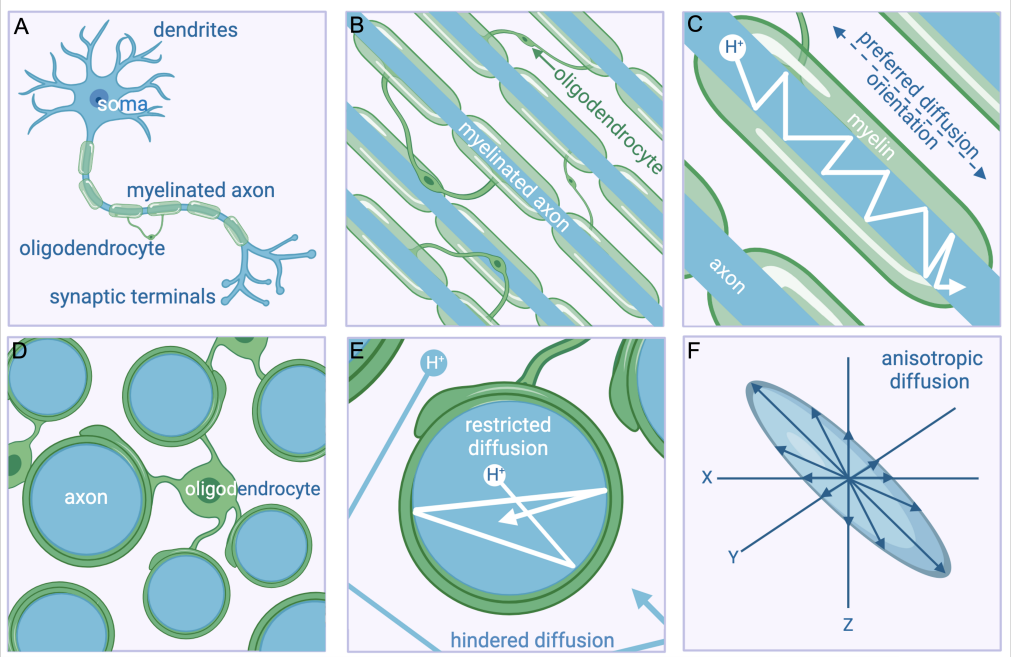


Figure 2.2: Exploring the brain with diffusion MRI. A) A schematic representation of a neuron, alongside a neighbouring oligodendrocyte. Oligodendrocytes, a specialised class of glial cells, form the myelin sheaths that insulate neurons in the central nervous system. B) A longitudinal section of an axonal bundle in the brain's white matter, enlarged in C) to demonstrate that the displacement of diffusing protons primarily occurs along the axon's length, as this path has fewer obstacles. D) A cross section of an axonal bundle, expanded in E) to illustrate that diffusion of protons within axons is restricted by cell membranes and myelin, whilst diffusion in the extracellular space is hindered by neighbouring cells. F) Visualisation of a diffusion tensor (ellipsoid) within a white matter imaging voxel. The tensor represents the magnitude and directionality of diffusion, with the longest axis indicating the average direction of white matter fibres in the voxel. Note that an imaging voxel typically encompasses a volume of $\sim$1mm^3, while axon diameter ranges between 1-5μm.

displacement of water molecules as they diffuse through neural tissue over time. At body temperature and over typical diffusion times (typically tens of milliseconds), the displacement of signal-bearing water molecules is on a cellular scale (i.e., $\sim$microns), as shown in Figure 2.2. Therefore, the path taken by diffusing water molecules will depend on the tissue's microstructure and the presence of structural barriers (Le Bihan, 1990). For instance, diffusion is isotropic (i.e., equal in all directions) within the ventricles, due to the absence of barriers. However, in white matter, diffusion

is anisotropic as it will be larger along the length of a tightly packed bundle of axons compared to across them, due to the barriers imposed by the axonal membranes and layers of myelin. Local measures of diffusion can provide information about cellular boundaries in the tissue (i.e., a large versus small displacement resulting from free versus restricted diffusion) and whether these boundaries are systematically coherent (e.g., as with axons bundled together in a white matter tract). Therefore, features derived from the measured diffusion profile/scatter pattern of water can be indirectly linked to the underlying microstructural properties (Beaulieu, 2002).

In white matter, the preferred diffusion orientation (PDO) will be along white matter bundles. Therefore, the PDO can be used to infer the orientation of an axonal bundle. By piecing together local measures of diffusion orientation, one can reconstruct in 3D the orientation where diffusion is greatest (i.e., the direction where diffusion is least restricted), which we infer to be the path taken by an axonal bundle. This method, referred to as tractography (Basser et al., 2000), has been described as *in vivo* 'virtual dissection' (Catani et al., 2002), as it allows the trajectories of white matter tracts, which connect different brain regions, to be estimated from measures obtained *in vivo* using dMRI. In fact, dMRI is the only non-invasive technique that can be used to study the structural connectivity of the brain (Zhang et al., 2022).

Diffusion MRI and tractography can be used to comprehensively map out the extrinsic anatomical connections between functionally specialised brain areas (Sotiropoulos and Zalesky, 2019; Van Essen et al., 2013; Sporns et al., 2005). This map of connections, referred to as a connectome, provides detailed insight into how the brain is organised. Because patterns of connectivity constrain the interaction and transfer of information between different regions, as well as the possible neural computations, brain connectivity has

functional implications on a systems-wide level (Denk et al., 2012). Therefore, dMRI and connectomics (i.e., the production/study of connectomes) are crucial for advancing our understanding of diseases and developing new therapeutics (Silasi and Murphy, 2014). Furthermore, since the pattern of connections between each functional brain unit and the rest of the brain is unique, connectomics can also be used to investigate variability between individuals, species, or developmental stages (Mars et al., 2018; Warrington et al., 2022).

Yet despite the potential of all these applications, dMRI cannot provide the vivid anatomical detail of classical histology. This is because the dMRI signal is averaged over the volume of tissue ($\sim$1mm^3) within an imaging voxel. This large volume can contain a wide range and large number of cellular, axonal, and dendritic processes (e.g., see variability in the fibre composition of the corpus callosum, Aboitiz et al. (1992)) so dMRI is limited to statistical descriptions of the tissue. Furthermore, multiple changes in the tissue's microstructure can produce a similar change in the dMRI signal (Jelescu et al., 2020). Decoding the information contained within the diffusion signal to generate a parameter map of microstructural tissue features, is therefore a challenging, and in general ill-posed, problem (Thomas et al., 2014). Researchers have developed different modelling approaches, which relate microstructural features with the dMRI signal, in attempts to mitigate this problem (Novikov et al., 2018). However, these processes have to make assumptions (e.g., about diffusivity or the fibre orientation distribution function) to constrain modelling parameters (Alexander et al., 2019).

Modelling Microstructure

The most common approach for analysing dMRI data is diffusion tensor imaging (DTI), which assumes a zero-mean Gaussian distribution (i.e., homogeneous and non-restricted) of diffusion displacements within tissue for the time diffusion is measured (Basser and Pierpaoli, 1996; Basser et al., 1994). DTI represents the diffusion scatter pattern of water as an ellipsoid/tensor, whose orientation, elongation (fractional anisotropy, FA), and average diameter (mean diffusivity, MD) will change according to the underlying tissue microstructure. Diffusion kurtosis imaging (DKI) was an early extension of the DTI model that captured non-Gaussian diffusion (kurtosis is a deviation from Gaussian behaviour, Jensen et al. (2005)). Although these approaches are simplistic, DTI/DKI metrics are very sensitive to changes in tissue microstructure (Pierpaoli and Basser, 1996). For instance, a change in fractional anisotropy or mean kurtosis can indicate demyelination, axonal degeneration, and/or inflammation (Bodini and Ciccarelli, 2009). However, these metrics lack specificity and fail in regions with high complexity. For example, in regions containing crossing fibres, the tensor will represent the mean diffusion along all the fibres in the voxel (Wheeler-Kingshott and Cercignani, 2009).

Building upon the idea of DTI to provide higher specificity, several models simplify brain tissue as a combination of different compartments (e.g., intracellular versus extracellular, intra-axonal versus extra-axonal), as shown in Figure 2.3 (Panagiotaki et al., 2012). These models aim to allow researchers to infer parameters from the diffusion signal which are more biologically interpretable. This could be, for example, the density of fibres, water fraction in different cell types, or membrane permeability. To achieve this, such models integrate complex biophysical descriptions of each tissue compart-

ment's architecture with formulations of the diffusion process (i.e., hindered extra-axonal diffusion versus restricted intra-axonal diffusion) in each of these environments (Jelescu et al., 2020). The observed signal is expressed as a linear weighted combination of such compartments; hence they are commonly termed as multi-compartment models (Panagiotaki et al., 2012).

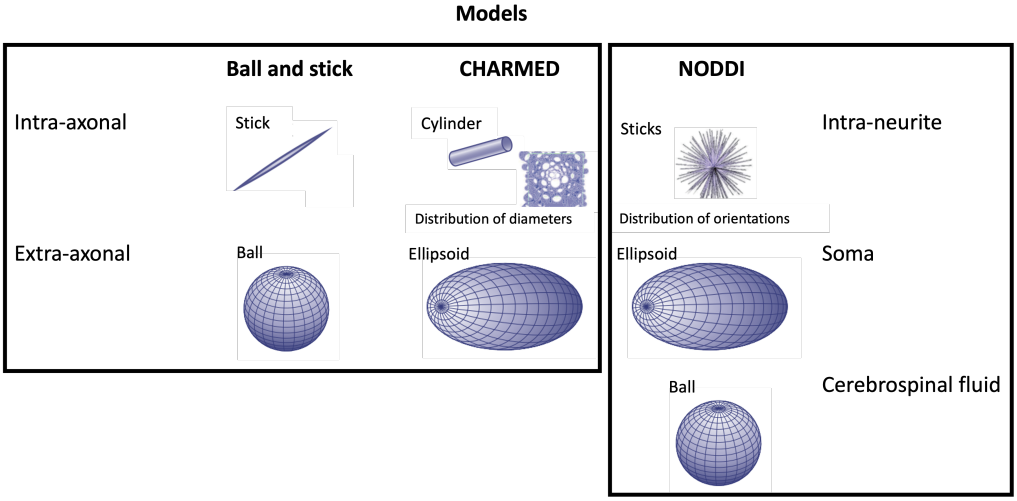


Figure 2.3: Overview of three different multi-compartment diffusion models.

Figure 2.3 shows how assumptions about the diffusion profile are related to the microstructure of the tissue compartments. For instance, the 'ball and stick' model (Behrens et al., 2003) assumes that extra-axonal diffusion is isotropic (i.e., ball), whilst intra-axonal diffusion is restricted and perfectly anisotropic (i.e., stick). In contrast, the composite hindered and restricted model of water diffusion (CHARMED) assumes that intra-axonal diffusion is restricted within cylinders of varying diameter, whilst extra-axonal diffusion can be described using an ellipsoid/tensor (Assaf and Basser, 2005). More recently, the neurite orientation dispersion and density imaging (NODDI) model was developed to disentangle the factors that contribute to fractional anisotropy (i.e., the elongation of the DTI tensor, Beaulieu (2002)) into indices that relate more specifically to tissue microstructure, so that these can be analysed independently. As the name suggests, NODDI allows for the estimation of neurite (i.e., axons and dendrites) density and orientation

dispersion (Zhang et al., 2012). The model achieves this by relaxing the assumption of fibre orientation homogeneity. Instead, NODDI assumes that intra-neurite diffusion can be modelled as a set of sticks which can be coherent in orientation, as axons are in the corpus callosum, or dispersed, as dendrites are in the cerebral cortex. In addition, diffusion is modelled as an ellipsoid in the cell bodies (i.e., soma) of neurons and glia, where it is hindered, whilst diffusion is modelled as a ball in the ventricles/cerebrospinal fluid, where it is isotropic. A major advantage to NODDI is that the protocol is feasible *in vivo* using standard clinical MRI scanners and sequences.

Ultimately, the measures derived from these multi-compartment models also have limited specificity, because we lack precise information about the tissue compartments and their contributions to the diffusion signal. This is exacerbated further by limits in our understanding of how well biophysical models can cope with changes introduced by disease (Jelescu et al., 2020). The tissue parameters are also often degenerate as multiple sets of parameters, some of which fall within biologically plausible ranges, can fit the signal equally well (Jelescu et al., 2016). The limitations in our ability to decode the diffusion signal into biologically meaningful measures that are specific and sensitive to the tissue microstructure is one of the biggest challenges facing the field (Novikov et al., 2018) as researchers need confidence in the accuracy of these measures for them to make sound conclusions.

There is also an additional level of complexity to consider. Some biophysical models, designed for tractography, aim to resolve the number of major fibre orientations within a voxel (Seunarine and Alexander, 2014). However, accurately determining the number and orientations of crossing fibre populations presents numerous challenges, particularly in regions where multiple fibre populations converge, such as the centrum semiovale. Moreover, dif-

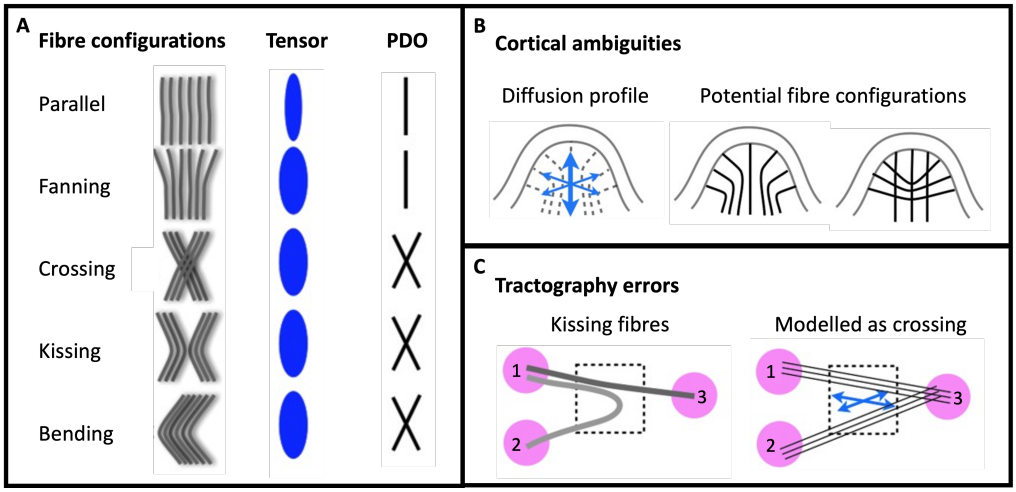


Figure 2.4: Ambiguities in mapping diffusion to axon geometry. A) Different axonal geometries can have a similar tensor profile. Modelling crossing fibres (e.g., two populations) allows for more than one preferred diffusion orientation (PDO). This can help distinguish some, but not all, of the cases. More elaborate models are needed to distinguish between increasingly complex configurations. B) In a cortical gyrus, the same diffusion profile could have very different implications for connectivity. This makes it challenging to determine how axons spread to various locations in the cortex. C) Tractography errors can arise when kissing fibres are modelled as crossing fibres as this can cause the algorithm to jump from one track to another, resulting in false positives (e.g., incorrectly identifying a connection between areas 2 and 3) and false negatives (e.g., missing the connection between areas 1 and 2). Modified from Jbabdi and Johansen-Berg (2011).

ferent fibre configurations can produce similar diffusion profiles, as shown in Figure 2.4. Models can also widely differ in their assumptions, such as the crossing angle of fibre populations or their curvature range, as there is debate over what is anatomically plausible, particularly in the cortex. These complexities can lead algorithms astray, with 'wrong turns' resulting in false positives and negatives. International challenges have underscored that even state-of-the-art methods of tractography are not immune to these limitations (Maier-Hein et al., 2017; Schilling et al., 2019b). Hence, to improve accuracy, there is a critical need for validation of microstructural models, and their use in tractography.

While phantoms or simulated data, which have a known ground truth, are

valuable for testing microstructural models and tractography algorithms, they offer only a simplified representation of the brain's complexity. Gaining accurate insights into the anatomy of the real brain requires direct observation of tissue architecture, typically performed *ex vivo*. Combining MRI with complementary techniques, such as optical imaging and microscopy, on the same sample offers a promising avenue for validation, as these methods directly visualise tissue microstrucure with superior resolution and specificity (Dyrby et al., 2018).

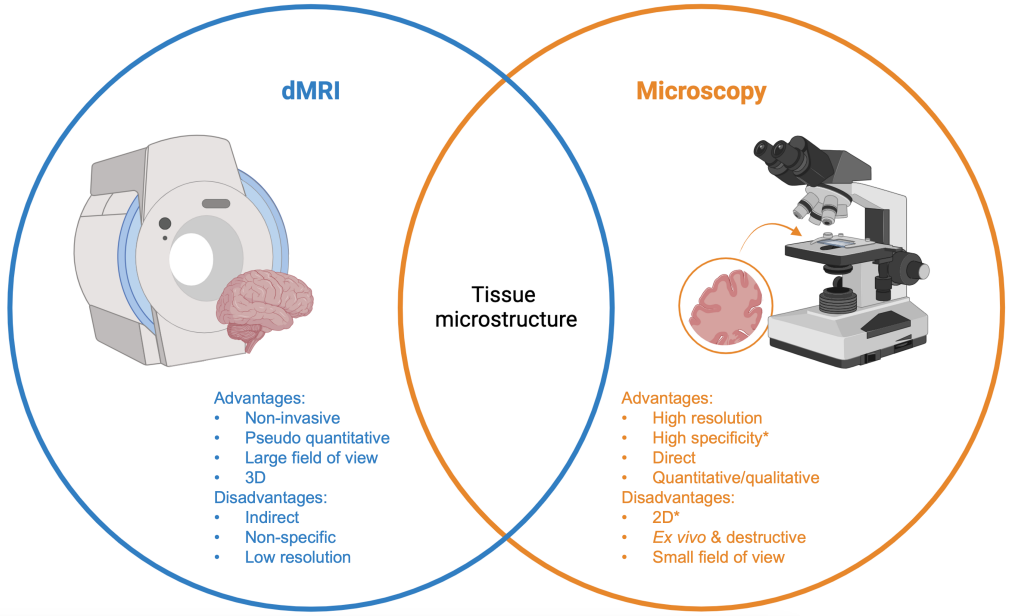


Figure 2.5: Despite important distinctions between these imaging modalities, microscopy and diffusion MRI can be used to study the same microstructural features (e.g., fibre orientation). By taking advantage of the breadth of information provided by these complementary techniques, it becomes possible to improve our understanding of the brain's complex tissue architecture and connectivity patterns. *The specificity of microscopy is dependent on the source of contrast. For example, well optimised tissue staining protocols should have low levels of non-specific staining. Also, some optical imaging techniques, such as confocal microscopy, are 3D.

Integrating MRI with microscopy (Howard et al. (2019)), as represented in Figure 2.5, can help us to understand the limitations of biophysical models and refine them so that they match observed tissue characteristics better (Alexander et al., 2019). This can assist in transforming sensitive

MRI markers to also being specific in what tissue changes they represent. Furthermore, combining these techniques can provide constraints for model parameters, thereby enhancing the accuracy of microstructural measures derived from MRI (Howard et al., 2019) and mitigating biases introduced by brain-wide assumptions. We discuss optical imaging and microscopy in more detail below, with a focus on how they can be used to validate and refine microstructural measures derived from MRI.

2.3 Optical Imaging and Microscopy

Optical imaging of brain tissue *ex vivo* is often considered the gold standard for evaluating or complementing MRI contrasts (Lazari and Lipp, 2021; Yendiki et al., 2022), reflecting its historical role as a primary means of understanding brain organisation and anatomy. While the invention of the light microscope in the 17$^{\text{th}}$ century marked a significant breakthrough in biology, it was the development of histological stains like Golgi and Nissl in the early 20$^{\text{th}}$ century that revealed the cellular and structural intricacies of brain tissue. By selectively labelling specific structures, such as neurons and neuronal connections, these stains enabled the differentiation of various cell types, cortical layers, and brain regions (Brodmann, 1909; Vogt and Vogt, 1903), based on cell morphology (cytoarchitectonics) and myelination (myeloarchitectonics).

Light microscopy has experienced a renaissance in the 21$^{\text{st}}$ century, thanks to remarkable advancements in tissue preservation, labelling techniques, and optics, as well as increases in computational power and automation (Balasubramanian et al., 2023). In this section, we explore the optical imaging techniques that complement dMRI (Yendiki et al. (2022)), summarised

in Table 2.1. We begin by highlighting the opportunities provided by light microscopy, before discussing how tissue sectioning and two-dimensional (2D) microscopy make comparison with MRI challenging. Then, we introduce next-generation approaches for tissue preparation, and new forms of 3D microscopy, which are poised to become the neuroanatomy tools of the future. In this way we demonstrate the vital role of microscopy in unravelling the complexities of brain architecture and organisation.

Technique	Scale	Dim	Feasible *in vivo*	Tissue staining needed	Multi-step registration to dMRI[#]
dMRI	mm	3D	✓		
PLI	↑	2D			✓
PS-OCT	μm	2D			
Light sheet microscopy		3D		✓*	
Widefield microscopy		2D		✓*	✓
Confocal microscopy	↓	3D		✓*	✓

Table 2.1: Overview of techniques used to explore tissue microstructure, which are discussed in more detail below (PLI: polarised light imaging, PS-OCT: polarisation-sensitive optical coherence tomography). The techniques are listed according to their resolution, ranging from a scale of ∼1mm for dMRI (upper limit) to ∼0.2μm for confocal microscopy (lower limit). [#]When combining dMRI with optical imaging of a thin tissue section or a small sample of brain tissue, rather than the whole organ, a complex multi-step registration is required. *Tissue staining is not necessary if contrast is provided by autofluorescence or endogenous expression of fluorescent proteins (e.g., as in transgenic mouse lines or mice infected with viral vectors).

Optical approaches are very versatile and offer myriad opportunities for studying biological systems, ranging from imaging single molecules and live cells to probing dynamic physiological functions, such as neuronal activation, signalling mechanisms or brain development, in real time. They encompass a diverse range of techniques, which are compatible with different labelling and imaging modalities and can be adapted to various experimental systems and resolutions. These features make optical imaging an indispensable tool

for advancing our understanding of brain structure and function.

Although there are some approaches which are designed to be minimally invasive, optical imaging of tissue microstructure is usually performed *ex vivo* on small samples of tissue rather than entire brains. This is due, in part, to a trade-off between FOV and image resolution. In addition, conventional microscopy is predominantly 2D and performed on thin sections of tissue to mitigate issues like image blurring and signal attenuation, which are caused by the scattering and absorption of light as it passes through tissue (Luker and Luker, 2008). These factors introduce numerous challenges when integrating and comparing conventional 2D optical imaging with 3D MRI, as outlined below.

2.3.1 Conventional 2D Approaches

Researchers often rely on 2D optical imaging techniques when comparing microstructural measures from dMRI and microscopy (Yendiki et al., 2022) as they are relatively quick and straightforward. 2D microscopy is also easier to automate (i.e., slide scanners), which allows for higher throughput. Although conventional 2D approaches are diverse, they can be split into two main categories: label-free methods and those which require exogenous contrast agents (Luker and Luker, 2008). Figure 2.6 provides a a side-by-side comparison of of these approaches.

Label-free techniques, such as polarisation light microscopy (PLI) and polarisation-sensitive optical coherence tomography (PS-OCT), exploit contrast arising from the interaction of light/photons with myelinated axons, a phenomenon known as birefringence. PLI measures how the polarisation state of light is altered when transmitted through thick sections

of brain tissue (50-100μm) and provides an in-plane resolution of ~1-100μm and a large field-of-view (<300cm^2). In contrast, PS-OCT uses optical interferometry to detect changes in the polarisation of light reflected (i.e., back-scattered) from tissue blocks, achieving resolutions of 1-20μm for imaging depths of ~1mm. Once the superficial layer of the tissue block has been imaged, it is sectioned to expose the subsequent layer. The development of these label free imaging approaches over the past 30 years marked an important breakthrough in light microscopy (Wang et al., 2020c), as they allow direct measurement of microstructural properties like fibre orientation (Axer et al., 2011; Wang et al., 2018a), without the need for multiple labelling steps or risk of signal loss due to photobleaching.

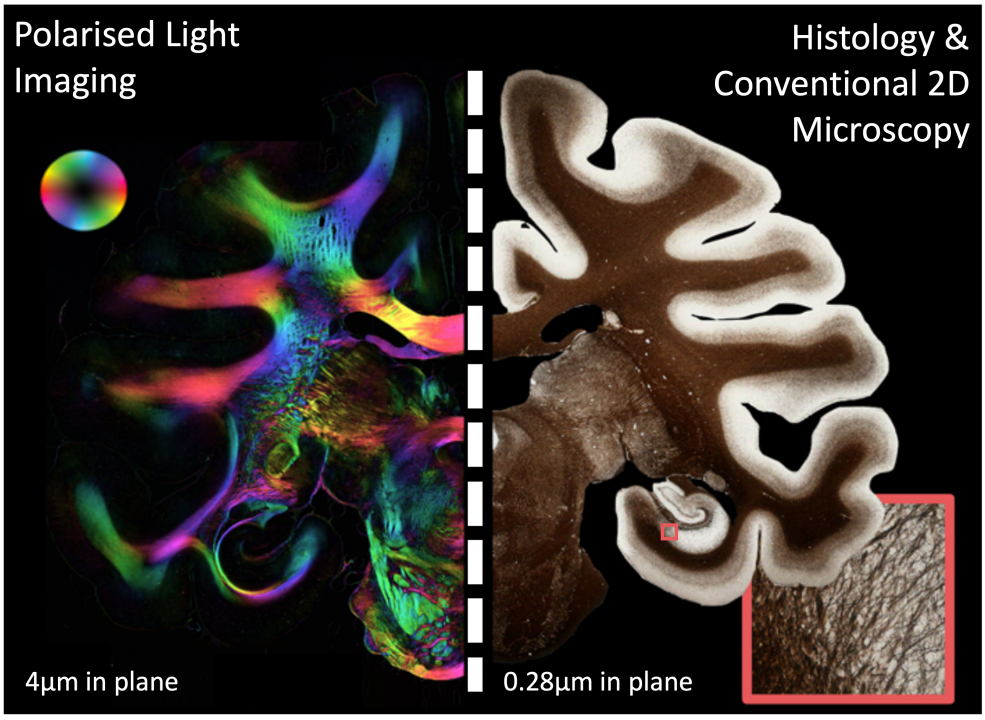


Figure 2.6: Comparing label-free approaches with tissue staining in a 50μm coronal section of macaque brain. Polarisation light microscopy (PLI), with a resolution of 4μm, is shown on the left. The pseudocolours correspond to orientations represented in the 2D colour wheel (L/R red, S/I blue). Myelin staining with Gallyas silver, imaged using conventional microscopy at 0.28μm resolution, is shown on the right. An enlarged region from the hippocampus highlights the detailed structure of myelinated fibres. Despite their differences, both modalities effectively capture the intricate myeloarchitecture. Modified from Howard et al. (2023).

The second category of imaging methods rely on exogenous contrast agents or labels to introduce signal or enhance tissue contrast before microscopy. These agents include histological stains, lipophilic dyes, tracers, oligonucleotide/RNA probes, nanobodies, and antibodies, conjugated to enzyme reporters or fluorescent labels (i.e., fluorophores). Fluorescent proteins may also be genetically encoded in experimental animals (e.g., mouse lines) or introduced into a specific cell population using helper viruses (Saleeba et al., 2019). This contrast is then visualised, usually with widefield microscopy, which uniformly illuminates the entire specimen with white or fluorescent light. As the name suggests, widefield microscopy has a relatively large FOV (millimetre scale). As such, it enables fast imaging of thin sections ($\sim$5-20μm) with high resolution ($\sim$0.2-1μm).

In multiplex imaging, microscopy is used to visualise and analyse several molecular targets or biological features (e.g., astrocytes, myelinated axons, inhibitory interneurons, etc) within the same sample. This is achieved using probes or antibodies conjugated to fluorophores that emit light at different wavelengths. The multiple targets can then be visualised and separated using excitation/emission filters or spectral imaging techniques. This provides a more complete picture of tissue microstructure than standard labelling methods.

While conventional 2D approaches have many advantages, tissue sectioning introduces numerous challenges when integrating and comparing optical imaging with MRI, as depicted in Figure 2.7. To begin with, additional steps, such as fixation, processing and embedding (e.g., in paraffin wax), are required to preserve the delicate microstructure of the tissue during sectioning. These procedures require expertise and extend the labour and time invested in microscopy, whilst also potentially altering tissue characteristics and introducing variability.

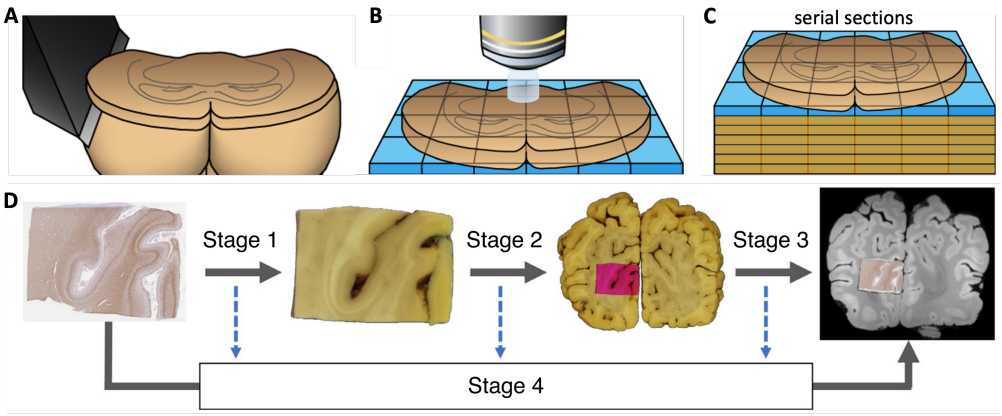


Figure 2.7: Challenges associated with tissue sectioning and 2D microscopy. A) Sections are cut from a tissue block, mounted on slides, and usually stained. B) As the field of view is limited in most forms of light microscopy, multiple images (i.e., tiles) need to be stitched together to create a mosaic image of the whole tissue section. C) If necessary, the sample can be reconstructed by aligning and stacking serial sections, however, this is labour-intensive. D) To compensate for the distortions and artefacts caused by sectioning, a complex multi-stage registration framework is required (Huszar et al., 2023). Although there are different strategies to integrate microscopy and MRI, a novel approach allows for registration of a stand-alone section to MRI, so that hundreds of serial sections are no longer necessary. First the microscopy image is registered to a block-face photograph, taken before sectioning, to correct for cutting distortions. Then, the image in 'block-face space' is registered to a photograph of the coronal brain slab. This facilitates the subsequent registration to MRI. However, each registration step has multiple free parameters that have to be specified, and registration quality will be impacted by artefacts.

More importantly, cutting tissue into thin 2D sections introduces irreversible section-unique non-linear physical deformations and artefacts, such as tears, folds, and bubbles, to the tissue (Taqi et al., 2018). A complex multi-stage registration framework is required to compensate for the cutting distortions and to integrate 2D microscopy with 3D MRI. Most of these frameworks require serial tissue sections, which are aligned to each other and stacked, as shown in Figure 2.7A-C), to reconstruct the sample in 3D, before registration of the resulting image volume to MRI. However, generating a coherent 3D reconstruction of the sample is labour-intensive and error-prone as sections can be lost or flipped unintentionally.

New tools (e.g., Huszar et al. (2023)) allow for registration of stand-alone sections to MRI via two photographic intermediaries, as shown in Figure 2.7D). However, each registration step has multiple parameters, including the deformation model, similarity and regularisation metrics, interpolation method, etc., which will need to be specified appropriately (Yendiki et al., 2022). This requires significant expertise. Furthermore, registration will still be affected by artefacts. Therefore, preserving the complex spatial organisation of structures within tissues and using 3D optical imaging techniques (Zhu et al., 2017) provide an attractive alternative.

2.3.2 Modern 3D Approaches

3D approaches image a volume of tissue, as opposed to a thin slice. The volume can range from a 3D tissue section to a whole organ. In the first approach, tissue is cut into thicker slices (50-100μm) as these suffer less severe distortions than those typically used (5-20μm). Thicker sections are often imaged with confocal microscopy, as it allows for the whole depth of the section to be sampled and minimises the out-of-focus light with a pinhole aperture (Ntziachristos, 2010). Confocal microscopy, which primarily uses fluorescence, provides superior contrast and resolution ($\sim$0.2μm) than wide-field microscopy, but is slower as it has a much smaller FOV. Consequently, scanning the full specimen requires the acquisition of significantly more images, referred to as tiles, which need to be stitched together. The sample is also vulnerable to photobleaching, as the whole volume is illuminated with a focused laser beam while each optical section (i.e., focal plane) is scanned, and a high-intensity is required to maintain signal strength at depth.

Nevertheless, the spatial information destroyed during tissue sectioning

remains irretrievable. Any structures which are crossing or are between sections cannot be studied, thereby significantly reducing the microstructural information available from microscopy. Furthermore, once a sample is sectioned and mounted on a slide for imaging, it is also impossible to view it along a different orientation/anatomical plane. These constraints severely impede our ability to investigate and understand the complex 3D organisation of the brain.

In an alternative approach, tissue sectioning is not necessary, due to the development of novel clearing techniques (Costantini et al., 2019; Tian et al., 2021) and light sheet microscopy (Dodt et al., 2007; Huisken, 2004), as shown in Figure 2.8. By combining these methods (Pawłowska et al., 2019), it is possible to optically (as opposed to mechanically) section tissue along multiple orientations, thereby preserving the 3D spatial organisation of structures within tissues.

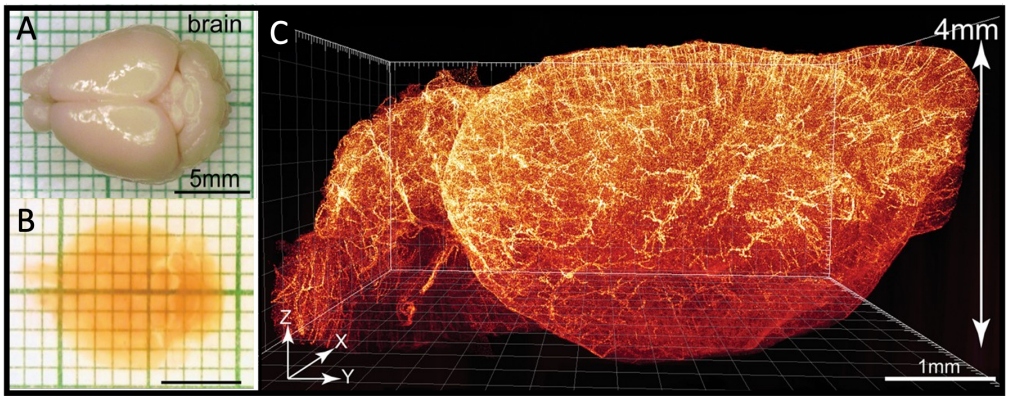


Figure 2.8: Demonstration of the power of combining tissue clearing techniques with light sheet microscopy to facilitate high speed whole-brain imaging. The adult mouse brain A) before and B) after tissue clearing with a solvent-based method. C) Light sheet microscopy was used, in this case, to image the vasculature system of the whole brain at sub-cellular resolution within 5 hours. Modified from Jing et al. (2018).

We will discuss how different clearing techniques can be used to render a tissue transparent, and the various advantages and disadvantages of these methods. Then, we will describe how light sheet microscopy allows for rapid

high-resolution imaging of intact tissue samples.

2.3.3 Tissue Clearing

The development of tissue clearing techniques is a recent and highly significant advancement as they allow structures deep within a tissue to be visualised, without the need for mechanical sectioning (Ntziachristos, 2010). Clearing techniques reduce the optical inhomogeneities in the sample, thereby minimising the image blurring and signal attenuation which results from scattering and absorption of light as it passes through tissues (Yu et al., 2021). These methods can be categorised according to whether they adopt a hydrogel/tissue transformation approach, or use aqueous solutions or organic solvents (Molbay et al., 2021). The field is rapidly evolving (Zhu et al., 2017), but some commonly used protocols are summarised in Table 2.2.

Technique	Description	Time	Pros	Cons
CLARITY	Tissue transformation/ hydrogel-based embedding clearing	Weeks	Strong clearing capability, neuron morphology preserved, well optimised for mouse	Tissue expansion, electrophoresis equipment required, challenges with immunostaining
CUBIC	Hydrophilic hyperhydrating detergent-based clearing	Days/ Weeks	Less expansion than CLARITY; immunostaining possible	Some tissue expansion or shrinkage, protein loss during clearing
3DISCO	Hydrophobic organic solvent-based clearing	Hour/ Days	Strong clearing capability	Fluorescence quenching, tissue shrinkage
iDISCO	Hydrophobic organic solvent-based clearing	Hours	Method optimised for immunostaining	Some tissue shrinkage

Table 2.2: Comparison of commonly used methods developed for clearing the mouse brain. Tissue transparency, size deformation, compatibility with immunostaining, fluorescence preservation, speed, and conservation of tissue architecture are key criteria.

In **hydrogel-based clearing techniques** (Gradinaru et al., 2018), samples are transformed into a tissue-hydrogel hybrid, followed by the removal of 'light scatterers', primarily lipids, which have a higher refractive index than

water. This process facilitates unimpeded light transmission, whilst also retaining proteins and neuronal morphology. The seminal method was CLARITY (Cleared Lipid-exchanged Acryl-hybridized Rigid Immunostaining/In situ hybridisation-compatible Tissue-hYdrogel), wherein the sample was infused with a hydrogel that was polymerised to act as a scaffold, followed by lipid dissolution and removal (i.e., clearing), using sodium dodecyl sulfate (SDS), an ionic detergent (Chung et al., 2013). As passive diffusion of large detergent micelles through tissue is very slow, electrophoresis equipment was used to accelerate delipidation.

In the original CLARITY protocol, the removal of lipids left the tissue softer and caused significant expansion (Chung et al., 2013). Some researchers capitalised on this expansion for nanoscale imaging of cellular structures like synapses, which are usually beyond the resolution of standard light microscopy (Parra-Damas and Saura, 2020). Efforts have been made to mitigate expansion, initially by using a passive form of CLARITY (i.e., without electrophoresis), but this method was only feasible for sections of tissue and took a considerable amount of time (Tomer et al., 2014). Since then, a new method of tissue preparation has been developed, which uses a flexible polyexpoxide to introduce controlled intra- and intermolecular cross-links between biomolecules. This method, named SHIELD (Stabilisation under Harsh conditions via Intramolecular Epoxide Linkages to prevent Degradation), protects tissue architecture against deformation during electrophoretic-driven delipidation (Park et al., 2019). In addition to addressing sample expansion, this method preserves protein fluorescence and retains antigenicity.

Although staining of CLARITY-cleared tissue was initially challenging (Jensen and Berg, 2017), combining electrophoresis with eFLASH (electrophoretically driven Fast Labelling using Affinity Sweeping in Hydrogel),

a technique which dynamically modulates chemical transport and reaction kinetics, has accelerated antibody penetration and improved distribution (Yun et al., 2019). This new approach is able to uniformly label an intact mouse brain in <24hours. Multiplex imaging is also now possible in CLARITY-cleared samples, as the SWITCH (System-Wide control of Interaction Time and kinetics of Chemicals) protocol makes the tissue-hydrogel hybrid resistant to heat and chemicals, thereby preserving sample integrity and securing tissue microstructure during multiple staining rounds (Murray et al., 2015). As such, CLARITY remains the most advanced clearing method and has been pivotal in dMRI validation studies with human (Leuze et al., 2021; Morawski et al., 2018) and rodent tissue (Goubran et al., 2019; Stolp et al., 2018; Johnson et al., 2023).

In the second category of clearing methods, delipidation and refractive index matching is achieved using either **hydrophobic** or **hydrophilic** reagents. Hydrophobic protocols, like 3DISCO (3D Imaging of Solvent-Cleared Organs), use organic solvents with higher refractive indices than water to dehydrate and delipidate samples (Ertürk et al., 2012). Variations of DISCO protocols remain a popular choice as they achieve excellent transparency while being reliable and easy to implement (Molbay et al., 2021). Alternatively, hydrophilic methods, like CUBIC (Clear, Unobstructed Brain Imaging Cocktails and Computational analysis), use detergents for delipidation, and hyperhydrating agents, such as urea, to expand tissues, thereby reducing the average refractive index (Susaki et al., 2015; Matryba et al., 2018). Aqueous protocols efficiently preserve fluorescent proteins, in contrast to organic solvents, which can also denature antigen-binding sites.

Although there is some variation, hydrophobic protocols are usually fastest, taking hours or days as opposed to weeks. Some organic solvent-based methods, such as iDISCO (immunolabelling-enabled 3D Imaging of Solvent-

Cleared Organs), still preserve antigenicity if properly optimised (Renier et al., 2014; Silvestri et al., 2016). However, not all microscopes are compatible with organic solvents as these have a high refractive index and are corrosive. In addition, the removal of water means that the sample shrinks and increases in density. However, this shrinkage is usually small when compared to the expansion that was seen with the original CLARITY protocol.

There are challenges common to all tissue clearing techniques. One major limitation is sample size, as successful clearing is typically achieved only with small samples (e.g., $\sim$1cm^3 or $\sim$3x3x0.5cm). However, such sizes often present difficulties in achieving consistent tissue staining. When relying on passive diffusion for immunolabelling, long incubation times and large quantities of antibody are required due to poor antibody penetration (Tian et al., 2021). The choice of fluorophore or fluorescent protein must also be carefully considered as tissue autofluorescence is common in the blue-green range and light scattering is more prominent with shorter wavelengths. As a general rule, it is best to use fluorophores in the red/far red spectrum (Pawłowska et al., 2019).

Certain tissues pose additional challenges, necessitating tailored protocols. For example, brain tissue has a relatively high lipid content, a factor that can increase with age (Hammelrath et al., 2016; Downes and Mullins, 2014) and vary significantly between species, according to the amount of myelination. Clearing aged human brains is particularly challenging (Rusch et al., 2022) due to the build up of lipofuscin, a breakdown product of old red blood cells, and neuromelanin (Moreno-García et al., 2018). Despite efforts, there is still not a clear method of removing these pigments, which can interfere with imaging by absorbing light (Molbay et al., 2021).

Although tissue clearing has been transformative in pushing the frontier of optical imaging to greater depths, light sheet fluorescence microscopy (LSFM) has been pivotal in extending this capability to whole-brain mapping on a microscopic level, as discussed below (Ntziachristos, 2010; Jiang et al., 2023).

2.3.4 Light Sheet Fluorescence Microscopy

LSFM is an important and innovative tool that facilitates fast volumetric imaging of intact tissue samples, organs, or organisms, which are transparent (e.g., zebrafish) or have been optically cleared (Dodt et al., 2007). For example, within just a few hours, LSFM can capture the intricate microstructural features of an entire mouse brain in 3D (Tomer et al., 2014). With spatial resolution of $\sim$1μm, LSFM bridges the gap between *ex vivo* MRI and confocal microscopy (Santi et al., 2009), whilst penetrating depths of $\sim$10mm. This form of fluorescence microscopy has been transformative because it scales up investigations to large samples and therefore reduces the bias that is inevitable when only a limited number of slides from a selected region can be studied (Ueda et al., 2020).

LSFM is sometimes referred to as selective plane illumination microscopy (Huisken, 2004) as it uniformly illuminates a single plane (i.e., optical section) of the sample, as shown in Figure 2.9A, by creating a thin sheet of light, usually from two opposing laser beams on either side of the sample (Dodt et al., 2007). This selective illumination minimises photobleaching and out-of-focus light or image blur.

In LSFM, the detection axis is oriented orthogonally to the illumination plane and the specimen is moved incrementally through the light sheet,

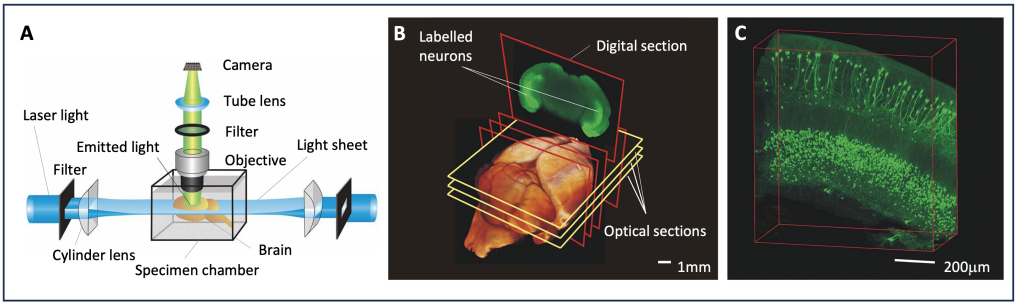


Figure 2.9: The principles of light sheet microscopy. A) The sample is mounted on a holder, and positioned in the centre of a glass specimen chamber full of clearing fluid. A thin slice of the sample is illuminated from both sides by a narrow sheet of light, formed by focusing laser beams. Fluorescent light, which is emitted by the illuminated section, is collected by the objective, positioned directly above the sample, and filtered, so that stray light is excluded, before being projected through a tube lens and captured by the digital camera. The sample is moved up/down (i.e., along the detection axis) in small increments, so that the illumination plane is always in focus, to image the rest of the sample. The result is several hundred optical sections, each illuminated and imaged individually. B) The rodent brain can be reconstructed from the image stack and sectioned digitally along any plane. C) The reconstructed image volume can also be analysed to obtain 3D measures of tissue microstructure. These measures can be averaged over the volume of tissue contained in an MRI voxel and then directly compared. Modified from Dodt et al. (2007).

along this detection axis. This procedure produces a z-stack of well-aligned optical sections of the sample, as shown in Figure 2.9B. Notably, this optical sectioning technique is non-destructive and avoids the artefacts associated with mechanical sectioning. As a result, it simplifies the reconstruction of tissue microstructure in 3D and facilitates registration to MRI data.

LSFM uses a low powered objective with a low numerical aperture, resulting in a considerably larger field of view (FOV) compared to confocal microscopy. This allows for optical sectioning of macroscopic samples at micrometre resolution (Dodt et al., 2007). However, the axial resolution (i.e., the resolution along the detection/z axis) decreases as one moves away from the 'beam waist', which is the thinnest portion of the light sheet (Santi et al., 2009). This region, known as the confocal parameter, has a relatively constant thickness that overlaps with the focal plane of the lens.

Initially, when investigating samples wider than the confocal parameter and requiring full-frame imaging, it was necessary to move the sample up through, and then across, the beam waist. This entailed capturing image columns separately and later stitching them together (Buytaert and Dirckx, 2007). This approach significantly extended imaging time and increased the risk of photobleaching, rendering the imaging of larger specimens, such as the rat brain, less feasible than that of the mouse brain (Tian et al., 2021).

Recent advances in LSFM have been integrated into commercially available systems. This is allowing researchers to optimise imaging for larger sample sizes, as shown in Figure 2.10. Furthermore, certain systems offer automated image acquisition and stitching capabilities, which are facilitating high-resolution imaging across large FOVs. These innovations are enabling imaging of the rat brain, which was previously considered impracticable (Ueda et al., 2020).

The final challenge with LSFM is computational. Data sets are exceptionally large (i.e., terabyte-scale) and significant image processing and analysis is required to extract accurate quantitative information about the density, spatial distribution, and orientation of labelled structures throughout the entire sample. There are currently several commercial and open-source software packages available, but they are all specialised for addressing specific challenges. Furthermore, there is a demand for the development of a framework of comprehensive image analysis tools that can efficiently and automatically process and mine the wealth of information in these datasets (Ueda et al., 2020).

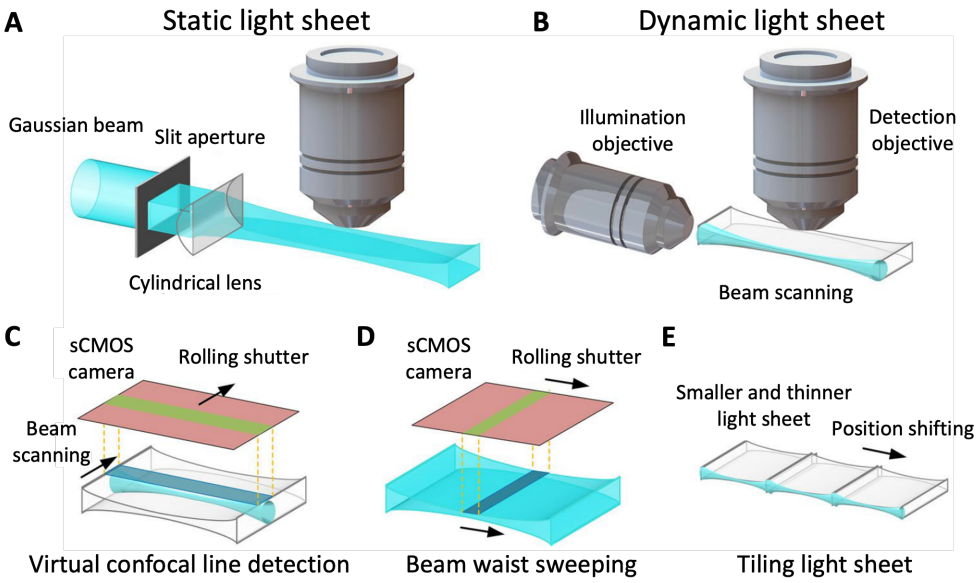


Figure 2.10: Recent advances have helped optimise light-sheet microscopy for imaging of large samples. A) A static light sheet can be used to capture a large field of view, but illumination and axial resolution will vary across the optical plane. B) By using a laser beam to create a dynamic light sheet that scans across the field of view, it is possible to achieve more uniform illumination. C) Synchronising the rolling shutter of next generation sCMOS (scientific complementary metal-oxide semiconductor) cameras with beam scanning allows for higher contrast and signal-to-noise as out-of-focus fluorescence (i.e., scattered light) is not detected. D) Synchronising the rolling shutter with beam waist seeping improves axial resolution. E) Tiling smaller and thinner light sheets improves axial resolution and extends the field of view but significantly increases acquisition time as the specimen has to be physically translated. Reproduced from Jiang et al. (2023).

2.4 Cross-resolution, Cross-modal Imaging

Mapping the brain's complex organisational structure and connectivity are critical to understanding its function, but brain organisation manifests across multiple scales. Although diffusion MRI (dMRI) has potential to map neuronal macrostructural properties, its measures are indirect, noisy, and of low spatial resolution (mm scale). As such, microscopy is used to validate MRI contrasts and provide confirmatory evidence of microstructural changes in pre-clinical animal models (μm scale). However, comparisons of traditional 2D microscopy with 3D MRI are inherently limited and

challenging.

In this thesis, I present a novel framework bringing together MRI and 3D light sheet microscopy of the cleared rat brain, as shown in Figure 2.11, to allow for novel explorations and comparisons between microstructural measures inferred from MRI (i.e., non-invasive, *in vivo/ex vivo*, macroscopic, fast), and those derived from next generation optical imaging techniques (i.e., invasive, *ex vivo*, microscopic, comparatively slow).

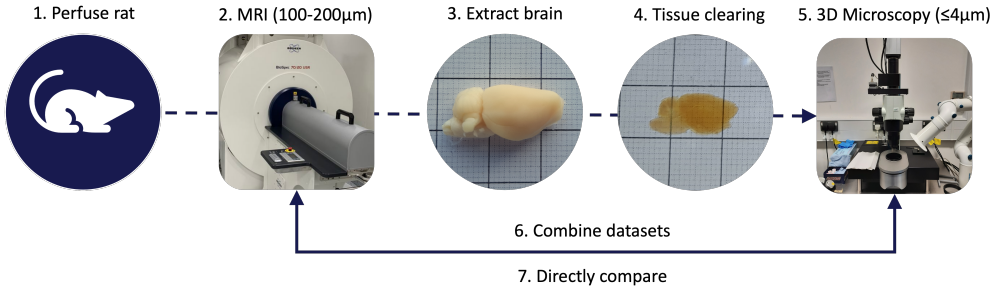


Figure 2.11: Workflow for a multimodal cross-resolution approach to whole-brain imaging.

Recent studies have attempted developing such frameworks. These efforts can be categorised into four groups based on the type of brain tissue (human/non-human primate or rodent) and the dimensionality of the optical imaging techniques (2D or 3D). Firstly, we will discuss several significant studies conducted using human/non-human primate tissue, before transitioning to those conducted in rodents. It is noteworthy that the studies involving rodents have been primarily limited to mice.

2.4.1 Existing Frameworks

In Casamitjana et al. (2022), a high resolution ($\sim$20μm) 3D volumetric reconstruction of the entire human brain has been achieved from 2D optical images of serial tissue sections, which were labelled with multiple histological and antibody-based stains (Amunts et al., 2013; Ding et al., 2016). These

whole-brain reconstructions were subsequently co-registered to standard MRI atlases (Casamitjana et al., 2022; Xiao et al., 2019) or corresponding MRI scans (Alkemade et al., 2022), establishing a spatial framework for integrative microscopy-neuroimaging analyses (Paquola et al., 2021). This framework has enabled researchers to move beyond considering brain organisation in terms of discrete areas, to having an understanding of how macro-scale patterns (e.g., gradients) of function or connectivity relate to cellular or axonal architecture (Axer and Amunts, 2022).

The studies using optical imaging to validate microstructural measures derived from dMRI (for overview see Lazari and Lipp (2021) or Yendiki et al. (2022)) differ from these approaches in that they usually perform 2D microscopy on a limited number of sections from human/non-human primate brain tissue (Howard et al., 2023; Tendler et al., 2022). To take full advantage of the complementary information provided by microscopy and dMRI, innovative data-fusion methods (Howard et al., 2019) and robust registration frameworks (Huszar et al., 2023) have been developed. These have demonstrated, for example, that microglial activation measures from microscopy are an excellent predictor of high fractional anisotropy (FA) and low radial diffusivity, indicating dMRI's sensitivity to some aspects of neuroinflammation (Kor et al., 2022).

Unfortunately, the microscopic measures in these studies are inherently 2D and confined to the optical plane (i.e., incapable of resolving depth-related measures). Consequently, researchers are actively investigating the opportunities afforded by advancements in 3D microscopy and tissue clearing for human brain tissue (Morawski et al., 2018). For example, a cross-resolution framework that allows for MRI-CLARITY comparison within the same sample of human brain tissue has indicated that orientation estimates derived from neuronal fibre staining, rather than vasculature autofluorescence,

closely align with the principal diffusion orientation obtained from dMRI (Leuze et al., 2021).

Several studies have combined dMRI with 3D microscopy of the mouse brain as it is much easier to clear. An early method called 3D-BOND (3D Bridging of Optically-clear histology with Neuroimaging Data), enabled the co-registration MRI and confocal microscopy data from cleared mouse hippocampus (Stolp et al., 2018). This study found that mean and radial diffusivities correlated with cellular and axonal densities. Furthermore, FA was shown to correlate with astrocytic density, while diffusion tensor orientation aligned with axonal orientation. Similarly, another study (Chang et al., 2017), which also used mouse brain tissue, *ex vivo* MRI and CLARITY, demonstrated that FA correlated with myelin immunostaining, especially in coherently oriented fibre tracts. In contrast, the association between radial diffusivity and myelin staining was less robust, suggesting that this DTI-derived measure might be less sensitive to myelin content.

Light sheet microscopy is now being used more widely as it facilitates comprehensive brain-wide comparison between dMRI and microscopy data. LSFM imaging of CLARITY cleared mouse brain was first combined with *in vivo* MRI and the Allen Mouse Brain Connectivity Atlas to develop the MIR-ACL (Multimodal Image Registration And Connectivity anaLysis) pipeline (Goubran et al., 2019). This allowed for the analysis of microstructural features across multiple white matter tracts and networks, along with their correspondence with dMRI-derived measures obtained *in vivo*. Furthermore, the application of MIRACL in a mouse model of stroke has demonstrated that histological changes occur in regions that are structurally connected to the ischaemic core. Moreover, Johnson et al. (2023) pushed the limits of resolution further by developing workflows to combine LSFM (1.8μm resolution) of CLARITY cleared mouse brain with ultra-high resolution

MRI (15μm resolution) from the same sample. This approach has shown, across 13 strains of the BXD mouse, how ageing is associated with differential changes in connectivity, underscoring the genetic dependence of the connectome.

2.4.2 Thesis Aims

This thesis aims to develop a cross-resolution and cross-modal imaging framework of the same rat brain that can be subsequently used to test the specificity of MRI-derived markers. Capabilities will be developed for imaging and analysing structural and diffusion MRI data (resolution in hundreds of microns), followed by tissue clearing and 3D light sheet microscopy (resolution in microns). Compared to the existing literature, this project will:

1. Optimise pre-clinical acquisition protocols for structural and diffusion MRI in rats, rather than mice. By adopting a multimodal approach, we aim to take advantage of the complementary information available from different MRI contrasts (Cercignani and Bouyagoub, 2018). We will also develop multimodal analysis pipelines that are fully integrated and optimised for rodent anatomical and diffusion MRI data. This will involve standardising and validating workflows.

2. Explore and establish protocols for clearing the intact rat brain. Unlike previous studies primarily conducted on the mouse brain, these methods will be applied to the rat brain, which is significantly larger and hence more challenging to clear. To achieve this, we will experiment with different solvent-based clearing techniques and develop well-optimised acquisition protocols for 3D light sheet microscopy (Silvestri et al., 2016). Establishing

these protocols for rats is valuable, given their widespread use as a prevalent model in neuroscience research (Iannaccone and Jacob, 2009).

3. Investigate and compare the efficacy of different approaches for immunolabelling white matter in the intact rat brain. Combining tissue clearing with white matter staining presents significant challenges, as clearing protocols can disrupt or remove myelin. Furthermore, antibodies often fail to penetrate deep within the brain, where white matter tracts are situated. This issue is particularly pronounced in the rat brain, given its considerably larger size compared to the mouse. To address these challenges and ensure consistent staining while preserving white matter integrity and achieving sample transparency, specialised methods are required. We will test clearing strategies that are compatible with white matter staining and assess electric field-enhanced immunolabelling. By adopting these methods, it will be possible to use structure tensor analysis to estimate fibre orientation in 3D, allowing for comparison with complementary measures derived from dMRI.

4. Build a cross-resolution registration framework that aligns and bridges information across scales (macroscopic to microscopic) to better understand the microstructural underpinnings of MRI contrasts. Here, we will capitalise on the 3D nature of light sheet microscopy to enable direct voxel-based comparisons, at the whole-brain level, within the same sample. By doing so, we aim to circumvent the challenges associated with comparing 2D microscopy with 3D MRI, including issues related to compensating for sectioning deformations during registration and the inherent limitations in comparing 2D microscopy measures with 3D parameters derived from dMRI.

By establishing a 3D multimodal, cross-resolution imaging pipeline for the rodent brain, our research enables the exploration of how effectively

diffusion models capture microscopic brain features and quantify tissue components. This is a crucial first step towards accurately identifying specific types of neuropathology (e.g., demyelination, axonal loss/degeneration, neuroinflammation, and gliosis) and monitoring developmental processes (e.g., myelination, dendritic arborization, and axonal growth) using measures obtained non-invasively with *in vivo* MRI. Achieving these aims will result in specific MRI contrasts that are better characterised and potentially more quantitative and robust.

Furthermore, this multiscale imaging framework could support the development and validation of novel MRI markers of tissue microsctructure for the human brain. This represents a shift from relying on the temporally and spatially limited data provided by histology, enabling longitudinal investigation within a single subject using *in vivo* methods.

Chapter 3

Ex vivo MRI of the Rat Brain: From Acquisition to Processing

3.1 Introduction

The ultimate aim of microstructural imaging is to non-invasively map a tissue's microscopic properties *in vivo*. Often referred to as 'virtual histology', this approach would allow for histological features, such as cellular architecture, to be quantified *in situ*, without the need for biopsy or tissue processing (Alexander et al., 2019). Some aspects of this are already achievable with MRI, as traditional contrasts can reliably identify neuroanatomical features like cortical thickness (Lerch et al., 2017). More recently, advanced techniques such as diffusion MRI (dMRI) are increasingly being used to probe the cellular architecture and spatial organisation of white and grey matter (Assaf et al., 2019). However, the complex relationship between these MRI contrast mechanisms and a tissue's cellular structure remains unresolved (Jelescu et al., 2020; Lampinen et al., 2023). Thus, comparisons between microstructural measures derived from MRI and those

obtained using classical histology and microscopy are essential (Dyrby et al., 2018), as MRI markers are often found to be sensitive to tissue changes but not specific to what is changing.

When undertaking comparisons with histology, *ex vivo* MRI benefits from a greater signal-to-noise ratio (SNR) than is possible *in vivo*, bridging the scales of resolution between *in vivo* MRI (millimetre scale) and microscopy (micrometre scale). Pre-clinical imaging also occupies a crucial position in advancing and validating MRI techniques (Homberg et al., 2021), as it offers researchers the unique capability to mechanistically explore how the tissue micro-environment influences image contrast (Oguz et al., 2012; Chang et al., 2017; Wang et al., 2020b). Despite the value of both *ex vivo* and pre-clinical imaging (Nieman et al., 2005), there are unresolved challenges that restrict advancement (Brockmann et al., 2007).

Challenges with acquisition arise, in part, from not all research centres having the local expertise to tailor acquisition pulse sequences and optimise sampling schemes. This is especially important for *ex vivo* imaging because tissue fixation reduces diffusivity by a factor of 2-3, and decreases longitudinal (T_1) and transverse (T_2) relaxation times, which would reduce SNR and contrast-to-noise ratio (CNR) if not addressed using an appropriate strategy (Barrett et al., 2023; Oguz et al., 2013).

Challenges with processing pre-clinical MRI data contribute to a lack of generalisability across studies and centres and poor translatability to human imaging (Hoyer et al., 2014). Data conversion (i.e., proprietary formats to NIFTI), skull stripping, registrations, and distortion correction, are indicative examples of steps that do not have a comprehensive solution, even though the complexity of the rodent brain (and hence of its images) is considerably lower than the human brain. The plethora of available atlases

and templates for the rat brain introduces another challenge (Barrière et al., 2019) as transparent reporting and efficient analysis by others is much more complex when there is no standard template.

When just considering the many methods developed for brain extraction in rodent MRI (Feo and Giove, 2019; Wood et al., 2013; Li et al., 2013; Chou et al., 2011; Cox, 1996; Delora et al., 2016; Hsu et al., 2020; Pontes-Filho et al., 2019; Roy et al., 2018; Oguz et al., 2014; Liu et al., 2020; Oguz et al., 2011; Lohmeier et al., 2019), the scale of the challenge becomes apparent. Some of these methods were developed for T1-weighted MRI (e.g., Oguz et al. (2014)), or are only semi-automated (Delora et al., 2016; Pagani et al., 2016; Lohmeier et al., 2019), thereby preventing these methods from being adopted in generalisable pipelines. Methods that have been modified from those used in human research appear to be more robust (Wood et al., 2013; Li et al., 2013), but without comparative studies it is not possible to identify the best approach.

For these reasons, this chapter describes original work aimed at **optimising acquisition** of structural and microstructural data (T2w and diffusion MRI) for the rat brain using two considerably different pre-clinical MRI setups. Additionally, it details the **development of automated pipelines** that standardise the processing of rodent data. This involved testing different tissue preparation methods and acquisition protocols, followed by the evaluation and optimisation of computational tools for standard processing. Tools that offer standardised solutions for processing human MRI were considered and adapted to suit the rat brain. The results demonstrate the generalisability of the developed approach, enabling consistent processing despite variations in tissue preparation, acquisition protocols, image contrast, and noise levels - areas where previous approaches often fail. Furthermore, we show generalisability across rodent species (i.e., mouse and rat brains with

their respective templates). This streamlined approach paves the way for enhancing reproducibility in pre-clinical MRI research, facilitating meaningful comparisons across various samples, modalities and studies.

3.2 Theory & Methods

3.2.1 *Ex-vivo* MRI for the Rat Brain

Animals and Tissue Collection

Six adult male (>10 weeks old) Sprague Dawley rats (Charles River, Margate, UK) were used to optimise MRI acquisitions. They were housed in groups of $\geq$2 in individually ventilated cages, maintained on a 12hr artificial light/dark cycle. The animals had at least a one-week acclimatisation period with *ad libitum* access to food and water. Environmental enrichment items, such as a cardboard tunnel, wooden chew, and nesting material, were provided. All animal procedures were conducted in compliance with UK Home Office licenses under the Animals (Scientific Procedures) Act 1896 and approved by the the University of Nottingham's Animal Welfare and Ethical Review Body.

Perfusion-fixation is the gold-standard method of tissue preservation as it reduces the post-mortem interval (i.e., time between death and fixation) to zero and thereby minimises autolytic changes in the tissue (Schilling et al., 2022). However, standardising these methods is crucial, as variations in fixation procedure (e.g., duration of post-fixation or fixation washout) can significantly affect morphology, volume fractions, membrane permeability, relaxation properties and diffusivity (Shepherd et al., 2009b,a; de Guzman et al., 2016).

To optimise sample preparation methods and MRI acquisition protocols, rats were humanely euthanised and transcardially perfused with 0.1M phosphate buffered saline, containing heparin (10μg/mL, Sigma-Aldrich, H3149-50KU), followed by 4% paraformaldehyde (PFA, Sigma-Aldrich 441244). To ensure optimal fixation, the PFA solution was freshly prepared, filtered and adjusted for pH (7.4), <24 hours before perfusion.

We did not have access to a perfusion pump, so we used syringes and a stopwatch to maintain a consistent flow rate of 50ml/min, closely matching the cardiac output of a healthy rat (48ml/min, Beznak (1958)). Maintaining this flow rate minimises the risk of fixation artifacts, such as T2 hyperintensities, in *ex vivo* MRI (Cahill et al., 2012). Additionally, it helps preserve anatomical features, such as cortical folding, and microstructural elements, such as the myelin sheath, in their native state (Dyrby et al., 2018).

Following perfusion, the heads of the rats were removed and all extraneous tissue was stripped from the skull (Nieman et al., 2018). This included removing all skin, cartilage and muscles. The ears and eyes, as well as the lower jaw and zygomatic, premaxilla and nasal bones were also removed. The skull was post-fixed in 4% PFA at 4°C for 24 hours before being transferred to a solution of 0.1M PBS, with 0.02% sodium azide (Sigma-Aldrich, S8032), for storage at 4°C (de Guzman et al., 2016). The brains were deliberately left within their skulls until after the MRI scanning, as extraction can cause damage or deformations, ultimately hindering the ability to gain insights into the brain's morphology *in situ*. Removing the skull would also impact on the accuracy of regional volume measures.

To investigate whether it was possible to improve image contrast and SNR in *ex vivo* MRI acquisitions, while also shortening overall scan time, the paramagnetic gadolinium-based contrast agent MultiHance (Bracco Imaging,

containing 0.5M gadopenate dimeglumine) was included at a concentration of 2mM in the perfusate (i.e., both PBS and PFA) and storage solutions for 2 out of 6 animals. Including contrast agent in all solutions helps the concentration of gadolinium contrast in brain tissue to equilibrate faster (Nieman et al., 2018) and reduces the risk of contrast washout. Gadolinium enhances image contrast by accelerating signal recovery and shortening T_1, thereby allowing for shorter repetition times (TR) and faster acquisitions. Previous studies have shown that using gadolinium in sample preparation does not impact on histology (Barrett et al., 2023).

Sample Preparation

Although diffusivity measures and FA appear to be stable in perfusion-fixed samples for a scan interval (i.e., time from death to scan) of up to 3 years (Dyrby et al., 2011), all imaging was conducted within 6 months of perfusion. This minimises volume changes related to fixation and storage (de Guzman et al., 2016). Prior to scanning, the storage solution (0.1M PBS containing 0.02% sodium azide) was refreshed daily with degassed 0.1M PBS for four consecutive days. Washing the samples helps to ensure the tissue is fully rehydrated and removes any remaining fixative. This improves diffusivity and T_2, which are significantly reduced by fixation (Shepherd et al., 2009b). Refreshing the storage solution with degassed PBS also helps to remove air bubbles that may be present in the sample (e.g., in the ventricles), thereby preventing large susceptibility artefacts. To prevent washout of the contrast agent in samples that were perfused with gadolinium, the solutions used to wash these samples also contained 2mM gadolinium.

The samples were scanned at two sites (Nottingham and Oxford), with some samples scanned at both sites. This resulted in a dataset that enabled

optimisation and generalisability tests across platforms. Table 3.1 details the time between fixation and scanning. Storage time varied more in Nottingham due to scanner breakdowns. Exact perfusion dates for rats 3 and 4 are unavailable due to pandemic-related disruptions.

Rat	Gd	Notts		Oxf	
		Days	Months	Days	Months
5	N	10	<1	38	**1**
6	Y	31	**1**	27	**1**
7	N	139	**4**	46	**1.5**
8	Y	142	**4**	67	**2**

Table 3.1: Time between fixation and MRI scanning of four rat brains across two sites (Nottingham and Oxford). Scanning after one month of storage in PBS ensures good contrast, while completing scans within five months minimises tissue volume variation induced by fixation and storage (de Guzman et al., 2016). Acquisitions meeting these conditions are highlighted in bold.

In Nottingham, each skull was wrapped in gauze and securely fixed in the centre of a 50cm^3 skirted, plastic centrifuge tube (Scientific Laboratory Supplies, G210261) to minimise movement during scanning. The degassed PBS was replaced by Fluorinert FC77 (Sigma Aldrich), a magnetic susceptibility matched and proton-free solution, taking care to ensure that no air bubbles were introduced. Using Fluorinert prevents off-resonance distortions at the tissue edges and clipping/ringing of the MR signal at low b values (Roebroeck et al., 2019). Others have confirmed that Fluorinert does not affect the histological properties of fixed tissue (Iglesias et al., 2018). The sample tube was then placed in approximately the same position in the scanner and left to equilibrate to room temperature.

In Oxford, each skull sample was positioned in a tube and held in place with supports, as shown in Figure 3.1, to minimise motion artefacts during scanning. The tube was filled with Fluorinert, and then degassed using a

vaccuum pump. After this, the sample tube was placed in the scanner in approximately the same position for imaging.

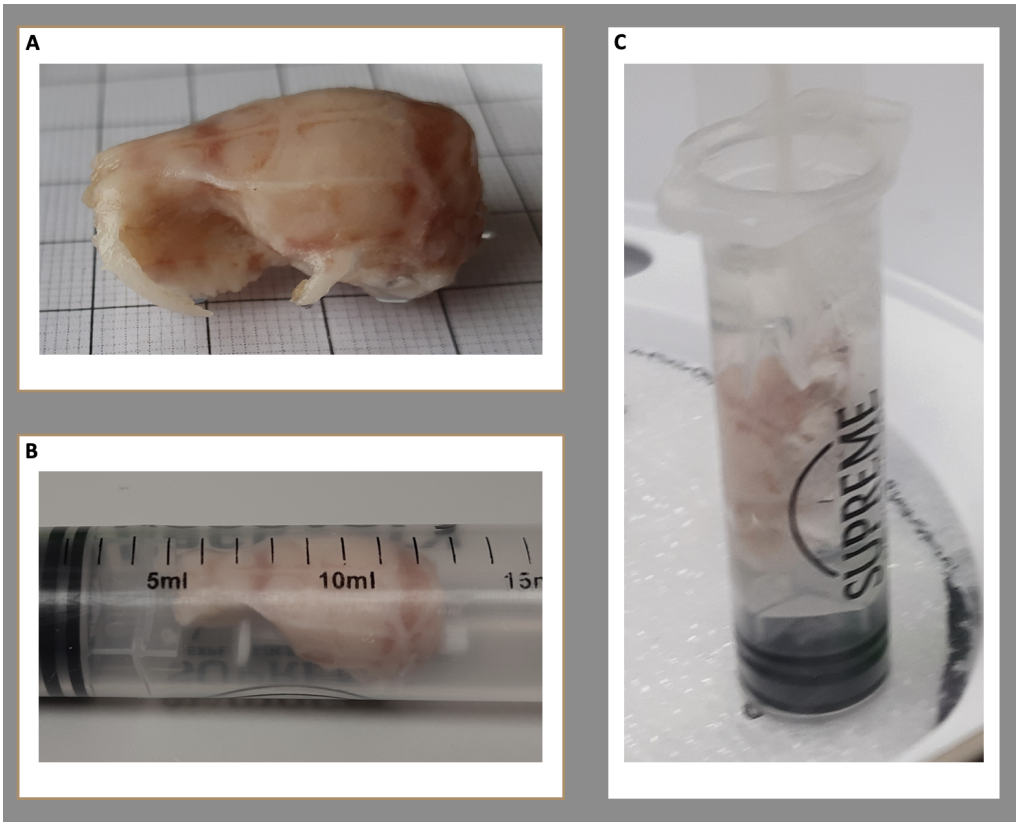


Figure 3.1: Preparing a rat skull for scanning in Oxford. The figure shows how **A**) the skull was stripped of all soft tissue, before **B**) being securely positioned in the centre of a tube, using supports to hold it in place. **C**) After filling the tube with Fluorinert, the contents was degassed using a vacuum pump.

MRI Acquisition

Scanning in Nottingham was conducted at the Medical Imaging Unit in the School of Medicine using a 30cm bore 7T MR scanner (Bruker Biospec 70/30) equipped with a 36mm gradient insert (1T/m) and a 72mm single-channel transmit/receive volume coil designed for rat head imaging (Bruker BioSpin). The scanner was operated via a Bruker Avance III console (BioSpec, Ettlingen, Germany) running ParaVision 6.0.1. Dr Malcolm Prior operated the scanner and assisted with image acquisition.

At the Wellcome Centre for Integrative Neuroimaging (WIN) in Oxford, imaging was performed using a more advanced (circa 2019) 7T Bruker system (BioSpec 70/20 USR) running Paravision 360. A cryogenically cooled transmit/receive surface coil was employed, enhancing SNR by reducing thermal noise. Dr Mohamed Tachrount operated the scanner and assisted with image acquisition.

At the start of each imaging session at both sites, radiofrequency (RF) coil tuning, matching, and shimming were performed to ensure efficient RF power transmission, minimise signal distortions, and enhance image quality. First, the Bruker Tune and Match interface was used to manually adjust the coil's resonance frequency and optimise impedance, thereby reducing signal loss and artefacts. Once tuning and matching were complete, Bruker's MapShim protocol was used for both global (first order) and local (second order) shimming. Global shimming corrected large-scale $B0$ field inhomogeneities associated with high field strength, while local shimming refined field homogeneity within the region of interest (i.e., the brain). The MapShim protocol acquires a $B0$ field map and iteratively adjusts shim currents via the console to optimise uniformity. These adjustments were retained for subsequent acquisitions.

To determine how tissue T_1 changes when using a gadolinium-based contrast enhancing agent in the sample preparation, the Nottingham scanner was used to map T_1 in two samples which were prepared with, and without, gadolinium. To do this, a 2D-rapid acquisition with relaxation enhancement (RARE) protocol was used, where TR was varied (i.e., RAREVTR) to fully sample the magnetisation recovery. For the control sample, prepared without gadolinium-contrast agent, T_1 was expected to be $\sim$1200ms, so TR = 1000, 1170, 1357, 1565, 1802, 2074, 2394, 2784, 3283, 3976, 5116, and 10000ms, and TE = 7.66ms (Liu et al., 2013). In the second sample, where

gadolinium contrast was included in the perfusate and storage solutions, T_1 was expected to be significantly shorter (∼100ms), so TR = 70, 100, 200, 300, 400, 500, 600, 700, 800, 900, 1363, and 1500ms, and TE = 7.87ms (Kim et al., 2009). To ensure full coverage, a series of 1mm thick coronal T1-weighted images were acquired across the whole brain.

T_1 values were estimated from RAREVTR acquisitions using the Image Sequence Analysis tool in Paravision 6. This tool fits a mono-exponential recovery curve to the measured signal intensities at different TRs ($S(TR)$) given by:

$$S(TR) = S_0(1 - e^{-TR/T_1}) \tag{3.1}$$

This approach estimates both the fully relaxed signal ($S0$) and T_1. However, it represents a simplification of the underlying tissue relaxation behaviour. T_1 tissue maps were generated in ImageJ using version 3 of the Bruker Open PV6 Macro, developed by Prof Pedro Ramos-Cabrer.

A 3D-RARE structural scan (100μm isotropic) was acquired for all samples. A T2-weighted sequence was chosen as it provides better soft-tissue contrast in rodents (Feo and Giove, 2019). Parameters were optimised to enhance grey-white matter contrast. As demonstrated in Table 3.2, efforts were made to keep spatial resolution, field of view (FOV) and TE relatively consistent across scans conducted with and without gadolinium contrast at both Oxford and Nottingham. However, ensuring a consistent TR proved challenging due to limitations with the Nottingham scanner.

Diffusion MRI was also performed. After evaluating both Echo Planar Imaging (EPI) and non-EPI readouts with a spin echo sequence, EPI protocols were selected for their ability to provide high-quality imaging within a practical scan time. In Nottingham, a dMRI protocol for *ex vivo* imaging was developed with the guidance of Dr Matteo Bastiano.

Site	Gd	Voxel size (μm^3)	TE (ms)	TR (ms)	Matrix size	Scan Time
Nottingham	N	100	28.6	5000	180x140x340	21h43m
	Y	100	28.6	**1500**	180x140x310	**5h57m**
Oxford	N	100	36	350	140x320x160	21m
	Y	100	36	350	140x320x160	21m

Table 3.2: Acquisition parameters for 3D-RARE anatomical scans (100μm isotropic) in Nottingham and Oxford

Additionally, in Oxford, dMRI sequences were designed in partnership with the local team, including Dr Cristiana Tisca, Dr Aurea Martins-Bach, and Dr Mohamed Tachrount. For all dMRI acquisitions, $b0$ volumes with inferior-to-superior and superior-to-inferior phase encoding directions were interspersed throughout the scan.

A multi-shell diffusion-weighted scan (200μm isotropic) was acquired for all samples using 2D-EPI (b=4000 and b=6000s/mm^2, 90-directions each). The parameters for these acquisitions are shown in Table 3.3. As the levels of noise were higher in Nottingham, it was necessary to average across 12 repeats. This made scans considerably longer. It was also not possible to reduce the TR below 6000ms when scanning samples perfused with gadolinium in Nottingham, as the gradients were already operating close to duty cycle limits.

3D-EPI acquisitions for multi-shell dMRI (200μm isotropic, b=4000 and b=6000 s/mm^2, 90-directions each) were explored for samples perfused with gadolinium. Using the Oxford scanner, 3D-EPI facilitated significant reductions in both TR and scan duration, as shown in Table 3.3. During setup, TR was maintained at >3 times greater than expected T_1 ($\sim$100ms for a sample perfused with 2mM gadolinium) to mitigate spin-history effects. Regrettably, usable dMRI data could not be obtained with a 3D-EPI readout

in Nottingham.

Site	Gd	EPI	Res (μm^3)	TE (ms)	TR (ms)	Matrix size	Rpts	Scan Time
Notts	N	2D	200	25	6000	100x100x120	12	31h12m
	Y	2D	200	25	6000	100x100x120	12	31h12m
Oxf	N	2D	200	30	4500	70x160x90	1	12h30m
	Y	2D	200	30	4500	70x160x90	1	12h30m
		3D	200	26	**300**	70x160x80	1	**10h40m**

Table 3.3: Parameters for multi-shell 2D and 3D-EPI dMRI acquisitions of control and gadolinium perfused samples scanned in Nottingham and Oxford (200μm isotropic, 90 directions each at b=4000 and b=6000 s/mm^2).

All dMRI protocols incorporated interspersed $b0$ volumes ($\geq$15) and shuffled diffusion directions over the course of scanning. In Nottingham, the shells (i.e., b=4000, 6000 s/mm^2) were also interleaved to minimise gradient overheating and reduce the duty cycle. These measures help mitigate systematic biases related to drift and heating during long scan times. This approach was necessary as sample temperature was neither measured nor actively regulated at either site. However, the cryo-coil in Oxford likely provided some degree of temperature stability throughout scanning.

The data collected is summarised in Table 3.4. The datasets are all isotropic, which is important when exploring morphology, as anatomical boundaries can only be identified by looking at multiple planes of orientation, and anisotropic voxels make it more difficult to control for partial voluming effects. Furthermore, anisotropic dMRI can skew estimates of fractional anisotropy, and bias tract orientation. Spatial resolutions for anatomical and diffusion-weighted scans were set at 100μm and 200μm, respectively, balancing resolution and scan duration to avoid prolonged sessions (i.e., several days). These resolutions (100-200μm) offer brain volume per voxel akin to human imaging (1-2mm), considering the rat brain's volume ($\sim$0.6ml)

is 0.05% that of the human brain (∼1200ml). High angular resolution (90 directions) and diffusion weightings (b=4000, 6000 s/mm^2), were chosen to compensate for the lower diffusion coefficients *ex vivo* (Dyrby et al., 2011).

		Nottingham		Oxford		
Rat	Gd	Anatomical (3D-RARE)	dMRI (2D-EPI)	Anatomical (3D-RARE)	dMRI (2D-EPI)	dMRI (3D-EPI)
3		✓	✓			
4		✓	✓x2			
5		✓	✓	✓	✓	
6	✓	✓	✓	✓		✓
7		✓x2	✓x2	✓	✓	
8	✓	✓	✓	✓	✓	✓

Table 3.4: Summary of MRI data acquired in Nottingham and Oxford.

Post-Acquisition File Conversion and Standardisation

Raw Bruker Paravision data files are not compatible with any standard processing or analysis software, and follow a proprietary format that can change between Paravision versions (Ioanas et al., 2020). This limits interoperability and generalisability. Although it is possible to export datasets from the console in more transferrable formats (e.g., DICOM files), Paravision does not currently export metadata in the formats required for processing. A conversion tool is therefore needed.

There are a number tools currently available for converting the raw Bruker files (e.g., DICOMIFIER, Bruker2nifti, Bru2Nii, pvconv, Bruker2Analyze etc), but many of these are not actively maintained or compatible with newer versions of Paravision. Instead, we chose to use `BrkRaw` (version 0.3.8.), a python-based package (Lee et al., 2023), as it directly converts the Bruker Paravision image matrices to the NIfTI (Neuroimaging Infor-

matics Technology Initiative) format, and generates supplementary text files containing key information, such as diffusion gradient directions. It is also the conversion tool recommended by large scale efforts to standardise pre-clinical image processing (Desrosiers-Gregoire et al., 2022).

However, `BrkRaw` still has issues in the way it: i) converts and processes diffusion-weighted scans, and ii) inconsistently handles raw data from different scanner software versions (e.g., Paravision 6 versus Paravision 360). For example, images acquired with a reversed phase-encoding direction are inverted and mislabelled by `BrkRaw`, as shown in Figure 3.2. To address these problems, we modified the code. This resulted in a stable and improved version of BrkRaw, which is now publicly available on GitHub.

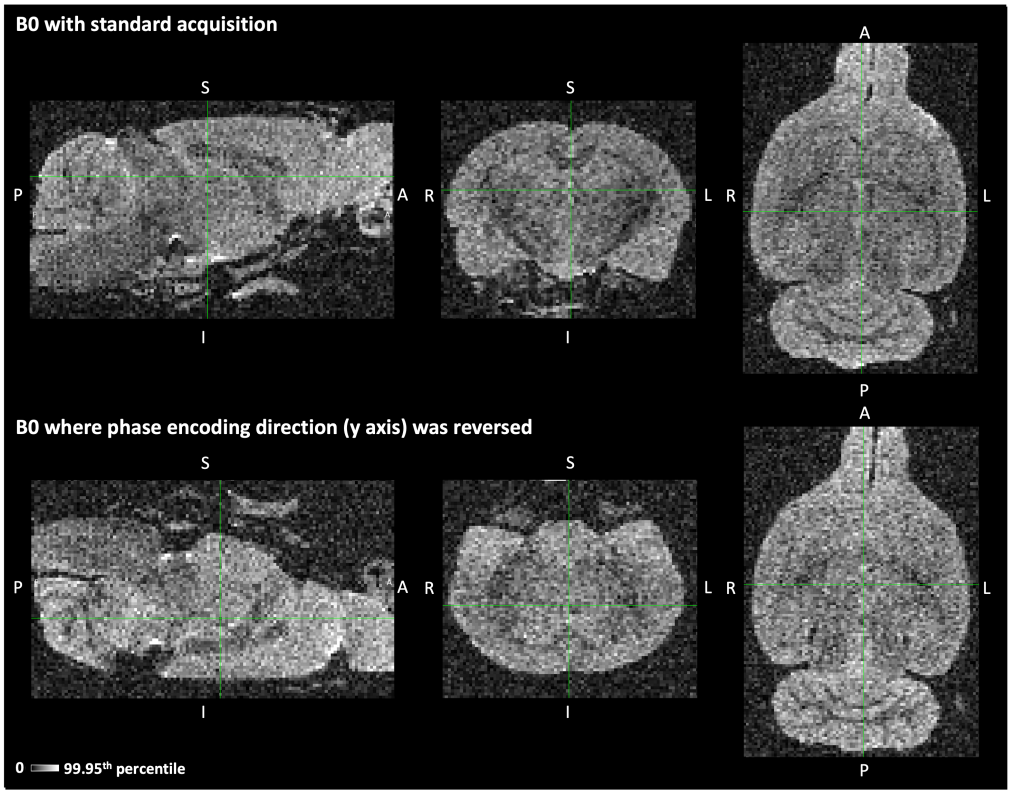


Figure 3.2: When the phase encoding direction (y axis) is reversed, Paravision 6 can invert the image matrix and label areas incorrectly (S/I swapped). This has to be corrected so that it is possible to estimate and remove susceptibility-induced distortions.

Building on this, we developed a new tool, (`rodent_preproc`), which uses

the modified version of BrkRaw to correctly convert Paravision data. In brief, rodent_preproc standardises the orientation of all scans by ensuring that the sform and qform matrices are diagonal and positive, and accounting for variation in phase encoding direction or sample orientation (e.g., due to the sample being placed in the scanner bore with the 'cerebellum' first, as opposed to 'nose' first). Following conversion, a visual inspection of the NIfTI images is recommended to verify that their orientation and anatomical labelling are consistent with the template (discussed below).

Although rodent_preproc ensures that the dMRI image volume order matches the corresponding `bval` files, it does not confirm that the orientations of diffusion vectors and the imaging coordinate system align. This difference can arise because diffusion gradient directions may be defined relative to the imaging (e.g., phase encoding direction) or lab (e.g., bore axis) reference frames. We did not find a standard or generalisable way to determine the coordinate system used, so we visually checked whether the orientations of diffusion vectors aligned with structures in the NIfTI images (e.g., the corpus callosum). If the orientation of the vector was inconsistent with the anatomical structures, we corrected the organisation of the vector matrix in the `bvec` files.

In the following sections, the anatomical and diffusion MRI processing pipelines are presented. These pipelines use the files generated by rodent_preproc. Unless stated otherwise, the workflow has been developed using the tools available in version 6.0.3. of FSL, the FMRIB Software Library (Jenkinson et al., 2012). FSLeyes was used for visualising results. An overview of the pipelines described in the following sections is shown in Figure 3.3.

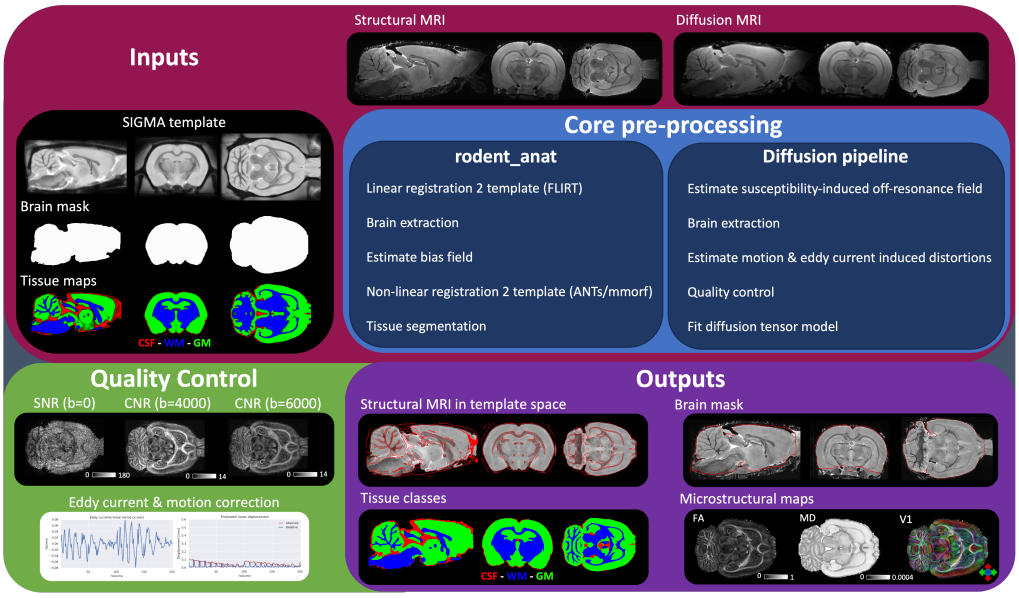


Figure 3.3: Schematic organisation of pre-processing pipelines for rodent neuroimaging data. The structural pipeline takes a T2-weighted scan and reference template (e.g., SIGMA rat brain template), with associated brain mask and tissue probability maps. Key steps involve alignment to the template, brain extraction, bias field correction, and tissue segmentation. The diffusion MRI pipeline requires two diffusion-weighted scans with opposing phase-encoding directions and performs brain extraction, corrections for motion and the off-resonance field induced by the susceptibility distribution and eddy currents, and quality control checks before fitting the diffusion tensor model. The outputs of the pipelines include the structural MRI in template space, a brain mask in native space, maps of the different tissue types, and outputs of the diffusion tensor model (i.e., fractional anisotropy, mean diffusivity, etc).

3.2.2 Anatomical MRI Processing Pipeline

A pipeline was first developed to process anatomical MRI data. This pipeline (`rodent_anat`) is publicly available on GitHub for others working in rodent imaging to use. The main steps performed in `rodent_anat` include bias field inhomogeneity correction, standard space registration, registration-based skull stripping and brain tissue segmentation.

Following NIFTI conversion and initial pre-processing (as detailed in the previous section), the pipeline begins with a linear registration to roughly align the image to a standard template. The affine transformation generated

from linear registration is used to generate a sample-specific brain mask from the template, which is applied to the structural scan to remove non-brain tissue to a first approximation. Subsequently, a bias field is estimated and removed from the brain-only image. This process minimises differences between the sample brain and template images to size and shape variations, which is necessary to prevent signal inhomogeneities biasing the alignment. Given the enhanced accuracy of linear registration with a skull-stripped image, this step is reiterated to ensure a robust starting point (i.e., initial affine transform) for the subsequent non-linear alignment of the structural scan to the standard template. Following non-linear registration, skull-stripping is conducted using a non-linearly registered brain mask from the template to the sample, following in spirit the approach used in the UK Biobank pipeline for robust population-level processing (Alfaro-Almagro et al., 2018). Finally, the brain is segmented into the three main tissue classes; grey matter (GM), white matter (WM), and cerebrospinal fluid (CSF). Individual steps are described more fully below.

Choosing a Standard Template

The plethora of rat atlases vary considerably according to the strain, age, and number of animals; resolution; contrasts; number of tissue classes and structures delineated; magnetic field strength; and method of construction. They also vary based on whether they were acquired *in vivo* versus *ex vivo*; are MRI-compatible and in stereotaxic space; are probabilistic; or have full coverage (i.e., whether the whole brain and skull are present). A comparison of the atlases currently available for rat imaging is included in Figure 3.5. Some of these atlases have significant technical limitations. For example, even though the Waxholm atlas (Osen et al., 2019; Papp et al., 2014) is the most detailed, it has prohibitively large data files; lacks tissue probability

maps (i.e., priors); and has poor generalisability as it was derived from single acquisition (i.e., susceptible to subject-specific anatomy and imaging artefacts).

Name	Modality	Magnet (T)	Contrast	Spatial resolution (μm^3)	Scan	No of animals	Strain	Template /Atlas	Priors	Coverage	MRI compat	References
Waxholm	Structure/ Diffusion	7	T_2* (GRE)	39 isotropic	*Ex vivo*	1	Sprague-Dawley	Yes/Yes	No	Full	Yes	Papp et al. (2014), Kjonigsen et al. (2015)
Tohoku	Structure	7	T_2 (RARE)	125×125×300	*In vivo*	30	Wistar	Yes/Yes	Yes	Partial	Yes	Valdes-Hernandez et al. (2011)
Schwarz (DPABI)	Structure	4.7	T_2 (RARE)	150×150×100	*In vivo*	97	Sprague-Dawley	Yes/Yes	Yes	Partial	Yes	Schwarz et al. (2006)
Ratat1	Structure	14.1	T_2 (SEMS)	50×50×200	*Ex vivo*	9	Long-Evans	Yes/Yes	No	Full	No	Wisner et al. (2016)
Karolinska	Structure	4.7	T_2 (RARE)	110×110×50	*In vivo*	5	Sprague-Dawley	Yes/No	No	Partial	Yes	Schweinhardt et al. (2003)
Figini	Structure	7	T_2 (SEMS)	170×170×580	*In vivo*	10	Sprague-Dawley	No/Yes	No	Partial	Yes	Figini et al. (2015)
Paxinos & Watson	Structure/ Diffusion	7	T_2* (GRE)	25×25×50	*Ex vivo*	5	Wistar	Yes/Yes	No	Full	No	Johnson et al. (2012)
Development	Structure/ Diffusion	7	T_2* (GRE)	25×25×50	*Ex vivo*	45	Wistar	Yes/Yes	No	Full	No	Calabrese et al. (2013)
SIGMA	Structure	11.7	T_2* (MGE)	90 isotropic	*Ex vivo*	6	Wistar	Yes/Yes	Yes	Full	Yes	Barrière et al. (2019)
	Structure/ Function	11.7	T_2 (RARE)	150 isotropic	*In vivo*	32	Wistar	Yes/Yes	Yes	Full	Yes	

Table 3.5: Comparison of rat brain MRI templates currently available. The templates with partial brain coverage were missing the olfactory bulb and/or the hindbrain. Those templates that are regarded as MRI compatible are provided in NIFTI format. The DPABI atlas is only split into two tissue classes; parenchyma and CSF, whilst all others are segmented into GM, WM and CSF. Modified from (Barrière et al., 2019).

After considering a number of options, the SIGMA MRI template, which is available on NITRC, was chosen for this work (Barrière et al., 2019). This template is derived from high resolution *in vivo* and *ex vivo* acquisitions, includes probability maps for the main tissue classes (i.e., GM, WM, and CSF), and features an anatomical 3D brain atlas with 123 defined structures. This atlas was created by merging the Waxholm (sub-cortical and brainstem emphasis) and Tohuku (cortical emphasis) atlases. The SIGMA template's popularity is on the rise, having been integrated into standardised protocols (Grandjean et al., 2020), primarily because it has fewer artefacts and superior *in vivo* contrast compared to Papp et al. (2014). The olfactory bulb was cropped out as it is not of interest.

Another advantage of the SIGMA template is its isotropic nature, mitigating challenges associated with aligning specimens scanned in varying orientations, as is common in *ex vivo* imaging. Registration to an isotropic template facilitates straightforward re-slicing and viewing of data along arbitrary planes. Nonetheless, to maintain flexibility, our pipeline is configured to accommodate the use of alternative atlases, such as those tailored for mice.

Registration to a Standard Template

Registration to the chosen template is a two-step process: a) Rough alignment using a global linear registration approach, b) More accurate alignment using non-linear registration, initialised from the linear alignment. An affine transform was created using `FLIRT` (12 degrees of freedom) to align the fine details of the sample image, post-brain extraction, with the template brain (Jenkinson and Smith, 2001; Jenkinson et al., 2002). This linear registration includes translation, rotation, scaling/zooming, and skewing/shearing parameters along each of the three axes in standard space. For completeness, it is worth mentioning that the workflow repeated linear registration after bias field correction. The affine transformation generated in the second iteration was then used to initialise the non-linear registration.

Expanding upon this linear alignment, in pursuit of the highest possible anatomical correspondence between the subject image and a standard template, two different volume-based non-linear registration methods were tested. The first method tested was the symmetric normalisation (SyN) algorithm (`antsRegistrationSyN.sh`, available on GitHub) from the Advanced Normalisation Tools (`ANTs`), version 2.1.0 (Avants et al., 2011). `ANTs` uses a plastic/large deformation framework, with an iterative process where

warps are updated by warping/resampling the previous warp with an update warp. `ANTs` is currently the default method of non-linear registration in `rodent_anat` as it is generally viewed as the gold-standard method for rodent imaging. The second method tested was the Multi-Modal Registration Framework (`MMORF_beta`, version 0.2.3), a recent non-linear multi-modal registration approach (Lange et al., 2020) available on GitLab. `MMORF` was developed to overcome the limitations of other elastic/small deformation frameworks of registration (e.g., `FNIRT`, from FSL), which are unable to model large deformations. `FNIRT` typically uses a high weight for the regularisation/smoothing of warps to ensure that warps are one-to-one and onto (i.e., each point in image A is mapped onto a unique point in image B, and every point in image B can be reached from image A) and invertible. In contrast, `MMORF` can maintain invertibility and minimise distortions in shape and volume, so that warps remain anatomically plausible, whilst also allowing for large deformations (Lange et al., 2020).

Brain Extraction

The removal of non-brain tissue from anatomical images, a process referred to as skull stripping or brain extraction, is a critical step in neuroimaging pipelines as it improves the performance of subsequent processing steps, such as tissue classification, registration, and bias field correction, by ensuring that they focus only on true brain variability and not the variability or signal intensity differences associated with the surrounding anatomy.

Human MRI acquisition methods benefit from standardisation, enabling the development of robust automated tools for brain extraction (e.g., Smith 2002). However, these tools are not directly transferrable to rodent neuroimaging due to wide variations in geometry, acquisition methods, and

imaging parameters, leading to significant diversity in intensity profiles, SNRs, tissue contrast levels, FOVs and resolutions. Furthermore, in rodent images, the proximity between the brain and the skull is closer, with lower contrast between brain and non-brain tissue, exacerbating partial voluming effects and complicating accurate non-brain tissue removal. Assumptions made by human brain skull-stripping tools regarding intensity profiles, shape, and anatomical organisation are often inappropriate for rodents. Therefore, brain extraction methods designed for human data typically perform sub-optimally on rodent data and require manual fine tuning of parameters by someone with expertise (Feo and Giove, 2019). This manual process is time-consuming, subjective, and lacks reproducibility and reliability.

As there has been no systematic comparison of the performance of different methods for removing non-brain tissue from rodent scans, 3 different methods were trialled. These methods relied on 1) the brain extraction tool (`BET`, Smith (2002)) included in FSL, which was developed for human data, 2) the rodent modified version of `BET`, referred to as `rBET` (Wood et al., 2013), and 3) a template-based process where the brain mask is used. A template-based process has proven successful in human neuroimaging studies (Leung et al., 2011) and is now routinely used in rodent neuroimaging (Liu et al., 2020). It involves the template brain mask being propagated to the subject image after registration.

Correcting for Bias Field/Signal Inhomogeneities

The stronger magnetic fields used in pre-clinical MRI result in an increase in bias fields and signal inhomogeneities. The FSL Automatic Segmentation Tool (`FAST`) can be used to generate a restored/bias corrected subject

brain and estimated bias field (Zhang et al., 2001). The default bias field smoothing extent (FWHM) used by FAST is 20mm. Because this is large when compared to the size of the rodent brain, various levels of smoothing were tested across multiple datasets with differing levels of bias field.

Although bias field correction does not always have a significant visual impact, differences in contrast impact on brain extraction, registration, and tissue segmentation. The undistorted subject image was therefore used to refine the brain extraction and registration, and for conducting tissue segmentation.

Tissue Segmentation

Most MRI pipelines include a segmentation step to classify each voxel in the acquired volume as WM, GM, or CSF. Automatic segmentation algorithms have been developed to replace manual volumetry, as this requires the expertise of trained anatomists, is time-consuming, and difficult to scale to multiple scans/brain regions. Automating this process can be challenging due to the folding pattern of the cortex, which is especially complex in humans.

Although rat brain segmentation strategies are still in active development (Feo and Giove, 2019), successful tools are available for the human brain. These can be split into clustering methods or template-based schemes. `FAST` (Zhang et al., 2001) is an example of a widely adopted clustering method which uses a statistical approach to classify voxels as each of the different tissue types, based on the image intensity distribution. Instead of treating the voxels as independent samples drawn from a population, it considers their spatial context (i.e., whether neighbouring voxels are classified as GM, WM, or CSF). Unfortunately, transferring clustering methods to pre-clinical

research is complicated by the fact that rodent MR images have less contrast and fewer defined structures (Feo and Giove, 2019). However, the SIGMA template comes with tissue probability maps. If these are provided as inputs (i.e., priors), with the FLIRT transform to template space, they can be used to initialise `FAST`, and refine the segmentation process.

Given that anatomical variability is lower in the rodent brain, template-based schemes are also attractive (Bai et al., 2012). In a template-based approach, the tissue probability maps from the template can be adapted to the subject image by applying the warps calculated during the non-linear registration step using trilinear interpolation. Here, the overall quality of the segmentation will depend on quality of the registration and algorithm used (e.g., `ANTs`), as well as the tissue classification accuracy of the template. The maps containing probability maps that are generated can then be thresholded (e.g., at >50%) so that they are binary and only include voxels that have a high probability of being each tissue type.

Both `FAST` and a template-based approach were tested to determine the best method for segmenting the rodent scans.

3.2.3 Diffusion MRI Processing Pipeline

In addition to the structural MRI pipeline, a rodent dMRI pipeline was developed. This pipeline incorporates standard processing and analysis procedures (Alfaro-Almagro et al., 2018; Bastiani et al., 2019; Glasser et al., 2013) to automatically generate various measures of tissue microstructure from the brain (Basser and Pierpaoli, 1996; Gyengesi et al., 2014; Zhang et al., 2012). While pre-processing *ex vivo* pre-clinical dMRI data shares similarities with human imaging due to common image artifacts, it also

presents unique challenges that must be addressed.

Systematic issues in pre-clinical diffusion-weighted imaging often include incorrect image orientation (as shown in Figure 3.2), inconsistencies between the ordering of volumes within 4D dMRI images and the values within corresponding bval files, and other similar problems. These issues may arise from differences in software versions (i.e., Paravision 6 versus Paravision 360) that encode crucial data differently, or they may occur during the conversion of scanner data. Methods to address these challenges are detailed in a previous section (`rodent_preproc`).

The rodent dMRI pipeline (`DiffPreproc_rodent`) performs the following steps to pre-process data: registration to the anatomical scan and template space to allow for skull stripping; correction of susceptibility-induced distortions (Andersson and Skare, 2002), eddy currents and sample motion (between and within volume) (Andersson and Sotiropoulos, 2016); identification and correction of outliers (Andersson et al., 2017); and calculation of quality control (QC) measures (Bastiani et al., 2019). These steps are required because EPI is particularly sensitive to field inhomogeneities, and rapidly switching diffusion-weighted gradients induces eddy currents in conductors within the bore. Despite the *ex vivo* nature of the samples, scanner vibration over the long scan times can mean that volumes are no longer well aligned. "Motion correction" addresses this. Where repeats were acquired, we estimated and corrected for susceptibility-induced distortions, eddy currents, and motion before averaging across repeats to ensure accurate alignment and minimise artifacts. Once pre-processing is complete, the pipeline then fits the diffusion tensor (DT) model to estimate fibre orientation and tissue microstructural parameters, such as the fractional anisotropy (FA) and mean diffusivity (MD).

`Topup` was used to estimate a susceptibility-induced off-resonance fieldmap using two opposing phase-encoding $b = 0$ s/mm^2 images (Andersson et al., 2003). FSL's `eddy` (Andersson and Sotiropoulos, 2016), was then used to retrospectively correct for the distortions resulting from sample motion and eddy currents. It uses a non-parametric framework to consider how sample motion will influence the off-resonance field which results from magnetic susceptibility and eddy currents. `Eddy` also replaces slices that are identified as being 'outliers', due to the signal loss that results from sample movement coinciding with the direction of the diffusion-encoding gradient (Andersson et al., 2016).

In terms of QC measures (Bastiani et al., 2019), the SNR and CNR were calculated for the dMRI measurements using `eddy_qc`. SNR maps were generated for the $b = 0$ s/mm^2 images by computing, for each voxel, the mean of signal intensity across the different $b = 0$ volumes divided by the standard deviation of these intensities. The average SNR was calculated across the whole brain. For CNR maps, a voxelwise calculation was performed for each b shell, reflecting the **angular contrast** across the diffusion-weighted volumes. For each voxel, the average distortion-free signal across the directions for each b shell (i.e., diffusion-related variance) was divided by the variance of the noise (as provided by the `eddy` tool in FSL). An average CNR for each b value was obtaining by averaging all CNR values within the brain.

There are some important variables that have to be provided to the pipeline inputs, such as the phase encoding direction (i.e., left/right, superior/inferior or anterior/posterior). Other inputs, such as the brain mask generated in the anatomical pipeline and the reversed phase-encode acquisition, must be provided for skull stripping and correction of susceptibility induced distortions respectively. If processing mouse data, a suitable template will also be required.

3.3 Results

This section presents examples of the acquired data and outputs from the various steps of the processing pipelines. Comparisons are made between the different methods tested during the development and optimisation of the pipelines for the rat brain. To illustrate the generalisability of the pipelines across different scanners, their performance is demonstrated on data acquired using different systems (Nottingham and Oxford). The flexibility of the pipelines is further showcased using mouse data acquired. In this case, only minimal changes were required (i.e., substituting the brain template with one suitable for mouse imaging).

3.3.1 Optimising Data Acquisition

A qualitative demonstration with representative examples of the acquired data is presented in Figure 3.4. These scans were obtained in Nottingham and Oxford for samples prepared with, and without, gadolinium.

While scanning samples at multiple sites presented challenges, this dataset allows for the evaluation of how variations in sample preparation methods (e.g., using gadolinium contrast in perfusate), scanner hardware (e.g., volume coil versus surface cryocoil), and acquisition sequences (e.g., 3D- or 2D-EPI dMRI) impact data quality, as discussed in the following sections.

Effects of Gadolinium on T_1

There was a 10-fold decrease in the average T_1, from approximately 1600ms to 130ms, between the control samples and those prepared with gadolinium (2mM), as shown in Figure 3.5. The GM in samples perfused with contrast

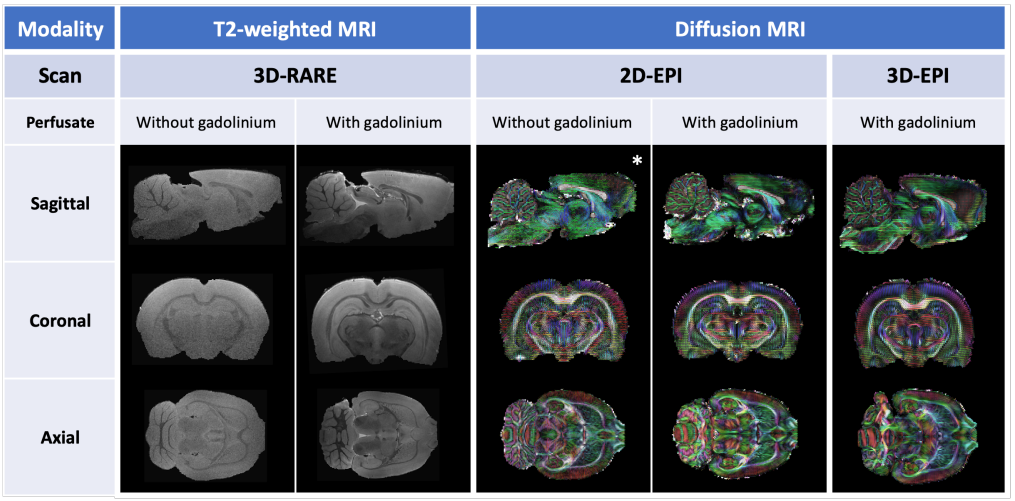


Figure 3.4: Processed anatomical and diffusion data for samples prepared with and without contrast. Images with an asterisk (*) are from scans acquired on the Nottingham system. Remaining images were acquired on the Oxford scanner. To demonstrate the quality of diffusion data, primary eigenvectors, colour coded by direction, are provided.

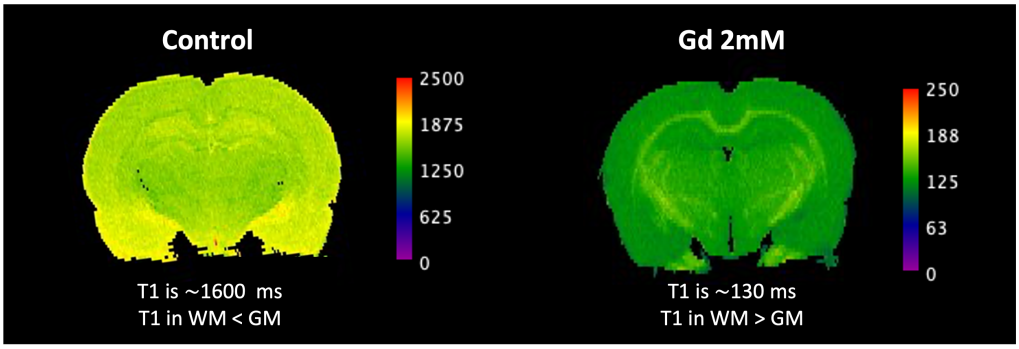


Figure 3.5: Including gadolinium contrast in the sample preparation led to a significant (>10 fold) reduction in T_1, as shown in the T_1 maps for a control (left) and gadolinium-perfused (right) sample. Please note the different colour scales used for image intensity.

agent became less intense (i.e., shorter T_1) than the WM, potentially because of greater blood flow and delivery of contrast agent to the GM. This contrast differs from what was seen in the control brain, where GM had a longer T_1 than WM.

Optimising Image Contrast and Scan Time for Anatomical MRI

The TR of the 3D-RARE acquisitions could be reduced by a factor of three (5000ms to 1500ms) for samples prepared with gadolinium, due to the ten-fold reduction in T_1. This shortened the overall scan time in Nottingham by at least two thirds (21h43m to 5h57m). Figure 3.6 demonstrates that for samples prepared with gadolinium, it was possible to enhance the image contrast in 3D-RARE acquisitions in Nottingham (GM/WM CNR increases from 0.31 to 0.75), whilst simultaneously reducing the overall scan time.

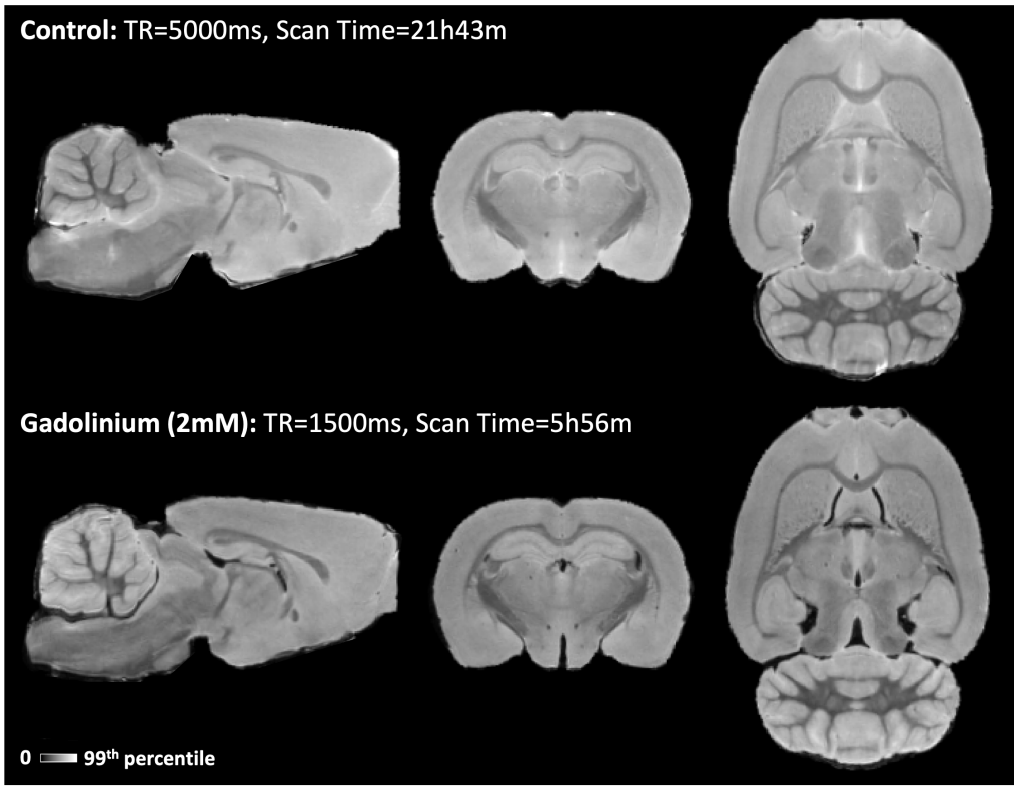


Figure 3.6: Including gadolinium in the sample preparation led to an increase in the contrast of anatomical scans in Nottingham, whilst also allowing for shorter acquisitions. This is demonstrated when comparing a control sample (above) with a sample prepared with gadolinium (below). Scans are shown in standard space.

In Oxford, the image contrast of 3D-RARE acquisitions with a short TR (i.e., 350ms) was much higher (GM/WM CNR increases from 1.19 to 1.54) in samples that were prepared with gadolinium, as shown in Figure 3.7.

This highlights the importance of controlling acquisition parameters for the T_1 of the sample. Given that the T_1 is ∼130ms in samples perfused with gadolinium, a TR of 350ms is appropriate (i.e., because TR is 2-3X larger than the tissue's T_1). However, a TR of 350ms is much too short for samples that don't contain any contrast agent, as T_1 is ∼1600ms.

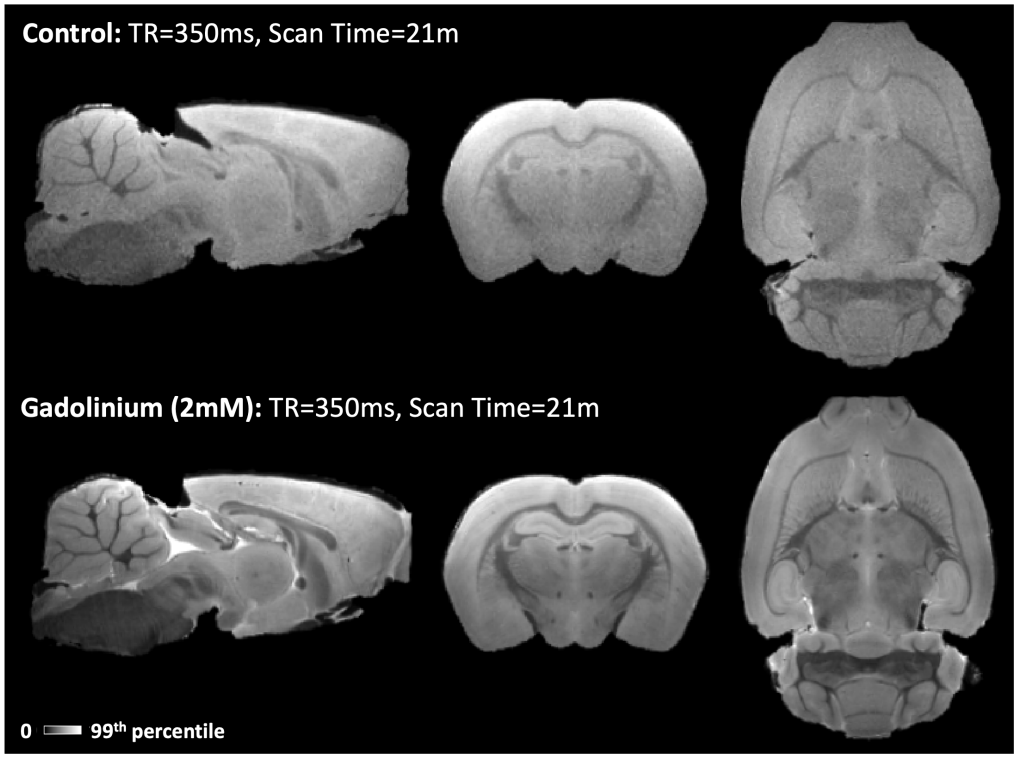


Figure 3.7: When TR was short (i.e., 350ms), the contrast of anatomical scans acquired in Oxford was much higher in samples that contained gadolinium contrast. This is demonstrated when comparing a control sample (above) with a sample prepared with gadolinium (below). Scans are shown in standard space.

Optimising Angular Contrast-to-Noise for Diffusion MRI

Due to the high levels of noise in the dMRI data acquired in Nottingham, it was necessary to average signal across 12 repeats. This made scans two and half times longer in Nottingham (31h12m as opposed to 12h30m). Furthermore, in Nottingham the TR could not be lowered below 6000ms when using a 2D-EPI readout, as this acquisition was already pushing the

limits of the duty cycle. This meant it was not possible to capitalise on the lower T_1 in samples perfused with gadolinium. In contrast, it was possible to reduce TR to 4500ms on the Oxford scanner.

Table 3.6 shows that including gadolinium in the sample preparation reduced the quality of diffusion data (SNR of $b0$ volumes = 3.60, angular CNR = 0.08-0.09) acquired in Nottingham, where options were limited to a 2D-EPI read-out and it was not possible to reduce the TR. This is not surprising to see given that the TR (6000ms) for the 2D-EPI dMRI acquisitions was >40 times longer than the T_1 (∼130ms) of samples prepared with gadolinium.

Sample	Average SNR (b=0s/mm^2)	Average CNR (b=4000s/mm^2)	Average CNR (b=6000s/mm^2)
Control	**4.97**	**0.17**	**0.17**
Gd	3.60	0.08	0.09

Table 3.6: Comparing quality for 2D-EPI dMRI scans acquired in Nottingham using the same parameters. Scans of control samples exhibited higher angular contrast, as TR could not be optimised for accelerated signal recovery with gadolinium.

To take advantage of the decrease in T_1 of samples prepared with gadolinium, a 3D-EPI dMRI acquisition, where TR is more flexible, was trialled. Unfortunately, the severity of the image artefacts in Nottingham rendered the acquired data unusable. However, researchers in Oxford have optimised 3D-EPI dMRI protocols for rodent MRI. As such, it was possible to use a 3D-EPI readout which allowed for a fifteen-fold reduction in the TR (reduced from 4500ms to 300ms). This reduced scan duration by 15% (reduced from 12h30m to 10h40m).

As shown in Table 3.7, the quality of diffusion data was greatest (SNR of $b0$ volumes = 60.61, angular CNR = 3.97-5.46) when a sample containing gadolinium was imaged in Oxford using a 3D-EPI dMRI readout, with a short TR (300ms).

Sample	Control	Gadolinium-perfused	
Acquisition	2D-EPI	2D-EPI	**3D-EPI**
Average SNR (b=0s/mm^2)	32.94	24.30	**60.61**
Average CNR (b=4000s/mm^2)	3.45	2.13	**5.46**
Average CNR (b=6000s/mm^2)	2.37	1.77	**3.97**

Table 3.7: Quality control metrics for dMRI acquisitions of samples scanned in Oxford using a 2D- or 3D-EPI readout. The samples were prepared with, or without gadolinium. Image quality is highest when scanning a sample containing gadolinium using a 3D-EPI readout, with a short TR (300ms).

Figure 3.8 clearly shows the significantly higher angular CNR in dMRI scans acquired in Oxford compared to those from Nottingham. This difference is likely due to the Oxford acquisition being optimised for the sample's T_1, reduced thermal noise from the cryo-coil, and the older scanner hardware in Nottingham. Higher angular CNR improves the estimation of complex fibre configurations, such as multiple crossing fibres within a voxel.

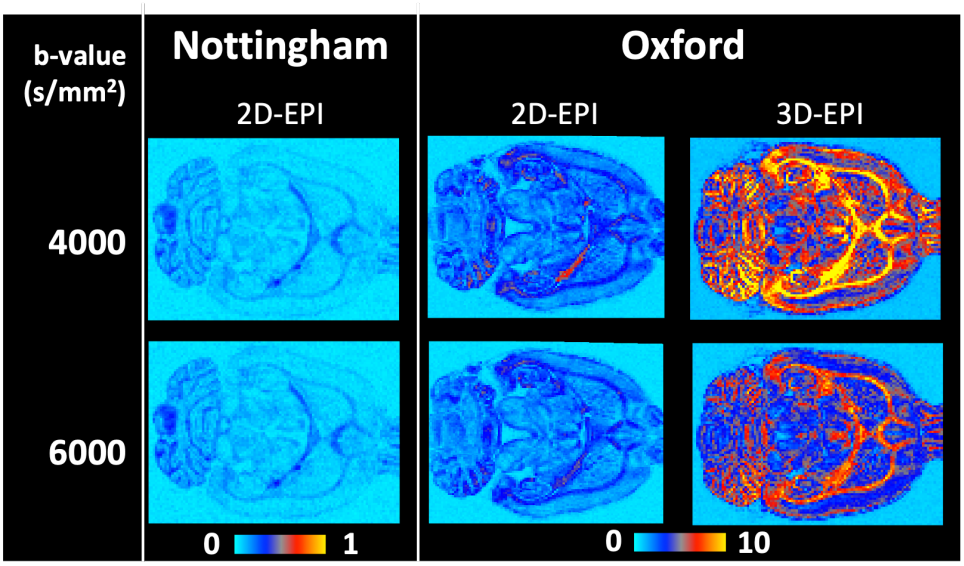


Figure 3.8: Mapping of average angular CNR for dMRI scans of a gadolinium-perfused sample (axial view). These scans were acquired at Nottingham (left), using a 2D-EPI readout, and Oxford (right), using a 2D-EPI or 3D-EPI readout.

3.3.2 Data Conversion and Image Pre-processing

As described in the methods section, and demonstrated in Figure 3.2, imaging data acquired using Bruker scanners can be inverted and labelled incorrectly. To confirm that all scans are being correctly oriented and labelled appropriately, without inadvertently swapping the left and right sides of the brain, a rat skull was scanned with a cod-liver oil capsule placed in the left eye socket. Figure 3.9 shows how the cod-liver oil capsule remains on the left hand side of the brain after converting the raw Bruker Paravision data files to the NIfTI format and doing some initial pre-processing that standardises image orientation.

Methods were developed to correct the diffusion gradient directions (i.e., `bvec` matrices) and ensure their orientation was consistent with that of the associated image matrices. To confirm that the conversion and pre-processing methods were correctly modifying the `bvec` files, `dtifit` was run prior to any distortion correction. The orientations (i.e., primary eigenvectors) were then visually checked, as shown in Figure 3.10, to confirm that they aligned with the trajectories of known white matter tracts.

To ensure that the diffusion gradient vector (i.e., `bvec` matrix) aligns with the image matrix, different adjustments were required for datasets acquired in Nottingham and Oxford. As the scanners at Nottingham and Oxford were operated using different software versions, this suggests that the architecture of diffusion data varies between these versions. Tests confirmed this variation. It was found that the adjustments needed could be standardised for datasets acquired in Nottingham using Paravision 6.0 software. However, in Oxford, the orientation of samples in the scanner bore was relevant. Table 3.8 summarises the necessary modifications for each dataset's `bvec` files, and illustrates how sample orientation in the scanner affects these adjustments.

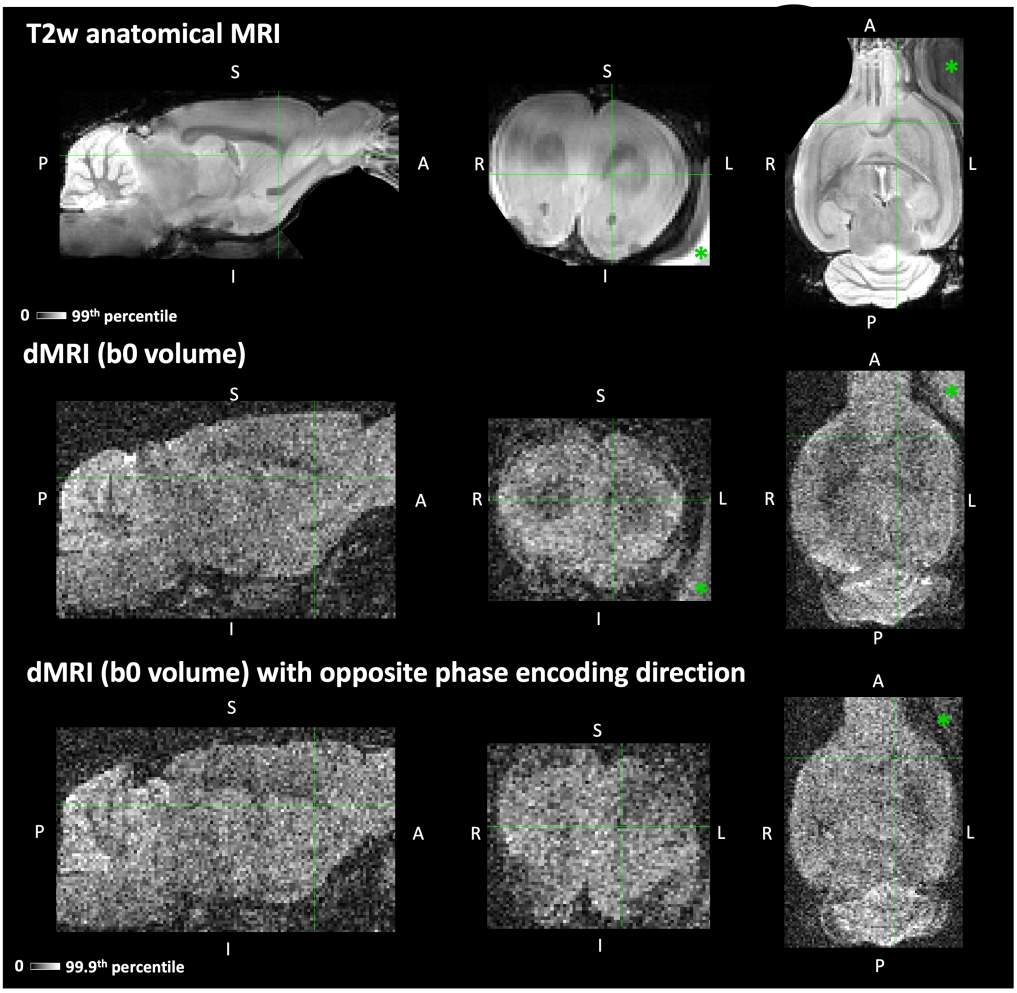


Figure 3.9: Confirming that the methods for standardising image orientation do not swap the left and right sides of the brain. The images above show that a cod-liver oil capsule (labelled with a *), placed in the left eye socket, always remains on the left hand side of the brain. The other parts of the brain (i.e., superior/inferior and anterior/posterior) are also correctly labelled.

This highlights the complexity of automating pipelines for processing dMRI data from multiple pre-clinical systems.

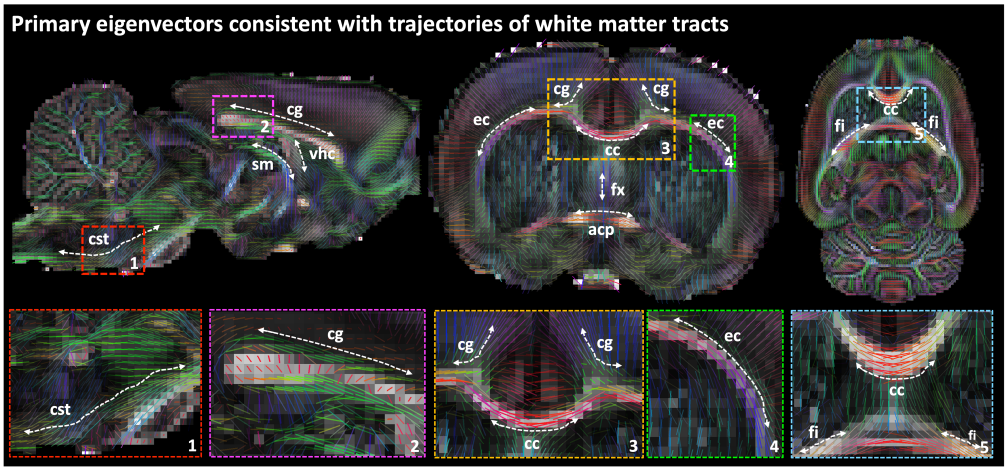


Figure 3.10: This figure confirms that the directions of diffusion encoding gradients are consistent with the orientation of diffusion-weighted images. When correct, primary eigenvectors align with the trajectories of known white matter tracts, labelled as follows: acp (anterior commissure, posterior part), cc (corpus callosum), cg (cingulum), cst (corticospinal tract), ec (external capsule), fi (fimbria), fx (fornix), sm (stria medullaris of the thalamus), and vhc (ventral hippocampal commissure). The top section displays sagittal, coronal, and transverse brain planes, while the bottom section features numbered panels with enlarged views of individual white matter tracts. Eigenvectors are presented as lines colour-coded by direction (red: left/right, blue: superior/inferior, green: anterior/posterior) and modulated by fractional anisotropy.

	Nottingham	Oxford	
Orientation	2D-EPI dMRI	2D-EPI dMRI	3D-EPI dMRI
nose first	neg_x, y, neg_z	x, **z, y**	x, **z, y**
cerebellum first	neg_x, **y, neg_z**	neg_x, **z, y**	neg_x, **z, y**

Table 3.8: The diffusion gradient vectors (i.e., `bvec` matrix) generated from data acquired using the Nottingham and Oxford scanners needed to be modified to ensure that they align with the associated images. For Nottingham datasets (acquired using Paravision 6 software), the x and z elements need to be negative. In contrast, the order of y and z elements need to be swapped for Oxford datasets (acquired using Paravision 360 software). However, if the sample was inserted into the Oxford scanner bore with the cerebellum first, the x elements of the `bvec` matrix also need to be become negative. This was true for dMRI data acquired using 2D- and 3D-EPI.

3.3.3 Anatomical MRI Pipeline

Brain Extraction

The FSL brain extraction tool (`BET`) either cropped anatomical scans without extracting the brain, as shown in the top panel of Figure 3.11, or had no effect. Various settings were adjusted, including the fractional intensity threshold, brain centre of gravity, gradient in fractional intensity threshold, and head radius measure, to evaluate their impact on `BET`'s performance. However, a suitable combination of settings could not be identified. Consistent with findings from previous studies (Li et al., 2013; Wood et al., 2013), it appears that `BET` is unable to effectively discriminate between brain and non-brain tissue in rodent MRI.

`rBET`, a modified version of `BET` was also tested(Wood et al., 2013). This tool, available on NITRC, adjusts surface meshes and the assumed shape and curvature of the brain to better suit rodent anatomy. As shown in Figure 3.11 (middle panel) `rBET` achieved better results than `BET` (top panel). However, the whole skull was not successfully removed and some brainstem and cerebellum was lost. Furthermore, this quality of result was only attained after extensive parameter adjustments (i.e., brain centre of gravity, radius of head, fractional intensity threshold, vertical gradient and brain surface smoothness). Applying the same set of parameters to another sample led to a worse outcome, with more skull remaining and/or more brain tissue lost. Since this approach was not generalisable to new datasets and could not be automated, a better solution was required.

The third method that was tested was template-based brain extraction. Here, the warp generated by non-linear registration (specifically using `ANTs`) was inverted and applied that to the template brain mask, using nearest

neighbour interpolation (i.e., so that the mask remained binary), to take it to subject space. The transformed mask was then applied to the scan to remove non-brain tissue. Figure 3.11 shows that the performance of this method (bottom panel) was highest.

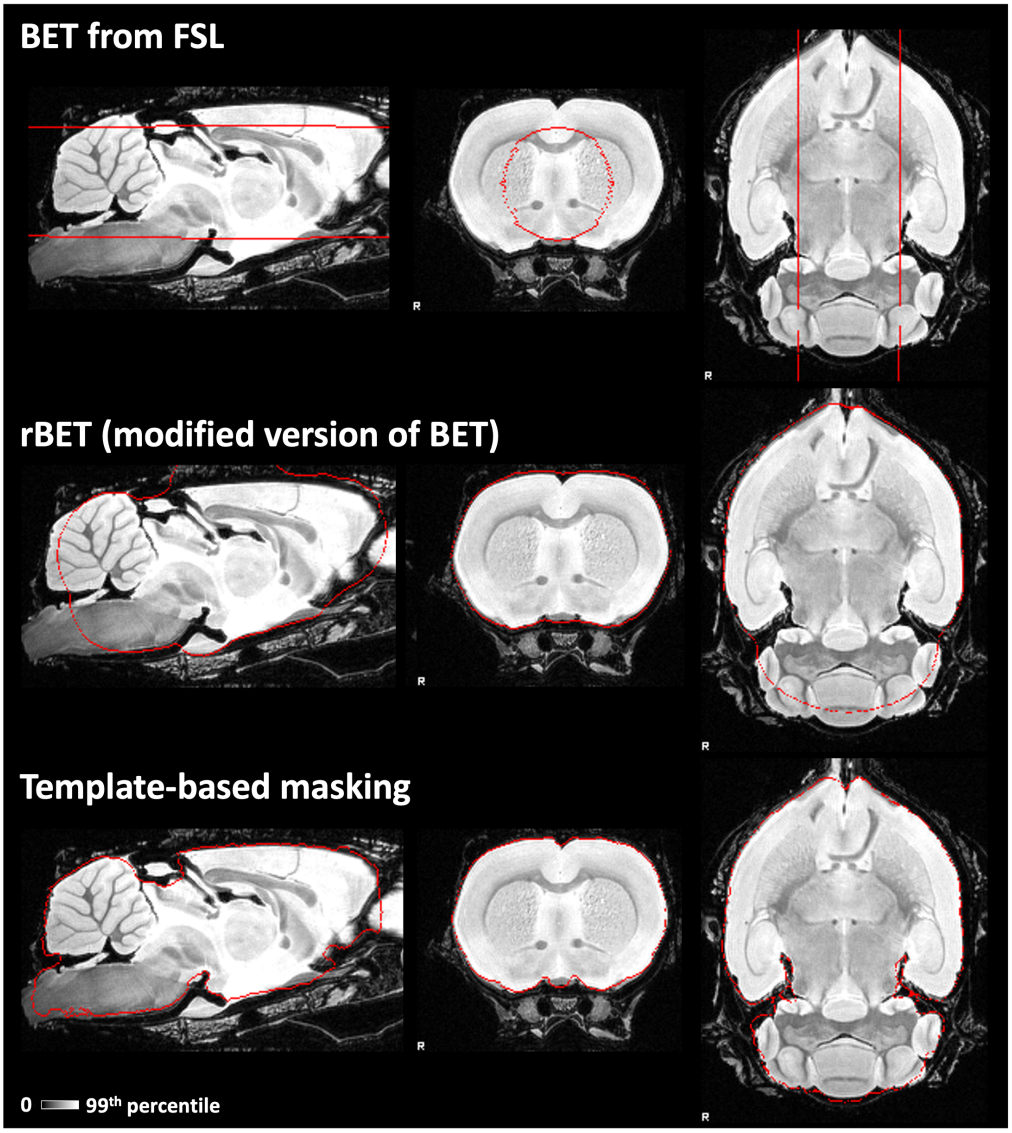


Figure 3.11: Comparisons between alternative methods for brain extraction, that use `BET` from `FSL` (top), `rBET` (middle), and a template-based approach (bottom). These results are for an anatomical T2-weighted scan (3D-RARE) of a control brain acquired on the Nottingham system. The red outline shows what these various approaches identify as being the boundary between the brain and skull.

Correcting for Bias Field/Signal Inhomogeneities

`FAST` was used to correct for bias field inhomogeneities in the brain extracted scans. As the default setting for spatial smoothing (20mm) used by `FAST` is large relative to the size of the rodent brain, a number of values (20, 10, 7, 5, 2 and 1mm) were tested. The aim was to ensure that `FAST` estimates a gradual bias field across the brain, without evidence of segmentation. To ensure that the pipeline could accommodate different levels of bias field and signal intensities, testing was done with datasets acquired at Nottingham and Oxford, using samples that were prepared with, and without, gadolinium contrast. However, the different methods of sample preparation did not appear to impact on the signal inhomogeneities observed.

Although the anatomical scans that were acquired at Nottingham, whilst using a volume coil, did not appear to have any significant signal inhomogeneities, gradual variations in image intensity may not always be visually obvious. Bias field correction was therefore still performed. As shown in Figure 3.12, a high degree of bias field smoothing (i.e., 10mm) was suitable for Nottingham data. This setting can be chosen in `rodent_anat` by using the appropriate flags (`--weakbias --biassmooth 10`).

In Oxford, a cryogenically-cooled surface coil was used for imaging. The bias field in these scans was much more noticeable. After testing, the appropriate scale for bias field smoothing was found to be 1mm. This setting can be chosen in `rodent_anat` by using the appropriate flags (`--strongbias --biassmooth 1`).

To produce an undistorted subject image in native space, the estimated bias field was used to correct T2-weighted scans (i.e., scans were divided by the estimated bias field using `fslmaths`). Before and after images are

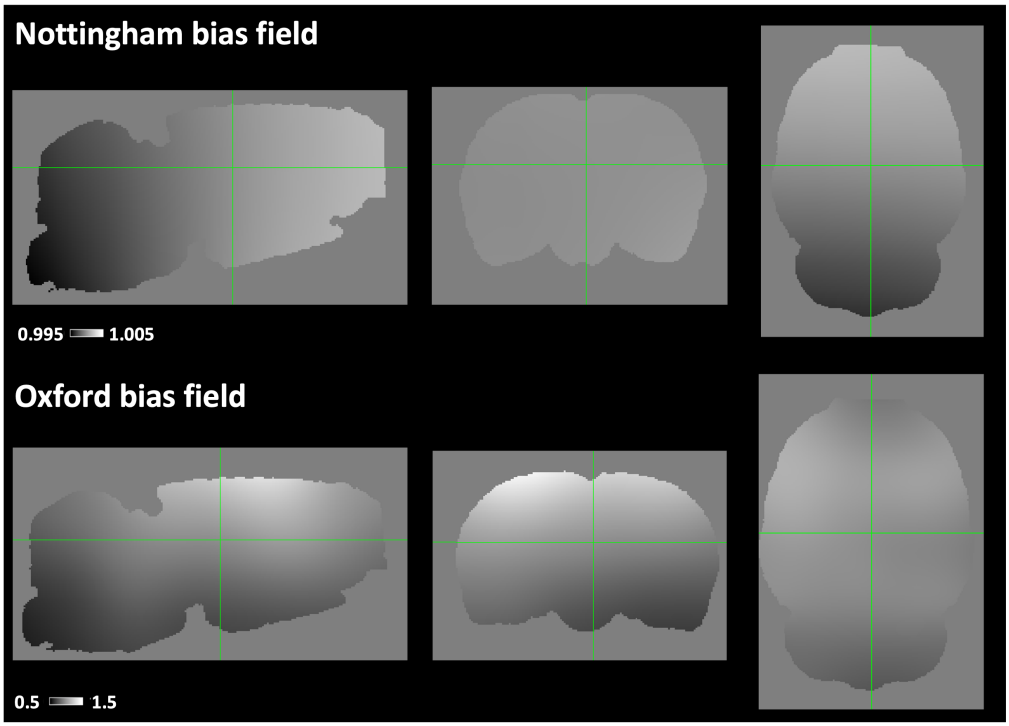


Figure 3.12: The bias field estimate (native space) generated by `FAST` for data acquired on the Nottingham (above) and Oxford (below) scanners. These samples contained no contrast agent and both were inserted into the scanner 'nose' first. Please note the different scales used for image intensity and that, as described in the text, the bias field smoothing for Nottingham and Oxford data was set to 10 and 1mm respectively.

provided in Figure 3.13.

Registration

The `ANTs` SyN algorithm was run as an intramodal registration (i.e., both scans are T2 weighted so a cross-correlation metric was used) of the skull-stripped bias-corrected sample brain to the standard template. The non-linear registration was initialised using the linear transformation generated by `FLIRT` to allow for comparison with `MMORF`. After registration was complete, the `ANTs` warps were converted so that they are compatible with `FSL`. This was achieved using the ITK-SNAP (Yushkevich et al., 2006) Convert 3D Medical Image Processing Tool (available online).

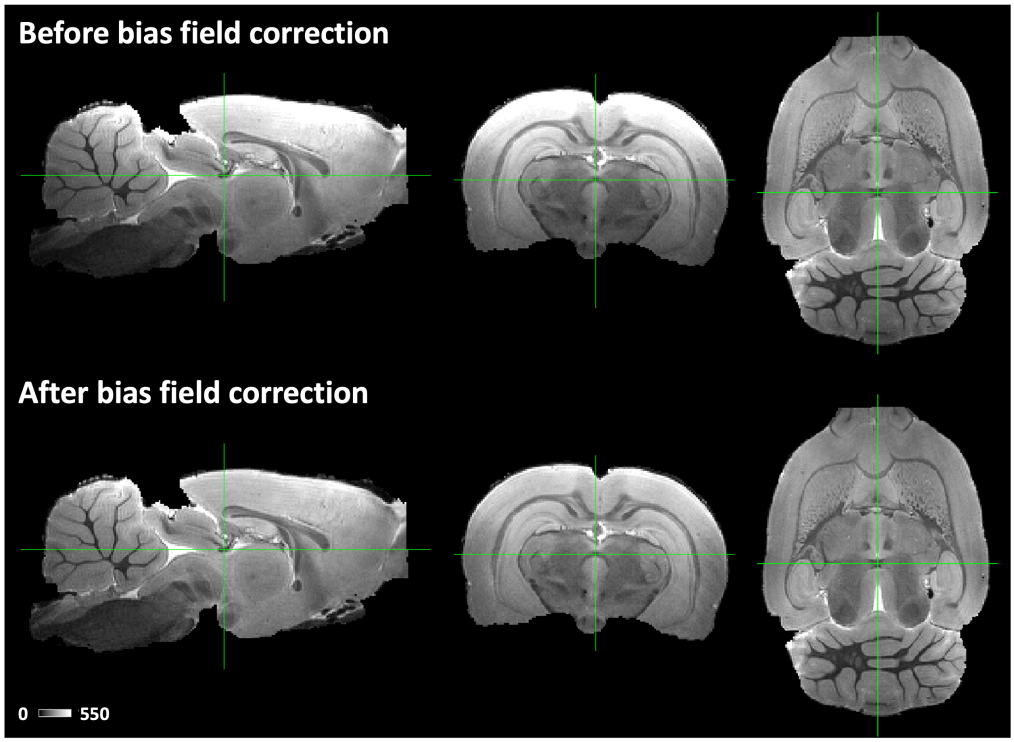


Figure 3.13: The effects of bias field correction for a dataset acquired in Oxford using a surface cryo-coil. This sample was prepared with gadolinium contrast.

When registering the bias-corrected sample brain to the standard template using `MMORF`, parameters first needed to be optimised to accommodate for the differences between human and rodent MRI, most notably the voxel size. In brief, the registration was most successful if the initial warp and bias field resolutions were reduced by a factor of 10 (i.e., to 3.2mm). An additional fine-level iteration round (total of 6 rounds) was required with a warp resolution of 0.2mm and regularisation of 1.8e-1. Five optimisation iterations were run for the coarsest-level round. A lower weighting was used for the template image cost function (i.e., 0.5 or 0.2 as opposed to 1) and bias field regularisation was adjusted (1e8, 1e8, 1e8, 1e7, 1e7 and 1e6). All iterations were run with a brain mask for the sample and template, and the final two iterations (i.e., warp resolutions of 0.4 and 0.2mm) were performed using the low memory optimisation strategy.

Figure 3.14 shows that both methods achieve very good alignment and improve on linear registration, as expected. `MMORF` also matched the performance of `ANTs`, as previously described in Lange et al. (2020). Subsequent steps use the `ANTs` warps as `MMORF` is still in development and is therefore subject to change.

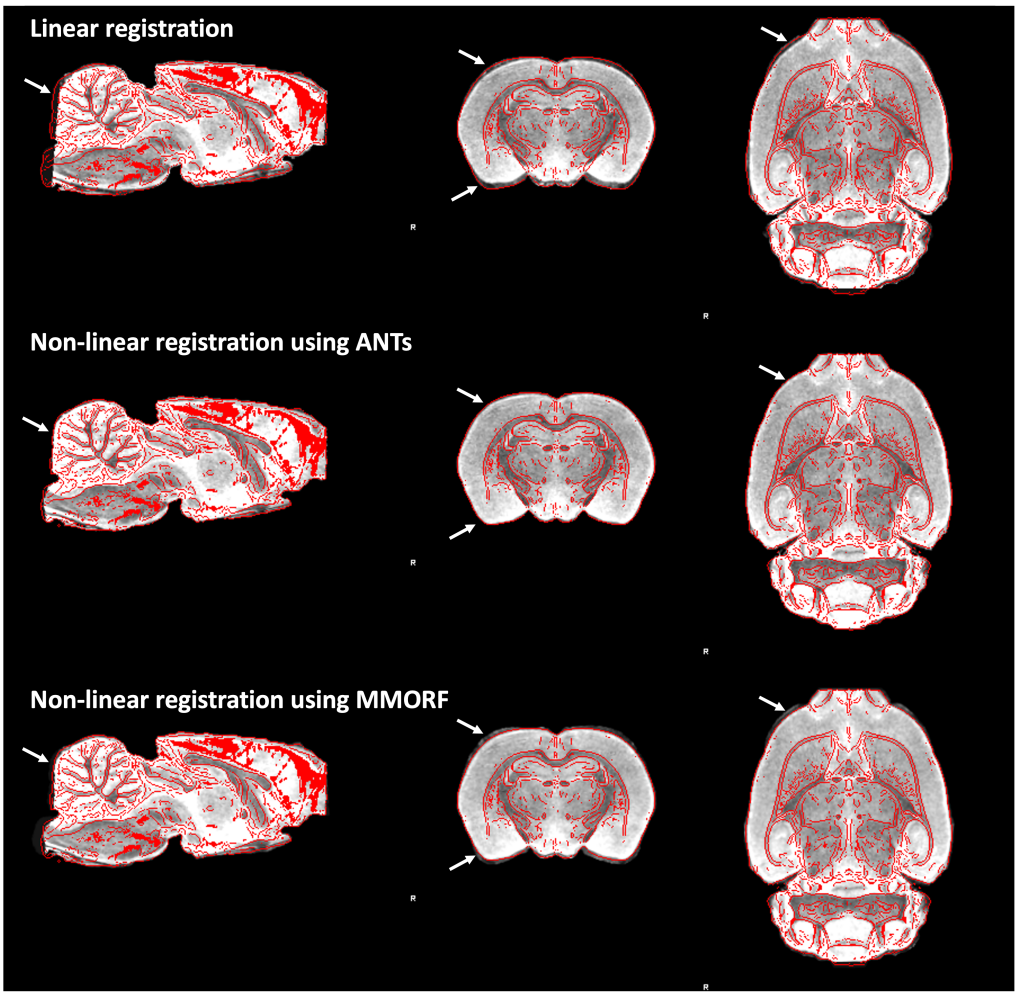


Figure 3.14: Registration of whole head sample to template using `FLIRT` (top), `ANTs` (middle) and `MMORF` (bottom). The outline of the standard template brain is superimposed in red over the subject image to demonstrate the alignment. Arrows indicate where alignment differs.

Tissue Segmentation

A clustering method, `FAST` and template-based scheme were tested for automatically segmenting the bias-field corrected brain image into different

tissue types. Both methods rely on probabilistic tissue classification maps from the template (for rats the SIGMA template was used). In `FAST`, these tissue maps can be specified as priors, to initialise the segmentation process. In contrast, for the template-based scheme, the template's tissue maps were warped to the subject image using the deformation field generated in the non-linear registration step (the default setting uses `ANTs`).

The results achieved with `FAST` and the template-based approach are compared in Figure 3.15. The template-based approach (shown in the bottom panel) performed better as it was able to identify areas of white matter that were missed by `FAST`.

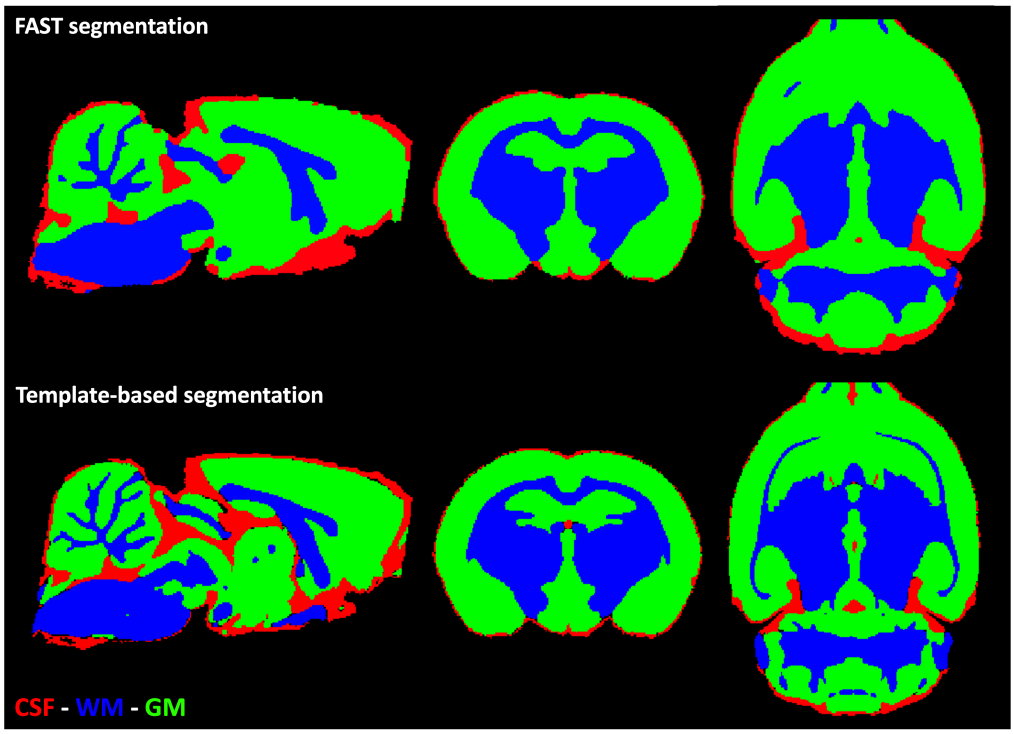


Figure 3.15: Tissue segmentation with `FAST` (top), a clustering method, and template-based approach (bottom).

Generalisability across Scanners and Rodents

Figure 3.16 demonstrates that the pipeline can generalise across different scanners and acquisition protocols. Here, segmentation results are shown

for scans acquired in Nottingham and Oxford using the same brain . As the template-based segmentation reflects all processing steps (i.e., registration, skull-stripping and bias-field correction), the similarity of the results suggest robustness of all the pipeline steps to differences across scanners.

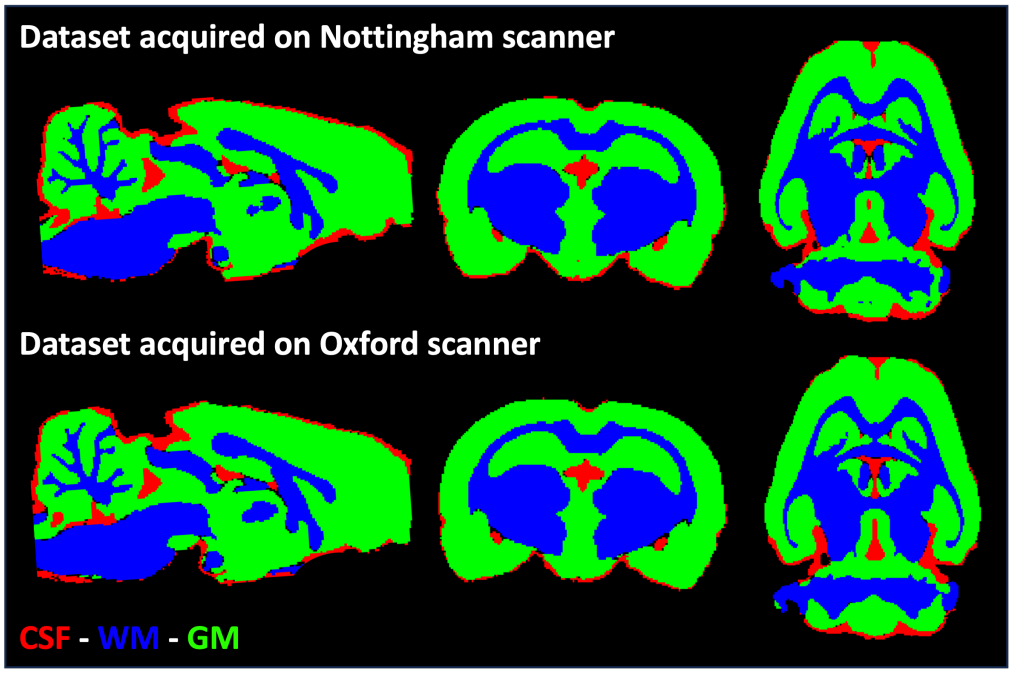


Figure 3.16: The anatomical pipeline generalises across different scanner models and imaging protocols. Here the results of tissue segmentation (using the template-based approach) are comparable on data acquired using the Nottingham (above) and Oxford (below) scanners.

The flexibility of the pipeline, which was developed for the rat brain, was tested on mouse brain data to determine how well it performs in a more demanding scenario. The only detail that was altered was the template. In this case, the Allen mouse brain template (0.07mm^3), was used. However, any template could be used, as long as it is specified. This can be done easily in `rodent_anat` by using the `--template` flag. Figure 3.17 shows that the pipeline works well on mouse data, with only this limited change.

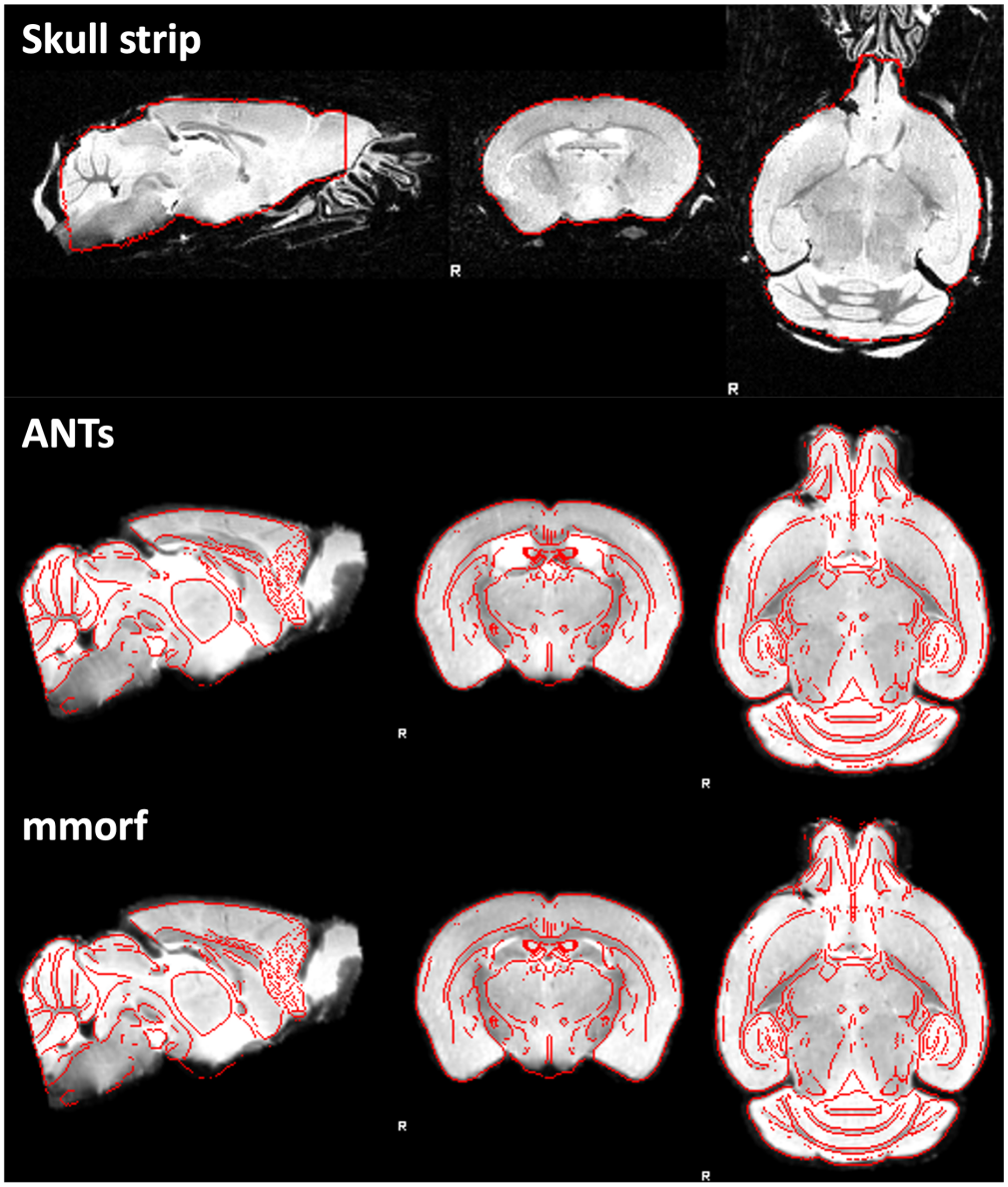


Figure 3.17: Performance of structural pipeline on mouse scan acquired at Nottingham. Data provided by Dr Mariah Lelos.

3.3.4 Diffusion MRI Pipeline

As with the anatomical pipeline, the performance of the dMRI pipeline across various steps was tested. The generalisability of the dMRI pipeline to data obtained using different scanners and acquisition protocols was also tested. Finally, the flexibility of the pipeline was tested using using mouse data.

Correcting Susceptibility-induced Distortions

Figure 3.18 demonstrates the estimated susceptibility/off-resonance field for data obtained on the Nottingham and Oxford scanners. It is apparent that the susceptibility-induced distortions are worse for data acquired in Nottingham, especially in the superior portion of the brain.

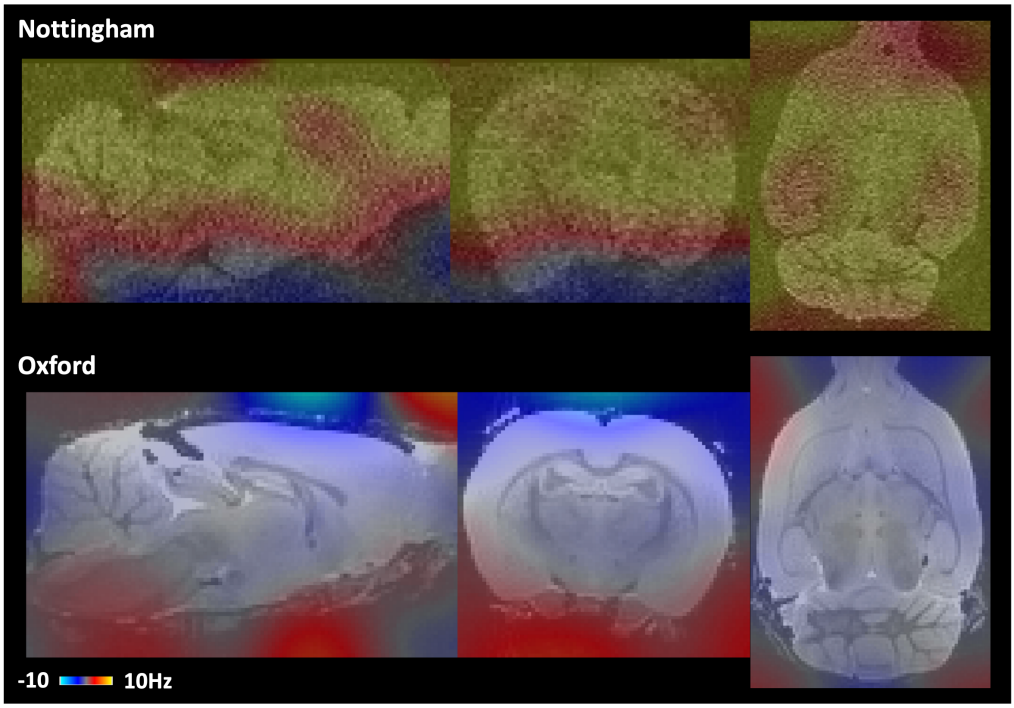


Figure 3.18: Estimated susceptibility/off-resonance field for data acquired on the Nottingham (above) and Oxford (below) scanners.

Fitting the Diffusion Tensor Model

Figure 3.19 demonstrates that the noise level for 2D-EPI dMRI scans obtained in Nottingham (31h12m) is significantly greater than what was achieved when scanning the same control sample in Oxford (13h4m). Nevertheless, it was still possible to identify key white matter tracts like the corpus callosum.

Figure 3.20 demonstrates that the pipeline can process dMRI data acquired

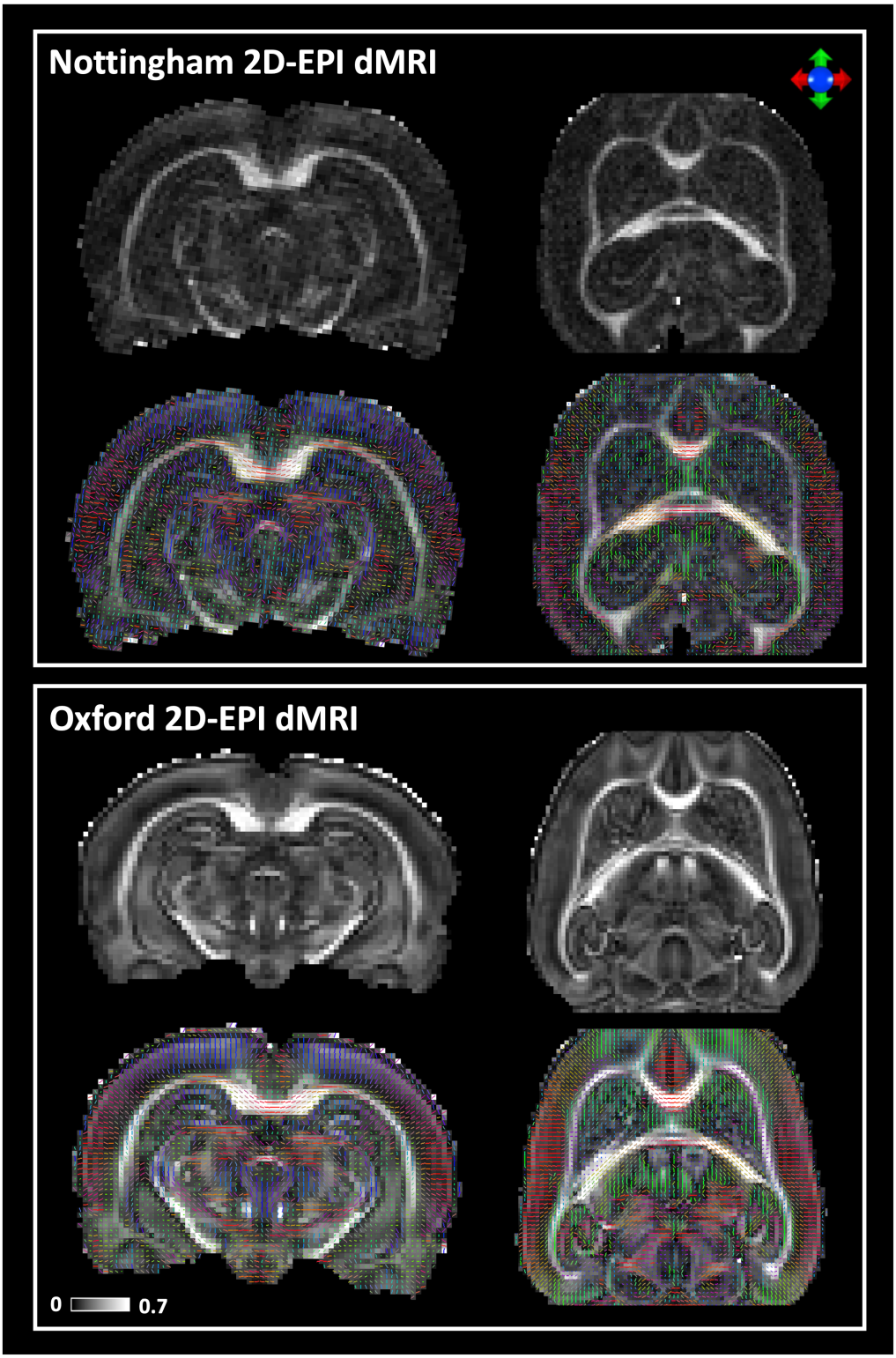


Figure 3.19: 2D-EPI dMRI acquisitions for the same control sample, scanned at Nottingham (top panel) and Oxford (bottom panel). The upper rows show the fractional anisotropy (grey scale) whilst the lower rows show the primary eigenvectors (colour coded by direction).

using a 2D-EPI (TR of 4500ms) or 3D-EPI readout (TR of 450ms). Visual inspection does not indicate an obvious difference in the contrast between these datasets. However, as described previously, quantitative quality control tests showed that the contrast to noise ratio was highest for acquisitions that used a 3D-EPI read-out.

3.4 Discussion

We have developed an acquisition protocol for multi-modal *ex vivo* MRI of the rat brain. This protocol optimises image contrast while accounting for the limitations of the scanner and acquisition methods. We also developed an automated image processing pipeline by adapting well-established human imaging tools for rodent data, addressing some of the challenges of processing pre-clinical data. This pipeline performs data conversion, registration, brain extraction and tissue segmentation, while also correcting for signal inhomogeneities, susceptibility-induced distortions, eddy currents, sample motion and outliers. In addition, it calculates QC measures and fits the diffusion tensor model to generate various measures of tissue microstructure. By using data from multiple pre-clinical imaging scanners, we demonstrated that the pipeline is robust and generalisable across different acquisition setups, hardware, image SNRs and CNRs, and even across rodent species (mouse and rat brains).

It was further shown that preparing samples with gadolinium (2mM) improves image contrast in structural MRI and could potentially reduce scan time. However, the impact of gadolinium on dMRI varies based on whether the acquisition is optimised for the sample's T_1. For instance, when it is possible to adopt a 3D-EPI readout with short TR (e.g., 300ms), there is

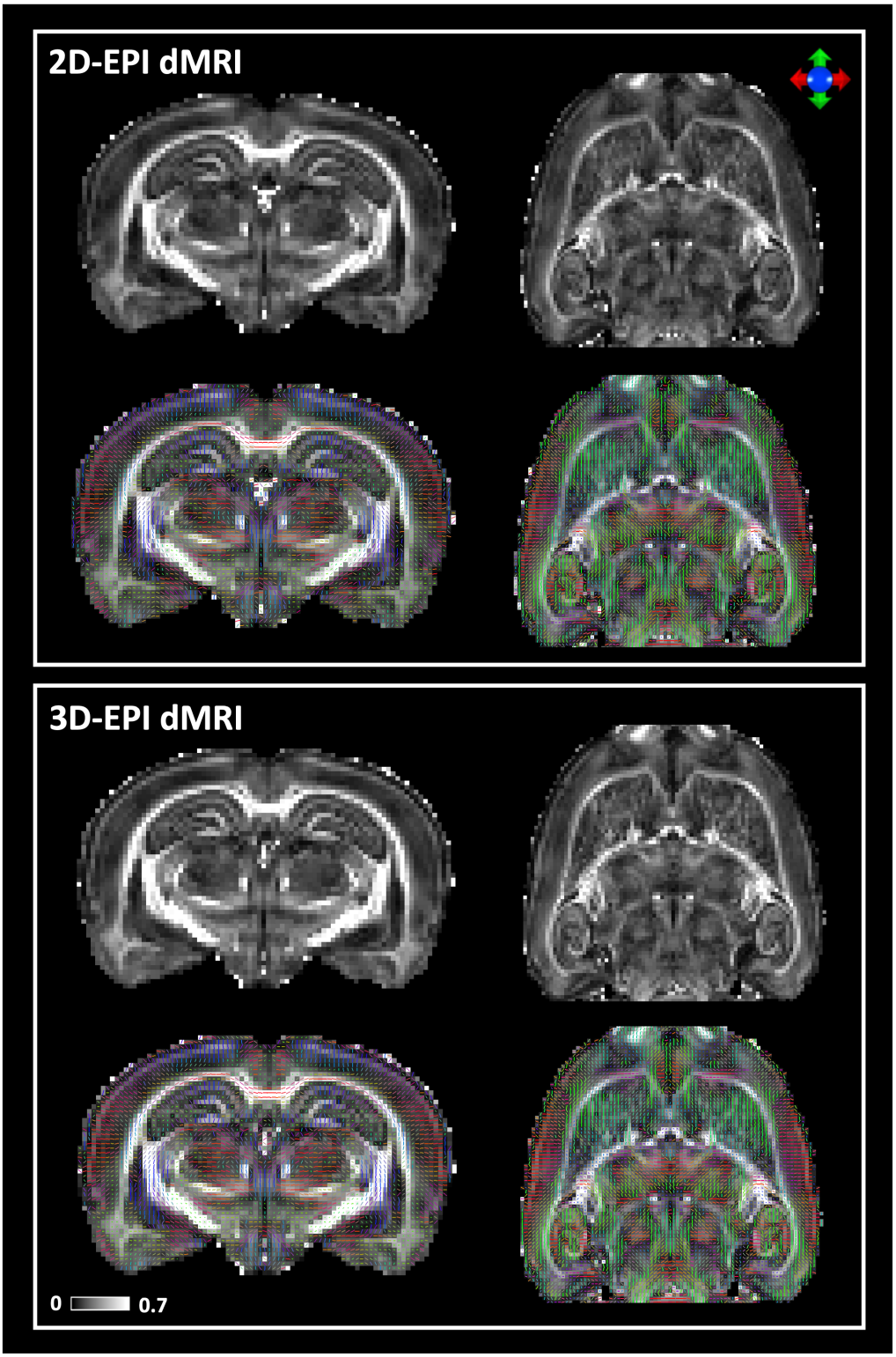


Figure 3.20: dMRI for the same sample, prepared with gadolinium, scanned in Oxford using a 2D-EPI (top panel) and 3D-EPI (bottom panel) readout. The upper rows show the fractional anisotropy (grey scale) whilst the lower rows show primary eigenvectors (colour coded by direction).

a significant gain in SNR and CNR for samples perfused with gadolinium. In contrast, when the scanner's capability is limited so that only a 2D-EPI readout with long TR (e.g., 6000ms) is possible for dMRI, the SNR and CNR is lower for samples prepared with gadolinium. This highlights the importance of considering the limitations of the scanner, before committing to a particular method of tissue preparation.

The current body of research offers substantial evidence supporting the use of gadolinium in sample preparation, as it significantly enhances SNR and allows for faster acquisitions (D'Arceuil et al., 2007). Incorporating gadolinium into sample preparation protocols appears to have a negligible impact on diffusion metrics, such as FA and MD, as evidenced by recent studies (Barrett et al., 2023), and likewise poses no significant interference with histology and immunohistochemistry (Spencer et al., 2006). Interestingly, the debate regarding gadolinium concentration in the perfusate has evolved. Some researchers advocate for a higher concentration (e.g., 15mM), arguing that less of the contrast crosses the blood-brain barrier at this stage (Johnson et al., 2012). However, it's worth noting that permeability increases during rehydration, allowing for a lower concentration (1-2mM) to be effective when storing the sample. Furthermore, a recent development is a calculator designed to optimise SNR-efficiency for *ex vivo* rodent dMRI, which is now available online (Barrett et al., 2023). This tool will be invaluable for future research, as it allows researchers to identify the optimal TR and gadolinium concentration for various TE values. Nevertheless, our findings emphasise that it is important to carefully consider whether the use of gadolinium is suitable for the research objective and methods. For instance, in studies focused on the quantitative assessment of relaxation time, gadolinium's effects on different tissue compartments remain unclear and may introduce confounding factors (Sébille et al., 2019). Therefore, careful consideration

of the potential impacts of gadolinium is essential when determining its appropriateness in experimental design.

Over the past 10 years, a number of pipelines have been specifically developed for processing rodent MRI data, focusing almost exclusively on the mouse brain. Of these, only a few allow dMRI data processing, such as `AIDAmri` (Pallast et al., 2019), `MouseMorph` and `MIDAS` (Budin et al., 2013). A common challenge for these tools is that they do not inherently generalise for the larger rat brain, for which there is much less progress (Im et al., 2021). Our work augments these efforts for processing multi-modal MRI. With a modular design that spans the different processing steps and modalities, it demonstrated robust behaviour against very different datasets; a common challenge which pipelines fail to address. Our approach is also flexible enough, enabling switching between different templates, unlike some of the previous approaches that are inherently designed against a fixed template (such as `AIDAmri`). This has enabled us to process both mouse and rat brain data by simply switching the target template.

Very recent developments in non-human primate imaging are moving towards the same direction. For instance, the `versaFlow` pipeline has a modular design that dynamically adapts its configuration so that it is optimal to the spatial and angular resolution of each dataset (Valcourt Caron et al., 2023). We have developed a user-friendly pipeline, implemented in `python` using a modular approach, which is actively maintained and available for others.

3.4.1 Limitations and Future Extensions

In the future, improvements to the setup used for sample immobilisation during scanning can be considered. Exploration is underway regarding the

use of 3D printed holders to tightly constrain the sample, thereby minimising motion during the scan. Additionally, the possibility of warming the sample to maintain physiological temperature for enhanced diffusivity and precise temperature control during scanning to avoid signal fluctuations is being contemplated (Roebroeck et al., 2019). However, such a set up would have to work very effectively, given how sensitive diffusivity, and as such the diffusion coefficient, is to small changes in temperature. An approach that may be more feasible is a setup that ensures that the air flowing around the sample is at constant temperature.

Further work could explore the extent to which resolution limits can be pushed using our available hardware. For example, other groups (Johnson et al., 2023) are now conducting ultra-high resolution scans (e.g., 15μm), referred to as magnetic resonance histology/microscopy, in rodents. However, these scans typically last >10days. Furthermore, imaging at higher spatial resolution is usually associated with lower sample sizes/throughput and statistical power. The advantage of the approach we have used is that the data size is more manageable (for example, <1GB instead of ∼250GB), and the impact of noise is lower. Given the SNR of dMRI scans at Nottingham is already low (SNR<10), it would be negligible at higher diffusion weightings, thereby preventing us from lowering the resolution further. However, it would be possible to push the resolution acquired using the Oxford scanner (e.g., from 200μm for dMRI to 100μm).

The method that we have adopted for brain extraction appears to be more robust than other methods (Smith, 2002) when tested on rat or mouse data, but new approaches, which have been designed for specific species, such as `bet4animal`, implemented with `FSL`, or `atlasBREX` (available on GitHub) have not been tested here. However, others have demonstrated that the atlas-based segmentation achieved using `atlasBREX` (Lohmeier et al., 2019)

works well in mice, even when there is considerable change (∼40%) in the volumes of large brain structures, such as the cerebellum (Ren et al., 2021).

Our pipeline has not been tested on any rodent data acquired *in vivo*. We have also not tested whether our pipeline can generalise to female rats, other strains, different ages, or disease models. This will be a good test of how robust our methods are, yet we have demonstrated robustness against the mouse brain.

3.4.2 Contributions

Dr Rebecca Trueman provided oversight with animal procedures. Clare Spicer and Dr Dave Watson assisted with perfusions. Professor Jason Lerch provided access to the pre-clinical scanning facility in Oxford and the acquisition sequences. Mouse tissue was provided by Dr Mariah Lelos. Dr Martin Craig assisted with standardising MRI preprocessing pipeline so that is consistent with the `fsl_anat` tool and accessible to other researchers. My personal contributions span all other aspects of the project: conceptualisation and project lead; sample collection and preparation; data acquisition across two sites; development, testing, and implementation of the processing pipelines; analysis and presentation of the results; and manuscript writing, editing and review.

Chapter 4

Passive Clearing and 3D Microscopy of the Rat Brain

4.1 Introduction

Understanding the intricate organisation of the brain at a microscale resolution is crucial for unravelling the complexities of neural circuits, physiological mechanisms, and pathological processes. Although magnetic resonance imaging (MRI) is a powerful tool for studying the brain, its resolution falls short when examining fine-grained anatomical structures. Despite the capability to achieve a mesoscopic resolution *ex vivo*, diffusion MRI (dMRI) only provides an indirect measure of microstructural properties and therefore has reduced biological specificity. Hence, many studies (Howard et al., 2019; Mollink et al., 2017; Schilling et al., 2019a; Seehaus et al., 2015) have complemented MRI with classical optical approaches, such as histology and microscopy, which enable direct visualisation of tissue micro-architecture with cellular and sub-cellular resolution. By integrating data across scales we can better relate macroscopic observations with the underlying tissue

microstructure, linking systems to cells. This approach has the potential to enhance our understanding of the accuracy and specificity of MRI acquisition and analysis methods.

Integration information across multiple scales is inherently challenging. While histology is often considered the gold standard, it has significant limitations. A key drawback is its invasive nature, necessitating small tissue samples (e.g., $\sim$1cm^3 biopsy). Due to the limited penetration depth of light in biological tissues ($<$100μm), this tissue sample must be thinly sectioned (5-80μm) and stained before the various tissue components can be identified through light microscopy. The resulting images are typically 2-dimensional (2D) and cover a restricted field of view. This limitation confines observations to the plane of sectioning and the specific area of the tissue examined, potentially missing crucial findings.

Moreover, the sectioning process is inherently destructive, introducing irreversible damage (e.g., tears), artefacts (e.g., folds), and non-linear physical deformations (e.g., curvature in the slicing plane). Collectively, these factors pose challenges to combining microscopy with modern brain imaging approaches and making quantitative comparisons in the same brain region. For instance, aligning histological data to 3D datasets, such as those acquired by MRI, is significantly difficult due to the distortions induced by sectioning and the 2D nature of the data (Alyami et al., 2022).

Different methods have been developed to overcome the challenges associated with integrating 2D microscopy with MRI. The typical approach involves first reconstructing the topology of the whole-brain from hundreds of serial sections (Pichat et al., 2018). To address sectioning distortions, images of the serial sections are first aligned with a reference photograph of the tissue block before sectioning (i.e., block-face photography). Subsequently,

this image stack is registered to the corresponding MRI scan. However, this approach is labour intensive, time consuming, inefficient, and difficult to automate. In addition, the outcome is sub-optimal and error prone, as sections can be lost, and inaccuracies (e.g., cutting at an off-plane angle) are propagated across many sections. An alternative approach facilitates the alignment of single-section microscopy images with MRI (Huszar et al., 2023). Although this is a significant development, substantial expertise is required to adapt the parameters for each stage of image registration so that the mapping from histology to MRI is accurate. Furthermore, regardless of the approach adopted, considerable effort is still needed to identify artefacts in the microscopy images (e.g., folded sections or uneven staining) and minimise their impact on registration. This demonstrates why a fundamentally different strategy is needed.

Tissue clearing has been heralded as the next generation of histology (Lai et al., 2018), marking a radical leap forward by eliminating the need for traditional sectioning methods. This advancement is possible as the technique renders biological tissue transparent. Transparency is achieved by selectively removing the tissue components (e.g., lipids) responsible for light scattering and absorption, and homogenising the refractive index of the tissue (Ariel, 2017). The outcome is a remarkable increase in light penetration, allowing for unimpeded examination, at cellular resolution, of the native tissue architecture in large, fully intact 3D samples.

The adoption of light sheet fluorescence microscopes has been key to leveraging tissue clearing, as they enable rapid, high-resolution volumetric imaging of large samples (Dodt et al., 2007). Due to their wide field of view, these microscopes make it possible to capture microstructural details across macroscopic distances in 3D. Light sheet microscopy is therefore well suited to looking at microscale structures that would otherwise span tissue sections.

Further innovations in tissue clearing and light sheet microscopy have continued to push the boundaries of our imaging capabilities, both in depth and breadth. This progress is particularly relevant to neuroscience research (Ueda et al., 2020), where brain-mapping efforts have been hampered by the staggering complexity of the mammalian brain, both in terms of scale and diversity. Tissue clearing and light sheet microscopy have become indispensable tools, providing the means for whole-brain profiling of cells and circuits in 3D at a microscopic resolution. This holistic approach, examining the whole brain rather than small isolated regions, can provide a panoramic understanding of how cellular processes, such as inflammation, unfold within the broader context of brain-wide networks.

Researchers (Goubran et al., 2019; Johnson et al., 2023; Chang et al., 2017) have explored how best to integrate microscopy of cleared brain tissue with MRI. However, the majority of studies have so far been limited to the mouse brain, despite the rat being widely used in cognitive and behavioural neuroscience research (Iannaccone and Jacob, 2009). This stems from a number of related factors. Firstly, most brain clearing protocols have been developed and optimised for the mouse (Dodt et al., 2007; Susaki et al., 2014; Chung et al., 2013; Hama et al., 2011) due, in part, to the availability of mouse lines that selectively express fluorescent reporter proteins (e.g., GFP) in a subset of cells or structures. There are also specific challenges associated with clearing and imaging the rat brain. The rat brain is 3-4x larger than that of the mouse (Welniak–Kaminska et al., 2019; Kovačević et al., 2005) and therefore beyond the imaging capabilities of even some of the most advanced light sheet microscopes. The rat brain also has a greater lipid content, due to more extensive myelination. This combined increase in volume and complexity means that it takes significantly longer (i.e., weeks/months instead of days) for reagents to passively diffuse through

the whole sample. As such, very few have explored whole-brain clearing for the adult rat brain.

Due to the many challenges associated with clearing and imaging large well-myelinated samples, such as the rat brain, we have sought to a) establish a protocol that can successfully clear whole hemispheres of the adult rat brain, b) develop methods that allow for 3D microscopy of the intact hemispheres at cellular resolution, and c) demonstrate that tissue clearing is possible for gadolinium-perfused brains (as needed for some MRI protocols). This has involved testing two different hydrophobic methods of passive tissue clearing (Renier et al., 2016; Branch et al., 2021), and assessing their performance in the rat brain. The results demonstrate that the AdipoClear+ protocol, which is simple and inexpensive, was able to achieve a high degree of transparency, whilst also preserving the 3D morphology of the sample. We show that this method, which does not require the expression of fluorescent reporters or any specialised equipment (e.g., electrophoretic systems or customised microscopes), is compatible with standard immunolabelling protocols. Due to the strengths of the AdipoClear+ protocol, we applied it to the same samples that previously underwent MRI. This has allowed us to anatomically align the 3D microscopy images with corresponding MRI volumes using a simple registration. The presented approach is therefore a much better solution to the challenge of combining microscopy with MRI.

4.2 Methods

Several factors influence the transparency of the brain after clearing, and consequently, the quality of the microscopy images (Silvestri et al., 2016). We have therefore standardised the methods and timings for each step in our

workflow. In particular, it was important to remove as much blood as possible during perfusion, as haemoglobin absorbs light, resulting in autofluorescence, which can be obstructive. This is achieved by including heparin, at a concentration of 10μg/mL (Sigma-Aldrich, H3149-50KU), in the phosphate buffered saline (PBS, Invitrogen, AM9624) used for transcardiac perfusion. It was also vital to avoid over-fixation, as excessive cross-linking of proteins masks antigen binding sites and prevents effective tissue clearing (Molbay et al., 2021). Therefore, the sample was post-fixed in 4% paraformaldehyde (PFA, Sigma-Aldrich, 441244-1KG) at 4°C for 24hrs, after which it was transferred to a solution of PBS, with 0.02% sodium azide (Sigma-Aldrich, S8032), for storage at 4°C.

Sample Preparation

Following MRI, the brain was carefully extracted from the skull. Although this process inevitably affects the brain's morphology, it is necessary as bone absorbs light and is impermeable to clearing solutions, unless decalcified. Additionally, the meninges were also removed, as these restrict antibody penetration. Subsequently, the brain hemispheres were separated by slicing along the midline. Separating the hemispheres makes imaging more feasible on commercial light-sheet microscopes (working distance ∼5mm).

The hemispheres were rinsed in a solution of PBS containing 0.02% sodium azide, at least 3 times for >30min each. Washes were performed with mild agitation on a rocker, whilst ensuring that samples were moving freely.

4.2.1 Tissue Clearing

For this part of the project we tested two hydrophobic/solvent-based clearing protocols on test tissue sections and whole hemispheres from two different brains. Hydrophobic protocols are generally faster and achieve better transparency than hydrophilic/aqueous (Susaki et al., 2014) or hydrogel-based (Chung et al., 2013) methods. However, the organic solvents used in hydrophobic protocols are highly volatile and toxic. Therefore, key steps should be performed in a fume hood with appropriate safety precautions, such as wearing double gloves. In addition, these organic solvents can be extremely corrosive and should only be used with suitable equipment (e.g., microscopes where the objectives are protected by a dipping cap, and plastic-ware that is chemically compatible with organic solvents).

iDISCO+ and AdipoClear+ Protocols

The iDISCO+ protocol is a simple and low-cost method that was developed for rapid clearing of the mouse brain (Renier et al., 2014). This protocol is compatible with immunolabelling (Renier et al., 2016) and easy to implement as it consists of immersing the sample in a series of solvents. Figure 4.1 summarises the key steps of iDISCO+ and related protocols. These include dehydration in ascending concentration of methanol; delipidation and permeabilisation with methanol and dichloromethane (DCM); and refractive index (RI) matching, which is performed with dibenzyl ether (DBE).

The iDISCO+ protocol has many benefits. A methanol pre-treatment step reduces tissue autofluorescence. Dehydrating with methanol also makes samples easier to handle (i.e., by hardening them) and avoids the significant

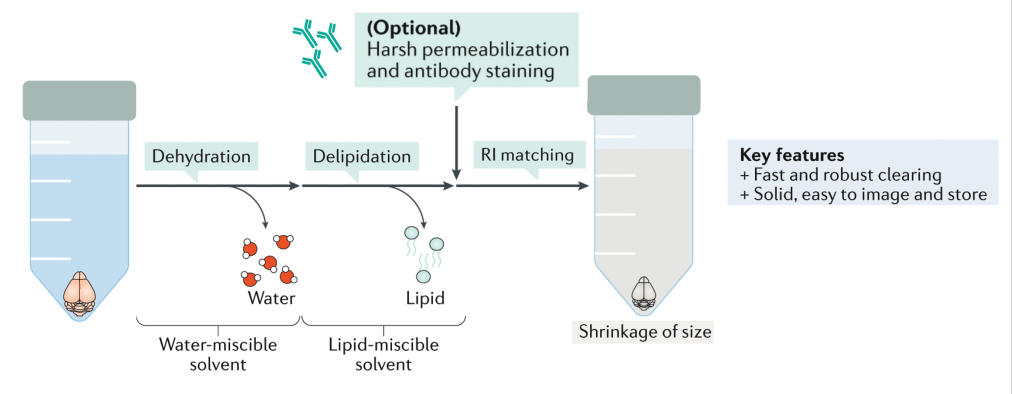


Figure 4.1: Key steps of hydrophobic methods of tissue clearing, such as iDISCO+, include dehydration, delipidation, and refractive index (RI) matching. If required, immunolabelling can be performed between lipid extraction and RI matching. Modified from Ueda et al. (2020).

tissue shrinkage seen with other DISCO clearing methods (Ueda et al., 2020).

AdipoClear+ is a modified version of the iDISCO+ protocol. It incorporates elements from the Adipo-Clear protocol, which was developed to clear adipose tissue while maintaining its structural integrity (Chi et al., 2018). Researchers have demonstrated that the AdipoClear+ protocol can successfully clear adult rat brain hemispheres (Branch et al., 2021), which are more myelinated and lipid dense than the mouse brain.

The success of AdipoClear+ lies in its utilisation of methyl-beta-cyclodextrin, a small oligosaccharide with a high affinity for cholesterol—a major component of myelin and cell membranes. By extracting cholesterol, it enhances membrane permeability, allowing for improved molecular diffusion throughout the sample. This increase in diffusivity facilitates both tissue clearing and immunolabelling processes (Mai et al., 2023) while preserving the intricate structural integrity of the rat brain.

Hydrophobic protocols preserve morphology and have a limited effect on sample size, so they are well suited for being used in conjunction with

MRI. As such, we tested how well iDISCO+ could clear rat brain tissue, as a ∼1mm thick sagittal section and whole hemisphere. The AdipoClear+ protocol was also tested on adult rat brain hemispheres from a different animal, to determine whether it achieved better transparency. AdipoClear+ takes significantly longer than iDISCO+ (≥6 weeks, as opposed to <1 month for rat brain hemispheres). The iDISCO+ and AdipoClear+ protocols can both be accessed online. Unless stated otherwise, all steps were performed at room temperature with gentle rocking. For iDISCO+, samples were incubated in ∼4.5mL, while for AdipoClear+, a volume of 20mL was used.

Dehydration, Delipidation and Permeabilisation

Both AdipoClear+ and iDISCO+ protocols use methanol (VWR, 20847.307) and DCM (Sigma Aldrich, 270997) for delipidation, but AdipoClear+ has additional steps and modifications. In AdipoClear+, a pre-treatment step was used where samples were washed in B1n buffer for 2hr, 4hr, and overnight. B1n consists of 0.1% TritonX-100 (Sigma-Aldrich, X100-500ML), 0.3M glycine (Sigma-Aldrich G7126-500G), 1mM sodium hydroxide, and 0.02% sodium azide in distilled water. To prevent oxidation and discoloration, AdipoClear+ always uses methanol with 2-mercaptoethanol (Sigma-Aldrich, M-7154) at a concentration of 120μM.

In both protocols, samples underwent a gradual dehydration before delipidation by immersing samples in increasing concentrations of methanol (i.e., 20, 40, 60, and 80%) for 1hr each. Two washes in 100% methanol for ≥1hr, ensured complete removal of water content.

In the iDISCO+ protocol, lipid extraction was achieved by incubating samples in 100% methanol at 4°C for ≥12hrs, followed by an overnight treatment in a 2:1 DCM/methanol solution. Delipidation was more extensive

in AdipoClear+ as samples were also washed in 100% DCM for 1hr, 3hr and then overnight.

Following delipidation with DCM, samples were washed in 100% methanol for 1hr, 3hr, and then bleached overnight in 5% hydrogen peroxide (Sigma-Aldrich 216763-100mL) at 4°C. This bleaching step reduced autofluorescence from residual blood (Renier et al., 2014) and enhanced tissue permeabilisation for improved antibody penetration (Molbay et al., 2021).

After bleaching, samples were rehydrated by transitioning through decreasing concentrations of methanol (i.e., 80, 60, 40, and 20%) for 1hr each. In iDISCO+, this was followed by washing in PBS for 1hr, and then twice in PBS containing 0.2% TritonX-100, for 1hr each. In AdipoClear+, samples were returned to B1n buffer for washes lasting 1hr, 3hr and overnight. Subsequently, samples were washed in SdC buffer, which is PBS with 0.02% sodium azide and 1% methyl-β-cyclodextrin (Sigma-Aldrich, 332615), for 4hr, 2x 24hr, and 2x 48hr to extract cholesterol. Finally, samples were permeabilised at 37°C for 6hr, and overnight with 5% dimethyl sulfoxide (DMSO, Tocris 3176) and 0.3M glycine (Sigma-Aldrich G7126-600G) in PTwH. This was followed by washing in PTwH for 3hr, 4hr and overnight. PTwH is composed of PBS with 0.1% Triton X-100, 0.05% Tween-20 (Sigma-Adrich, P416-100mL), 2μg/mL heparin, and 0.02% sodium azide. These washes, with micelle-forming detergents, like Triton X-100 and Tween-20, help dissolve the lipid bilayer, further permeabilising the tissue.

Whole-mount Immunolabelling

We subsequently investigated if these clearing protocols are suitable for immunolabelling our targets of interest: axons and white matter tracts. This is crucial because methanol has mild denaturing effects. Moreover,

the hydrophobic protocols efficiently remove lipids, the primary (∼70%) component of myelin, thereby posing a challenge for white matter staining.

For the examination of axons and white matter, our focus was on labelling myelin, neurofilaments, and dopaminergic projection fibres. We evaluated the efficacy of the following primary antibodies: rabbit anti-myelin basic protein (MBP, Cell Signalling Technology, 62596, 1:100), rabbit anti-neurofilament-H (NF-H, Sigma, AB1991, 1:100) and rabbit anti-tyrosine hydroxylase (TH, Millipore, AB152, 1:500). To mitigate interference from autofluorescence and minimise light scattering and absorption — factors that are more prominent at shorter wavelengths (488/561nm) — we selected a second antibody which was conjugated to a fluorophore in the far-red region of the spectrum, specifically goat anti-rabbit AlexaFluor 647 (Invitrogen A27040, 1:500).

Immunolabelling was conducted after delipidation and before refractive index matching. Samples were permeabilised further by incubating them in PBS with 0.2% TritonX-100, 20% DMSO, and 0.3M glycine at 37°C for 2 days. Subsequently, they were blocked in PBS with 6% donkey serum (Jackson Immunoresearch, 017-000-121), 0.2% TritonX-100, and 10% DMSO at 37°C for an additional 2 days. In the AdipoClear+ protocol, heparin at 2μg/ml was added to disrupt the extracellular matrix, ensuring effective diffusion of high-molecular-weight antibodies. In both protocols, samples were then incubated in primary and secondary antibodies sequentially at 37°C, each for 7 days.

For iDISCO+, the primary and secondary antibodies were prepared in a solution of PBS with 3% donkey serum, 10μg/ml heparin, and 0.2% Tween-20. The solution for primary incubation also contained 5% DMSO. In AdipoClear+, the primary antibody was prepared in PTwH with 0.3M

glycine, 5% DMSO, and 3% donkey serum, while the secondary antibody was prepared in PTwH. Heparin and glycine were included in these buffers to reduce non-specific staining. Glycine also reduces autofluorescence (Weiss et al., 2021).

Following primary and secondary antibody incubations, samples underwent washing. In iDISCO+, samples were washed 4-5 times in PBS containing 0.2% Tween-20 and 10μg/mL heparin, with an additional overnight wash. AdipoClear+ had a more extensive washing process, with PTwH washes lasting 3hrs, 4hrs, 12hrs, and then 4 x 24hrs.

After immunolabelling, samples were shielded from light. In the AdipoClear+ protocol, samples were further incubated in 2% PFA at 4°C overnight to stabilise morphology and prevent antibody dissociation.

Refractive Index Matching

The refractive index (RI) of a medium indicates the extent to which it alters the path and speed of light passing through it. For biological tissues like the brain, the amount of refraction depends on the volume and RI of its components - water (RI: 1.33), lipids (RI: 1.45-1.47) and proteins (RI: >1.5). Light scatters as it passes through tissue components with different RIs, so homogenising the tissue's RI is crucial for optimal clearing. Imaging also improves if there is index matching between the tissue, imaging media, and optical components like lenses (RI of crown glasses: ∼1.5).

Methods of index matching differ according to the clearing protocol used. In organic solvent-based protocols, such as iDISCO+ and AdipoClear+, index matching begins with dehydration (removes water) and further delipidation with DCM (removes remaining lipid content), thereby increasing the RI of

the tissue (only protein remaining, therefore RI: ¿1.5). Subsequently, the sample is immersed and impregnated with DBE (RI: 1.56), which is also used during imaging. By the end of solvent based protocols, when index matching is complete, the brain is usually hard and transparent, resembling glass or plastic.

Dehydration was achieved by immersing the samples in increasing concentrations of methanol (i.e., 20, 40, 60, and 80%) for 1hr each, followed by two washes in 100% methanol for ≥1hr each, and overnight incubation in 100% methanol at 4°C. Subsequently, samples were placed in a solution of 2:1 DCM/methanol for 2-3hrs. In iDISCO+, samples underwent two 15min washes in 100% DCM, without shaking, to remove remaining methanol. Meanwhile, in AdipoClear+, washes in 100% DCM were more extensive, lasting 1hr, 3hr, and 2x 24hrs.

The final step aims to impregnate the tissue with DBE, which has a similar RI to the protein content that remains in the brain after delipidation and dehydration. In both protocols, samples were transferred to 100% DBE. In the AdipoClear+ protocol, this was refreshed after 1hr, 4hr, and overnight. For long term storage, samples were held in glass vials filled with DBE to prevent oxidation and maintain a stable RI.

4.2.2 Light Sheet Fluorescence Microscopy

All cleared samples were imaged at the University of Birmingham's Centre of Membrane Proteins and Receptors (COMPARE) using a commercially available light sheet microscope (UltraMicroscope II, LaVision BioTec). This microscope, shown in Figure 4.2, features a MVPLAPO 2x/0.5 objective lens (Olympus) with dipping cap (5.7mm working distance) and MVX10

zoom body (Olympus, zoom ratio of 0.63×–6.3×). It is configured such that the detection/optical axis (i.e., top-down) is orthogonal to the illumination axis/light sheet (i.e., lateral). The Andor Zyla (2160 x 2560 pixel) sCMOS CCD 16-bit camera (LaVision BioTec) collects light in parallel, rather than point-wise, for faster detection and reduced sample photobleaching.

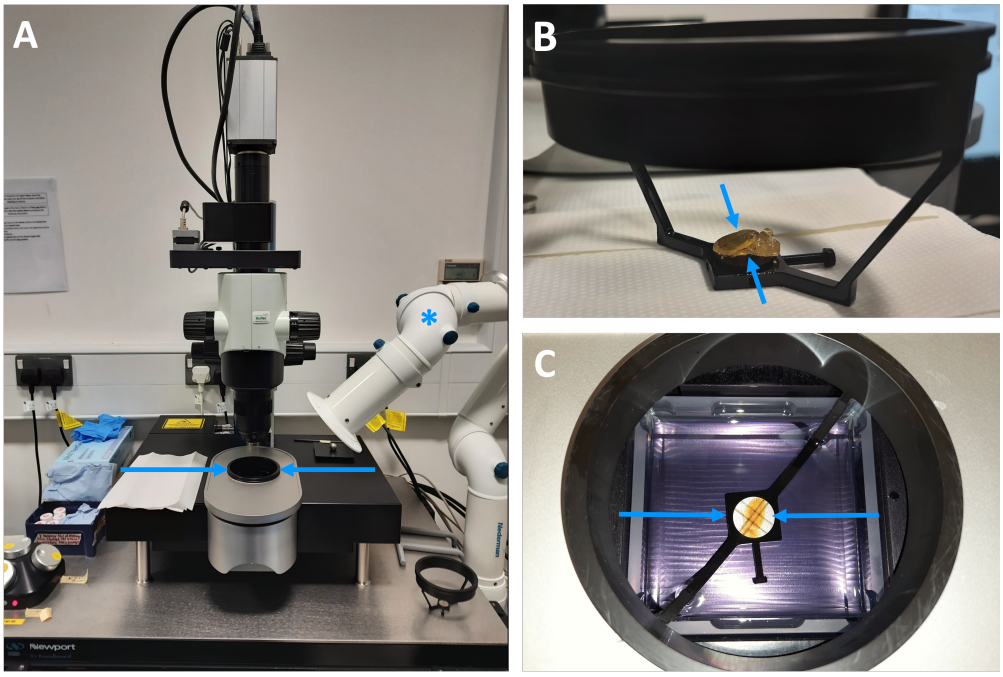


Figure 4.2: A) The LaVision Biotec UltraMicroscope II with zoom body optics is configured with the objective orthogonal to the light sheet, indicated with blue arrows. An extractor system, shown with an asterisk symbol, removes fumes. B) The sample, mounted on a flat disc, is securely fastened to the cradle, as depicted from the side. C) Top view of the imaging chamber, with the sample oriented perpendicular to the light sheet.

Samples were individually mounted onto the holder (i.e., a small disc), in sagittal orientation along the flat edge of the midline, using silicon-based high temperature grease (Molykote 44 Medium) or pins. This orientation reduces scattering as the illumination and detection light paths are through thinnest portions of sample (i.e., along the anterior/posterior and left/right axes respectively). After securing the holder into the cradle, the sample was lowered into the imaging chamber, made of 100% quartz (LaVision BioTec) and filled with 100% DBE. An extractor system minimised the

accumulation of fumes.

The light sheet microscope features 488nm, 561nm, and 640nm lasers with corresponding emission filters at 575/40, 620/60, and 680/30. Cylindrical lenses generate three light sheets; a main beam, and two lateral beams tilted at ∼10-11°in the XY plane. The lateral beams allow for areas behind obstructions (e.g., bubbles or debris) to be visualised. Before each imaging session, the lateral and central light sheets were aligned for left and right illumination. The sheetmotor was also calibrated.

Imaging was conducted using ImspectorPro software (LaVision BioTec, version 7.1.15), and data were saved as ome-tiff (Open Microscopy Environment-Tagged Image File Format) files. Sample autofluorescence was captured through the 488 or 561nm channels, whilst immunolabelling was imaged using the 640nm channel. Chromatic correction was applied between channels. Each hemisphere or section was imaged as a z-stack at low magnification (i.e., zoom of 0.63-0.8X), with a step size of 4-10μm, to capture general structure and tissue morphology. The workflow acquired the entire z stack before switching channels. As the samples were larger than the field of view at 0.63/0.8x zoom (effective magnification of 1.26/1.6x), two image stacks of the anterior and posterior portions were acquired. These stacks had >30% overlap.

To optimise illumination, so that it was as even as possible across the camera's field of view, samples were illuminated from both sides using three light sheets at maximum width and waist thickness. A wider sheet distributes light evenly across the XY field of view, minimising signal differences between the centre and edge. A thicker waist (i.e. low numerical aperture) makes for a flatter sheet with more consistent, albeit lower, resolution across the XZ plane. These parameters were best suited for capturing our large samples

at low magnification.

The software employed real-time linear interpolation to blend images acquired with left and right-sided illumination over a small user-defined area. The horizontal focus for left and right sided illumination was placed in the centre of the field of view.

4.2.3 Data Conversion and Image Processing

The image stacks of the anterior and posterior portions of the brain hemisphere were stitched together using the Grid/Collection Stitching plugin (version 1.2) for ImageJ (Preibisch et al., 2009). The fused images were then exported as a 3D volume.

The high resolution (e.g., 3.8μm x 3.8μm x 4μm) 3D microscopy files were converted to nifti format, so that they are compatible with neuroimaging data, using the python libraries `tifffile` (doi: 10.5281/zenodo.6795860) and `nibabel` (doi: 10.5281/zenodo.591597). Converting microscopy images to nifti format allowed us to use software tools, processing techniques, and more elaborate forms of analysis (e.g., cortical mapping), which have been developed for MRI. For instance, the `FSL` tools `FLIRT`, `applywarp` or `fslmaths` were used to down-sample microscopy images to a lower (e.g., 10μm) isotropic resolution using the `--applyisoxfm`, `--supersample` or `--subsamp2` flags respectively. The non-parametric `N4BiasFieldCorrection` algorithm from `ANTs` was also used to normalise gradual variations in image intensity across the 3D volume (Tustison et al., 2010).

4.2.4 Registration of Microscopy Imaging to MRI

Table 4.1 summarises the 3D microscopy and MRI data available from the same rodent brains. These datasets were used to explore various registration methods for aligning microscopy images with corresponding MRI scans. The autofluorescence signal was used for an intensity-based alignment to MRI as it provides general information about overall structure (e.g., the outline of the brain) and has excellent contrast between grey and white matter.

Rat	Gd	Clearing protocol	3D light-sheet microscopy	MRI data used for registration		
				Site	Anatomical	Diffusion
5		AdipoClear+	autofluorescence	Oxford	3D-RARE	2D-EPI
6	✓	AdipoClear+	autofluorescence	Oxford	3D-RARE	3D-EPI

Table 4.1: Summary of 3D light sheet microscopy and 3D MRI data used to test co-registration. The microscopy data (4x4x10μm) was acquired from single brain hemispheres whereas MRI data (100-200μm isotropic) was whole brain. The extended AdipoClear+ protocol was used to clear these samples.

A number of MRI contrasts were evaluated as the target image for registration purposes including the structural T2-weighted scan, average b0, and mean diffusivity, all of which had undergone pre-processing through our automated pipelines. Since tissue clearing and light sheet microscopy were performed on a hemisphere, as opposed to the whole brain, we masked the MRI scans to remove the missing hemisphere.

Firstly, we performed linear registrations using `FSL-FLIRT` with increasing degrees of freedom (i.e., rigid and affine). Secondly, we performed non-linear registration using `ANTs` (Avants et al., 2011), initialised using the linear affine registration.

To identify the optimal settings for image registration using `ANTs`, we ran a brute force search across a large parameter space. Given the computational

demands of non-linear registration, we down-sampled the microscopy images to 100μm isotropic. We tested various options, including: 1) different intensity processing options (e.g., histogram matching, outlier clipping, and an initial moving transform to quickly align images based on their centre of mass), 2) different linear registration options (rigid and affine transformations), and 3) different diffeomorphic registration methods using the symmetric normalisation (SyN) and b-spline SyN algorithms (Tustison and Avants, 2013). Mutual information was used as the similarity metric for the rigid and affine transformations, while cross-correlation was employed for the non-linear registration stage.

To compare the registrations generated during this brute force search (comprising a total of 480 registrations per MRI contrast, with 384 involving non-linear deformations), we cross-correlated the registration output (i.e., the microscopy image after transformation) with a reference image (mean diffusivity) using `fslcc`. The correlation coefficient served as a simple metric of alignment performance. To provide a baseline for comparison, we performed a standard non-linear registration using the default settings in ANTS (`antsRegistrationSyN.sh`).

4.3 Results

This section compares the performance of two hydrophobic clearing methods, namely iDISCO+ and AdipoClear+, for clearing large volumes of rat brain tissue. To illustrate the efficacy of these methods, we present images captured with 3D light sheet microscopy. Subsequently, we demonstrate the power of this 3D microscopy approach in enabling excellent alignment to 3D MRI data using conventional registration approaches.

4.3.1 Optimisation of Tissue Clearing

Table 4.2 summarises the effects of sample size and the duration of delipidation and permeabilisation incubations, on the transparency of rat brain tissue achieved using the iDISCO+ and AdipoClear+ protocols.

Sample size	Protocol	No. weeks	Outcome
∼1mm thick section	iDISCO+	1	Successful
Whole hemisphere	iDISCO+	4	Unsuccessful
Whole hemisphere	**AdipoClear+**	**6**	**Successful**
Whole hemisphere	AdipoClear+	3	Unsuccessful

Table 4.2: Assessing hydrophobic clearing protocols (iDISCO+ and AdipoClear+) on rat brain samples, examining the impact of varying sample size and the duration of delipidation and permeabilisation steps.

For whole rat brain hemispheres, the optimal approach involved gradual clearing with the AdipoClear+ protocol over 6 weeks, as shown in Figure 4.3 (left panel). This extended protocol rendered the sample fully transparent, allowing deep structures to be clearly visualised. In contrast, a shorter duration resulted in incomplete lipid removal, which impaired refractive index matching. As a result, the central region of the hemisphere remained opaque, leading to image blurring (right panel).

In the following sections, further detail is provided for results using the two clearing protocols.

iDISCO+

Figure 4.4 shows that the iDISCO+ protocol could successfully clear a ∼1mm thick sagittal section of rat brain tissue, despite the fact that this clearing protocol was developed specifically for mouse brains. Sample autofluorescence provided good contrast between white matter and grey

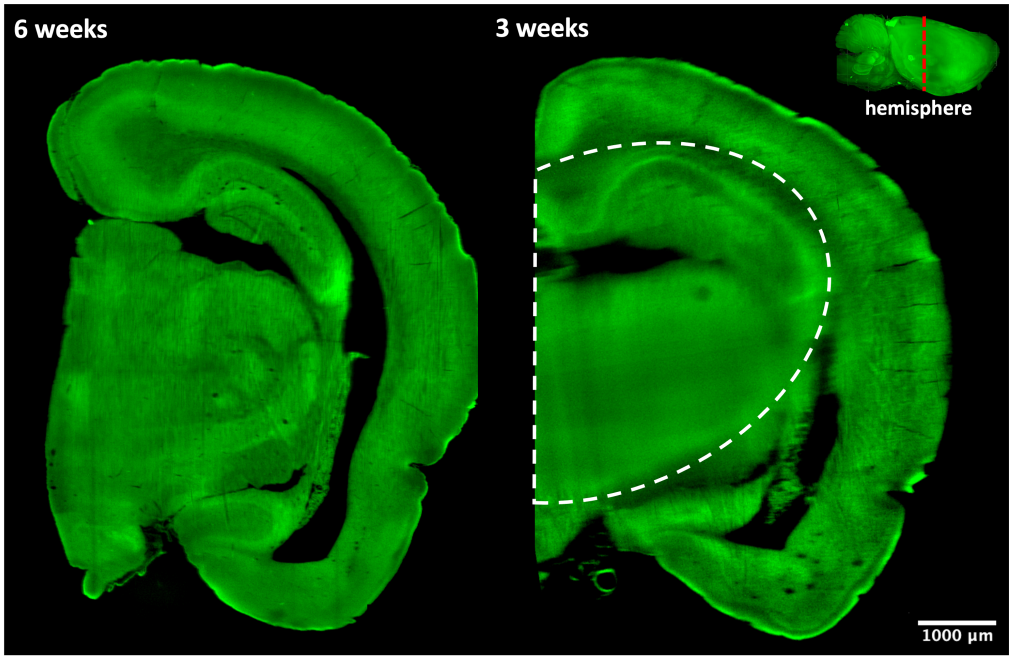


Figure 4.3: The AdipoClear+ protocol effectively clears an intact rat brain hemisphere, shown here as a coronal section at the location indicated by the red mark (inset at top right), when extended over a 6-week period (left panel). Reducing the clearing time to 3 weeks (right panel) resulted in incomplete delipidation, leaving the sample partially opaque. This incomplete clearing is reflected in the blurred central region of the sample (outlined in white).

matter. In the cerebellum, autofluorescence was prominently associated with the white matter core.

Although the iDISCO+ protocol was compatible with immunolabelling, the penetration of antibodies appears to have been poor as most of the antibody signal was restricted to the surface, as shown in Figure 4.4 (left panel). However, the neurites of dopaminergic neurons were successfully labelled through the molecular and granular layers of the cerebellum (right panel). This suggests that antibody penetration was better in this region, potentially due to a higher surface area to volume ratio for the cerebellum.

Unfortunately, the iDISCO+ protocol was unable to clear an entire rat brain hemisphere, even when extended to 4 weeks. The centre of the hemisphere remained opaque, indicating incomplete delipidation, while the observed

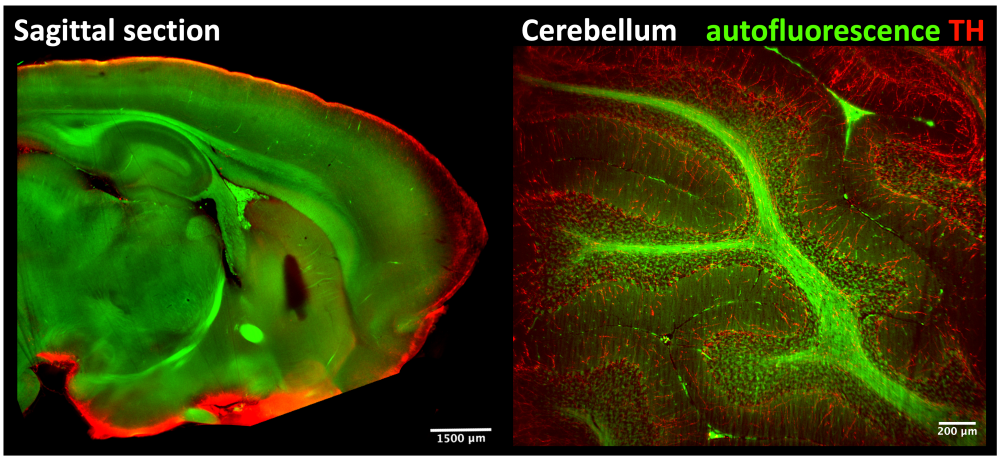


Figure 4.4: Pseudo-coloured images, captured using light sheet microscopy, of a ∼1mm thick sagittal section of rat brain cleared using the iDISCO+ protocol. The left-hand portion of the figure shows the anterior part of the sagittal section. The cerebellum is shown at higher magnification on the right. The sample's autofluorescence (green) provides excellent contrast between white and grey matter. Dopaminergic projections (red) were labelled with antibodies specific for tyrosine hydroxylase.

discoloration suggested tissue oxidation. As such, it was not possible to image the sample using light sheet microscopy.

AdipoClear+

Figure 4.5 demonstrates how AdipoClear+ evenly cleared an intact hemisphere of rat brain. Although dehydration with methanol induced shrinkage, the protocol did not cause significant geometric distortions. This size reduction can be advantageous, as it facilitates imaging of the entire hemisphere on the Ultramicroscope II without the need for remounting.

Figure 4.6 demonstrates successful refractive index matching, the final step of tissue clearing, in rat brain tissue using AdipoClear+. The quality and speed of this process (∼30 minutes) is a key advantage of hydrophobic methods. The tissue, shown at time 0, begins to become translucent after 10 minutes. It achieves full transparency after 25-30 minutes, as evidenced

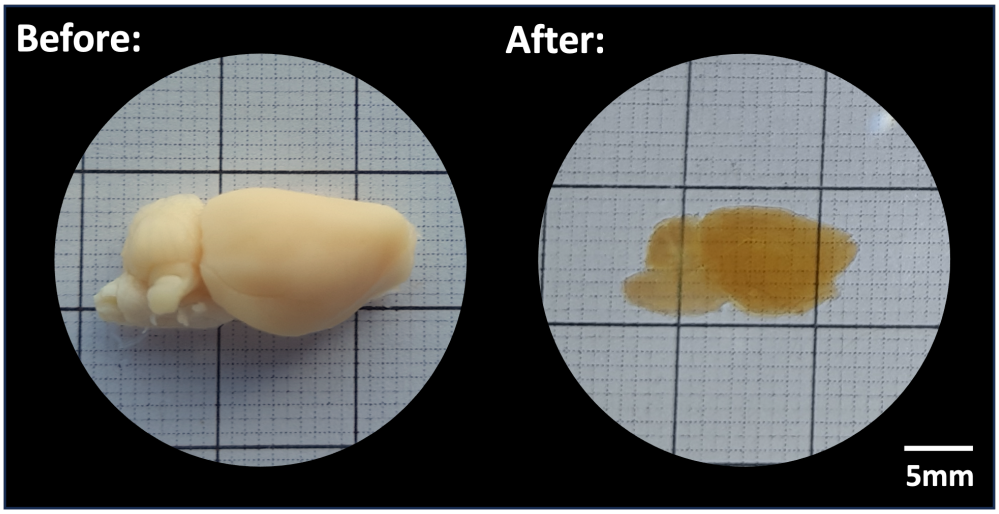


Figure 4.5: The AdipoClear+ protocol was able to successfully clear an intact hemisphere of rat brain. This process is associated with shrinkage but not large geometric distortions. Although the sample is amber in colour, it is completely transparent and does not distort the pattern below or prevent imaging. A yellow-brown tint is common for larger samples and occurs due to the continued absorption of blue and near-UV light by remaining protein. As such, this amber colour suggests good protein retention (Weiss et al., 2021; Richardson et al., 2021).

by the grid lines of paper under the tissue no longer being obscured.

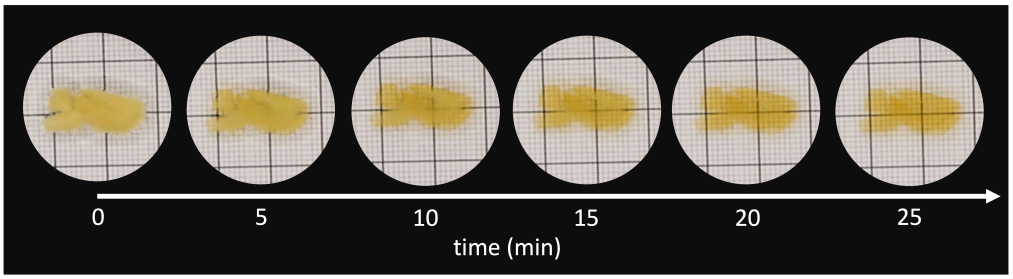


Figure 4.6: Time course for refractive index matching of a sagittal section of rat brain in DBE. This final step takes ∼30 minutes with the Adipoclear+ protocol.

After clearing with AdipoClear+, it was possible to use a light sheet microscope to rapidly image ($\leq$ 2hrs) the entire rat brain hemisphere as a 3D volume, as shown in Figure 4.7, with an in-plane resolution of 4μm x 4μm and slice thickness of $\leq$10μm.

The AdipoClear+ protocol enabled the visualisation of microstructural properties and major anatomical structures across the whole rat brain

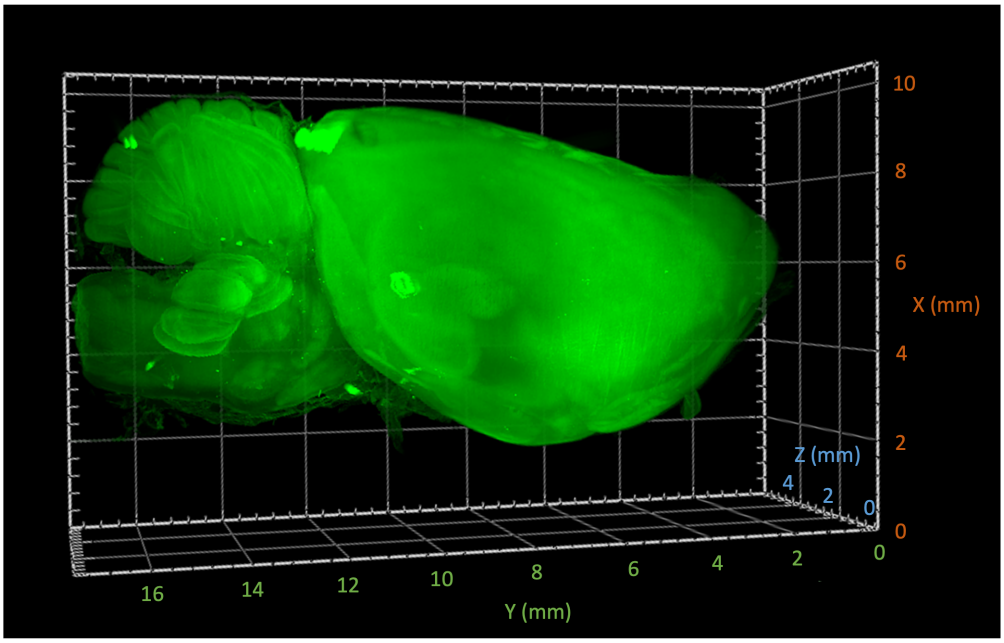


Figure 4.7: 3D light sheet microscopy captured the autofluorescence from an intact rat brain hemisphere cleared with AdipoClear+. This is shown as a maximum intensity projection along the z-axis, over a span of ∼5mm.

hemisphere. As shown Figure 4.8 (top panel), autofluorescence provided excellent contrast between white and grey matter. Sharp images could be obtained at various depths, without any loss in resolution or image blurring. This indicates that clearing was consistent throughout the entire volume. However, a stripe/streak artefact appears as shadowing and signal attenuation along the direction of the light sheet's propagation, visible in Figure 4.8 (bottom panel). This artefact is common in light sheet microscopy of large samples (Ricci et al., 2022), and results from light scattering or absorption at the sample's surface (i.e., the tissue boundary) or by small structures such as air bubbles and pigmentation. The observed striping pattern aligns with the shape of the light sheet, which consists of a main beam flanked by two lateral beams angled at 10-11°.

Figure 4.9 shows snapshots of sagittal slices of the same 3D microscopy volume, before (top) and after (bottom) correcting for low frequency variations in intensity. This correction preserved the intrinsic white and grey matter

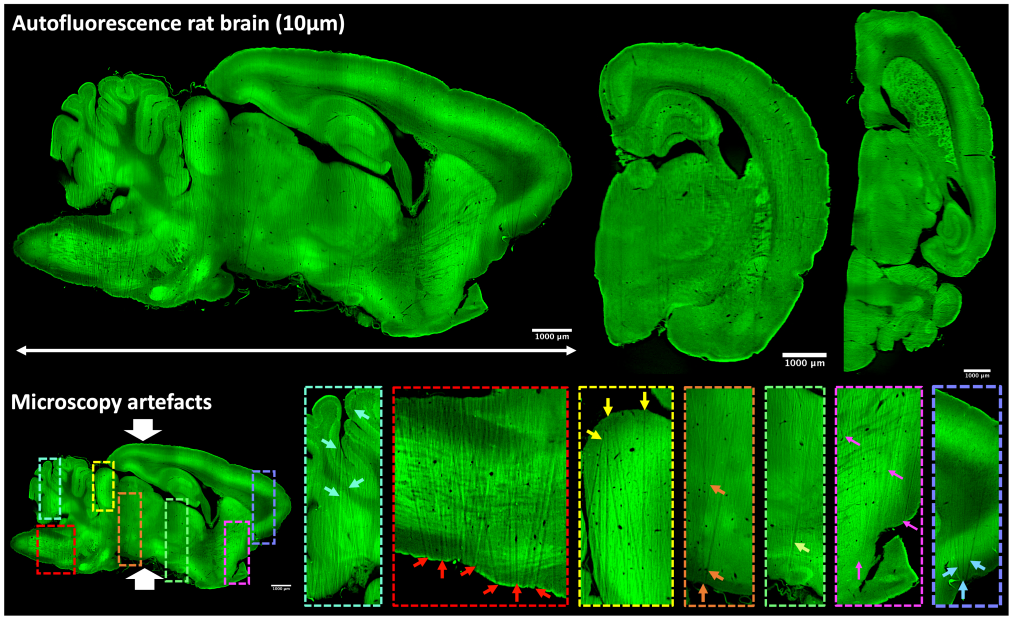


Figure 4.8: Autofluorescence imaging of a rat brain hemisphere following clearing with AdipoClear+. The top panel shows that autofluorescence reveals valuable anatomical details, including the brain's overall structure and white-gray matter contrast. Since light sheet microscopy produces 3D data, the sample can be examined along multiple planes. The sagittal view reveals non-uniform illumination along the direction of the double-sided arrow, even with dual-sided illumination and three light sheets at maximum width. The bottom panel illustrates the striping artifact, with small coloured arrows in expanded insets marking its presence. This artefact is inherent to lateral illumination in light sheet microscopy of large samples. White block arrows indicate the illumination axis.

contrast. The intensity inhomogeneities originate from various factors. The biggest contributor is uneven illumination, which is most apparent when imaging across the camera's full field of view (i.e., as opposed to cropping) at low magnification. The power profile of a light sheet is Gaussian across the Y dimension so, even at 100% sheet width, there will be a difference between the illumination intensity at the middle and edge of the sample. In addition, there are always small differences in the intensity of the left and right light sheets. Other factors include the clearing (light absorption inconsistencies due to uneven clearing), optics (radial aberrations in the objective result in lower intensities at the edges of the field of view), and processing (we are fusing image stacks that were acquired independently).

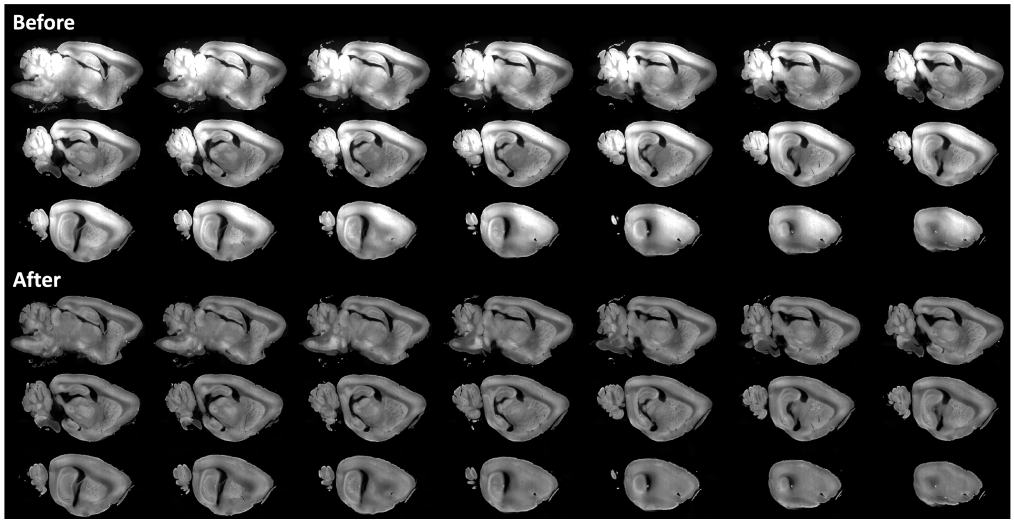


Figure 4.9: Sagittal slices of the same sample, imaged using 3D microscopy. The autofluorescence of a rat brain hemisphere cleared with AdipoClear+ before (top) and after (bottom) correcting for intensity inhomogeneities.

Clearing of Gadolinium-enhanced Brains

Figure 4.10 illustrates that including gadolinium contrast in the sample preparation did not adversely affect tissue clearing or autofluorescence. This is a significant finding given the substantial gains in MRI signal-to-noise ratio (SNR) achieved by using gadolinium to lower sample T_1, as discussed in the previous chapter. To our knowledge, this is the first demonstration of this effect. The images in Figure 4.10 depict light-sheet microscopy results following the AdipoClear+ protocol for a control brain perfused with the standard protocol (left) compared to a brain perfused with 2mM gadolinium (right). The presence of gadolinium did not interfere with the clearing protocol, as the samples exhibited similar levels of transparency. Additionally, the quality of autofluorescence in the imaging was comparable between the gadolinium-treated and control samples.

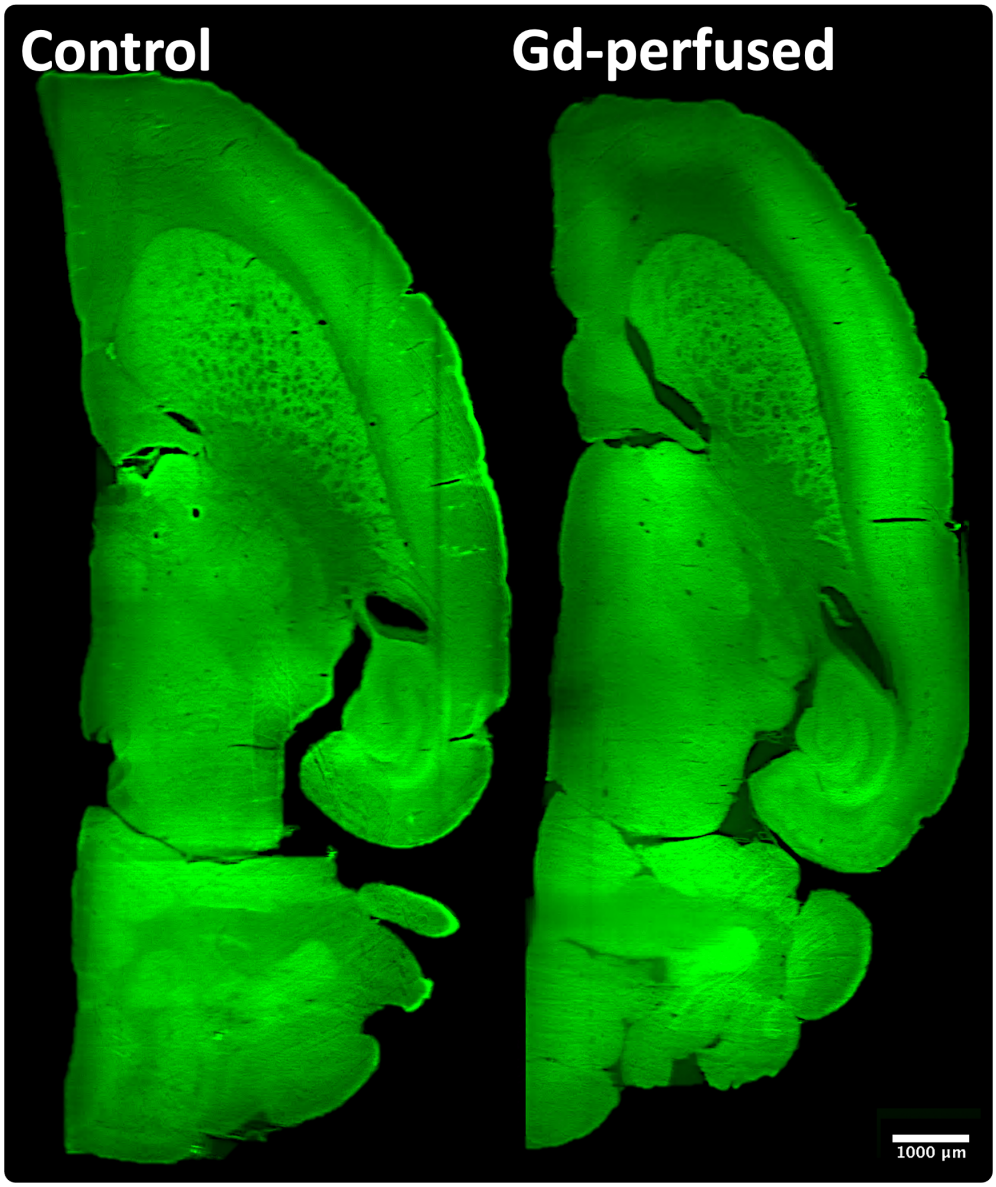


Figure 4.10: Tissue clearing achieved similar levels of transparency in control samples (left) and those prepared with gadolinium contrast in the perfusate (right). The autofluorescence signal was also comparable. The presented images show a horizontal view of the brain hemispheres.

Whole-mount Immunolabelling

The compatibility of AdipoClear+ with immunolabelling was evident as specific staining was observed in localised areas. However, the majority of the signal remained confined to the surface of the sample, as shown in Figure 4.11. The limited depth of staining might suggest that the antibody

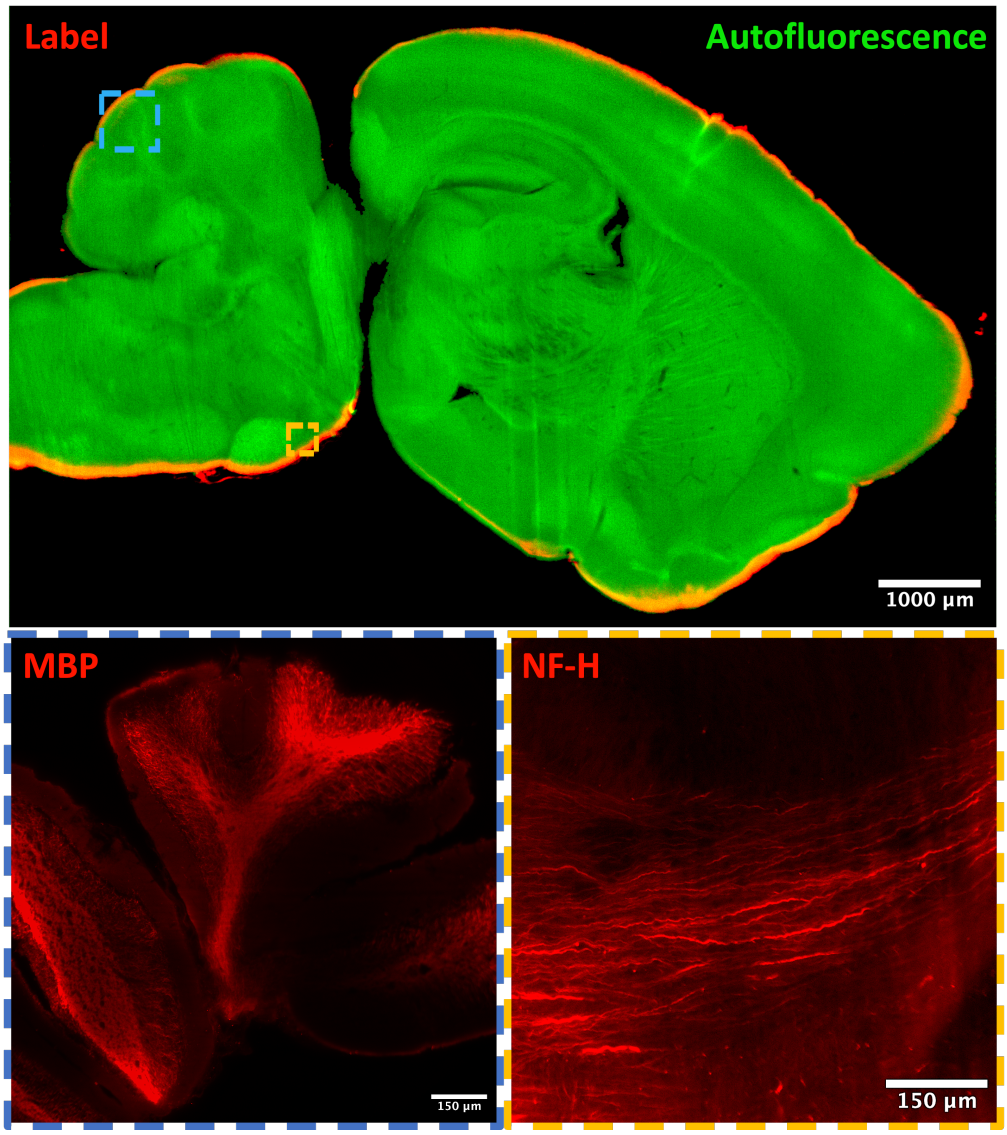


Figure 4.11: The AdipoClear+ protocol is compatible with immunolabelling, but staining is limited by poor antibody penetration. In the top panel, which shows the hemisphere in sagittal view, antibody signal (red) is concentrated on the sample's surface. Specific staining can be seen, but it is restricted to small regions close to the sample's surface. These regions are shown at higher magnification below. MBP staining (lower left) is concentrated in the white matter core and granular layer of the cerebellum. NF-H staining (lower right) highlights the 'wave-like' undulations of fibres in the brainstem.

incubation period (5-7 days) was insufficient for the antibody to diffuse through the sample. Nevertheless, similar surface saturation occurred even when employing comparable incubation times for ∼1mm thick sagittal sections of rat brain, as shown previously with iDISCO+ (see left panel of Figure 4.4). These sections, which have a much greater surface area to

volume ratio, demonstrated the same pattern of surface saturation with tyrosine hydroxylase staining.

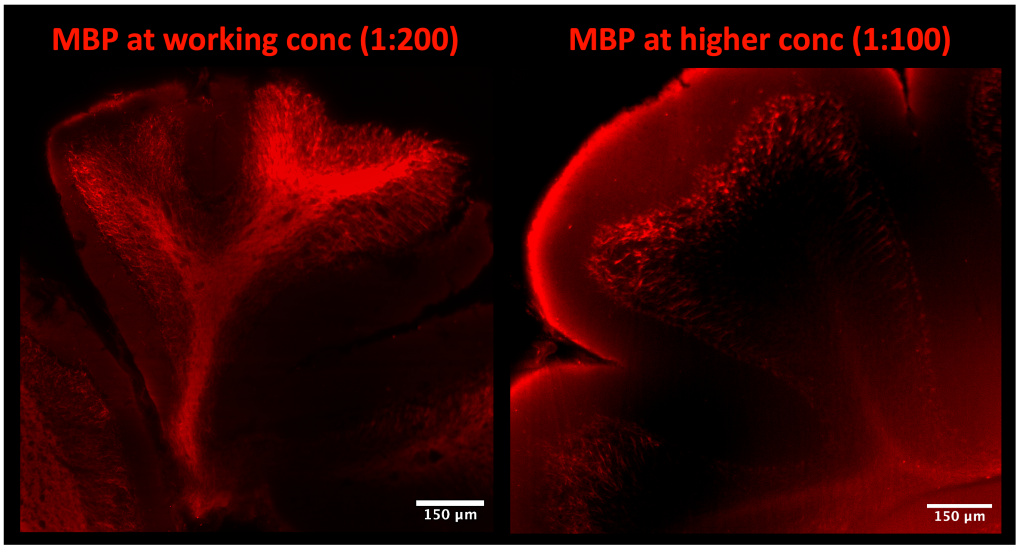


Figure 4.12: At a 1:200 concentration, MBP staining (left) can be seen in the white matter core of the cerebellum. Increasing the antibody concentration to 1:100 (right) does not improve penetration in the cerebellum. Instead, there appears to be a build up of antibody on the cerebellum's surface and limited staining of the granular layer in the folium (i.e., cerebellar ridge/gyrus).

The ring-like staining pattern, which was observed, raises the possibility that antibody binding on the sample's surface forms a dense network (i.e., due to aggregation), hindering unbound antibody penetration. This hypothesis is supported by the drop in penetration seen when increasing the antibody concentration, as shown in Figure 4.12. Alternatively, the sample's structure may lack sufficient porosity to enable the antibody to access deeper levels by passive diffusion. However, this would be surprising given that the AdipoClear+ protocol features enhanced permeabilisation. Active approaches of antibody transport (Yun et al., 2019; Kim et al., 2015) can improve antibody penetration and achieve more uniform staining in <24hours, as shown in the next chapter of the thesis.

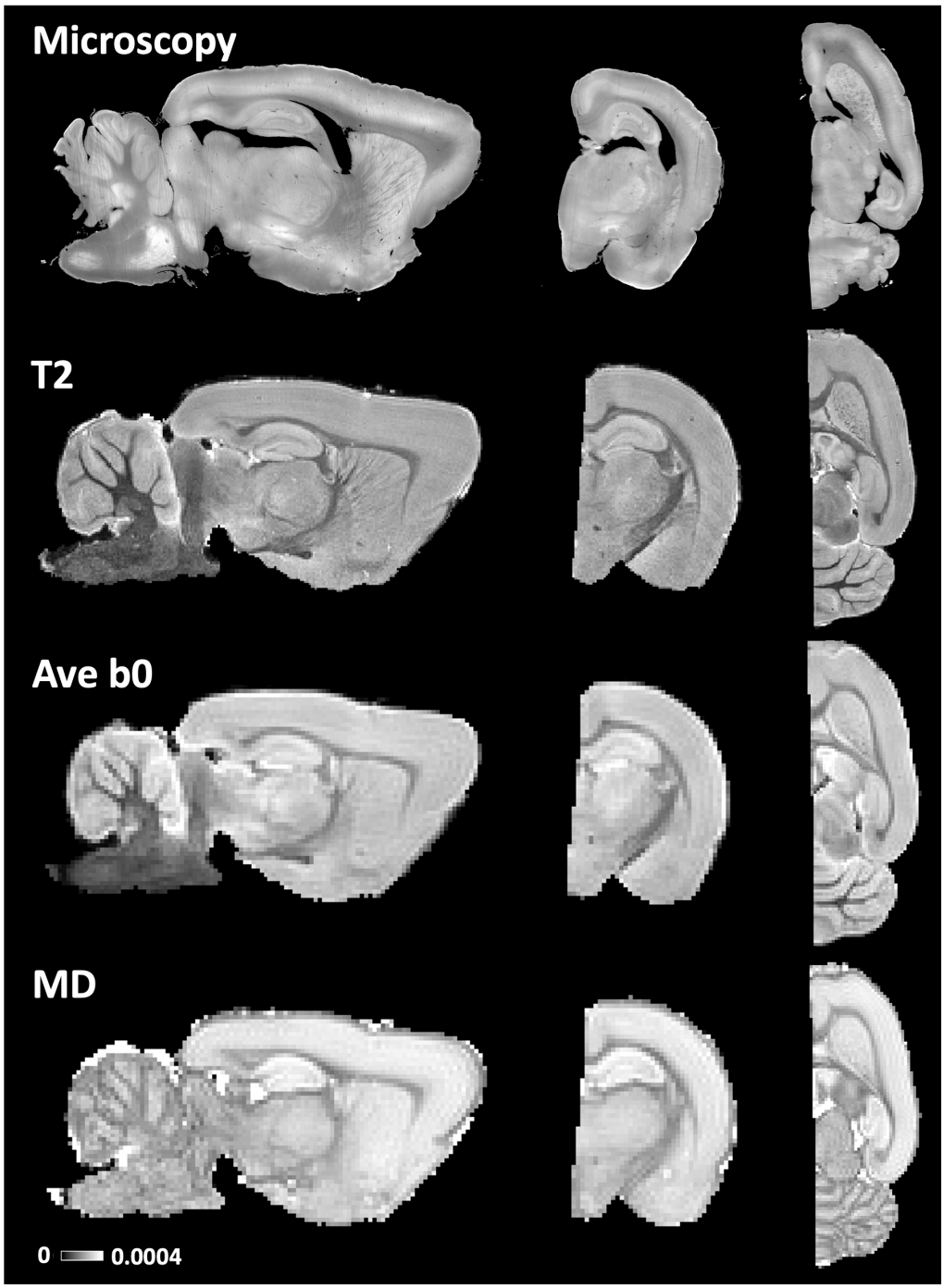


Figure 4.13: Comparing autofluorescence contrast in 3D microscopy (top row) with the tissue contrast seen in MRI scans (bottom three rows) of the same animal, **before co-registration** (MD: mean diffusivity). Although the ventricles are much more pronounced after hydrophobic clearing, due to shrinkage that occurs with dehydration, the brain's morphology is consistent with what was observed during MRI.

4.3.2 Registration of Microscopy Imaging to MRI

Figure 4.13 demonstrates how the autofluorescence signal of AdipoClear+ cleared rat brain hemispheres compares to the contrast of MRI scans acquired previously. There are differences in the image contrast of these modalities, yet the autofluorescence contrast resembles a T2-weighted contrast (dark in white matter, bright in grey matter), hence it is also commensurate to the $b = 0$ EPI T2-weighted contrast.

Figure 4.14 shows the success of aligning 3D microscopy to MRI with standard registration tools. Even a simple affine transformation (`FLIRT`, `FSL`), with 7 or 12 degrees of freedom (DOF), aligns the 3D microscopy and T2-weighted MRI scan reasonably well. This demonstrates that the distortions that occur during the tissue clearing process are mostly low level global changes (e.g., shrinkage). A conventional non-linear registration (`ANTs`), with default parameters, achieves very good alignment between the 3D microscopy and MRI. This is in contrast to the challenges of aligning traditional 2D histology to MRI, which require bespoke and complex multi-stage non-linear registration frameworks (Huszar et al., 2023). The high level of distortions and deformations seen with histology occur as a result of tissue sectioning and processing.

The improved alignment achieved using a non-linear warp field, as opposed to linear transformations, indicates that some non-linear deformations occur during tissue preparation for light sheet microscopy. These deformations arise from shape changes when the brain is removed from the skull, as well as changes induced by the clearing process itself. Although the latter changes are generally global and well-captured by affine transforms, the non-linear deformations that occur necessitate the use of a non-linear warp field for optimal alignment.

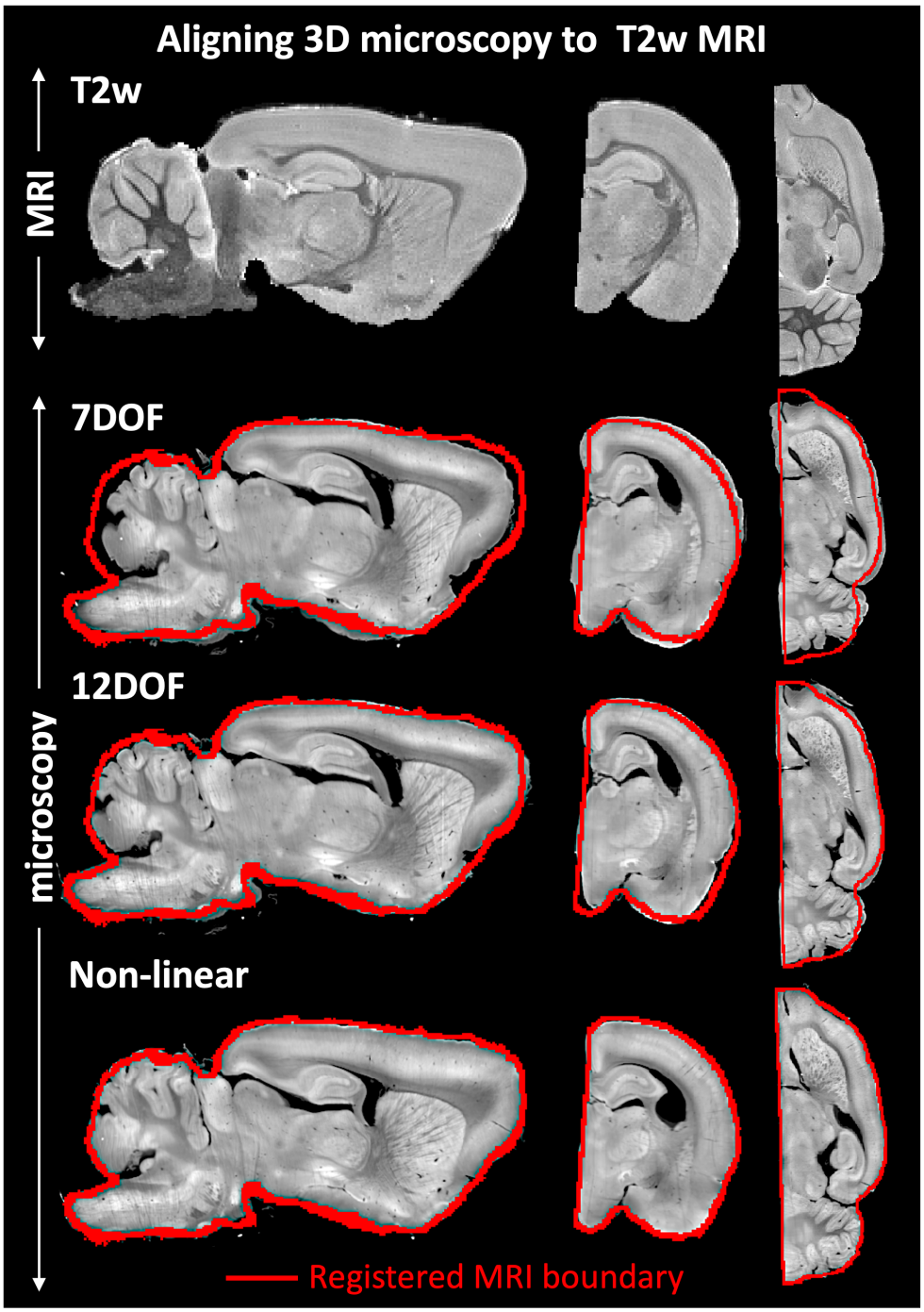


Figure 4.14: Registering sample autofluorescence to the corresponding T2-weighted MRI scan. The microscopy image is shown in each case overlaid by the boundary of the T2-weighted MRI image (red outline). A conventional non-linear registration approach, using `ANTs`, performs very well, but even linear registration (i.e., affine transformation with 7 or 12 degrees of freedom) provides reasonable results due to the limited deformations that occur with 3D microscopy.

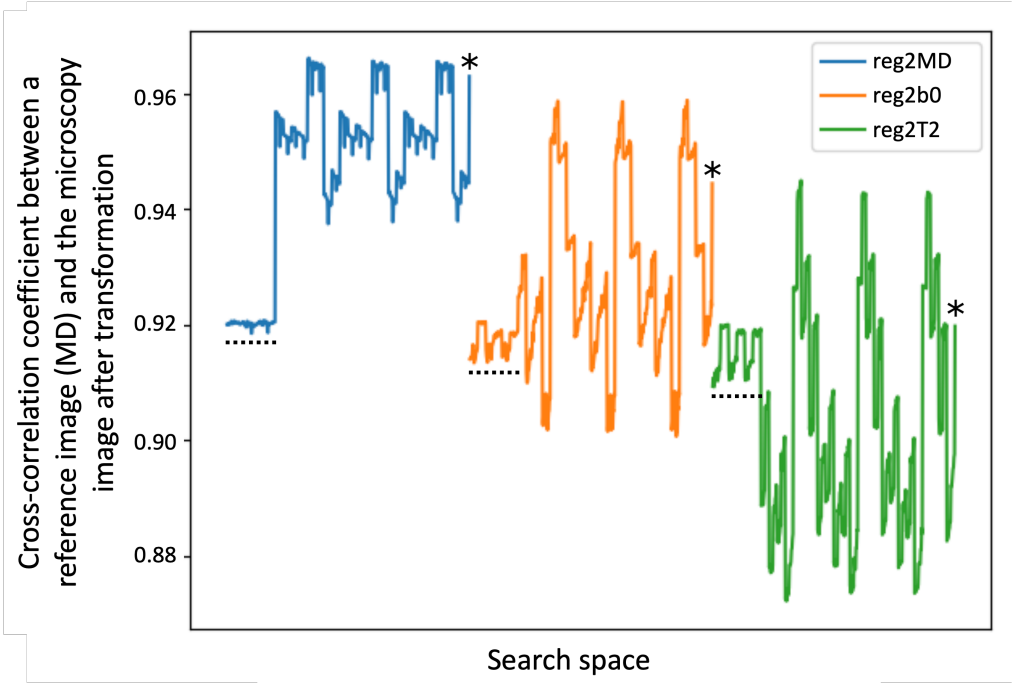


Figure 4.15: Searching for the optimal parameters for registering 3D microscopy to MRI. The graph shows the cross-correlation between the registration output (i.e., the microscopy image after transformation) with the mean diffusivity image. Using the default settings (marked with *) for non-linear registration of 3D microscopy to MRI contrasts (i.e., MD, b0 and T2) yielded a good result, with only small benefit achieved using a bespoke approach. Non-linear registration only consistently outperformed linear registration (marked with ...) for the registration of 3D microscopy to mean diffusivity (MD).

We subsequently conducted a brute force search to identify the optimal parameters for non-linear registration of 3D microscopy data to the corresponding MRI scans using `ANTs`. Figure 4.15 shows that the best registration results, as measured by a high cross-correlation coefficient, were achieved when mapping microscopy data to mean diffusivity (MD). Using the default settings (`antsRegistrationSyN.sh`) yielded an outcome that was comparable to the best performing registrations, justifying that the default call was already optimal. We also found that some parameter settings for non-linear registration of 3D microscopy to the average b0 or T2-weighted scans led to overfitting of local features, and a result that was worse than that achieved with linear registration, demonstrating that the solution space was not

always stable.

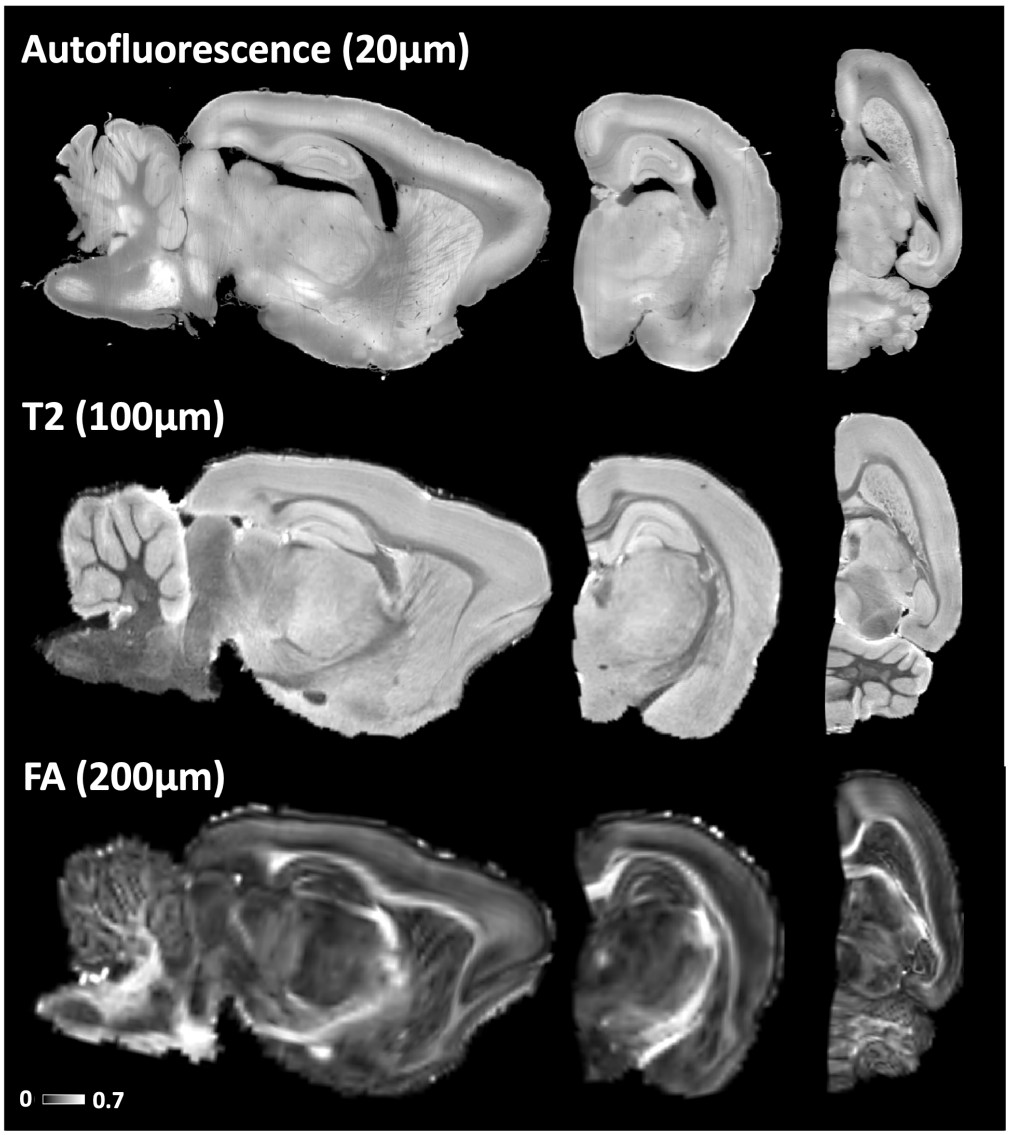


Figure 4.16: Direct comparison across modalities and resolutions, after registration. Here we show the autofluorescence signal (top row), obtained with 3D microscopy, in native space. The T2-weighted MRI scan (middle row) and fractional anisotropy (bottom row), derived from dMRI, are shown in microscopy space after non-linear registration with default parameters (`antsRegistrationSyN.sh`).

A good alignment was achieved for subcortical structures and cortical boundaries when registering 3D microscopy to MRI, as shown in Figure 4.16. This will allow for direct comparison between measures derived from MRI and 3D microscopy in the same rat brain hemisphere.

Figure 4.17 shows how the multiscale imaging framework that we have

developed allows for comparison over at least one order of magnitude, from micron-scale microscopy images to MRI at the sub-millimetre scale.

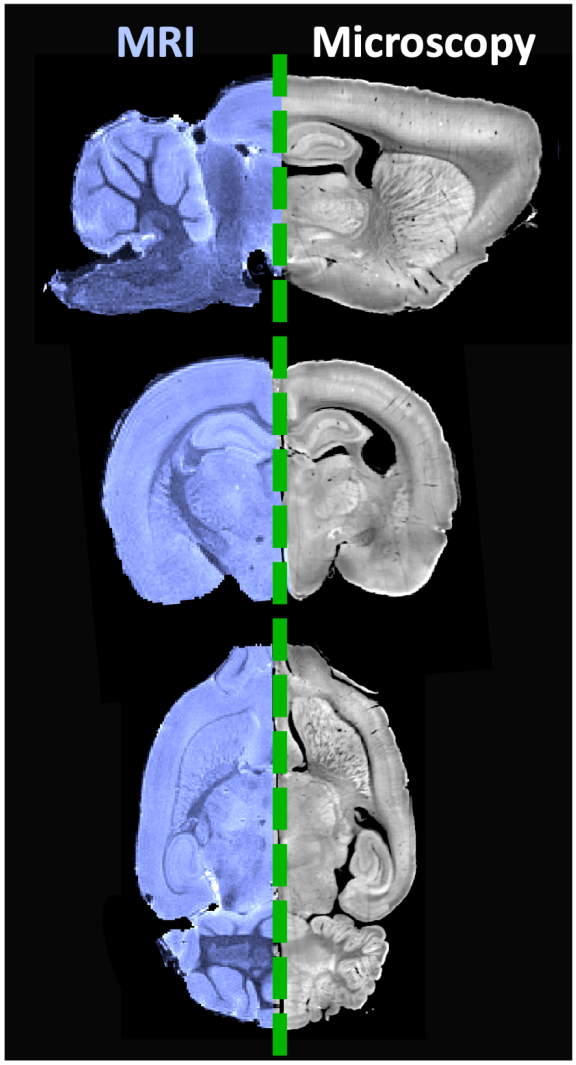


Figure 4.17: Combining 3D microscopy and MRI for the same brain enables direct comparison. This figure shows the alignment of white and grey matter boundaries integrating the T2-weighted MRI (left) with the intrinsic contrast provided by autofluorescence from 3D light sheet microscopy (right). For visualisation purposes, the microscopy image is displayed at 20μm resolution, though the true resolution is $\leq$10μm. The T2-weighted MRI was acquired at a resolution of 100μm.

4.4 Discussion

We found that AdipoClear+ stands out as a straightforward method for successfully clearing adult rat brain hemispheres. This protocol is notable for its low cost and simple implementation, as it does not require specialised equipment or custom-built microscopes. Unlike iDISCO+, AdipoClear+ is optimised for the higher lipid content of the rat brain. The prolonged delipidation process and inclusion of methyl-beta-cyclodextrin, which facilitates cholesterol extraction, are crucial in the AdipoClear+ protocol for effective membrane permeabilisation (Mai et al., 2023) and complete removal of dense myelin lipids in the rat brain (Branch et al., 2021).

The success of AdipoClear+, coupled with the excellent autofluorescence signal in the light-sheet microscopy images, provides superb contrast and a relatively homogeneous image intensity across the whole brain hemisphere. However, it is important to note that AdipoClear+ required at least a month for complete delipidation, permeabilisation, and refractive index matching. Failure to adhere to this timeline resulted in insufficient sample transparency, preventing high-resolution microscopy, particularly towards the hemisphere's centre.

For the first time, we confirmed the compatibility of AdipoClear+ with gadolinium-enhanced perfusion of the brain, an approach that significantly improves MRI contrast and SNR (see previous chapter and also Kim et al. (2009)). This finding is important for multi-scale brain imaging, as the reduced T_1 of gadolinium-perfused tissue enables faster structural and diffusion imaging acquisitions with improved contrast. Notably, we achieved homogenous tissue clearing in both PFA-perfused and gadolinium-perfused brains.

The immunocompatibility of the iDISCO+ and AdipoClear+ protocols was also confirmed. This is a significant advancement considering that previous applications of tissue clearing techniques with the rat brain relied on transgenic lines expressing fluorescent reporters (Stefaniuk et al., 2016). Our results demonstrate specific labelling of myelin — a challenging target, as lipids are removed during clearing. Furthermore, we demonstrated successful labelling of neurofilaments and tyrosine hydroxylase. However, penetration of labelling in deeper structures was found to be a significant challenge. Attempts to specifically enhance the autofluorescence of myelin, through additional fixation and incubation with glycerol (Costantini et al., 2021), did not yield appreciable improvements. In the next chapter, we tackle this problem using a different approach: active clearing and active immunolabelling.

The autofluorescence captured from rat brain hemispheres, cleared with AdipoClear+, provided detailed structural information, which was leveraged to align the 3D microscopy images to the corresponding MRI scans. This was possible because AdipoClear+ preserves the morphology of the whole hemisphere, unlike alternative methods of tissue clearing (Johnson et al., 2023) which induce significant distortions. The success of conventional registration methods, which used the default settings for `ANTs` (i.e., `AntsRegistrationSyN.sh`), to combine 3D microscopy data with MRI, further underscores the benefits of using tissue clearing. Complex multi-stage registration frameworks and extensive parameter optimisation, which were previously required (Huszar et al., 2023) with histology are no longer necessary. The simplicity of the registration with tissue clearing reduces the barriers for others seeking to adopt a similar approach. It also facilitates larger studies and automated high-throughput analysis, further enhancing the appeal of tissue clearing methodologies.

4.4.1 Limitations and Future Extensions

We cleared and imaged individual rat brain hemispheres in ∼6 weeks. Although clearing the entire rat brain would have been ideal, that would have taken significantly longer as passive diffusion in lipid-dense tissues is slow. Furthermore, imaging a whole rat brain would require a light sheet microscope with a larger working distance and travel range, such as the BLAZE (Miltenyi Biotec) or SmartSPIM (Life Canvas Technologies), rather than the UltraMicroscope II. Nevertheless, our setup provides proof of principle by demonstrating the feasibility of clearing rodent brains at a larger scale than typically attempted before (Goubran et al., 2019; Johnson et al., 2023; Stolp et al., 2018; Chang et al., 2017).

Although we demonstrated specific labelling for difficult targets, the penetration of antibodies remained poor. Achieving uniform immunostaining in large samples is a common challenge (Ariel, 2017) and several techniques have been developed to accelerate and improve antibody penetration. By switching to an approach that actively labels samples using electrophoresis (Kim et al., 2015), we hope to rapidly and uniformly stain the intact rat brain, whilst also preserving the complex tissue architecture (Park et al., 2019). This will allow us to characterise the organisation of specific structures deep within the rat brain, and relate these findings to measures obtained non-invasively with MRI. We explore this route in the following chapter of this thesis.

The quality of our microscopy images was not severely impacted by the scatter/stripe artefact and it was no longer visible after down-sampling. However, we tested a simple approach that had been used previously (Branch et al., 2021), to see if it could minimise the artefact, whilst retaining useful signal. This approach involved applying a bidimensional band-pass

Fourier filter targeting streaks with an angular orientation of +/-10.5°. Unfortunately, this method resulted in blurring, residual scatter, and in some cases, the emergence of new artefacts. While more complex approaches are available (Ricci et al., 2022), they often prove to be computationally expensive. However, it would be worthwhile exploring the multidirectional stripe remover developed by Liang et al. (2016), as it has been shown to work better than two competing methods when tested with data acquired on an UltraMicroscope II.

In future work, we will validate our registration workflow by assessing the accuracy of the alignment of anatomical structures in MRI and microscopy images. This would require us to first identify distinct anatomical landmarks that are discernible in both microscopy and MRI modalities. After establishing these common reference points, it would be possible to obtain an overall measure of target registration error by averaging the root mean squared error for each set of landmarks after transformation. It would also be worthwhile testing registration performance under challenging conditions. This could be achieved by using noisy data (e.g., where MRI or clearing was not optimal) or images with significant intensity inhomogeneities. This will allow us to demonstrate that our multimodal imaging dataset can be seamlessly translated from the microscopic to macroscopic scale.

4.4.2 Contributions

Dr Joao Correia provided expertise with the optimisation of parameters for image acquisition on the UltraMicroscope II. My personal contributions include: conceptualisation and project lead; protocol development; tissue processing and staining; acquisition of light sheet microscopy data; visualisation and interrogation of microscopy data; data conversion and processing;

MRI-microscopy co-registration; analysis and presentation of results; and manuscript writing, editing and review.

Chapter 5

Active Clearing and Staining in the Intact Rat Brain

5.1 Introduction

As presented in the previous chapter, technical developments in tissue clearing and light sheet microscopy are revolutionising our ability to explore neural anatomy in 3D. By transforming the optical properties of tissue, clearing techniques increase the penetration depth of light from <100μm to >1cm. This enables 3D microscopy of intact samples, preserving the brain's complex architecture and connectivity while avoiding the physical distortions and artefacts (e.g., tears and folds) caused by tissue sectioning. Recent advances in the optics of light sheet fluorescence microscopes are also allowing for rapid *in toto* imaging of larger samples, such as the rodent brain, at cellular and subcellular resolutions (μm scale). Despite these advancements, this emerging field still faces unresolved challenges.

One of the primary challenges is visualising specific structures and molecules

within large samples. Early clearing studies relied on the genetic expression of fluorescent proteins in transgenic mouse lines (Chung et al., 2013). While this method can successfully label a high proportion of the target cells, the complexity of stably introducing a transgene presents significant hurdles. More recently, neural circuits have been visualised in mice by combining tissue clearing with viral tracers, which can induce the expression of fluorescent proteins in specific cell populations (Pisano et al., 2022). However, the variability in expression levels, which is influenced by factors such as virus titre, serotype, and promoter, remains a significant challenge (Saleeba et al., 2019).

These challenges are compounded by the fact that many clearing protocols quench fluorescence signals (Ertürk et al., 2012; Dodt et al., 2007; Renier et al., 2014; Kuwajima et al., 2013). The limited genetic toolbox available for rats and non-human primates further restricts the utility of genetic approaches in certain model systems (Ellenbroek and Youn, 2016). Consequently, researchers have turned to alternative methods for labelling structures within large samples.

Many tissue clearing studies now use staining techniques to label features of interest, rather than relying on genetic expression. However, achieving uniform stain penetration in large samples is challenging. A common issue (that was demonstrated in the previous chapter, Figure 4.11) is the saturation of fluorescent signal on the sample's surface, particularly with abundant targets like myelin or neurofilament, where labelling occurs faster than diffusion (Weiss et al., 2021). This surface aggregation can block further penetration into the tissue, especially in canonical labelling, where both primary and secondary antibodies are required (Richardson et al., 2021). Unfortunately, additional delipidation, longer incubation times, or higher concentrations often fail to improve penetration (Adolfs et al., 2021).

Achieving uniform and deep stain penetration in large samples is challenging due to the slow and uneven nature of molecular diffusion. Although the exact kinetics of diffusion in cleared tissue are not fully understood, several factors significantly influence staining outcomes (Weiss et al., 2021; Choi et al., 2021). Sample thickness and tissue permeability — which is dependent on the sample's density and composition — play a critical role (Choi et al., 2021). However, tissue clearing processes, such as delipidation and dehydration (i.e., in solvent-based protocols), alter composition and density, leading to variable effects on permeability and diffusion rates. Additionally, the size of the staining molecule is crucial; larger molecules like antibodies (∼150 kDa) diffuse slowly (∼100μm-1mm/day (Susaki et al., 2020)), while smaller molecules like nanobodies (∼15 kDa) penetrate more quickly and evenly, but have a limited range of targets (Cai et al., 2023; Vigouroux et al., 2017).

In addition to these challenges, some clearing protocols remove relevant targets (e.g., proteins/mRNA) or denature epitopes. The techniques used to preserve sample integrity during clearing (e.g., fixation, hydrogel embedding) can also mask antigen-binding sites. Unfortunately, standard antigen retrieval methods (like enzymatic digestion, heat or pressure) cannot easily reverse this masking without compromising tissue integrity during clearing. Additionally, clearing protocols may distort tissue morphology through shrinkage or expansion, and damage delicate structures, impacting the localisation, appearance, quantification and interpretation of staining patterns.

Despite the plethora of clearing protocols available, it is challenging to identify which protocol will be suitable for a particular experimental question or tissue type (Weiss et al., 2021). Furthermore, staining protocols require optimisation across many experimental conditions (concentration, temperature, time, pH, etc), adding further complexity to the process of

tissue clearing (Avilov, 2021).

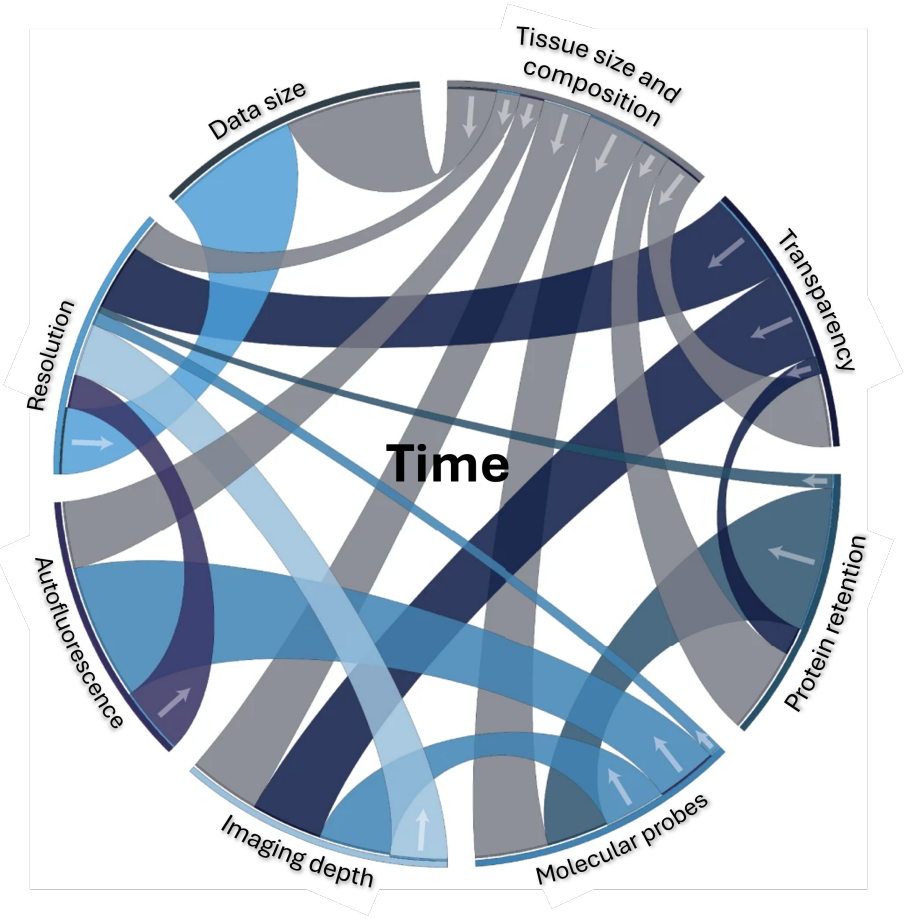


Figure 5.1: Interactions between key variables in tissue clearing, staining, and microscopy require trade-offs. Arrows and colours indicate cause-and-effect relationships, with ribbon size indicating the strength of these connections. Time/speed, shown in the centre, is a common factor influencing decision making. Other important considerations include cost (financial and labour), protocol complexity/feasibility, compatibility, sample integrity, and available equipment. Example: increasing sample size will lengthen the clearing and staining time, affect the choice of probes and protocols, and significantly increase data size. Modified from Weiss et al. (2021).

This complexity arises not only because there are many factors to consider and optimise, but also due to the interactions between these factors, as illustrated in Figure 5.1. Furthermore, troubleshooting problems is challenging when multiple steps are involved, some of which are independent of the clearing and staining protocols (e.g., fixation). Optimising individual conditions can also become costly and impractical (Ariel, 2017) when clearing protocols are already long (i.e., lasting many weeks/months), labour-intensive, and

expensive (e.g., requiring large volumes of antibodies).

Fortunately, novel methods have been developed to enhance antibody penetration and achieve more even staining in large samples (Chung et al., 2013). One strategy involves dynamically modulating reaction kinetics in a controlled manner (Murray et al., 2015; Yun et al., 2019). Another approach applies an external force to accelerate label penetration and lipid extraction. Both of these techniques allow for **active**, as opposed to passive, labelling and clearing. However, they also require new preservation methods (Park et al., 2019; Murray et al., 2015) to protect tissue morphology and microstructure from the deformation and heating induced by an external force, and the conditions (e.g., pH, temperature) used to modulate reaction kinetics.

In this research chapter, we leveraged advances in tissue clearing to address the challenges of staining white matter in the intact rat brain. Instead of using a passive, organic solvent-based clearing protocol (presented in Chapter 4), we explored an active approach that incorporated tissue preservation, detergent-based delipidation, electrotransport, and modulation of diffusion-reaction kinetics. Our objectives were to: (a) adapt tissue preservation and active clearing protocols from the mouse brain to the larger, more lipid-dense rat brain; (b) develop new protocols for active staining of the rat brain using antibodies for neurofilament and myelin; and (c) establish a pipeline for extracting microstructural information from 3D light-sheet microscopy images of these actively stained samples, enabling direct comparisons across imaging modalities when combined with MRI.

Although this approach requires specialised equipment (i.e., electrophoretic device), costly consumables, and expertise in new techniques, our results demonstrate that it is possible to scale these methods up to the rat brain,

achieving uniform clearing and deeper antibody penetration in a significantly shorter time frame (i.e., weeks instead of months). The active preservation of key biomolecules (proteins, nucleic acids, transcripts) and compatibility with other molecular tools (Park et al., 2019) allow this approach to be expanded for identifying imaging signatures and mechanisms of cellular changes. Moreover, the automation, standardised reagents (concentration, pH), and precise control (temperature, current, electric field strength) provided by the electrophoretic device make this approach less labour-intensive and more reproducible than organic solvent-based methods.

5.2 Methods

5.2.1 Sample Preparation

Transcardial perfusion of rats and tissue processing were performed as described previously. In brief, four rats were perfused with heparinised (Sigma-Aldrich, H3149-50KU) phosphate buffered saline (0.1M PBS, Invitrogen, AM9624) followed by 4% paraformaldehyde (PFA, Sigma-Aldrich, 441244-1KG). The brains from all samples were carefully extracted from the skull, and the hemispheres were separated along the midline. The samples were then post-fixed in PFA at 4°C for 24hrs before being transferred to PBS containing 0.02% sodium azide (PBSN, Sigma-Aldrich, S8032) for storage at 4°C.

We explored the effects of two different pre-treatment and delipidation methods (described below) on active clearing and neurofilament staining in two hemispheres. After identifying the most effective method for the rat brain, we applied it to a third sample to evaluate myelin staining. The final

sample was cleared and neurofilament staining was performed to assess the compatibility of these active protocols with gadolinium perfusion (2mM MultiHance, Bracco Imaging) and *ex vivo* MRI. We then integrated the microscopy and MRI data from this sample. However, as this sample was ∼2 years old and had previously undergone passive delipidation using the extended AdipoClear+ protocol (described in Chapter 4), we plan to repeat this test with fresh samples to validate the MRI-microscopy comparisons.

5.2.2 Pre-treatment

Although not typically part of active clearing and staining protocols (Yun et al., 2019), we tested whether incubating samples in hydrogen peroxide could reduce autofluorescence from blood vessels and minimise the microscopy artefacts caused by pigmentation. This method, which is commonly used in solvent-based protocols (Renier et al., 2014), is effective across various pigments. To avoid damaging delicate tissue structures, we limited bleaching to an overnight incubation at 4°C using 5% hydrogen peroxide (Sigma-Aldrich 216763-100mL) in PBS.

5.2.3 Tissue Preservation

Classical histology relies on aldehyde-based chemical fixation to preserve tissue architecture during processing, sectioning, and staining. However, some forms of tissue clearing have required new techniques capable of preserving the integrity of larger samples whilst their chemical composition and optical properties are transformed (Ueda et al., 2020). These innovative forms of sample preservation constitute a new field of tissue engineering, where the physicochemical properties of tissues — including optical transparency,

molecular permeability, mechanical properties, and overall size — are precisely manipulated. Such modifications allow for the detailed interrogation of the microenvironment while maintaining spatial information and tissue complexity in 3D (Gradinaru et al., 2018). Additionally, these techniques are crucial for protecting tissue architecture from deformation/damage during electrophoresis and preventing the loss of important biomolecules.

Tissue preservation techniques used with active clearing can be broadly categorised into two main approaches (Choi et al., 2021), as shown in Figure 5.2. The first approach involves synthetic hydrogel-based methods like CLARITY (Chung et al., 2013). In this method, the sample is infused with a hydrogel that is polymerised to create a scaffold which anchors biomolecules in place. This results in a tissue-hydrogel hybrid that retains its mechanical and molecular stability after delipidation.

The second approach builds on traditional aldehyde-based fixation by using a polyepoxide chemical to form intra- and inter-molecular crosslinks. Each polyexpoxy molecule has a flexible backbone and multiple epoxide groups that react with the amide groups of biomolecules (proteins and nucleic acids), anchoring them in their physiological location and preserving tissue architecture. This method, known as inter-biomolecular fixation, includes techniques like SHIELD (Stabilisation under Harsh conditions via Intramolecular Epoxide Linkages to protect Degradation, Park et al. (2019)).

In the original CLARITY protocol, delipidation resulted in sample softening and significant expansion/distortion (Chung et al., 2013). In contrast, the newer fixation-based approach better preserves sample integrity, volume and fluorescence (Park et al., 2019). This method also mitigates other drawbacks of hydrogel-based techniques, such as loss of biomolecular tertiary structure and antigenicity. In addition, SHIELD preservation enables

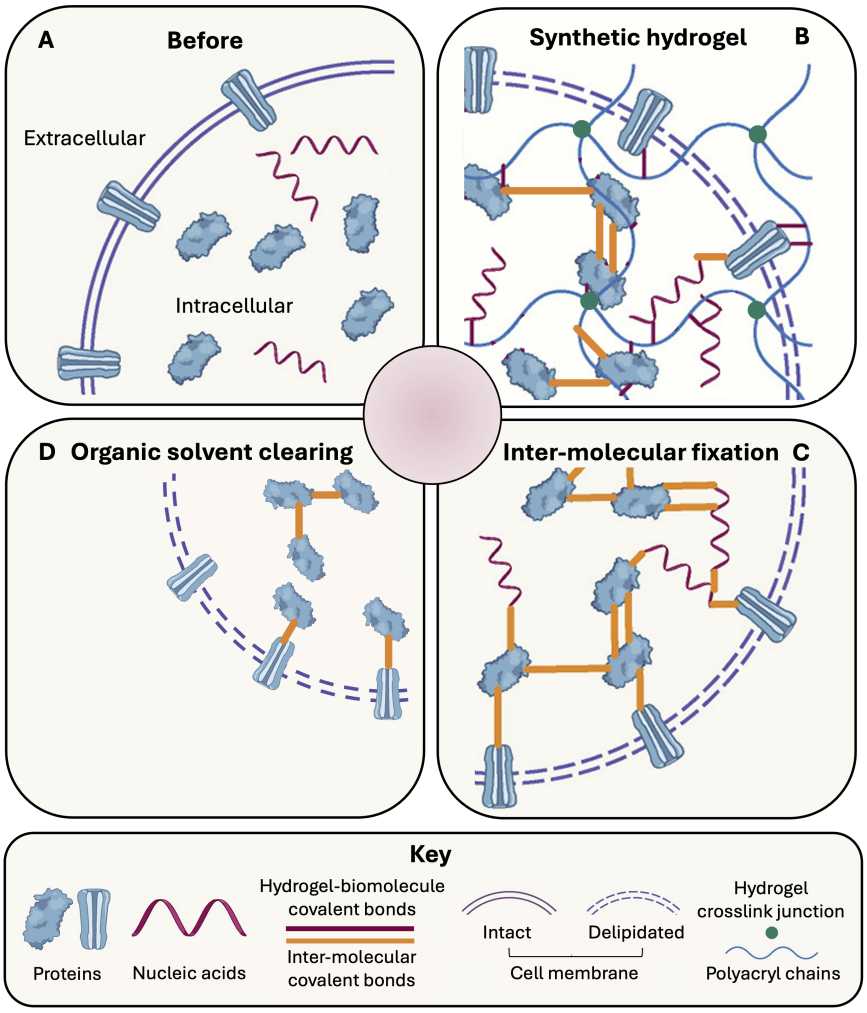


Figure 5.2: The principles of tissue preservation in active clearing techniques. A) Schematic of the cell in its natural state, which is intrinsically opaque due to refractive index inhomogeneities. Tissue preservation techniques aim to stabilise cellular architecture, allowing samples to be rendered optically transparent after rigorous delipidation with detergent, while preserving important biomolecules in their physiological locations. B) Synthetic hydrogel-based techniques, such as CLARITY, generate a polyacrylamide hydrogel lattice (depicted as wavy blue lines) that acts as an external scaffold to which biomolecules are anchored and crosslinked. C) Inter-biomolecular fixation methods, such as SHIELD, use a polyexpoxide-mediated reaction to crosslink amino groups (-NH_2) of nucleic acids and proteins, thereby creating a mesh of inter- and intra-molecular bonds that stabilises tissue architecture. This method preserves fluorescence and the integrity of transcripts, whilst also preventing the loss of biomolecules and their reactivity. D) In contrast, organic solvent-based clearing protocols, such as AdipoClear+, which only use aldehyde based fixation for preservation, are often associated with shrinkage and loss of antigens and/or fluorescence. Based on Choi et al. (2021).

samples to withstand harsh conditions (e.g., heat, aggressive detergents, non-physiological pH) and enables repeated labelling.

We used SHIELD preservation (Park et al., 2019) in combination with the SWITCH (System-Wide control of Interaction Time and kinetics of CHemicals) technique (Murray et al., 2015) to control the reactivity of the polyepoxide with primary amines. This method suppresses intra- and inter-biomolecular crosslinking until the polyepoxy has fully permeated the sample, after which a synchronised crosslinking reaction uniformly preserves large samples. Furthermore, the polyglycerol-3-polyglycidyl ether concentration can be adjusted to either favour antigenicity and penetration (by decreasing concentration) or to better preserve proteins, mRNA, and tissue integrity (by increasing concentration).

In the first stage, each rat brain hemisphere was incubated in 50mL of SHIELD-OFF buffer at 4°C with shaking for 6 days. The low temperature and neutral pH (∼7.4) of the SHIELD-OFF buffer suppress crosslinking. SHIELD-OFF buffer is prepared on ice by mixing deionised water, SHIELD buffer, and SHIELD epoxy (LifeCanvas Technologies) in a 1:1:2 ratio. This results in a phosphate buffered solution of 10% of polyglycerol-3-polyglycidyl ether (Yun et al., 2019).

In the second stage, each hemisphere was incubated in 40mL of pre-warmed SHIELD-ON buffer (LifeCanvas Technologies, 0.1M sodium carbonate buffer) at 37°C with shaking for 24 hours (Yun et al., 2019). The higher temperature and basic pH (∼10) of the SHIELD-ON buffer increases polyepoxide reactivity tenfold to synchronise crosslinking across the sample (Park et al., 2019). Samples were then stored at 4°C in PBS containing 0.02% sodium azide (PBSN).

5.2.4 Electrophoretic-driven Clearing and Staining

Passive diffusion of detergent molecules and molecular probes (e.g., antibodies) through large tissue samples is inherently slow and uneven, leading to inconsistent lipid extraction and staining, even after extended incubation periods lasting weeks/months. Reducing these prolonged timescales and minimising inhomogeneities in clearing and labelling have been key objectives (Weiss et al., 2021).

Acceleration of both delipidation and staining in large tissue samples was first achieved using electrophoresis equipment (Chung et al., 2013; Kim et al., 2015). Applying an external electric field facilitated the active transport of electrically charged detergent molecules, lipid micelles, and antibodies through the tissue, along the direction of the electric field. However, using a static electric field leads to an obvious gradient in lipid content and antibody binding across the sample. Stronger electric fields also deform sample morphology and damage integrity due to the displacement of the tissue matrix, which has a net charge, as well as bubble formation and runaway heating.

These challenges led to the development of novel technique, referred to as stochastic electrotransport (Kim et al., 2015). This method enables the rapid and uniform dispersion of highly electromobile species, such as lipid micelles and antibodies, through a diffusion-like process. The active electrotransport is isotropic because the sample holder is rotated by a motor, allowing the sample to experience a rotational electric field. The effects of the field are selective as endogenous biomolecules, which have low electromobility (Richardson et al., 2021), remain stationary in their physiological locations, stabilised by the crosslinks formed during SHIELD preservation (Kim et al., 2015). Stochastic electrotransport significantly

reduces diffusion timescales and allows for the use of stronger electric fields without causing damage or deformation to samples. This technique also makes it feasible to delipidate and label larger tissues, such as the entire rat brain, which would be difficult to achieve with passive diffusion alone.

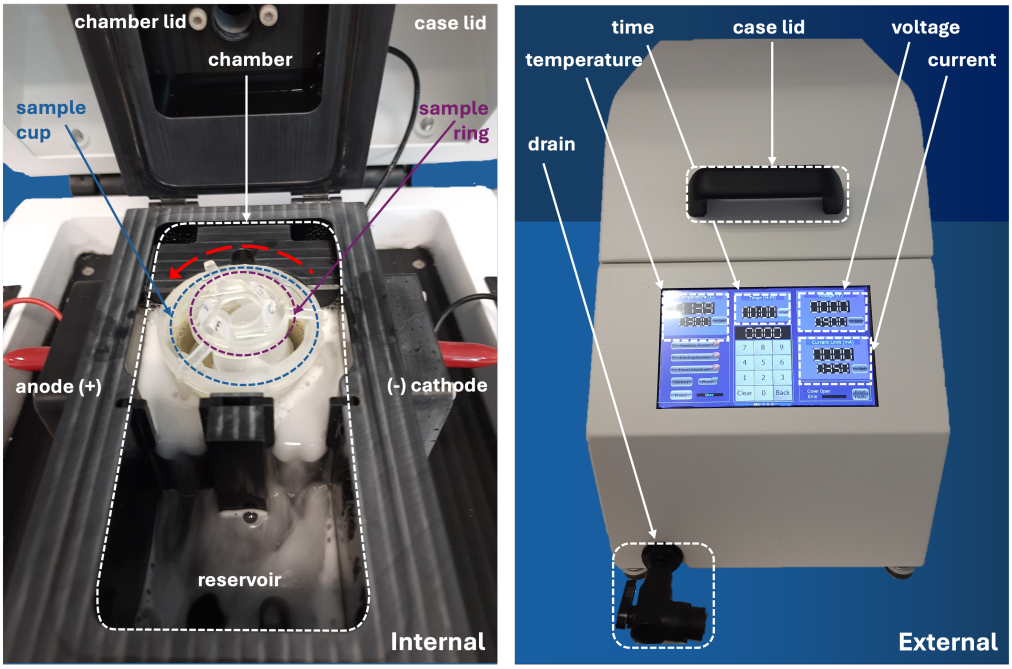


Figure 5.3: The SmartBatch+ device is designed for the active delipidation and labelling of large samples. Samples are suspended vertically in mesh bags from a sample ring into the buffer solution within the sample cup (left panel). The sample cup is positioned between the anode (+) and cathode (-), which generate a static electric field across the chamber. To ensure that the samples are not subjected to a unidirectional electric field, the sample cup rotates slowly in an anticlockwise direction (indicated by the red arrow). A pump circulates the buffer solution through the sample chamber from a reservoir located below the chamber. The reservoir can be emptied using the drainage tap on the front of the device (right panel). Experimental conditions are controlled via a touch-screen. Electrophoresis can commence once the samples are loaded and the chamber and case lids are securely closed.

The SmartBatch+ device (LifeCanvas Technologies), shown in Figure 5.3, was used in our experiments. This is a commercial system designed for active delipidation and labelling of large samples using stochastic electrotransport. This system accelerates molecular transport, reducing processing times from weeks/months to days. With precise control over temperature and other

settings, the SmartBatch+ prevents heat damage, standardises processes, and improves reproducibility (Richardson et al., 2021). In addition, the device accommodates 4 rat brains (or 12 mouse brains), making it ideal for batch processing.

Total diffusion time depends on sample thickness. To optimise this, non-spherical samples should be positioned with their thinnest dimension aligned with the direction of the electric field. For brain hemispheres, orienting them vertically in the chamber with the cerebellum at the bottom reduces processing time and minimises damage.

Active Delipidation

Myelin, one of the staining targets in white matter, is predominantly composed of lipids (Morell and Quarles, 1999), so overly aggressive delipidation risks destroying the feature of interest. However, adequate delipidation is essential to achieve optical clearing and facilitate stain penetration into the white matter. To balance these needs, we tested two types of delipidation buffer. The first is a standard delipidation buffer (LifeCanvas) with a proprietary formulation (Kim et al., 2015; Yun et al., 2019). The second is a customised sodium dodecyl sulphate (SDS)-based buffer (LifeCanvas), likely similar to published formulations (Yun et al., 2019) containing 300mM SDS, 10mM sodium borate, and 100mM sodium sulphite (pH 9). SDS is extremely effective at solubilising membrane lipids but can also denature proteins. Although SDS-based delipidation is slower (>10 days for a rat brain hemisphere) and can compromise sample integrity, it may be more effective for staining challenging targets like white matter.

Samples were preincubated in 20 mL of delipidation buffer at 45°C with gentle shaking for ≥24 hours. Following preincubation, the hemispheres

were suspended in mesh bags in the SmartBatch+ device's clearing cup containing >35mL of delipidation buffer. This was refreshed every 2-3 days during electrophoresis to prevent acidification. The clearing cup was then securely positioned within the SmartBatch+ device, and the chamber was filled with conduction buffer (LifeCanvas). Although the exact content of the conduction buffer is proprietary, it is likely similar to published formulations, containing detergent at its critical micelle concentration (e.g., 10 mM SDS) to maintain miceller equilibrium with the delipidation buffer, balancing surfactant micelle formation and dissociation, and reducing the rate of detergent breakdown (Kim et al., 2015). The conduction buffer probably also contains a counter ion (e.g., lithium hydroxide, 10mM) to optimise micelle size for efficient lipid extraction (Kim et al., 2015).

Electrophoresis was conducted at 40V and 1250 mA, with the temperature maintained at $\leq$42°C to preserve the tissue's mechanical properties. Under these conditions, complete delipidation of the rat brain hemispheres was achieved in 6 days using the standard buffer, or in $\geq$10 days with the SDS-based buffer. The exact timing is sample-dependent, with delipidation considered complete once the samples became homogeneously translucent.

After delipidation with the standard buffer, samples were returned to PBSN for storage at 4°C. Samples that were delipidated in SDS-based buffer were first washed in PBS for 3 days, refreshing the solution at least once. This is necessary as residual SDS precipitates at low temperatures, which would damage tissue architecture. SDS can also disrupt labelling by interfering with the electrostatic interactions between the probe and its target.

Active Whole-mount Immunolabelling

We aimed to stain the rat brain with labels that are both specific (high affinity for a single target) and selective (low affinity for similar sites) for axons in white matter. To achieve this, we used antibodies targeting neurofilament (NF-H) and myelin basic protein (MBP). Unlike genetic manipulation, antibodies allow for flexible targeting of various molecular markers within the same sample. Antibody labelling is also directly transferable to clinical samples.

To overcome the challenges of labelling abundant targets in large samples, we used stochastic electrotransport combined with eFLASH (electrophoretically driven Fast Labelling using Affinity Sweeping in Hydrogel), a novel technique that dynamically modulates probe-target binding affinity. This dual strategy accelerates antibody penetration and prevents the surface depletion of antibody (Murray et al., 2015; Yun et al., 2019), effectively resolving the significant mismatch between slow diffusion and fast antibody binding rates. Instead of requiring weeks and large quantities of antibody, this method achieves deeper penetration within a day using only microgram amounts. Furthermore, eFLASH is generalisable across probes and can deliver multiple probes simultaneously.

Each brain hemisphere was preincubated in 20mL of Primary Sample Buffer (LifeCanvas) at 45°C with light shaking for ≥24hr, refreshing the solution once. While the contents of the Primary Sample Buffer is proprietary, it is likely similar to published formulations (0.9% sodium deoxycholate, 20% D-sorbitol, 160mM CAPS, 240mM Tris, pH 9.6, Yun et al. (2019)).

After pre-incubation, each sample was placed in a single sample staining cup containing 9mL of Primary Sample Buffer and 400μL of normal donkey

serum (Jackson Immunoresearch, 017-000-121), which was then loaded into the device. For **myelin staining**, 20μg of mouse monoclonal anti-MBP (Encor, MCA-797) and 15μg of AlexaFluor 647-conjugated Fab Fragment donkey anti-mouse IgG (H+L) (Jackson Immunoresearch, 715-607-003) were added. For **neurofilament staining**, 40μg of mouse monoclonal NF-H antibody (Encor, MCA-9B12) was used. The staining cup's nanoporous membrane retained the probes inside, preventing dilution. The SmartBatch+ chamber was then filled with Primary Device Buffer (LifeCanvas, proprietary contents), which originally contained 0.2% sodium deoxycholate, 20% D-sorbitol, 160mM CAPS, and 240mM Tris (Yun et al., 2019). Electrophoresis was conducted at 90V, 350 mA and 30°C for 18 hours, or until the the staining cup's pH dropped below 8.0.

After myelin staining, samples were washed in 40mL of PBSN for ∼8hrs, refreshing the solution once. They were then fixed overnight in 20mL of 4% PFA at room temperature to prevent antibody dissociation. Following fixation, samples were returned to PBSN for storage in the dark at 4°C.

Neurofilament-stained samples were preincubated in 20mL of Secondary Sample Buffer (LifeCanvas) for 6-8 hours at 37°C with gentle shaking, refreshing the solution at least once. The device chamber was filled with Secondary Device Buffer (LifeCanvas). Each neurofilament-stained sample was then loaded into a staining cup containing 9mL of Secondary Sample Buffer, 400μL of donkey serum and 80μg of CF640R-conjugated donkey anti-mouse IgG (H+L) (Biotium 20177). Electrophoresis was conducted at 90V, 400 mA and 30°C for 12 hours. The buffer in the staining cup was then refreshed, and electrophoresis continued for an additional 3 hours. This cycle was repeated to ensure uniform secondary antibody penetration and complete labelling. After staining, samples were washed in 40mL of PBSN for ∼8hrs, refreshing the solution once, and then fixed overnight in

20mL of 4% PFA at room temperature to prevent antibody dissociation. Finally, neurofilament-stained samples were stored in PBSN in the dark at 4°C.

5.2.5 Refractive Index Matching

Optical clearing of delipidated brain hemispheres was performed in a step-wise manner. First, each sample was gently shaken in 50mL of a 50/50 mix of EasyIndex (LifeCanvas Technologies) and deionised water at 37°C for 24hrs. Following this, the samples were transferred to 100% EasyIndex and incubated at 37°C for another 24 hours or until fully transparent. EasyIndex (refractive index=1.52) has a proprietary formulation; however, its original composition included diatrizoic acid, N-methyl-D-glucamine, and iodixanol in deionised water (Park et al., 2019).

Technique	Detergent-based (active)		Solvent-based (passive)
Method	Std delipidation	SDS delipidation	AdipoClear+
Preservation^{x}	7 d	7 d	N/A
Pretreatment	N/A	1 d*	9 d**
Delipidation	7 d	15 d	20 d
Labelling^{+}	**5 d**	**5 d**	**26 d**
RI matching	2 d	2 d	11 d
Total	3 w	1 m	>2 m

Table 5.1: Comparison of time required for detergent-based clearing and labelling with active electrotransport versus a hydrophobic/solvent-based technique that relies on passive diffusion. Notably, active labelling with stochastic electrotransport is at least five times faster than passive labelling (Std: standard, SDS: sodium dodecyl sulphate, d: day, w: week, m: month, RI: refractive index). ^{x}Preservation/inter-molecular fixation with SHIELD, pretreatment with hydrogen peroxide* and methanol**, $^{+}$assumes sequential immunolabelling with primary and secondary antibodies.

Table 5.1 compares the processes and time requirements of the active clearing

and labelling approach adopted here with the passive solvent-based protocol previously used. AdipoClear+, a solvent-based method, relied on passive and slow diffusion of mild, non-denaturing detergents (e.g., Triton) and organic solvents (i.e., dichloromethane and dibenzyl ether) for delipidation and refractive index matching (RI=1.56). In contrast, the active approach uses stochastic electrotransport alongside more aggressive, denaturing detergents (e.g., SDS) and aqueous solutions to accelerate clearing and labelling.

5.2.6 Light Sheet Fluorescence Microscopy

Samples were imaged using a UltraMicroscope II (LaVision BioTec), as previously described, or the UltraMicroscope BLAZE Imaging System (Miltenyi Biotec, Surrey). While the BLAZE system shares the same basic configuration as the UltraMicroscope II, with the illumination plane orthogonal to the detection axis, it offers significant advantages, including enhanced image resolution and reduced acquisition times. The key improvement is the use of three multi-immersion planar objectives with additional magnification lenses instead of a zoom body, providing superior optical quality and a longer working distance ($\leq$1.7cm instead of 0.5mm) with minimal distortions at the edge of the field of view. The BLAZE also allows for high resolution imaging of larger samples with faster throughput (e.g., up to 2 whole rat brains simultaneously), as shown in Figure 5.4, thanks to the small objective diameter and larger sample chamber (500ml as standard), which makes it easier to capture the edges of large samples without remounting.

Samples were mounted onto the BLAZE holder in sagittal orientation along the flat edge of the midline, and secured using silicon-based high temperature grease (Molykote 44 Medium) or UV-activated adhesive (BONDIC). The holder was then lowered into the imaging chamber containing CUBIC-R+

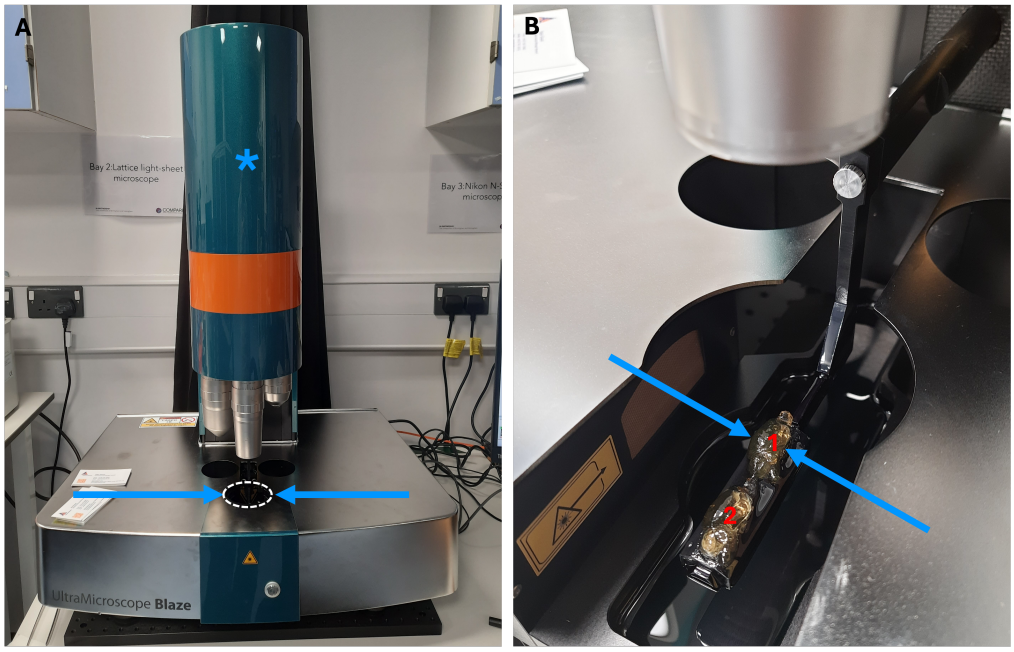


Figure 5.4: A) The BLAZE Imaging System is configured with objectives positioned orthogonally to the light sheet, as indicated by the blue arrows. The detection unit, marked with an asterisk, is fully automated, enabling seamless switching between three multi-immersion planar objectives (1.1x, 4x, and 12x) and magnification lenses. This setup is optimised for high-resolution imaging, providing a total magnification range of 0.66-30x. B) Two rat brain hemispheres (labelled 1 and 2) are mounted on a narrow holder, oriented perpendicular to the light sheet. The holder is automatically lowered into the imaging chamber, which contains a refractive index-matched imaging solution, where the samples are imaged sequentially.

(TCI Chemicals, M3294, RI=1.520) or EasyIndex-Matched Immersion Oil (LifeCanvas, RI=1.52). Imaging in EasyIndex was avoided as it evaporates, leading to a variable refractive index.

Volumetric imaging on the BLAZE system was performed using dual-sided illumination with 3 aligned light sheets. The 561nm and 640nm laser lines were used to capture autofluorescence and immunolabelling, with emission filters at 620nm and 680nm, respectively. Images were captured with a 5.5-megapixel sCMOS camera (2160 x 2560 pixels, 100fps). Depending on the desired resolution, we used either a 1.1x objective lens (0.1 numerical aperture, 17mm working distance) or a 4x objective lens (0.35 numerical aperture, 16mm working distance) with the associated dipping cap. This

setup achieved an in-plane/lateral resolution of 9.48x9.48μm or 1.62x1.62μm. The slice thickness corresponded to 6μm or 3μm, respectively.

Dynamic horizontal focusing and mosaic acquisitions were used for imaging with the 4x objective on the BLAZE microscope. This technique involves sweeping the horizontal focus across the field of view while capturing sequential image tiles along the X and Y axes, which were later stitched together. To maximise axial resolution, imaging was performed with a high numerical aperture (0.06) and a wide (70%) light sheet, producing a thin sheet optimized for a narrow field of view. Although this method is more time consuming, it offers significant advantages for imaging large samples, as the final stitched image exhibits more uniform illumination across the XY plane and improved optical sectioning in the Z-dimension.

Method	Samples				
Gd perfusion					✓
MRI				✓	✓
H_2O_2 pretreatment		✓	✓	✓	✓
Passive delipidation				✓	✓
Active delipidation	Std	SDS			
Active staining	NF-H	NF-H	MBP	MBP	NF-H
Imaging on UM2	✓		✓		
Imaging on BLAZE		✓	✓	✓	✓

Table 5.2: Summary of samples imaged using the UltraMicroscope II (UM2) and BLAZE Imaging Systems. All samples were cleared using active delipidation, either with the standard (Std) or SDS-based buffer, followed by active staining for neurofilament or myelin. Two samples had previously undergone MRI, enabling the integration of microscopy and MRI data. However, it is important to note that these particular samples had also been subjected to passive delipidation using the extended AdipoClear+ protocol and were ∼2yrs old at the time of imaging.

Images were captured using ImspectorPro software (version 7.6.2) and exported as ome-tiff files for further processing. Table 5.2 provides a summary

of the samples imaged.

5.2.7 Data Conversion and Image Processing

The images collected using dynamic focusing were stitched together using the Grid/Collection Stitching plugin (version 1.2) of ImageJ (Preibisch et al., 2009) to generate a composite image of each optical section. This process was repeated across the depth of imaging for each channel, resulting in two high-resolution 3D image stacks for each brain hemisphere. These stacks were converted to NIfTI format and processed as previously described. Processing included downsampling image volumes to an isotropic resolution and correcting sample autofluorescence for intensity inhomogeneities using the non-parametric `N4BiasFieldCorrection` algorithm (Tustison et al., 2010). The bias field estimates from the autofluorescence images were used to correct the corresponding immunolabelling images.

5.2.8 Structure Tensor Analysis

Structure tensor analysis (STA) is a form of image texture analysis that uses intensity gradients to estimate features, such as structural orientation. The original implementation (Budde and Frank, 2012; Budde and Annese, 2013) was extended from 2D histological sections to 3D image volumes (Khan et al., 2015) acquired using confocal or two-photon microscopy (Schilling et al., 2016; Costantini et al., 2021).

3D STA involves first computing the direction-dependent spatial derivatives (i.e., gradients of image intensity) at each point *(x, y, z)* in an image volume *I(x, y, z)*. A common method of computing spatial derivatives involves first convolving/filtering the image with a Gaussian kernel. Varying the

width σ_g (i.e., standard deviation) of this kernel varies the length-scale used for computing the spatial derivatives and offers a smoother numerical differentiation than simply using finite differences. These provide an image gradient vector $\nabla I = [I_x, I_y, I_z]$, where $I_x = \partial I/\partial x$, $I_y = \partial I/\partial y$ and $I_z = \partial I/\partial z$.

The structure tensor *S(x,y,z)* is a symmetric positive-definite 3x3 matrix that represents the covariance of the partial derivatives of the image intensity. I.e:

$$S = \begin{bmatrix} I_x^2 & I_{xy} & I_{xz} \\ I_{xy} & I_y^2 & I_{yz} \\ I_{xz} & I_{yz} & I_z^2 \end{bmatrix} \tag{5.1}$$

where in practice the covariance entries S_{ij} are spatially averaged over a neighbourhood N using a Gaussian filter σ_N (Köthe, 2003). This is done for robustness against noise, but also for making S sensitive to 3D features (rather than 1D).

The eigen-decomposition of the tensor S defines an ellipsoid that provides information on structural boundaries. The axes of this ellipsoid are scaled by the eigenvalues, and their orientations are defined by the eigenvectors. The eigenvector corresponding to the largest eigenvalue will indicate the direction of largest intensity change in the image (i.e., at boundaries and edges), while the eigenvector corresponding to the smallest eigenvalue, representing the direction of minimal intensity change, aligns with the orientation of the primary structure, such as a fibre bundle. This holds true when the neighbourhood N is sufficiently large relative to the radius of curvature of the structural feature being analysed. If N is too small, the fibre bundle will appear locally planar, leading all gradient vectors to align in a similar direction. In general, if N spans the entire cross-section of a

fibre bundle, the third eigenvector should accurately reflect the bundle's orientation.

Various hyper-parameters, such as σ_g, σ_N and N, need to be tuned for each dataset based on the size of the structures of interest and the levels of noise. These properties will be dependent on the stain used and the image resolution.

To explore whether STA was able to accurately extract measures of fibre orientation from autofluorescence signal, or if white matter staining was required, we tested it on images acquired from 60μm sagittal rat brain sections. These sections were prepared using glycerol, which enhances myelin autofluorescence (Costantini et al., 2021), and stained with an MBP antibody.

First, free-floating tissue sections underwent overnight fixation in 4% PFA, followed by sequential overnight incubations at 4°C in 10% and 20% glycerol (Honeywell 49770) in a solution of 2% dimethyl sulfoxide (DMSO, Tocris 3176) and 4% PFA. Before staining, sections were permeabilised overnight in PBS containing 10% bovine serum albumin (BSA, Fisher Scientific BP9702-100), 0.5% Triton (Sigma-Aldrich, X100) and 10% DMSO. They were then incubated for three days with a rabbit monoclonal anti-MBP antibody (Cell Signalling Technology 62596SF, 1:500) diluted in PBS with 2% BSA, 0.1% Triton, 5% DMSO, and 0.3M glycine (Sigma-Aldrich, G7126). After four 5 minute PBS washes, sections were incubated for 24 hours in goat anti-rabbit AlexaFluor 546 (Invitrogen A11010, 1:500) diluted in PBS with 2% BSA, and 0.1% Triton. Following final PBS washes, sections were mounted on gelatinised slides and coverslipped using Vectashield hardset aqueous mounting medium (Vector Labs, H-1400-10). 2D images were acquired using a Zeiss LSM Exciter microscope with a 10x objective and then analysed

used 2D STA.

We then applied STA to 3D images of a cleared rat brain hemisphere acquired via light-sheet microscopy, as described above, since this approach has not been previously explored.

5.2.9 Registration of Microscopy to MRI

Rat	Gd	Clearing protocol	3D light-sheet microscopy		MRI data used for registration		
					Site	Anatomical	Diffusion
7	N	SDS-based	autofluorescence	MBP	Oxford	3D-RARE	2D-EPI
8	Y	SDS-based	autofluorescence	NF-H	Oxford	3D-RARE	3D-EPI

Table 5.3: Summary of 3D light sheet microscopy and 3D MRI data used to test co-registration. The microscopy data (10x10x6μm) was acquired from a single brain hemisphere whereas MRI data (100-200μm isotropic) was whole brain.

Table 5.3 summarises the 3D microscopy and MRI data available from the same rodent brains. To align anatomical structures common to the microscopy images and MRI scans, we used the methods described in Chapter 4. In brief, the tools `FSL-FLIRT` and `ANTs` were used to calculate the linear transformation and non-linear warp required to align the autofluorescence channel with the MRI contrast (Avants et al., 2011). The optimal warp was then applied to the stained channel.

5.3 Results

This section presents the impact of sample preparation, novel tissue preservation techniques, and active electrotransport on optical clearing and staining of rat brain hemispheres, using images captured with 3D light sheet microscopy. These findings are contrasted with those obtained using the

solvent-based AdipoClear+ method. In addition, it compares how active delipidation with two different detergent-based buffers affects sample integrity, transparency, and white matter staining. The section also demonstrates how immunolabelling of myelin and neurofilament can be accelerated using stochastic electrotransport. Finally, it presents evidence supporting the potential of active techniques for validating MRI-derived microstructural measures, such as fibre orientation.

5.3.1 Optimisation of Sample Preparation

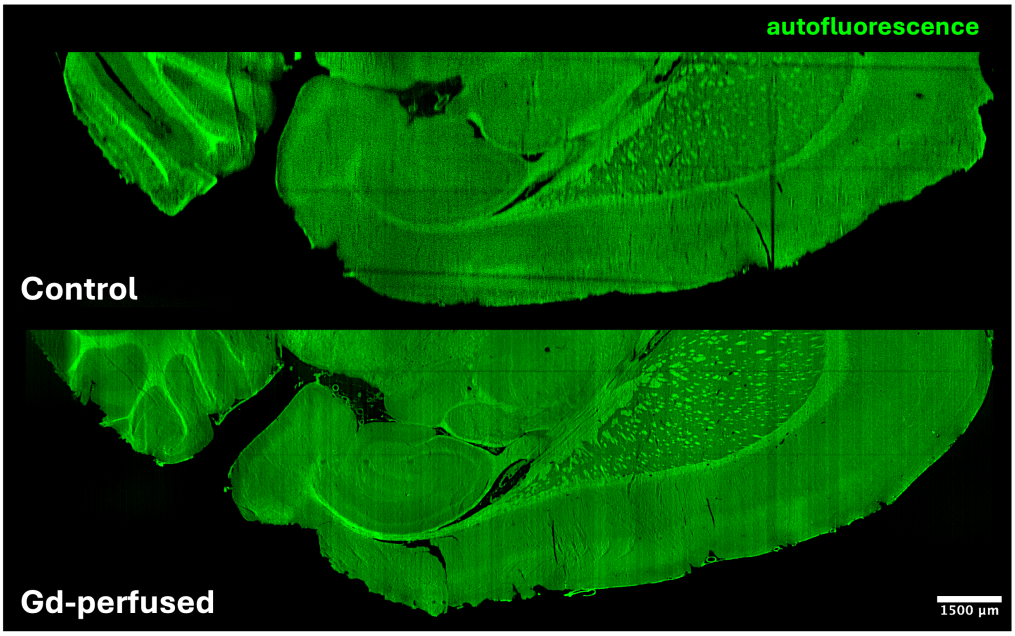


Figure 5.5: Active clearing with an SDS-based buffer resulted in similar levels of transparency in control samples (top) and those prepared with gadolinium contrast (bottom). The autofluorescence signal was also comparable. The images display horizontal sections of the cleared rat brain hemispheres.

Including gadolinium contrast in the perfusate solution during sample preparation did not adversely affect tissue clearing and sample autofluorescence, as shown in Figure 5.5. This demonstrates that this active approach for optical clearing and detergent-based delipidation are compatible with the use of gadolinium contrast to enhance the signal-to-noise ratio in *ex vivo*

MRI. The methods described in this chapter can therefore be integrated into a pipeline for conducting both MRI and light sheet microscopy on the same rat brain.

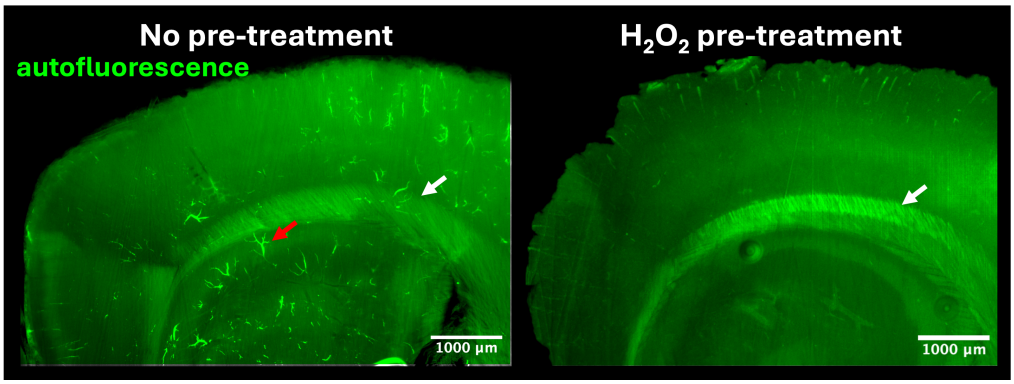


Figure 5.6: A 200μm maximum intensity projection (left) demonstrates the extent of autofluorescence in blood vessels (red arrow) in unbleached samples. Pre-treating rat brain hemispheres with an overnight incubation in 5% hydrogen peroxide (right) fully removed this source of autofluorescence. These images show a lateral sagittal view of a rat brain hemisphere with the corpus callosum indicated (white arrow).

Overnight incubation of rat brain hemispheres in 5% hydrogen peroxide significantly reduced the autofluorescence signal from blood vessels, as shown in Figure 5.6. This suggests that residual blood remained in the brain vessels, despite the use of heparinised PBS during transcardial perfusion. Importantly, this hydrogen peroxide pre-treatment did not destroy the targeted epitope, as demonstrated in Section 5.3.4.

5.3.2 Tissue Preservation and Processing

Figure 5.7 illustrates the changes in appearance, integrity, and size of a mouse brain during the application of novel tissue preservation and processing techniques. These changes are consistent with those observed in a rat brain hemisphere (not shown). SHIELD preservation had minimal impact on the sample's size and appearance. After active delipidation with the standard buffer, the brain became translucent and exhibited minor

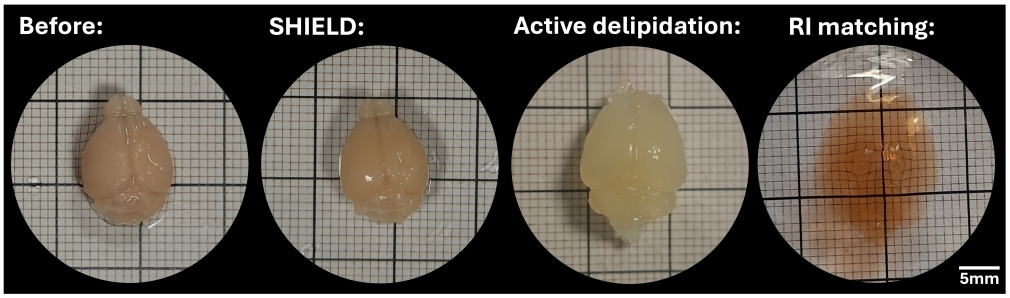


Figure 5.7: Active clearing in the rodent brain. These images show how the appearance of a mouse brain changes during active clearing and are provided for context. We adapted this protocol for rat brain hemispheres and observed similar changes. The protocol consists of STEP 1: inter-molecular fixation using SHIELD, STEP 2: active delipidation with the standard buffer, and STEP 3: refractive index (RI) matching. SHIELD fixation preserves tissue integrity without visibly altering the sample. After delipidation, some sample expansion occurs, and full transparency is achieved following RI matching.

expansion, contrasting with the significant shrinkage caused by dehydration in solvent-based protocols like AdipoClear+. Following delipidation, optical clearing in a refractive index-matched aqueous solution rendered the sample completely transparent. The entire process for a rat brain hemisphere takes 16 days, compared to 40 days for passive delipidation and RI matching using the extended AdipoClear+ protocol.

Figure 5.8 shows the differences in autofluorescence contrast between samples cleared using the AdipoClear+ protocol and those cleared with active delipidation using an SDS-based buffer. This comparison highlights how the method of lipid extraction — whether through organic solvents or aggressive anionic detergents — affects the overall fluorescence profile of the entire sample and its cellular structures. The figure also highlights the effects of dehydration in solvent-based protocols like AdipoClear+, evident when comparing sample volume and ventricle size with the active detergent-based approach. While sample hardening in AdipoClear+ minimises surface damage, SDS-based delipidation softens the tissue, which can increase fragility.

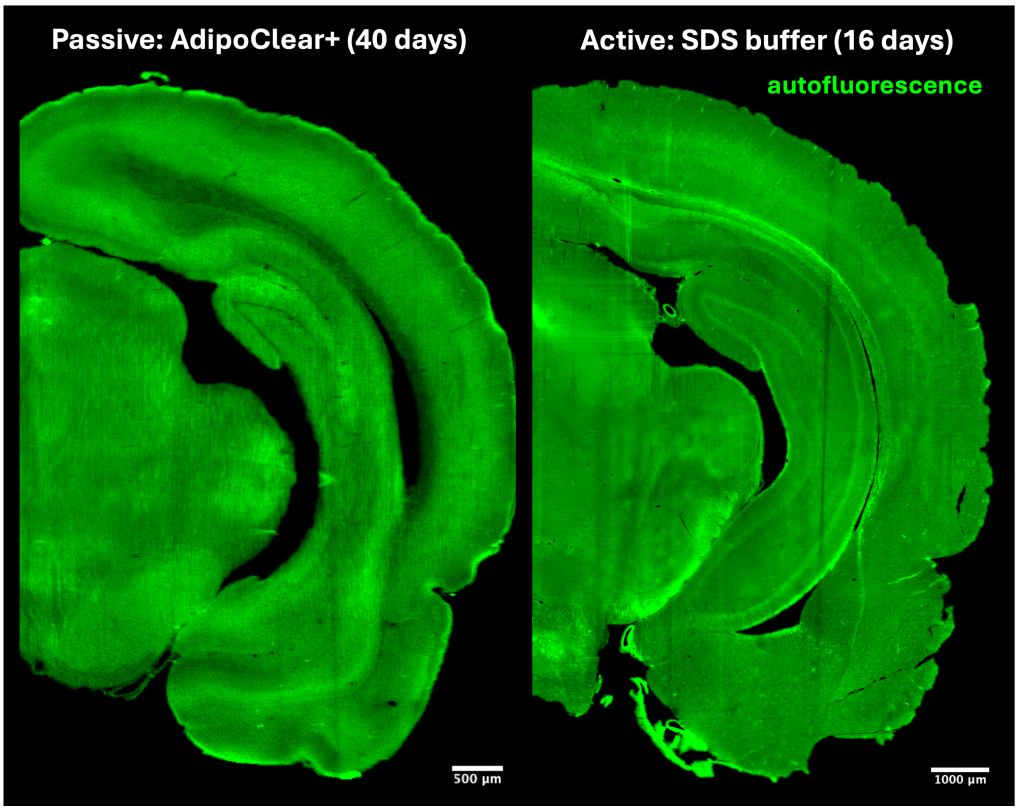


Figure 5.8: Autofluorescence of rat brain hemispheres cleared using two different protocols: the extended AdipoClear+ protocol (left), which took 40 days, versus active delipidation with an SDS-based buffer (right), achieved in 16 days. Both images present a coronal view of the rat brain hemispheres under 561nm illumination. Please note the different image scales.

5.3.3 Optimising Active Delipidation

Figure 5.9 shows the effects of 10 days of active delipidation with an SDS-based buffer on a rat brain hemisphere. Although SDS-based delipidation did lead to sample softening, minor expansion, and some loss of integrity, the hemisphere was robust enough to proceed with immunolabelling and microscopy.

Active delipidation with the SDS-based buffer took at least twice as long as using the standard buffer (15 versus 7 days). However, this method is still 25% faster than passive delipidation with the extended AdipoClear+ protocol (20 days). In addition, active delipidation is significantly less

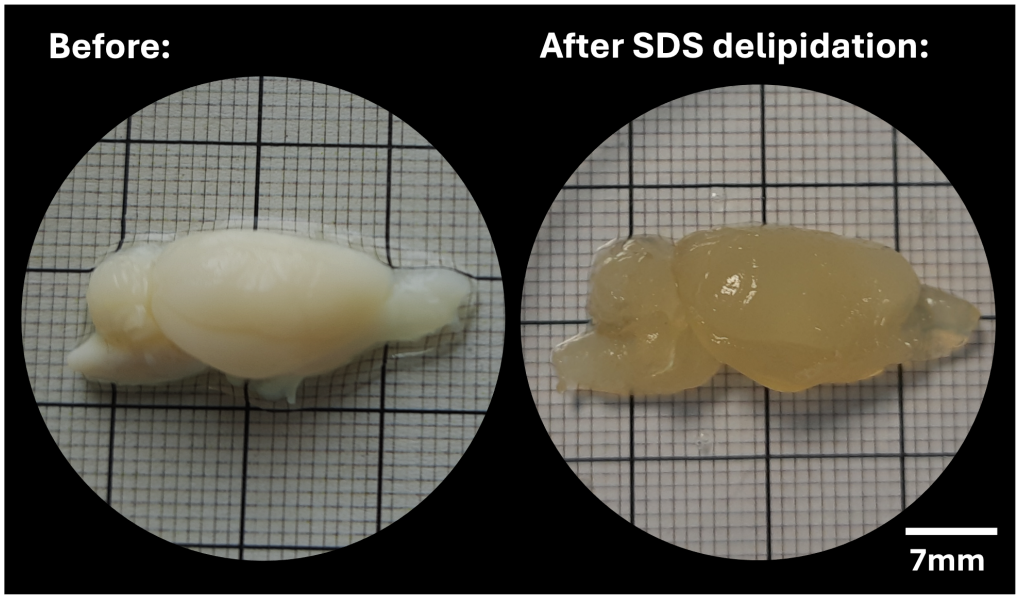


Figure 5.9: A rat brain hemisphere before (left) and after (right) 10 days of active delipidation with an SDS-based buffer. Post-delipidation, the sample became translucent, slightly swollen, and showed some alterations in shape.

labour-intensive, as the SmartBatch+ device is fully automated and only requires a solution change every 2 days. In contrast, the AdipoClear+ protocol can require up to 7 solution changes per day.

5.3.4 Optimising Active Immunolabelling

Figure 5.10 demonstrates that stochastic electrotransport and eFLASH effectively reduce surface depletion and enhance antibody penetration. This is achieved by modulating binding affinity and significantly accelerating antibody dispersal. Active immunolabelling for MBP was completed in just 18 hours, with the primary and secondary antibodies delivered simultaneously, and required only 20μg of primary antibody. In contrast, passive labelling with the AdipoClear+ protocol requires 5-8 day incubations (Branch et al., 2021), with primary and secondary antibodies delivered sequentially, and requires 45μg of primary antibody. Overall, the active approach reduces the total staining time, including pre-incubations, fixation, and washing, to

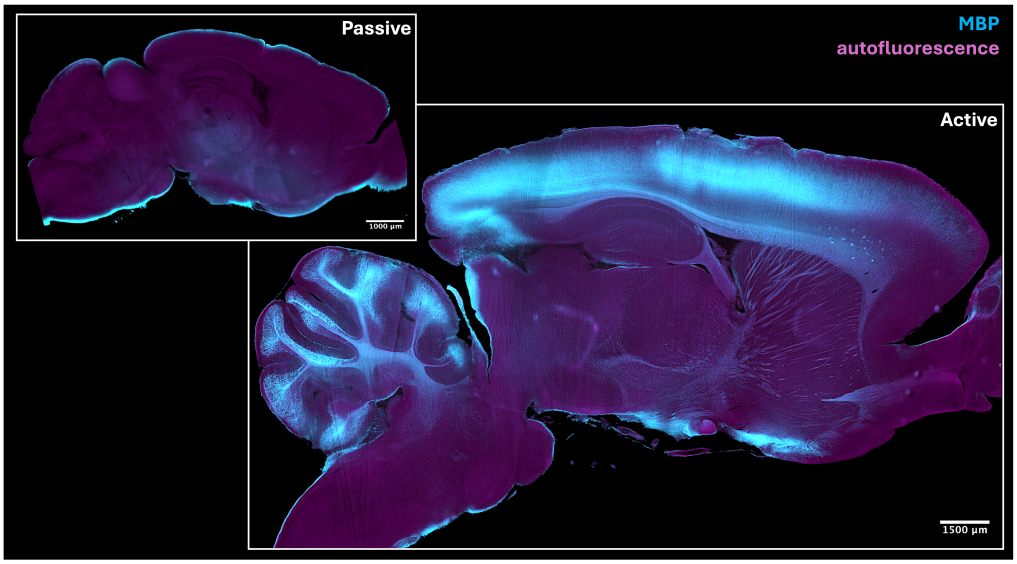


Figure 5.10: Stochastic electrotransport and eFLASH significantly improve antibody penetration and reduce surface depletion. The larger image shows fluorescence after active labelling with the MBP antibody following SDS-based delipidation, while the smaller image depicts results from passive immunolabelling using the extended AdipoClear+ protocol. In both cases, the logarithm of intensity values is used for the stained channel (cyan). It is important to note that this figure does not present a direct comparison, as the protocols used to generate the images differ. Instead, it is intended to illustrate how the challenge of labelling large, lipid-dense samples can be addressed.

3 days, compared to 2-3 weeks for passive diffusion.

Although myelin labelling in the core of the rat brain hemisphere was not achieved, the combination of stochastic electrotransport and eFLASH techniques enabled deep penetration of the myelin antibody into the cortex. Figure 5.11 shows that myelin staining was relatively uniform across the cortex and reveals the myelin distribution within the grey matter in detail. Active MBP staining highlights the lamination pattern and intricate intracortical myeloarchitecture, with most fibres running vertically between cortical layers, alongside clear evidence of arborisation and horizontal branching.

Active electrotransport also enabled uniform labelling of the cerebellum, as shown in Figure 5.12. In contrast, the AdipoClear+ protocol resulted in

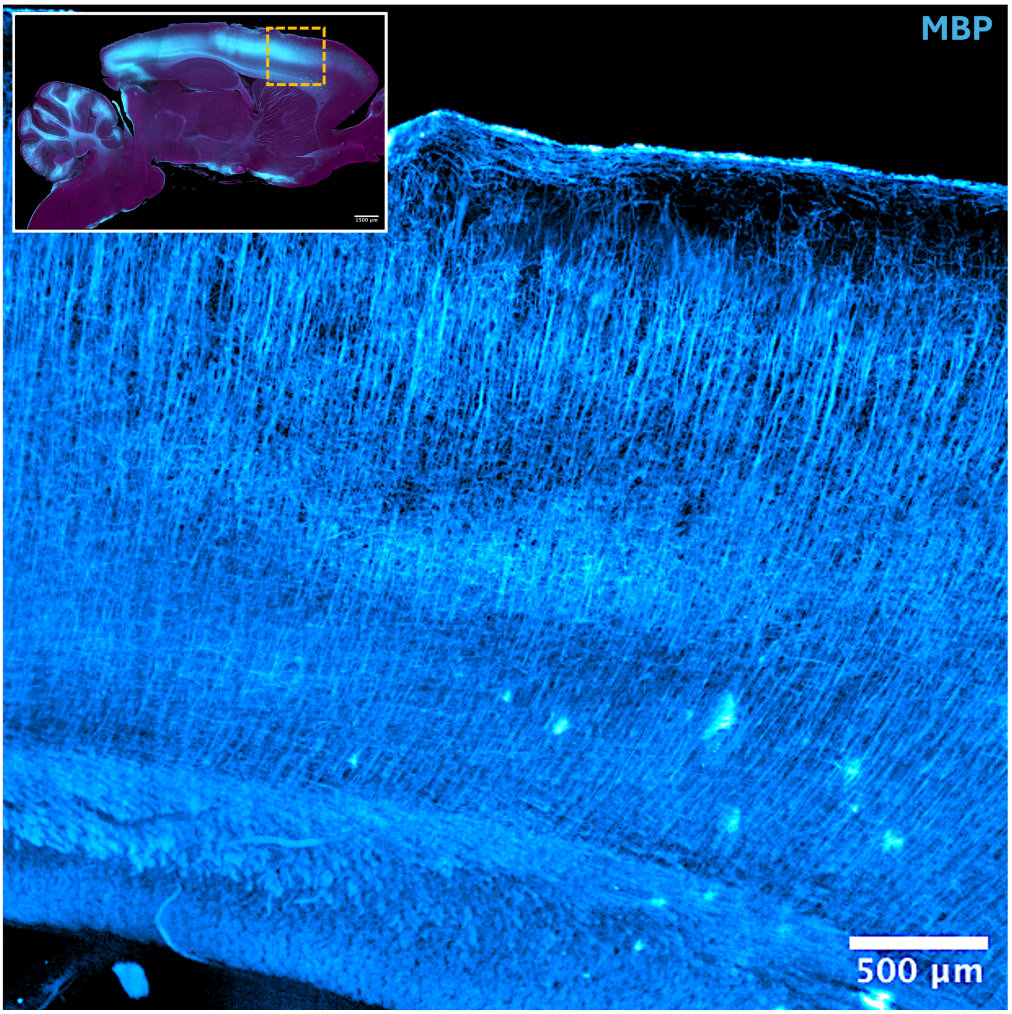


Figure 5.11: A high magnification view of the cortex, shown as a maximum intensity projection over 50μm, demonstrates the level of microstructural detail that can be obtained with active labelling of myelin. The entire immunolabelling process, including pre-incubations, fixation, and washing, took only 3 days.

limited antibody penetration, with myelin staining limited to surface regions of the cerebellum. Increasing the antibody concentration in AdipoClear+ did not improve penetration, demonstrating the limitations of labelling with passive diffusion.

Figure 5.13 shows high-magnification images of the cerebellum, comparing passive and active immunolabelling with the MBP antibody. This provided clear visualisation of individual fibres, showcasing the enhanced resolution achieved with this method. The preservation of sample size during the

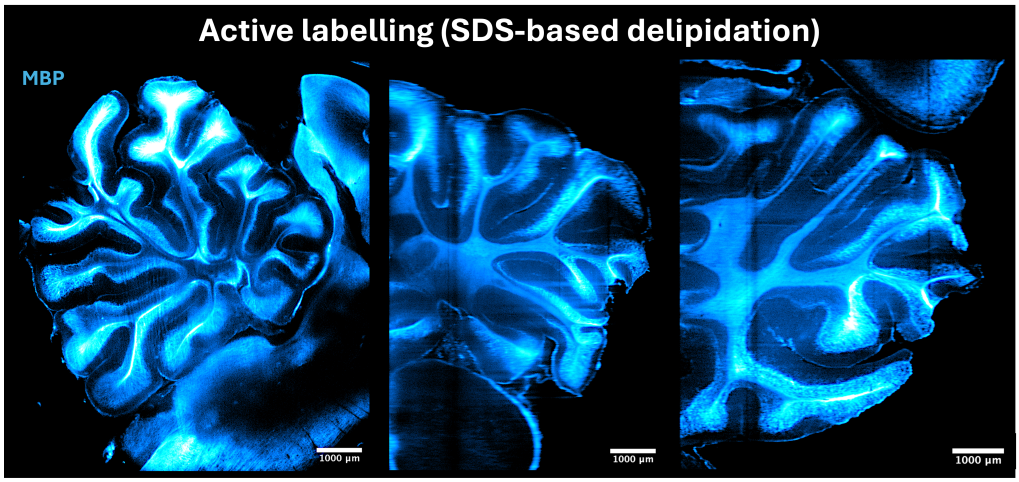


Figure 5.12: Stochastic electrotransport and eFLASH ensures complete and uniform labelling of myelin in the cerebellum when using SDS-based delipidation. The logarithm of intensity values is displayed. These images were captured on the BLAZE microscope using the 1.1x objective.

active protocol likely contributed to the observed level of detail. In contrast, the extended AdipoClear+ protocol resulted in significant shrinkage and some non-specific staining. Additionally, antibody penetration was limited to superficial layers (e.g., close to the flat face of the hemisphere), with deeper sections of the cerebellum showing incomplete staining.

Figure 5.14 demonstrates how active delipidation with an SDS-based buffer for $\geq$10 days significantly enhances sample clarity and the signal-to-noise ratio, in a different stain using NF-H antibody. In comparison, standard delipidation buffers used for 6 days failed to eliminate all optical inhomogeneities, leading to increased scatter artefacts. Additionally, the SDS-based method produced a more uniform neurofilament staining profile and more complete labelling of structures. Figure 5.14 also demonstrates how the advanced optics of the BLAZE microscope have resulted in a more consistent illumination profile, improved optical sectioning, and higher image quality.

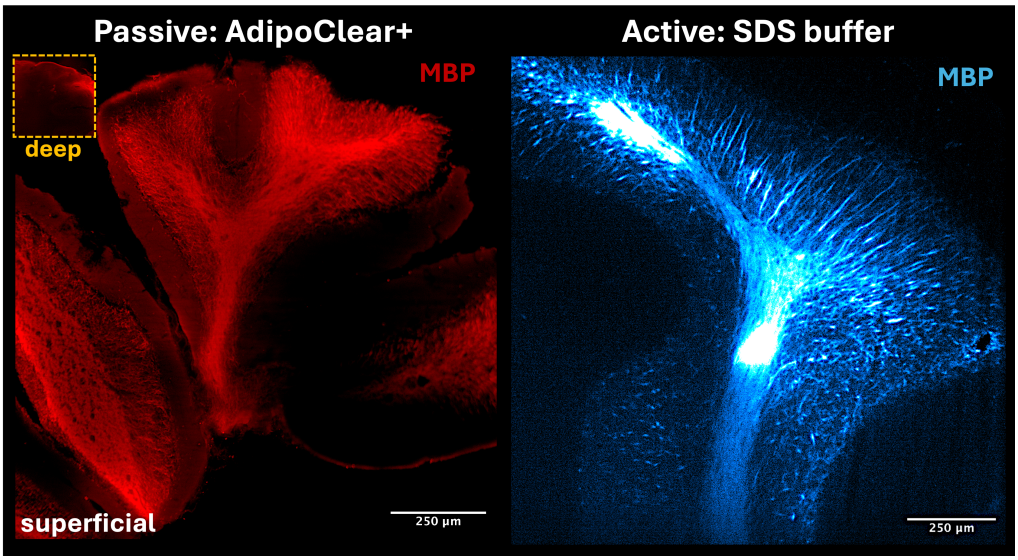


Figure 5.13: Comparison of passive (left) versus active (right) MBP labelling in the cerebellum of cleared brain tissue, imaged at high magnification. Passive labelling using the AdipoClear+ protocol resulted in significant shrinkage and some non-specific staining, with incomplete antibody penetration into deeper layers of the cerebellum, as highlighted in the inset. In contrast, active immunolabelling with SDS-based delipidation enabled clear identification of individual fibres. The logarithm of intensity values is displayed. Images were captured using the UltraMicroscope II (left) or BLAZE imaging system (right) at high magnification.

5.3.5 Structure Tensor Analysis and Comparison to MRI

To determine if the autofluorescence signal could be used to accurately estimate fibre orientation, we applied structure tensor analysis (2D) to high-magnification images of autofluorescence and myelin staining in the striatum. These images were obtained from thin sections of rat brain prepared using a protocol that enhances myelin autofluorescence (Costantini et al., 2021) and stained with an MBP antibody. As shown in Figure 5.15, myelin staining, which offered better contrast, yielded less noisy estimates of fibre orientation and higher precision (i.e., lower dispersion). This finding underscores the importance of developing protocols for white matter staining in the intact brain to accurately measure fibre orientation.

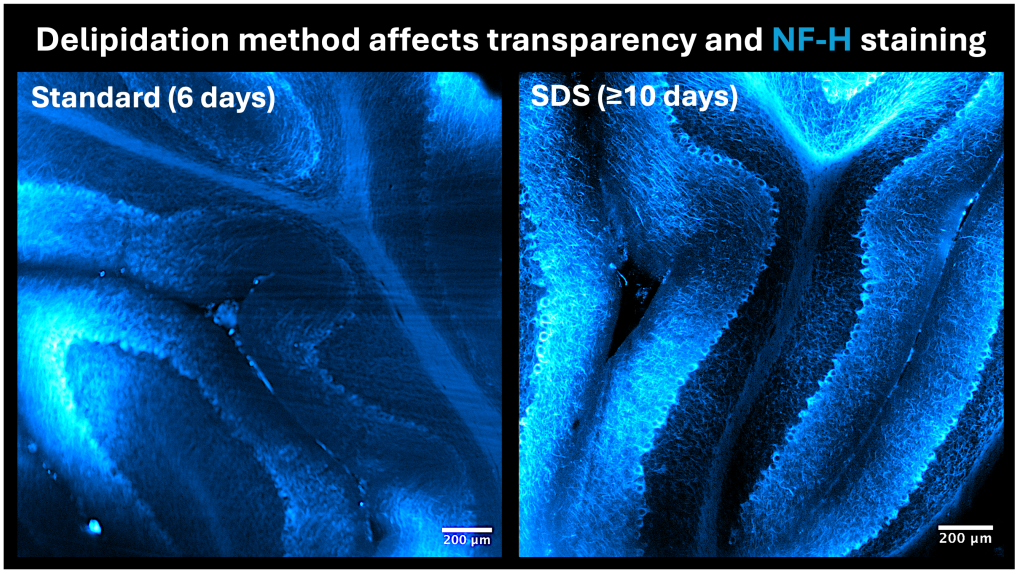


Figure 5.14: SDS-based delipidation enhances optical transparency and the signal-to-noise ratio for immunostaining. The images presented here display the logarithm of intensity values for NF-H staining in the cerebellum of a rat brain hemisphere at high magnification, comparing standard delipidation buffers (left) with SDS-based depilidation (right). The images were acquired using the Ultramicroscope II and BLAZE, respectively.

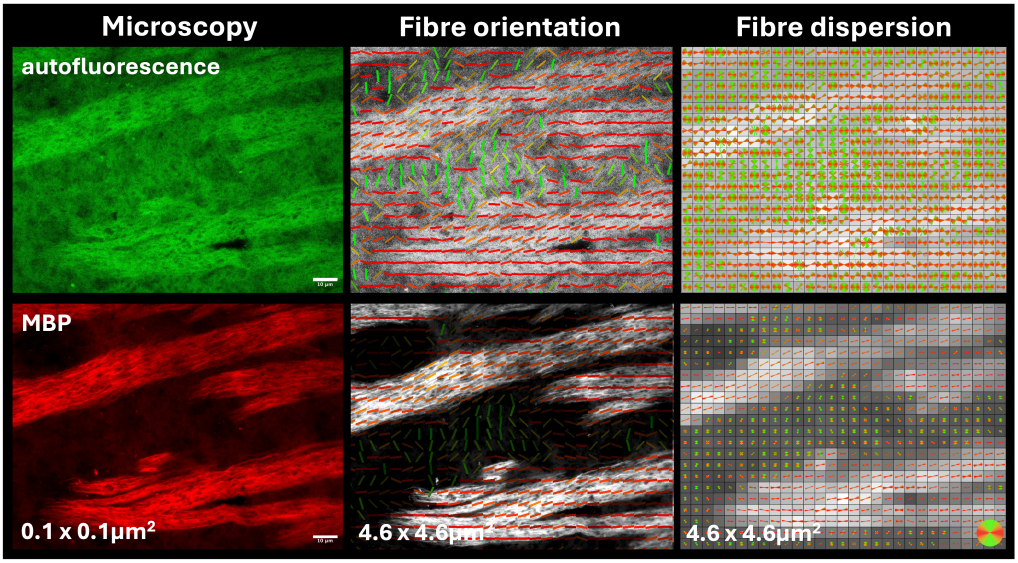


Figure 5.15: Comparison of fibre orientation and dispersion estimates derived from autofluorescence signal (top) and myelin-staining (bottom) in the striatum. The autofluorescence-based estimates are noisier and less distinct compared to the clearer and more defined fibre orientations seen with the myelin-stained image. The images show a high magnification view (scale bar 10μm) of a 60μm thick sagittal section from the rat brain. Fibre orientations and dispersions are reported in a downsampled grid with a resolution of 4.6 x 4.6μm^2.

Structure tensor analysis (2D) of myelin staining in the cerebellum of a passively cleared brain hemisphere provided fibre orientation estimates that align with the stained structures, as shown in Figure 5.16.

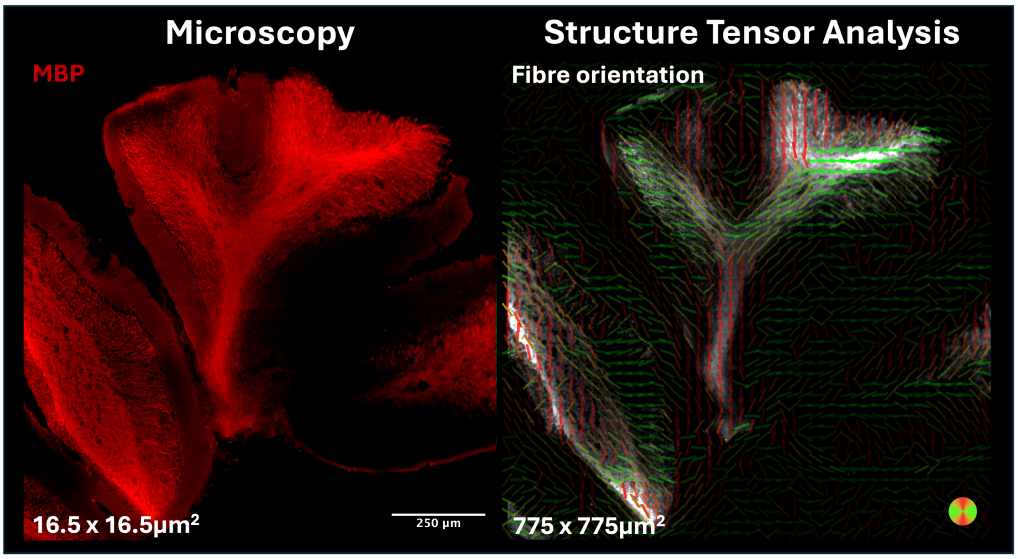


Figure 5.16: Structure tensor analysis (2D) of myelin staining (16.5μm resolution) in the cerebellum of a passively cleared brain hemisphere provided estimates of fibre orientation in the cerebellum that align with the stained structures. Fibre orientations are shown at a resolution of 775μm for ease of visualisation.

Figure 5.17 shows the autofluorescence signal from an actively cleared brain hemisphere, overlaid with the primary eigenvector (i.e., preferred diffusion orientation) from the diffusion tensor model. In this case, a linear transformation with 12 degrees of freedom was able to align the MRI contrast with the autofluorescence signal. This demonstrates the effectiveness of the sample preservation and active clearing protocols in maintaining the sample's volume and morphology. Once structure tensor analysis is fully implemented in 3D, we will be able to directly compare the orientations derived from MRI with the estimates obtained from structure analysis of the microscopy images.

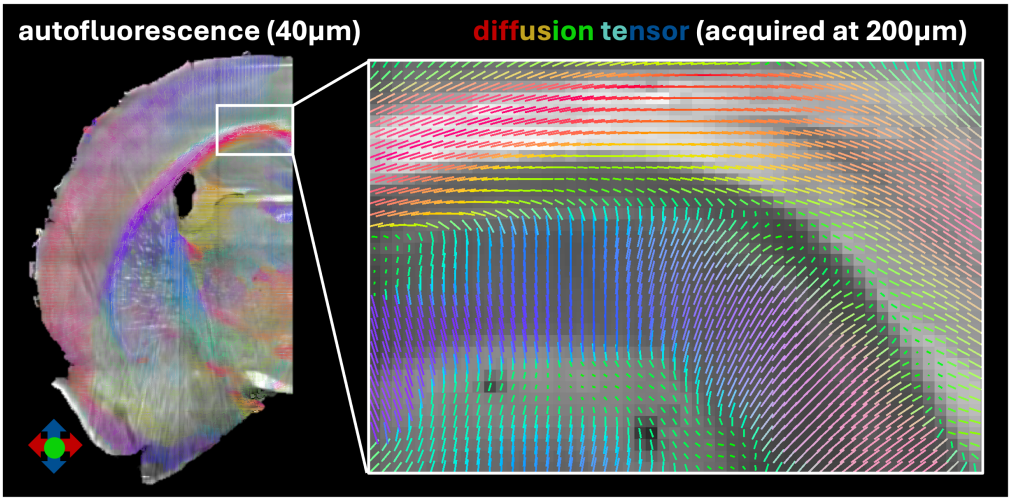


Figure 5.17: After co-registering the MRI and autofluorescence signal from the same sample, we can compare the fibre orientations derived from diffusion tensor imaging (DTI) with the intrinsic contrast of the tissue. In this example, we present a coronal section of a brain hemisphere that was actively cleared using SDS-based delipidation. The primary eigenvector, obtained from fitting the diffusion tensor, shows good alignment with the autofluorescence signal. For visualisation purposes, the 3D microscopy image is shown with a resolution of 40μm.

5.4 Discussion

We successfully adapted and developed novel active clearing techniques from the mouse brain to the larger, more lipid-dense rat brain. This involved extending the SHIELD preservation and active detergent-based delipidation protocols to ensure the protection of tissue architecture, retention of key biomolecules, preservation of structural integrity, and complete lipid extraction in the rat brain. This approach has been shown to preserve sample volume significantly better than solvent-based AdipoClear+ method. In addition, we demonstrated that these active clearing methods are compatible with gadolinium contrast, facilitating their integration with MRI.

Combining tissue clearing with staining in large, intact samples has been a major challenge, particularly for abundant targets like myelin and neurofilament. Here, we extended advanced immunolabelling techniques to

the larger rat brain, demonstrating that an active staining approach, incorporating stochastic electrotransport and eFLASH, significantly enhances the efficiency and effectiveness of immunolabelling. Antibody penetration was significantly improved, achieving labelling of MBP and NF-H within just 3 and 7 days, respectively, using only 20 or 40μg of antibody. This active approach not only accelerated the staining process but also increased signal intensity, enabling the visualisation of individual fibres with minimal non-specific background. In contrast, passive staining methods, such as those employed in the AdipoClear+ protocol, resulted in poor antibody penetration, higher levels of non-specific binding, and long incubation periods, usually spanning several weeks.

We tested two different delipidation buffers to identify an active clearing method which achieves optical transparency, uniform antibody penetration, and low levels of non-specific binding. Our findings demonstrated that active delipidation using SDS-based buffers significantly enhanced sample clarity and enabled more complete neurofilament labelling with higher signal levels. However, this method was more time consuming (requiring $\geq$10 days for delipidation plus 3 days for washing) and reduced sample integrity. In contrast, active clearing with standard buffer was completed in just 6 days, without noticeable changes in sample integrity, but it failed to eliminate all optical inhomogeneities and staining appeared less complete. These results underscore the interdependency of processes in active labelling protocols and the trade-offs involved.

Although we were unable to label myelin or neurofilament in the core of the rat brain hemisphere, we successfully achieved uniform and complete staining in the cerebellum and cortex. This outcome highlights the potential of our approach for high-resolution imaging of microstructure in the intact brain. Further optimisation of key parameters involved in active

delipidation and active labelling - such as antibody, detergent, and bile salt concentrations; pH; temperature; duration; electric field strength; and fixation - alongside fine-tuning of the diffusion-reaction kinetics, could enhance antibody penetration and improve staining consistency. Additionally, antibody fragments, small-molecule dyes, nanobodies, and custom probes may provide more effective alternatives for labelling of dense structures in large samples (Cai et al., 2023; Kanatani et al., 2024; Meslier et al., 2024). This area remains largely unexplored, particularly in the context of the rat brain and white matter staining, presenting opportunities for further methodological advancements.

By adopting the SmartBatch+ device and adapting protocols for use with rat brains, we have ensured that we can automate the processing and staining of up to 4 rat brains (or 12 mouse brains) simultaneously with minimal labour. This change has reduced the overall processing time — from fixation to imaging — to just one month, which is at least 50% faster than the extended AdipoClear+ protocol. Unlike the labour-intensive AdipoClear+ method, which involves handling hazardous chemicals, this detergent based method for active clearing and labelling is both safer and more efficient, yielding superior results. Furthermore, the standardisation of methods and reagents, along with precise control over key conditions such as temperature, electric field strength, and current, has significantly improved reproducibility.

Integrating tissue preservation and active labelling techniques with MRI represents a significant advancement in validating microstructural imaging measures, providing deeper insights into the brain's complex architecture. By extending these techniques to the larger rat brain, we have expanded opportunities for validation to more experimental contexts. Unlike AdipoClear+, this new approach preserves sample size which means that even linear transformation can successfully align 3D microscopy images with MRI. The

preservation of sample size also allows for visualisation of smaller structures (e.g., individual fibres) with greater contrast.

We demonstrated how 2D structure tensor analysis of microscopy data provides measures of microstructure, such as fibre orientation. While we demonstrated STA's application with MBP staining, this versatile technique can be applied to other forms of microscopy and staining methods (Schurr and Mezer, 2021). We also demonstrated that STA on the non-stained autofluorescence images returned valid fibre orientations in the striatum, albeit with lower precision than in the stained samples. In future, we plan to fully implement structure tensor analysis (STA) in 3D light sheet microscopy.

By combining MRI with active staining and STA, we will be able to conduct independent validation of microstructural measures within the same sample. STA's ability to analyse structures in 3D will allow for the extraction of multiple principal axes from a single image, a significant improvement over traditional techniques that only capture structures orthogonal to the tissue section. This 3D capability is critical for studying brain regions with substantial heterogeneity in fibre orientation (e.g., centrum semiovale).

5.4.1 Limitations and Future Extensions

Despite successfully clearing and immunolabelling rat brains that had previously undergone MRI, and co-registering MRI acquisitions with whole-brain light sheet microscopy data from the same samples, we have yet to perform any quantitative analysis. Below, we outline the reasons for this, along with the quantitative approaches we plan to use for multimodal and cross-scale comparisons.

The sheer volume of data generated by high-resolution light sheet fluorescence microscopy, which can amount to several terabytes for a single rat brain hemisphere, has been a significant bottleneck in this work. Analysing such large datasets and drawing reliable conclusions within a reasonable time frame poses a significant challenge. This issue is compounded by the current lack of advanced tools for efficient data visualisation and processing. Moreover, there is a critical need for automated detection methods that can accurately recognise and correct imaging or clearing artefacts, while also quantifying features, such as cells, based on phenotype or morphology. Without these advances, the full potential of these powerful datasets will remain unrealised.

The computational efficiency of 3D STA offers a potential solution to the challenges of processing such large volumes of data, but it has previously been limited to confocal and two-photon microscopy (Schilling et al., 2016; Costantini et al., 2021). These modalities offer isotropic or near isotropic resolution but are often slow and restricted to small samples. Extending 3D STA to light sheet microscopy data presents exciting opportunities to explore the complex microstructure of intact organs (e.g., the brain). However, it also presents significant challenges as light sheet microscopy has a lower axial resolution, determined by the thickness and shape of the excitation light sheet(s), compared to its lateral resolution, which depends on the numerical aperture, magnification, and effective camera pixel size in the detection path. This anisotropy can distort structure tensor calculations and other forms of quantitative multiscale analysis, which rely on accurate local gradients.

Additionally, uneven illumination, optical aberrations (spherical and chromatic), scattering artefacts, and mosaic acquisitions can introduce intensity variations that further complicate tensor-based analysis. Characterising the

point spread function (PSF) in 3D light sheet microscopy is a crucial first step in addressing these issues. Following the methods described in Aakhte et al. (2025), we plan to embed sub-resolution fluorescent silica beads in RI-matched agarose gel and image them using the same parameters (i.e., laser wavelength and intensity, sheet thickness and width, number of sheets, magnification factor, step size, etc) as our cleared samples. Accurate PSF measures in x, y and z will enable us to correct distortions and resample the data to achieve isotropic resolution before performing 3D STA.

Once the challenges of implementing 3D STA on light sheet microsocopy are addressed, we will use FSL's `vecreg` tool to transform STA-derived fibre orientation maps into MRI space while preserving directionality. To evaluate the agreement between STA- and DTI-derived orientation maps, we will compute cosine similarity (0 = no alignment, 1 = perfect alignment) and angular error (0°= identical orientations, 90°= perpendicular orientations). These metrics will be visualised in 3D or averaged across specific regions to highlight areas where the microscopy- and MRI-based fibre orientation estimates converge or diverge. Similar approaches can also be applied to compare fibre dispersion and anisotropy (Schilling et al., 2018).

The methods outlined above could be applied in a longitudinal study using a rat model of injury or disease to evaluate whether dMRI can accurately: a) detect early signs of axonal degeneration; b) differentiate healthy regions (i.e., no evidence of damage) from those with axonal degeneration; c) monitor changes in fibre integrity and orientation over time to identify regional vulnerability; and d) assess recovery or the impact of therapeutic interventions. Furthermore, these methods could contribute to refining dMRI acquisition sequences, computational models, and analysis techniques to maximise alignment and accuracy.

5.4.2 Contributions

Dr Brian Nguyen (LifeCanvas Technologies) and Dr Michelle Bedenbaugh (Vanderbilt University) provided an introduction to active clearing and labelling techniques in the mouse brain and advice on applying these methods to the rat brain. Dr Jak Grimes (Miltenyi Biotec, Surrey) and Dr Joao Correia (University of Birmingham) provided guidance on optimising parameters for the optical imaging of samples. Dr Jak Grimes also acquired the data shown in Figure 5.12 using our sample. My personal contributions to this project include: conceptualisation and project lead; protocol development; tissue collection, processing and staining; microscopy data acquisition and processing; structure tensor analysis of microscopy images; analysis and presentation of results; and manuscript writing, editing and review.

Chapter 6

Conclusions & Future Directions

6.1 Main Contributions

The rapid advancement of sophisticated bioimaging techniques, such as dMRI and light sheet microscopy, is revealing the brain's astonishing complexity and diversity. However, integrating information across different scales and techniques remains a significant challenge. This difficulty arises from the inherent limitations of each imaging modality and the complexities of developing methods and datasets that are compatible and comparable. Overcoming these technical and scientific barriers is essential for gaining a more comprehensive understanding of brain anatomy and function, as well as for exploring how neural circuits contribute to complex behaviours and cognitive processes.

This thesis introduces a cross-resolution, multimodal whole-brain imaging framework for the rat, integrating MRI with 3D light sheet microscopy.

Unlike previous studies focused on the mouse brain or small tissue samples, the rat brain poses unique challenges: it is four times larger than the mouse brain and contains more myelin, making it difficult to clear for 3D microscopy. Additionally, pre-clinical MRI methods for the rat are not well-established or validated, necessitating the development of new protocols tailored to this species. By addressing these challenges, this thesis advances the field of rodent brain imaging beyond existing models, spanning modalities, tissue states, and scales.

In **Chapter 3**, we address long-standing challenges in pre-clinical imaging by optimising sample preparation and acquisition protocols for *ex vivo* structural and diffusion MRI of the rat brain. We demonstrated that gadolinium perfusion, combined with alternative imaging sequences, significantly improved image contrast and reduced acquisition time. In addition, we developed a robust, reproducible image processing pipeline that generalises effectively across multiple scanners, handling significant variations in signal, noise, and contrast. This pipeline standardises data conversion and pre-processing while correcting for inhomogeneities and distortions, and provides microstructural measures, such as fractional anisotropy and mean diffusivity, that can be directly compared with complementary measures from 3D microscopy.

Chapter 4 extends upon this by establishing protocols for clearing and optically imaging microscopic structures in the intact rat brain. We developed and validated a passive solvent-based clearing protocol with improved delipidation and permeabilisation. This protocol is compatible with gadoliunium-enhanced *ex vivo* MRI, and provides a cost-effective and simple solution to rat brain clearing. Moreover, we optimised acquisition protocols for 3D light sheet microscopy, allowing us to capture the intrinsic contrast (i.e., autofluorescence) of whole brain hemispheres as a single volume. Our

findings demonstrated that standard registration approaches could align 3D microscopy data with MRI scans without requiring ad-hoc or specialised parameter optimisation. This contrasts with the complex and often bespoke approaches required to anatomically align classical 2D histology with MRI, emphasising the value of tissue clearing and light sheet microscopy in multiscale brain mapping.

Finally, **Chapter 5** addresses the challenge of combining tissue clearing with immunolabelling in large lipid-dense samples, such as the intact rat brain, which are poorly penetrated by antibodies. To overcome this obstacle, we adapted advanced labelling techniques previously used in the mouse brain to actively transport antibodies through samples while modulating their binding affinity. This accelerated the labelling process and significantly improved antibody penetration, yielding high-contrast, specific labelling of myelin and neurofilament without the tissue shrinkage commonly seen with passive solvent-based methods. By applying structure tensor analysis, we were able to estimate microstructural features, such as fibre orientation, from microscopy. In future these measurements will be directly compared, on a voxel-wise basis, with complementary dMRI measures acquired from the same sample.

Despite the significant advances presented in this thesis, several limitations and key considerations must be acknowledged.

One important limitation is the small number of samples (n=4) that underwent MRI, tissue clearing, immunolabelling, and light sheet microscopy. This primarily reflects the time, cost, and number of steps involved in processing each sample through the full workflow. However, small sample sizes — even as low as n=1 — are not uncommon in studies which integrate multiple complementary imaging techniques on the same sample (Howard

et al., 2023; Tendler et al., 2022).

Another important limitation is the absence of quantitative comparisons between MRI and microscopy. This was due to the substantial effort required to establish and optimise protocols for multimodal MRI, tissue clearing, immunolabelling, and light sheet microscopy in the intact rat brain. Additionally, 3D structure tensor analysis had not previously been implemented in light sheet microscopy, further contributing to the methodological challenges.

A key consideration when using light sheet microscopy is its restriction to a limited number of channels that are unaffected by autofluorescence, absorption, or scatter artefacts (Murray et al., 2015; Ku et al., 2016). As a result, only one or two targets can be stained per sample. The stripping and relabelling of cleared samples is also not currently feasible. This limits the sensitivity of light sheet microscopy to a subset of the tissue microstructure. In contrast, MRI and electron microscopy are sensitive to a wide range of microstructural features. Traditional histological methods also offer greater flexibility, allowing multiple staining panels to be applied to a single section or series of sections. This enables simultaneous analysis of multiple features, including co-expression patterns. Additionally, section-based staining and slide scanning have higher throughput, facilitating exploratory studies that can refine our understanding of how diffusion properties relate to brain microstructure. For example, a recent study found that, after accounting for demyelination, axonal loss, and microglia infiltration, the stain area fraction of activated microglia (i.e., CD68 staining) was the strongest predictor of high fractional anisotropy and low radial diffusivity (Kor et al., 2022).

Furthermore, unlike polarisation-sensitive optical coherence tomography, which can be performed on unstained tissue, light sheet microscopy re-

quires extensive processing, clearing/delipidation and staining. These steps fundamentally alter the tissue's physical and chemical state, potentially introducing discrepancies between stained structures and those influencing molecular water diffusion, as measured by dMRI. Although the myelinated axons observed through our staining techniques and the fibre orientations extracted via structure tensor analysis are commonly recognised as features affecting the molecular diffusion of water, the relationship between measures derived from microscopy and MRI is not always straightforward. Additionally, fundamental differences in imaging mechanisms and their unique sources of noise can complicate interpretations when using light sheet microscopy to validate dMRI-derived microstructural measures.

A final consideration is the high cost and specialised equipment required for the active techniques we converged on in Chapter 5. The reagents involved are expensive, have limited shelf lives (<1yr) and require specialised commercial instruments. These factors make the techniques feasible only in well-funded, large-scale laboratories or multi-user facilities. The cost and accessibility barriers highlight the need for more affordable alternatives, as evidenced by ongoing efforts to develop simpler and more affordable tissue-clearing approaches (Zheng and Rinaman, 2016).

6.2 Future Directions

This thesis establishes a foundation for future research integrating whole-brain 3D microscopy and MRI within the same sample. Here we outline potential future directions that could further advance technical methodologies and yield biological insights.

6.2.1 Specific MRI contrasts

Enhancing the cellular specificity of MRI contrasts has been a long-standing goal in neuroimaging (Dyrby et al., 2018), as it would transform MRI into a tool capable of mapping brain architecture at the cellular level. Achieving this would enable researchers to investigate brain development and natural variability in healthy individuals, creating new opportunities for the early detection of pathology or disease susceptibility.

In Chapter 5, we demonstrated specific labelling of myelin and neurofilament in intact brain tissue and provided an example of how image processing can be used to derive further biophysical parameters, such as fibre orientation from microscopy, which can be subsequently compared with corresponding MRI measures. Such an active immunolabelling paradigm is highly flexible, enabling the staining of a wide range of targets. Preliminary results, shown in Figure 6.1, demonstrate our ability to simultaneously visualise microglia, astrocytes and white matter in the intact mouse brain using techniques that are compatible with gadolinium-perfusion. Building on this foundation, we propose using our multiscale framework to gain deeper insights into the specific biophysical changes that current MRI modalities can detect. Furthermore, this imaging framework can support the development of novel MRI contrasts and validate their accuracy in capturing specific cellular structures.

This would involve generating a comprehensive dataset by combining multi-dimensional MRI and multi-contrast 3D microscopy in the same specimens. Ideally, the MRI data would include *in vivo* and *ex vivo* acquisitions, using quantitative and diffusion-weighted sequences designed to be maximally sensitive to different cellular compartments and tissue types. This approach would enable us to disentangle the MRI signal into distinct biological sources,

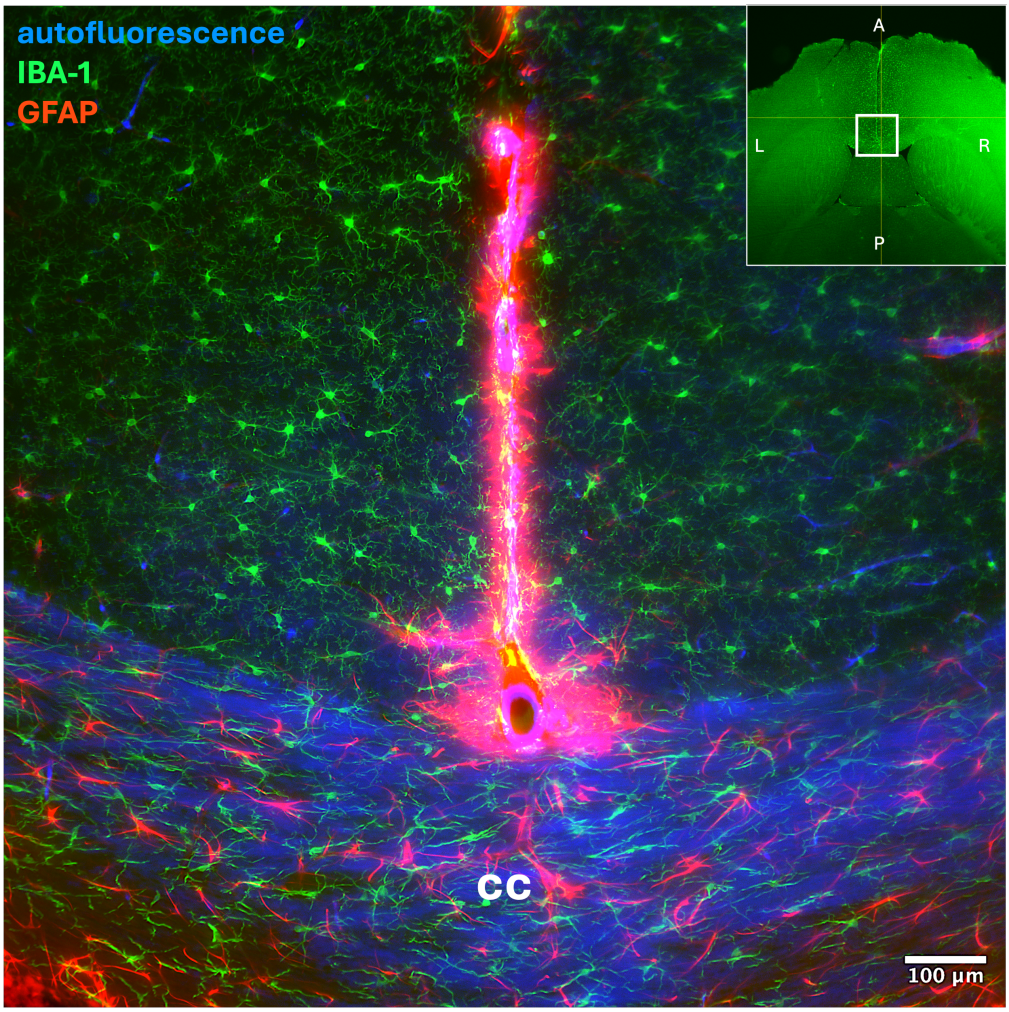


Figure 6.1: Immunolabelling of microglia (green) and astrocytes (red) in the intact mouse brain, with autofluorescence (blue) highlighting white matter tracts, such as the corpus callosum (cc). The inset (top right) shows the relative position of this high-resolution light sheet microscopy image within the medial frontal region of the brain, displayed in a horizontal view. This sample was perfused with 2mM gadolinium contrast during fixation. The bright vertical band of staining in the centre of the image could result from antibody accumulation in the meninges, which are difficult to remove between the left and right hemispheres.

such as neurons, astrocytes, and microglia, based on morphology, size, and localisation within grey or white matter. The 3D microscopy would employ specific immunolabelling to map these cell types throughout the brain and quantify them according to their size and morphological features. Rodent models (e.g., recombinant inbred mouse strains) with well characterised variations in cell density or morphology in key brain regions would be

used to validate and enhance the accuracy of these contrasts. A recent comprehensive resource (Howard et al., 2023) is following a similar approach of fusing MRI with 2D histology contrasts. The addition of 3D microscopy in such efforts would provide complementary information and benefits.

6.2.2 Mapping cellular and molecular mechanisms

Understanding cellular and molecular mechanisms underlying brain 'function' and 'dysfunction' remains a major challenge, largely due to the lack of technologies capable of capturing both molecular profiles and morphological properties of cells across local circuits and brain-wide networks. This complexity is exemplified in chronic pain, a prevalent condition with substantial impact, whose mechanisms remain poorly understood, limiting treatment options. Even with consistent peripheral pathology, pain severity varies, suggesting an important role for supraspinal mechanisms (Nijs et al., 2021). While neuronal mechanisms have been the primary focus, emerging evidence points to neuroinflammation, particularly glial activation, as a potential causal factor in pain.

We propose expanding our cross-resolution imaging framework to integrate spatial, molecular, morphological and connectivity data from the same tissue sample. A possible extension could involve combining spatially resolved single-cell transcriptomics with 3D microscopy and MRI, as outlined in Figure 6.2, to map the molecular and cellular mechanisms of glial activation in a rodent model of chronic pain. Spatial transcriptomics provides a comprehensive gene expression profile for all brain cell types within a single tissue slice. By adopting this cross-scale, multi-omic approach, we could explore pain-related differences in cell-type distributions, morphological features, phenotypes, and fibre organisation, while linking these findings

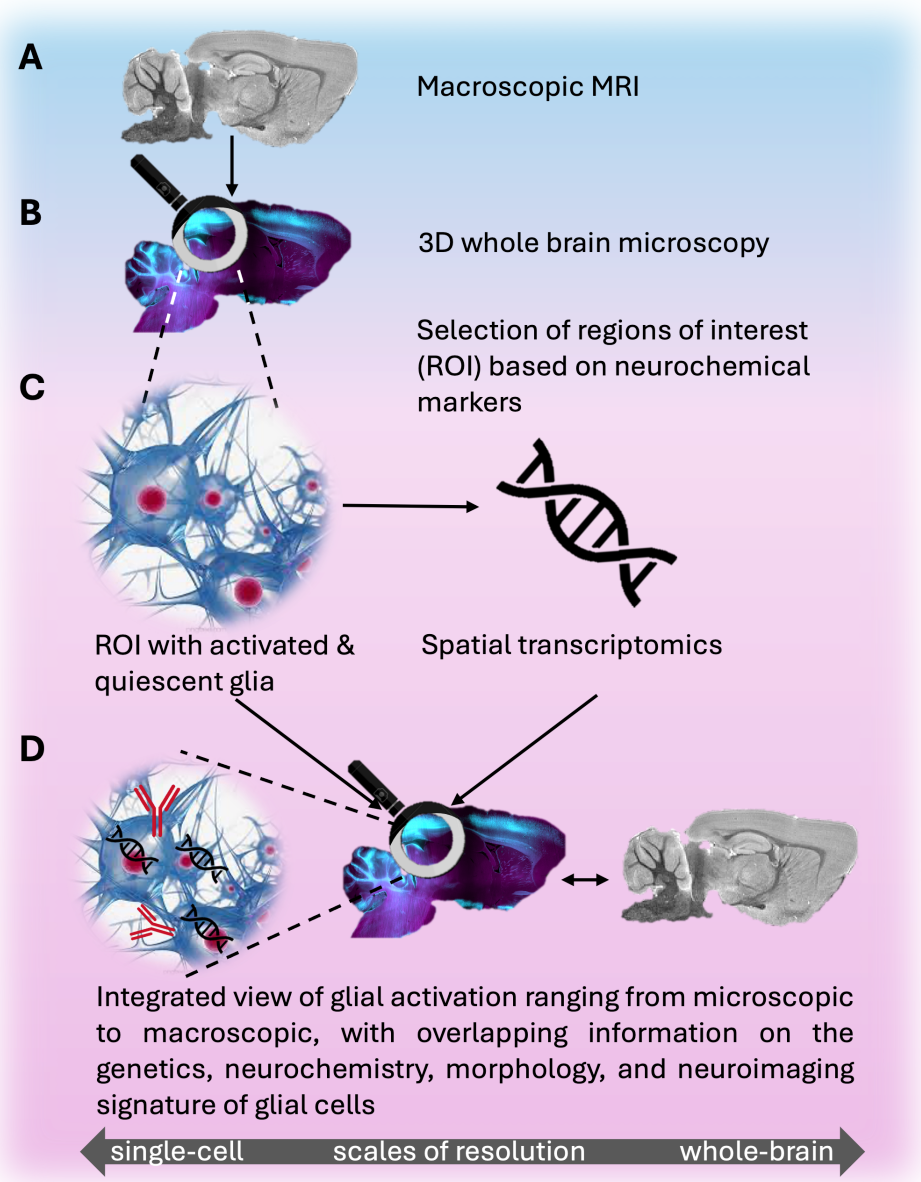


Figure 6.2: A) The proposed extended framework starts with high resolution structural and diffusion *ex vivo* MRI, followed by **B)** whole brain tissue clearing, immunolabelling, and 3D light sheet microscopy, to isolate regions of interest based on markers of glial activation. **C)** Profiling regions of interest with spatial transcriptomics will identify molecular mechanisms that underly glial contributions to pain. Overall, this will lead to **D)** a comprehensive (i.e., whole brain) method of connecting genes, cell populations, biological pathways, and brain microstructure to a neuroimaging signature of inflammation.

to macroscopic measures of anatomy or connectivity that can be obtained non-invasively using MRI. Combining tissue clearing with the ability to do

spatial transcriptomics is an active field of research (Wang et al., 2018b), and enabling such a non-trivial task would open new unique opportunities for exploring brain mechanisms.

6.2.3 Neural connectivity mapping

For diffusion MRI, researchers have harnessed the higher signal amplitude available at high and ultra-high field and gradient strengths to push the spatial resolution limits of dMRI for brain connectivity mapping. Smaller voxel sizes allow for complex white matter fibre architectures, including crossing fibres, fibre dispersion, and curvature, to be resolved across the whole brain. However, validating the anatomical accuracy of these structures using 2D histology remains difficult. To address this, we propose adapting the cross-resolution multimodal imaging framework we have developed to higher resolutions (Johnson et al., 2023). By creating a dataset where *ex vivo* MRI (e.g., $\geq$50μm) is conducted at high field strengths (e.g., on a $\geq$9.4T Bruker or Agilent system) alongside light sheet microscopy performed at high magnification (e.g., using at least a 4x objective and providing a resolution of $\sim$4μm isotropic), we can compare the neuronal fibre orientation patterns from 3D microscopy with the fibre orientation distribution obtained from dMRI for the same tissue volume. This approach is especially valuable in areas like the centrum semiovale, which has a high proportion of crossing fibres or in regions with high within-voxel curvature and fanning (Bastiani et al., 2017). The ease of registering whole-brain 3D microscopy with 3D MRI, combined with the minimal change in sample volume achieved through the clearing technique described in Chapter 5, makes this framework especially promising, particularly when compared to previous studies that focused on small regions of interest within sectioned tissue (Schilling et al.,

2016, 2018).

6.2.4 Data fusion and joint modelling

The co-registered datasets generated using this framework could facilitate the development of joint models that integrate complementary information from 3D microscopy and MRI into a unified biophysical model of tissue architecture and microstructure (Howard et al., 2019). By incorporating detailed local anatomical features (e.g., fibre orientation and dispersion in 3D) from whole-brain light sheet microscopy, these models can more accurately guide parameter selection for diffusion modelling. As a result, microstructural measures from MRI (e.g., the number of distinct fibre populations within a voxel in diffusion MRI) will more closely reflect the underlying biology. It also has important implications for applications like tractography, where the substantial variation in fibre bundle characteristics, both between and within white matter tracts, challenges the assumption of uniform brain-wide parameters (Behrens et al., 2007).

In addition, these joint models could provide the basis for transfer learning from microscopy to *in-vivo* MRI (Zhu et al., 2024). Models that have been trained on datasets with both 3D microscopy and MRI from the same samples could be applied to useen MRI data, using prior knowledge from microscopy to constrain and guide MRI estimates, ultimately enhancing accuracy and precision.

References

M. Aakhte, G. F. Müller, J. Li, K. R. Weiss, L. Roos, A. M. Diniz, J. Wenzel, M. Schwaninger, T. Moser, and J. Huisken. Isotropic, aberration-corrected light sheet microscopy for rapid high-resolution imaging of cleared tissue, 2 2025.

F. Aboitiz, A. B. Scheibel, R. S. Fisher, and E. Zaidel. Fiber composition of the human corpus callosum. *Brain Research*, 598(1-2), 12 1992. ISSN 00068993. doi: 10.1016/0006-8993(92)90178-C.

Y. Adolfs, D. D. Raj, S. Brignani, and R. J. Pasterkamp. Protocol for tissue clearing and 3D analysis of dopamine neurons in the developing mouse midbrain. *STAR Protocols*, 2(3):100669, 9 2021. ISSN 26661667. doi: 10.1016/j.xpro.2021.100669. URL https://linkinghub.elsevier.com/retrieve/pii/S2666166721003762.

D. C. Alexander, T. B. Dyrby, M. Nilsson, and H. Zhang. Imaging brain microstructure with diffusion MRI: practicality and applications. *NMR in Biomedicine*, 32(4), 4 2019. ISSN 0952-3480. doi: 10.1002/nbm.3841. URL https://analyticalsciencejournals.onlinelibrary.wiley.com/doi/10.1002/nbm.3841.

F. Alfaro-Almagro, M. Jenkinson, N. K. Bangerter, J. L. Andersson, L. Griffanti, G. Douaud, S. N. Sotiropoulos, S. Jbabdi, M. Hernandez-Fernandez, E. Vallee, D. Vidaurre, M. Webster, P. McCarthy, C. Rorden, A. Daducci, D. C. Alexander, H. Zhang, I. Dragonu, P. M. Matthews, K. L. Miller, and S. M. Smith. Image processing and Quality Control for the first 10,000 brain imaging datasets from UK Biobank. *NeuroImage*, 166, 2 2018. ISSN 10538119.

doi: 10.1016/j.neuroimage.2017.10.034.

A. Alkemade, P.-L. Bazin, R. Balesar, K. Pine, E. Kirilina, H. E. Möller, R. Trampel, J. M. Kros, M. C. Keuken, R. L. A. W. Bleys, D. F. Swaab, A. Herrler, N. Weiskopf, and B. U. Forstmann. A unified 3D map of microscopic architecture and MRI of the human brain. *Science Advances*, 8(17), 4 2022. ISSN 2375-2548. doi: 10.1126/sciadv.abj7892. URL https://www.science.org/doi/10.1126/sciadv.abj7892.

W. Alyami, A. Kyme, and R. Bourne. Histological Validation of MRI: A Review of Challenges in Registration of Imaging and Whole-Mount Histopathology. *Journal of Magnetic Resonance Imaging*, 55(1):11–22, 1 2022. ISSN 1053-1807. doi: 10.1002/jmri.27409.

K. Amunts, C. Lepage, L. Borgeat, H. Mohlberg, T. Dickscheid, M.-E. Rousseau, S. Bludau, P.-L. Bazin, L. B. Lewis, A.-M. Oros-Peusquens, N. J. Shah, T. Lippert, K. Zilles, and A. C. Evans. BigBrain: An Ultrahigh-Resolution 3D Human Brain Model. *Science*, 340(6139), 6 2013. ISSN 0036-8075. doi: 10.1126/science.1235381.

J. L. Andersson and S. Skare. A Model-Based Method for Retrospective Correction of Geometric Distortions in Diffusion-Weighted EPI. *NeuroImage*, 16(1):177–199, 5 2002. ISSN 10538119. doi: 10.1006/nimg.2001.1039.

J. L. Andersson and S. N. Sotiropoulos. An integrated approach to correction for off-resonance effects and subject movement in diffusion MR imaging. *NeuroImage*, 125:1063–1078, 1 2016. ISSN 10538119. doi: 10.1016/j.neuroimage.2015.10.019.

J. L. Andersson, S. Skare, and J. Ashburner. How to correct susceptibility distortions in spin-echo echo-planar images: application to diffusion tensor imaging. *NeuroImage*, 20(2):870–888, 10 2003. ISSN 10538119. doi: 10.1016/S1053-8119(03)00336-7.

J. L. Andersson, M. S. Graham, I. Drobnjak, H. Zhang, N. Filippini, and M. Bastiani. Towards a comprehensive framework for movement and distortion correction of diffusion MR images: Within volume movement. *NeuroImage*,

152:450–466, 5 2017. ISSN 10538119. doi: 10.1016/j.neuroimage.2017.02.085.

J. L. R. Andersson, M. S. Graham, E. Zsoldos, and S. N. Sotiropoulos. Incorporating outlier detection and replacement into a non-parametric framework for movement and distortion correction of diffusion MR images. *NeuroImage*, 141: 556–572, 11 2016. ISSN 10538119. doi: 10.1016/j.neuroimage.2016.06.058.

P. Ariel. A beginner's guide to tissue clearing. *The International Journal of Biochemistry & Cell Biology*, 84:35–39, 3 2017. ISSN 13572725. doi: 10.1016/j.biocel.2016.12.009. URL https://linkinghub.elsevier.com/retrieve/pii/S135727251630396X.

Y. Assaf and P. J. Basser. Composite hindered and restricted model of diffusion (CHARMED) MR imaging of the human brain. *NeuroImage*, 27(1), 8 2005. ISSN 10538119. doi: 10.1016/j.neuroimage.2005.03.042.

Y. Assaf, H. Johansen-Berg, and M. Thiebaut de Schotten. The role of diffusion MRI in neuroscience. *NMR in Biomedicine*, 32(4):e3762, 4 2019. ISSN 0952-3480. doi: 10.1002/nbm.3762. URL https://onlinelibrary.wiley.com/doi/abs/10.1002/nbm.3762.

B. B. Avants, N. J. Tustison, G. Song, P. A. Cook, A. Klein, and J. C. Gee. A reproducible evaluation of ANTs similarity metric performance in brain image registration. *NeuroImage*, 54(3), 2 2011. ISSN 10538119. doi: 10.1016/j.neuroimage.2010.09.025.

S. V. Avilov. Navigating across multi-dimensional space of tissue clearing parameters. *Methods and Applications in Fluorescence*, 9(2):022001, 4 2021. ISSN 2050-6120. doi: 10.1088/2050-6120/abe6fb.

M. Axer and K. Amunts. Scale matters: The nested human connectome. *Science*, 378(6619):500–504, 11 2022. ISSN 0036-8075. doi: 10.1126/science.abq2599.

M. Axer, D. Grässel, M. Kleiner, J. Dammers, T. Dickscheid, J. Reckfort, T. Hütz, B. Eiben, U. Pietrzyk, K. Zilles, and K. Amunts. High-Resolution Fiber Tract Reconstruction in the Human Brain by Means of Three-Dimensional Polarized Light Imaging. *Frontiers in Neuroinformatics*, 5, 2011. ISSN 1662-5196. doi: 10.3389/fninf.2011.00034.

M. Axer, S. Strohmer, D. Gräßel, O. Bücker, M. Dohmen, J. Reckfort, K. Zilles, and K. Amunts. Estimating Fiber Orientation Distribution Functions in 3D-Polarized Light Imaging. *Frontiers in Neuroanatomy*, 10, 4 2016. ISSN 1662-5129. doi: 10.3389/fnana.2016.00040.

J. Bai, T. L. H. Trinh, K.-H. Chuang, and A. Qiu. Atlas-based automatic mouse brain image segmentation revisited: model complexity vs. image registration. *Magnetic Resonance Imaging*, 30(6), 7 2012. ISSN 0730725X. doi: 10.1016/j.mri.2012.02.010.

H. Balasubramanian, C. M. Hobson, T.-L. Chew, and J. S. Aaron. Imagining the future of optical microscopy: everything, everywhere, all at once. *Communications Biology*, 6(1):1096, 10 2023. ISSN 2399-3642. doi: 10.1038/s42003-023-05468-9.

R. L. C. Barrett, D. Cash, C. Simmons, E. Kim, T. C. Wood, R. Stones, A. C. Vernon, M. Catani, and F. Dell'Acqua. Tissue optimization strategies for high-quality ex vivo diffusion imaging. *NMR in Biomedicine*, 36(3), 3 2023. ISSN 0952-3480. doi: 10.1002/nbm.4866.

D. A. Barrière, R. Magalhães, A. Novais, P. Marques, E. Selingue, F. Geffroy, F. Marques, J. Cerqueira, J. C. Sousa, F. Boumezbeur, M. Bottlaender, T. M. Jay, A. Cachia, N. Sousa, and S. Mériaux. The SIGMA rat brain templates and atlases for multimodal MRI data analysis and visualization. *Nature Communications*, 10(1):5699, 12 2019. ISSN 2041-1723. doi: 10.1038/s41467-019-13575-7. URL http://www.nature.com/articles/s41467-019-13575-7.

P. Basser and C. Pierpaoli. Microstructural and Physiological Features of Tissues Elucidated by Quantitative-Diffusion-Tensor MRI. *Journal of Magnetic Resonance, Series B*, 3(111):209–219, 1996.

P. J. Basser, J. Mattiello, and D. LeBihan. MR diffusion tensor spectroscopy and imaging. *Biophysical Journal*, 66(1):259–267, 1994.

P. J. Basser, S. Pajevic, C. Pierpaoli, J. Duda, and A. Aldroubi. In vivo fiber tractography using DT-MRI data. *Magnetic Resonance in Medicine*,

44(4), 10 2000. ISSN 0740-3194. doi: 10.1002/1522-2594(200010)44:4⟨625::AID-MRM17⟩3.0.CO;2-O.

M. Bastiani and A. Roebroeck. Unraveling the multiscale structural organization and connectivity of the human brain: the role of diffusion MRI. *Frontiers in Neuroanatomy*, 9, 6 2015. ISSN 1662-5129. doi: 10.3389/fnana.2015.00077. URL http://journal.frontiersin.org/Article/10.3389/fnana.2015.00077/abstract.

M. Bastiani, M. Cottaar, K. Dikranian, A. Ghosh, H. Zhang, D. C. Alexander, T. E. Behrens, S. Jbabdi, and S. N. Sotiropoulos. Improved tractography using asymmetric fibre orientation distributions. *NeuroImage*, 158:205–218, 9 2017. ISSN 10959572. doi: 10.1016/j.neuroimage.2017.06.050.

M. Bastiani, M. Cottaar, S. P. Fitzgibbon, S. Suri, F. Alfaro-Almagro, S. N. Sotiropoulos, S. Jbabdi, and J. L. Andersson. Automated quality control for within and between studies diffusion MRI data using a non-parametric framework for movement and distortion correction. *NeuroImage*, 184:801–812, 1 2019. ISSN 10959572. doi: 10.1016/j.neuroimage.2018.09.073.

C. Beaulieu. The basis of anisotropic water diffusion in the nervous system - a technical review. *NMR in Biomedicine*, 15(7-8):435–455, 11 2002. ISSN 0952-3480. doi: 10.1002/nbm.782. URL https://onlinelibrary.wiley.com/doi/10.1002/nbm.782.

T. Behrens, M. Woolrich, M. Jenkinson, H. Johansen-Berg, R. Nunes, S. Clare, P. Matthews, J. Brady, and S. Smith. Characterization and propagation of uncertainty in diffusion-weighted MR imaging. *Magnetic Resonance in Medicine*, 50(5), 11 2003. ISSN 0740-3194. doi: 10.1002/mrm.10609.

T. Behrens, H. J. Berg, S. Jbabdi, M. Rushworth, and M. Woolrich. Probabilistic diffusion tractography with multiple fibre orientations: What can we gain? *NeuroImage*, 34(1):144–155, 1 2007. ISSN 10538119. doi: 10.1016/j.neuroimage.2006.09.018.

H. Benveniste and S. Blackband. MR microscopy and high resolution small animal MRI: applications in neuroscience research. *Progress in Neurobiology*, 67(5):

393–420, 8 2002. ISSN 03010082. doi: 10.1016/S0301-0082(02)00020-5. URL https://linkinghub.elsevier.com/retrieve/pii/S0301008202000205.

R. F. Betzel and D. S. Bassett. Multi-scale brain networks. *NeuroImage*, 160: 73–83, 10 2017. ISSN 10538119. doi: 10.1016/j.neuroimage.2016.11.006. URL https://linkinghub.elsevier.com/retrieve/pii/S1053811916306152.

M. Beznak. Cardiac Output in Rats During the Development of Cardiac Hypertrophy. *Circulation Research*, 6(2):207–212, 3 1958. ISSN 0009-7330. doi: 10.1161/01.RES.6.2.207.

B. Bodini and O. Ciccarelli. Diffusion MRI in Neurological Disorders. In *Diffusion MRI*, pages 175–203. Elsevier, 2009. doi: 10.1016/B978-0-12-374709-9.00009-2. URL https://linkinghub.elsevier.com/retrieve/pii/B9780123747099000092.

A. Branch, D. Tward, J. T. Vogelstein, Z. Wu, and M. Gallagher. An optimized protocol for iDISCO+ rat brain clearing, imaging, and analysis. *bioRxiv*, 3 2021. URL https://doi.org/10.1101/639674.

M. A. Brockmann, A. Kemmling, and C. Groden. Current issues and perspectives in small rodent magnetic resonance imaging using clinical MRI scanners. *Methods*, 43(1):79–87, 9 2007. ISSN 10462023. doi: 10.1016/j.ymeth.2007.07.001.

K. Brodmann. *Vergleichende Lokalisationslehre der Gross- Hirnrinde in ihren Prinzipien Dargestellt und Grund des Zelle- nbaues*. Barth, Leipzig, 1909.

M. D. Budde and J. Annese. Quantification of anisotropy and fiber orientation in human brain histological sections. *Frontiers in Integrative Neuroscience*, 7, 2013. ISSN 1662-5145. doi: 10.3389/fnint.2013.00003.

M. D. Budde and J. A. Frank. Examining brain microstructure using structure tensor analysis of histological sections. *NeuroImage*, 63(1):1–10, 10 2012. ISSN 10538119. doi: 10.1016/j.neuroimage.2012.06.042. URL https://linkinghub.elsevier.com/retrieve/pii/S105381191200657X.

F. Budin, M. Hoogstoel, P. Reynolds, M. Grauer, S. K. O'Leary-Moore, and I. Oguz. Fully automated rodent brain MR image processing pipeline on a Midas server: from acquired images to region-based statistics. *Frontiers in*

Neuroinformatics, 7, 2013. ISSN 1662-5196. doi: 10.3389/fninf.2013.00015.

J. A. N. Buytaert and J. J. J. Dirckx. Design and quantitative resolution measurements of an optical virtual sectioning three-dimensional imaging technique for biomedical specimens, featuring two-micrometer slicing resolution. *Journal of Biomedical Optics*, 12(1), 2007. ISSN 10833668. doi: 10.1117/1.2671712.

L. S. Cahill, C. L. Laliberté, J. Ellegood, S. Spring, J. A. Gleave, M. C. van Eede, J. P. Lerch, and R. M. Henkelman. Preparation of fixed mouse brains for MRI. *NeuroImage*, 60(2):933–939, 4 2012. ISSN 10538119. doi: 10.1016/j.neuroimage.2012.01.100. URL https://linkinghub.elsevier.com/retrieve/pii/S1053811912001188.

R. Cai, Z. I. Kolabas, C. Pan, H. Mai, S. Zhao, D. Kaltenecker, F. F. Voigt, M. Molbay, T.-l. Ohn, C. Vincke, M. I. Todorov, F. Helmchen, J. A. Van Ginderachter, and A. Ertürk. Whole-mouse clearing and imaging at the cellular level with vDISCO. *Nature Protocols*, 18(4):1197–1242, 4 2023. ISSN 1754-2189. doi: 10.1038/s41596-022-00788-2. URL https://www.nature.com/articles/s41596-022-00788-2.

A. Casamitjana, M. Lorenzi, S. Ferraris, L. Peter, M. Modat, A. Stevens, B. Fischl, T. Vercauteren, and J. E. Iglesias. Robust joint registration of multiple stains and MRI for multimodal 3D histology reconstruction: Application to the Allen human brain atlas. *Medical Image Analysis*, 75:102265, 1 2022. ISSN 13618415. doi: 10.1016/j.media.2021.102265. URL https://linkinghub.elsevier.com/retrieve/pii/S1361841521003108.

M. Catani, R. J. Howard, S. Pajevic, and D. K. Jones. Virtual in Vivo Interactive Dissection of White Matter Fasciculi in the Human Brain. *NeuroImage*, 17(1), 9 2002. ISSN 10538119. doi: 10.1006/nimg.2002.1136.

M. Cercignani and S. Bouyagoub. Brain microstructure by multi-modal MRI: Is the whole greater than the sum of its parts? *NeuroImage*, 182:117–127, 11 2018. ISSN 10538119. doi: 10.1016/j.neuroimage.2017.10.052. URL https://linkinghub.elsevier.com/retrieve/pii/S1053811917308868.

E. H. Chang, M. Argyelan, M. Aggarwal, T.-S. S. Chandon, K. H. Karlsgodt,

S. Mori, and A. K. Malhotra. The role of myelination in measures of white matter integrity: Combination of diffusion tensor imaging and two-photon microscopy of CLARITY intact brains. *NeuroImage*, 147:253–261, 2 2017. ISSN 10538119. doi: 10.1016/j.neuroimage.2016.11.068. URL https://linkinghub.elsevier.com/retrieve/pii/S1053811916306863.

J. Chi, A. Crane, Z. Wu, and P. Cohen. Adipo-Clear: A Tissue Clearing Method for Three-Dimensional Imaging of Adipose Tissue. *Journal of Visualized Experiments*, (137), 7 2018. ISSN 1940-087X. doi: 10.3791/58271. URL https://www.jove.com/t/58271/adipo-clear-tissue-clearing-method-for-three-dimensional-imaging.

S. W. Choi, W. Guan, and K. Chung. Basic principles of hydrogel-based tissue transformation technologies and their applications. *Cell*, 184(16): 4115–4136, 8 2021. ISSN 00928674. doi: 10.1016/j.cell.2021.07.009. URL https://linkinghub.elsevier.com/retrieve/pii/S0092867421008357.

N. Chou, Jiarong Wu, J. Bai Bingren, Anqi Qiu, and Kai-Hsiang Chuang. Robust Automatic Rodent Brain Extraction Using 3-D Pulse-Coupled Neural Networks (PCNN). *IEEE Transactions on Image Processing*, 20(9), 9 2011. ISSN 1057-7149. doi: 10.1109/TIP.2011.2126587.

K. Chung, J. Wallace, S.-Y. Kim, S. Kalyanasundaram, A. S. Andalman, T. J. Davidson, J. J. Mirzabekov, K. A. Zalocusky, J. Mattis, A. K. Denisin, S. Pak, H. Bernstein, C. Ramakrishnan, L. Grosenick, V. Gradinaru, and K. Deisseroth. Structural and molecular interrogation of intact biological systems. *Nature*, 497(7449):332–337, 5 2013. ISSN 0028-0836. doi: 10.1038/nature12107. URL http://www.nature.com/articles/nature12107.

I. Costantini, R. Cicchi, L. Silvestri, F. Vanzi, and F. S. Pavone. In-vivo and ex-vivo optical clearing methods for biological tissues: review. *Biomedical Optics Express*, 10(10), 10 2019. ISSN 2156-7085. doi: 10.1364/BOE.10.005251.

I. Costantini, E. Baria, M. Sorelli, F. Matuschke, F. Giardini, M. Menzel, G. Mazzamuto, L. Silvestri, R. Cicchi, K. Amunts, M. Axer, and F. S. Pavone. Autofluorescence enhancement for label-free imaging of

myelinated fibers in mammalian brains. *Scientific Reports*, 11(1):8038, 4 2021. ISSN 2045-2322. doi: 10.1038/s41598-021-86092-7. URL https://www.nature.com/articles/s41598-021-86092-7.

R. W. Cox. AFNI: Software for Analysis and Visualization of Functional Magnetic Resonance Neuroimages. *Computers and Biomedical Research*, 29 (3), 6 1996. ISSN 00104809. doi: 10.1006/cbmr.1996.0014.

A. E. de Guzman, M. D. Wong, J. A. Gleave, and B. J. Nieman. Variations in post-perfusion immersion fixation and storage alter MRI measurements of mouse brain morphometry. *NeuroImage*, 142:687–695, 11 2016. ISSN 10538119. doi: 10.1016/j.neuroimage.2016.06.028.

A. Delora, A. Gonzales, C. S. Medina, A. Mitchell, A. F. Mohed, R. E. Jacobs, and E. L. Bearer. A simple rapid process for semi-automated brain extraction from magnetic resonance images of the whole mouse head. *Journal of Neuroscience Methods*, 257, 1 2016. ISSN 01650270. doi: 10.1016/j.jneumeth.2015.09.031.

W. Denk, K. L. Briggman, and M. Helmstaedter. Structural neurobiology: missing link to a mechanistic understanding of neural computation. *Nature Reviews Neuroscience*, 13(5), 5 2012. ISSN 1471-003X. doi: 10.1038/nrn3169.

G. Desrosiers-Gregoire, G. A. Devenyi, J. Grandjean, and M. M. Chakravarty. Rodent Automated Bold Improvement of EPI Sequences (RABIES): A standardized image processing and data quality platform for rodent fMRI. *biorxiv*, 9 2022. URL https://doi.org/10.1101/2022.08.20.504597.

S. Ding, J. J. Royall, S. M. Sunkin, L. Ng, B. A. Facer, P. Lesnar, A. Guillozet-Bongaarts, B. McMurray, A. Szafer, T. A. Dolbeare, A. Stevens, L. Tirrell, T. Benner, S. Caldejon, R. A. Dalley, N. Dee, C. Lau, J. Nyhus, M. Reding, Z. L. Riley, D. Sandman, E. Shen, A. Kouwe, A. Varjabedian, M. Write, L. Zollei, C. Dang, J. A. Knowles, C. Koch, J. W. Phillips, N. Sestan, P. Wohnoutka, H. R. Zielke, J. G. Hohmann, A. R. Jones, A. Bernard, M. J. Hawrylycz, P. R. Hof, B. Fischl, and E. S. Lein. Comprehensive cellular-resolution atlas of the adult human brain. *Journal of Comparative Neurology*, 524(16), 11 2016.

ISSN 0021-9967. doi: 10.1002/cne.24080.

H.-U. Dodt, U. Leischner, A. Schierloh, N. Jährling, C. P. Mauch, K. Deininger, J. M. Deussing, M. Eder, W. Zieglgänsberger, and K. Becker. Ultramicroscopy: three-dimensional visualization of neuronal networks in the whole mouse brain. *Nature Methods*, 4(4):331–336, 4 2007. ISSN 1548-7091. doi: 10.1038/nmeth1036. URL http://www.nature.com/articles/nmeth1036.

N. Downes and P. Mullins. The Development of Myelin in the Brain of the Juvenile Rat. *Toxicologic Pathology*, 42(5):913–922, 7 2014. ISSN 0192-6233. doi: 10.1177/0192623313503518.

T. B. Dyrby, W. F. Baaré, D. C. Alexander, J. Jelsing, E. Garde, and L. V. Søgaard. An ex vivo imaging pipeline for producing high-quality and high-resolution diffusion-weighted imaging datasets. *Human Brain Mapping*, 32(4), 4 2011. ISSN 10659471. doi: 10.1002/hbm.21043.

T. B. Dyrby, G. M. Innocenti, M. Bech, and H. Lundell. Validation strategies for the interpretation of microstructure imaging using diffusion MRI. *NeuroImage*, 182:62–79, 11 2018. ISSN 10538119. doi: 10.1016/j.neuroimage.2018.06.049. URL https://linkinghub.elsevier.com/retrieve/pii/S1053811918305561.

E. D'Angelo and V. Jirsa. The quest for multiscale brain modeling. *Trends in Neurosciences*, 45(10):777–790, 10 2022. ISSN 01662236. doi: 10.1016/j.tins.2022.06.007.

H. E. D'Arceuil, S. Westmoreland, and A. J. de Crespigny. An approach to high resolution diffusion tensor imaging in fixed primate brain. *NeuroImage*, 35(2), 4 2007. ISSN 10538119. doi: 10.1016/j.neuroimage.2006.12.028.

N. El-Ayache and J. J. Galligan. The Rat in Neuroscience Research. In *The Laboratory Rat*, pages 1003–1022. Elsevier, 2020. doi: 10.1016/B978-0-12-814338-4.00028-3. URL https://linkinghub.elsevier.com/retrieve/pii/B9780128143384000283.

B. Ellenbroek and J. Youn. Rodent models in neuroscience research: is it a rat race? *Disease Models & Mechanisms*, 9(10), 10 2016. ISSN 1754-8411. doi:

10.1242/dmm.026120.

A. Ertürk, K. Becker, N. Jährling, C. P. Mauch, C. D. Hojer, J. G. Egen, F. Hellal, F. Bradke, M. Sheng, and H.-U. Dodt. Three-dimensional imaging of solvent-cleared organs using 3DISCO. *Nature Protocols*, 7(11):1983–1995, 11 2012. ISSN 1754-2189. doi: 10.1038/nprot.2012.119. URL http://www.nature.com/articles/nprot.2012.119.

R. Feo and F. Giove. Towards an efficient segmentation of small rodents brain: A short critical review. *Journal of Neuroscience Methods*, 323, 7 2019. ISSN 01650270. doi: 10.1016/j.jneumeth.2019.05.003.

S. Foxley, V. Sampathkumar, V. De Andrade, S. Trinkle, A. Sorokina, K. Norwood, P. La Riviere, and N. Kasthuri. Multi-modal imaging of a single mouse brain over five orders of magnitude of resolution. *NeuroImage*, 238:118250, 9 2021. ISSN 10538119. doi: 10.1016/j.neuroimage.2021.118250.

M. F. Glasser, S. N. Sotiropoulos, J. A. Wilson, T. S. Coalson, B. Fischl, J. L. Andersson, J. Xu, S. Jbabdi, M. Webster, J. R. Polimeni, D. C. Van Essen, and M. Jenkinson. The minimal preprocessing pipelines for the Human Connectome Project. *NeuroImage*, 80:105–124, 10 2013. ISSN 10538119. doi: 10.1016/j.neuroimage.2013.04.127.

D. Goerzen, C. Fowler, G. A. Devenyi, J. Germann, D. Madularu, M. M. Chakravarty, and J. Near. An MRI-Derived Neuroanatomical Atlas of the Fischer 344 Rat Brain. *Scientific Reports*, 10(1):6952, 12 2020. ISSN 2045-2322. doi: 10.1038/s41598-020-63965-x.

M. Goubran, C. Leuze, B. Hsueh, M. Aswendt, L. Ye, Q. Tian, M. Y. Cheng, A. Crow, G. K. Steinberg, J. A. McNab, K. Deisseroth, and M. Zeineh. Multimodal image registration and connectivity analysis for integration of connectomic data from microscopy to MRI. *Nature Communications*, 10(1): 5504, 12 2019. ISSN 2041-1723. doi: 10.1038/s41467-019-13374-0. URL http://www.nature.com/articles/s41467-019-13374-0.

V. Gradinaru, J. Treweek, K. Overton, and K. Deisseroth. Hydrogel-Tissue Chemistry: Principles and Applications. *Annual Review of Biophysics*, 47(1):355–376,

5 2018. ISSN 1936-122X. doi: 10.1146/annurev-biophys-070317-032905.

J. Grandjean, G. Desrosiers-Gregoire, C. Anckaerts, D. Angeles-Valdez, F. Ayad, D. Barrière, I. Blockx, A. Bortel, M. Broadwater, B. Cardoso, M. Célestine, J. Chavez-Negrete, S. Choi, E. Christiaen, P. Clavijo, L. Colon-Perez, S. Cramer, T. Daniele, E. Dempsey, Y. Diao, A. Doelemeyer, D. Dopfel, L. Dvořáková, C. Falfán-Melgoza, F. Fernandes, C. Fowler, A. Fuentes-Ibañez, C. Garin, E. Gelderman, C. Golden, C. Guo, M. Henckens, L. Hennessy, P. Herman, N. Hofwijks, C. Horien, T. Ionescu, J. Jones, J. Kaesser, E. Kim, H. Lambers, A. Lazari, S.-H. Lee, A. Lillywhite, Y. Liu, Y. Liu, A. López-Castro, X. López-Gil, Z. Ma, E. MacNicol, D. Madularu, F. Mandino, S. Marciano, M. McAuslan, P. McCunn, A. McIntosh, X. Meng, L. Meyer-Baese, S. Missault, F. Moro, D. Naessens, L. Nava-Gomez, H. Nonaka, J. Ortiz, J. Paasonen, L. Peeters, M. Pereira, P. Perez, M. Pompilus, M. Prior, R. Rakhmatullin, H. Reimann, J. Reinwald, R. de Rio, A. Rivera-Olvera, D. Ruiz-Pérez, G. Russo, T. Rutten, R. Ryoke, M. Sack, P. Salvan, B. Sanganahalli, A. Schroeter, B. Seewoo, E. Selingue, A. Seuwen, B. Shi, N. Sirmpilatze, J. Smith, C. Smith, F. Sobczak, P. Stenroos, M. Straathof, S. Strobelt, A. Sumiyoshi, K. Takahashi, M. Torres-García, R. Tudela, M. van den Berg, K. van der Marel, A. van Hout, R. Vertullo, B. Vidal, R. Vrooman, V. Wang, I. Wank, D. Watson, T. Yin, Y. Zhang, S. Zurbruegg, S. Achard, S. Alcauter, D. Auer, E. Barbier, J. Baudewig, C. Beckmann, N. Beckmann, G. Becq, E. Blezer, R. Bolbos, S. Boretius, S. Bouvard, E. Budinger, J. Buxbaum, D. Cash, V. Chapman, K.-H. Chuang, L. Ciobanu, B. Coolen, J. Dalley, M. Dhenain, R. Dijkhuizen, O. Esteban, C. Faber, M. Febo, K. Feindel, G. Forloni, J. Fouquet, E. Garza-Villarreal, N. Gass, J. Glennon, A. Gozzi, O. Gröhn, A. Harkin, A. Heerschap, X. Helluy, K. Herfert, A. Heuser, J. Homberg, D. Houwing, F. Hyder, G. Ielacqua, I. Jelescu, H. Johansen-Berg, G. Kaneko, R. Kawashima, S. Keilholz, G. Keliris, C. Kelly, C. Kerskens, J. Khokhar, P. Kind, J.-B. Langlois, J. Lerch, M. López-Hidalgo, D. Manahan-Vaughan, F. Marchand, R. Mars, G. Marsella, E. Micotti, E. Muñoz-Moreno, J. Near, T. Niendorf, W. Otte, P. Pais, W.-J.

Pan, R. Prado-Alcalá, G. Quirarte, J. Rodger, T. Rosenow, C. Baptista, A. Sartorius, S. Sawiak, T. Scheenen, N. Shemesh, Y.-Y. Shih, A. Shmuel, G. Soria, R. Stoop, G. Thompson, S. Till, N. Todd, A. Van Der Linden, A. van der Toorn, G. van Tilborg, C. Vanhove, A. Veltien, M. Verhoye, L. Wachsmuth, W. Weber-Fahr, P. Wenk, X. Yu, V. Zerbi, N. Zhang, B. Zhang, L. Zimmer, G. Devenyi, M. Chakravarty, and A. Hess. StandardRat: A multi-center consensus protocol to enhance functional connectivity specificity in the rat brain. *bioRxiv*, 2020.

E. Gyengesi, E. Calabrese, M. C. Sherrier, G. A. Johnson, G. Paxinos, and C. Watson. Semi-automated 3D segmentation of major tracts in the rat brain: comparing DTI with standard histological methods. *Brain Structure and Function*, 219(2), 3 2014. ISSN 1863-2653. doi: 10.1007/s00429-013-0516-8.

H. Hama, H. Kurokawa, H. Kawano, R. Ando, T. Shimogori, H. Noda, K. Fukami, A. Sakaue-Sawano, and A. Miyawaki. Scale: a chemical approach for fluorescence imaging and reconstruction of transparent mouse brain. *Nature Neuroscience*, 14(11):1481–1488, 11 2011. ISSN 1097-6256. doi: 10.1038/nn.2928.

L. Hammelrath, S. Škokić, A. Khmelinskii, A. Hess, N. van der Knaap, M. Staring, B. P. Lelieveldt, D. Wiedermann, and M. Hoehn. Morphological maturation of the mouse brain: An in vivo MRI and histology investigation. *NeuroImage*, 125:144–152, 1 2016. ISSN 10538119. doi: 10.1016/j.neuroimage.2015.10.009.

J. R. Homberg, R. A. Adan, N. Alenina, A. Asiminas, M. Bader, T. Beckers, D. P. Begg, A. Blokland, M. E. Burger, G. van Dijk, U. L. Eisel, Y. Elgersma, B. Englitz, A. Fernandez-Ruiz, C. P. Fitzsimons, A.-M. van Dam, P. Gass, J. Grandjean, R. Havekes, M. J. Henckens, C. Herden, R. A. Hut, W. Jarrett, K. Jeffrey, D. Jezova, A. Kalsbeek, M. Kamermans, M. J. Kas, N. N. Kasri, A. J. Kiliaan, S. M. Kolk, A. Korosi, S. M. Korte, T. Kozicz, S. A. Kushner, K. Leech, K.-P. Lesch, H. Lesscher, P. J. Lucassen, A. Luthi, L. Ma, A. S. Mallien, P. Meerlo, J. F. Mejias, F. J. Meye, A. S. Mitchell, J. D. Mul, U. Olcese, A. O. González, J. D. Olivier, M. Pasqualetti, C. M. Pennartz, P. Popik, J. Prickaerts, L. M. de la Prida, S. Ribeiro, B. Roozendaal, J. I.

Rossato, A.-A. Salari, R. G. Schoemaker, A. B. Smit, L. J. Vanderschuren, T. Takeuchi, R. van der Veen, M. P. Smidt, V. V. Vyazovskiy, M. Wiesmann, C. J. Wierenga, B. Williams, I. Willuhn, M. Wöhr, M. Wolvekamp, E. A. van der Zee, and L. Genzel. The continued need for animals to advance brain research. *Neuron*, 109(15):2374–2379, 8 2021. ISSN 08966273. doi: 10.1016/j.neuron.2021.07.015. URL https://linkinghub.elsevier.com/retrieve/pii/S0896627321005365.

A. F. Howard, J. Mollink, M. Kleinnijenhuis, M. Pallebage-Gamarallage, M. Bastiani, M. Cottaar, K. L. Miller, and S. Jbabdi. Joint modelling of diffusion MRI and microscopy. *NeuroImage*, 201:116014, 11 2019. ISSN 10538119. doi: 10.1016/j.neuroimage.2019.116014. URL https://linkinghub.elsevier.com/retrieve/pii/S1053811919305956.

A. F. D. Howard, I. N. Huszar, A. Smart, M. Cottaar, G. Daubney, T. Hanayik, A. A. Khrapitchev, R. B. Mars, J. Mollink, C. Scott, N. R. Sibson, J. Sallet, S. Jbabdi, and K. L. Miller. An open resource combining multi-contrast MRI and microscopy in the macaque brain. *Nature Communications*, 14(1):4320, 7 2023. ISSN 2041-1723. doi: 10.1038/s41467-023-39916-1.

C. Hoyer, N. Gass, W. Weber-Fahr, and A. Sartorius. Advantages and Challenges of Small Animal Magnetic Resonance Imaging as a Translational Tool. *Neuropsychobiology*, 69(4), 2014. ISSN 0302-282X. doi: 10.1159/000360859.

L.-M. Hsu, S. Wang, P. Ranadive, W. Ban, T.-H. H. Chao, S. Song, D. H. Cerri, L. R. Walton, M. A. Broadwater, S.-H. Lee, D. Shen, and Y.-Y. I. Shih. Automatic Skull Stripping of Rat and Mouse Brain MRI Data Using U-Net. *Frontiers in Neuroscience*, 14, 10 2020. ISSN 1662-453X. doi: 10.3389/fnins.2020.568614.

J. Huisken. Optical Sectioning Deep Inside Live Embryos by Selective Plane Illumination Microscopy. *Science*, 305(5686), 8 2004. ISSN 0036-8075. doi: 10.1126/science.1100035.

I. N. Huszar, M. Pallebage-Gamarallage, S. Bangerter-Christensen, H. Brooks, S. Fitzgibbon, S. Foxley, M. Hiemstra, A. F. Howard, S. Jbabdi, D. Z.

Kor, A. Leonte, J. Mollink, A. Smart, B. C. Tendler, M. R. Turner, O. Ansorge, K. L. Miller, and M. Jenkinson. Tensor image registration library: Deformable registration of stand-alone histology images to whole-brain post-mortem MRI data. *NeuroImage*, 265:119792, 1 2023. ISSN 10538119. doi: 10.1016/j.neuroimage.2022.119792. URL https://linkinghub.elsevier.com/retrieve/pii/S1053811922009132.

P. M. Iannaccone and H. J. Jacob. Rats! *Disease Models & Mechanisms*, 2 (5-6):206–210, 4 2009. ISSN 1754-8411. doi: 10.1242/dmm.002733. URL https://journals.biologists.com/dmm/article/2/5-6/206/2203/Rats.

J. E. Iglesias, S. Crampsie, C. Strand, M. Tachrount, D. L. Thomas, and J. L. Holton. Effect of Fluorinert on the Histological Properties of Formalin-Fixed Human Brain Tissue. *Journal of Neuropathology & Experimental Neurology*, 77(12):1085–1090, 12 2018. ISSN 0022-3069. doi: 10.1093/jnen/nly098. URL https://academic.oup.com/jnen/article/77/12/1085/5144755.

S.-J. Im, J.-Y. Suh, J.-H. Shim, and H.-M. Baek. Deterministic Tractography Analysis of Rat Brain Using SIGMA Atlas in 9.4T MRI. *Brain Sciences*, 11 (12):1656, 12 2021. ISSN 2076-3425. doi: 10.3390/brainsci11121656.

H.-I. Ioanas, M. Marks, C. M. Garin, M. Dhenain, M. F. Yanik, and M. Rudin. An Automated Open-Source Workflow for Standards-Compliant Integration of Small Animal Magnetic Resonance Imaging Data. *Frontiers in Neuroinformatics*, 14, 2 2020. ISSN 1662-5196. doi: 10.3389/fninf.2020.00005.

S. Jbabdi and H. Johansen-Berg. Tractography: Where Do We Go from Here? *Brain Connectivity*, 1(3), 9 2011. ISSN 2158-0014. doi: 10.1089/brain.2011.0033.

I. O. Jelescu, J. Veraart, E. Fieremans, and D. S. Novikov. Degeneracy in model parameter estimation for multi-compartmental diffusion in neuronal tissue. *NMR in Biomedicine*, 29(1), 1 2016. ISSN 09523480. doi: 10.1002/nbm.3450.

I. O. Jelescu, M. Palombo, F. Bagnato, and K. G. Schilling. Challenges for biophysical modeling of microstructure. *Journal of Neuroscience Methods*, 344: 108861, 10 2020. ISSN 01650270. doi: 10.1016/j.jneumeth.2020.108861. URL

https://linkinghub.elsevier.com/retrieve/pii/S0165027020302843.

I. O. Jelescu, F. Grussu, A. Ianus, B. Hansen, R. L. C. Barrett, M. Aggarwal, S. Michielse, F. Nasrallah, W. Syeda, N. Wang, J. Veraart, A. Roebroeck, A. F. Bagdasarian, C. Eichner, F. Sepehrband, J. Zimmermann, L. Soustelle, C. Bowman, B. C. Tendler, A. Hertanu, B. Jeurissen, M. Verhoye, L. Frydman, Y. van de Looij, D. Hike, J. F. Dunn, K. Miller, B. A. Landman, N. Shemesh, A. Anderson, E. McKinnon, S. Farquharson, F. D. Acqua, C. Pierpaoli, I. Drobnjak, A. Leemans, K. D. Harkins, M. Descoteaux, D. Xu, H. Huang, M. D. Santin, S. C. Grant, A. Obenaus, G. S. Kim, D. Wu, D. L. Bihan, S. J. Blackband, L. Ciobanu, E. Fieremans, R. Bai, T. Leergaard, J. Zhang, T. B. Dyrby, G. A. Johnson, J. Cohen-Adad, M. D. Budde, and K. G. Schilling. Recommendations and guidelines from the ISMRM Diffusion Study Group for preclinical diffusion MRI: Part 1 – In vivo small-animal imaging. *arXiv*, 9 2022.

M. Jenkinson and S. Smith. A global optimisation method for robust affine registration of brain images. *Medical Image Analysis*, 5(2), 6 2001. ISSN 13618415. doi: 10.1016/S1361-8415(01)00036-6.

M. Jenkinson, P. Bannister, M. Brady, and S. Smith. Improved Optimization for the Robust and Accurate Linear Registration and Motion Correction of Brain Images. *NeuroImage*, 17(2):825–841, 10 2002. ISSN 10538119. doi: 10.1016/S1053-8119(02)91132-8. URL http://linkinghub.elsevier.com/retrieve/pii/S1053811902911328.

M. Jenkinson, C. F. Beckmann, T. E. Behrens, M. W. Woolrich, and S. M. Smith. FSL. *NeuroImage*, 62(2), 8 2012. ISSN 10538119. doi: 10.1016/j.neuroimage.2011.09.015.

J. H. Jensen, J. A. Helpern, A. Ramani, H. Lu, and K. Kaczynski. Diffusional kurtosis imaging: The quantification of non-gaussian water diffusion by means of magnetic resonance imaging. *Magnetic Resonance in Medicine*, 53(6), 6 2005. ISSN 0740-3194. doi: 10.1002/mrm.20508.

K. H. R. Jensen and R. W. Berg. Advances and perspectives in tissue clearing

using CLARITY. *Journal of Chemical Neuroanatomy*, 86:19–34, 12 2017. ISSN 08910618. doi: 10.1016/j.jchemneu.2017.07.005.

T. Jiang, H. Gong, and J. Yuan. Whole-brain Optical Imaging: A Powerful Tool for Precise Brain Mapping at the Mesoscopic Level. *Neuroscience Bulletin*, 39 (12):1840–1858, 12 2023. ISSN 1673-7067. doi: 10.1007/s12264-023-01112-y.

D. Jing, S. Zhang, W. Luo, X. Gao, Y. Men, C. Ma, X. Liu, Y. Yi, A. Bugde, B. O. Zhou, Z. Zhao, Q. Yuan, J. Q. Feng, L. Gao, W.-P. Ge, and H. Zhao. Tissue clearing of both hard and soft tissue organs with the PEGASOS method. *Cell Research*, 28(8), 8 2018. ISSN 1001-0602. doi: 10.1038/s41422-018-0049-z.

G. A. Johnson, E. Calabrese, A. Badea, G. Paxinos, and C. Watson. A multidimensional magnetic resonance histology atlas of the Wistar rat brain. *NeuroImage*, 62(3):1848–1856, 9 2012. ISSN 10538119. doi: 10.1016/j.neuroimage.2012.05.041. URL https://linkinghub.elsevier.com/retrieve/pii/S1053811912005290.

G. A. Johnson, Y. Tian, D. G. Ashbrook, G. P. Cofer, J. J. Cook, J. C. Gee, A. Hall, K. Hornburg, Y. Qi, F.-C. Yeh, N. Wang, L. E. White, and R. W. Williams. Merged magnetic resonance and light sheet microscopy of the whole mouse brain. *Proceedings of the National Academy of Sciences*, 120(17), 4 2023. ISSN 0027-8424. doi: 10.1073/pnas.2218617120. URL https://pnas.org/doi/10.1073/pnas.2218617120.

E. L. Kaijzel, E. R. van Beek, M. A. Stammes, I. Que, A. B. Chan, C. W. Lowik, and L. J. Cruz. Traumatic Brain Injury: Preclinical Imaging Diagnostic(s) and Therapeutic Approaches. *Current Pharmaceutical Design*, 23(13):1909–1915, 5 2017. ISSN 13816128. doi: 10.2174/1381612823666170116141116.

S. Kanatani, J. C. Kreutzmann, Y. Li, Z. West, L. L. Larsen, D. V. Nikou, I. Eidhof, A. Walton, S. Zhang, L. R. Rodríguez-Kirby, J. L. Skytte, C. G. Salinas, K. Takamatsu, X. Li, D. H. Tanaka, D. Kaczynska, K. Fukumoto, R. Karamzadeh, Y. Xiang, N. Uesaka, T. Tanabe, M. Adner, J. Hartman, A. Miyakawa, E. Sundström, G. Castelo-Branco, U. Roostalu, J. Hecksher-Sørensen, and P. Uhlén. Whole-brain spatial transcriptional analysis at cellular

resolution. *Science*, 386(6724):907–915, 11 2024. ISSN 0036-8075. doi: 10.1126/science.adn9947. URL https://www.science.org/doi/10.1126/science.adn9947.

A. R. Khan, A. Cornea, L. A. Leigland, S. G. Kohama, S. N. Jespersen, and C. D. Kroenke. 3D structure tensor analysis of light microscopy data for validating diffusion MRI. *NeuroImage*, 111:192–203, 5 2015. ISSN 10538119. doi: 10.1016/j.neuroimage.2015.01.061. URL https://linkinghub.elsevier.com/retrieve/pii/S1053811915000889.

S. Kim, S. Pickup, O. Hsu, and H. Poptani. Enhanced delineation of white matter structures of the fixed mouse brain using Gd-DTPA in microscopic MRI. *NMR in Biomedicine*, 22(3):303–309, 4 2009. ISSN 0952-3480. doi: 10.1002/nbm.1324.

S.-Y. Kim, J. H. Cho, E. Murray, N. Bakh, H. Choi, K. Ohn, L. Ruelas, A. Hubbert, M. McCue, S. L. Vassallo, P. J. Keller, and K. Chung. Stochastic electrotransport selectively enhances the transport of highly electromobile molecules. *Proceedings of the National Academy of Sciences*, 112(46), 11 2015. ISSN 0027-8424. doi: 10.1073/pnas.1510133112.

D. Z. Kor, S. Jbabdi, I. N. Huszar, J. Mollink, B. C. Tendler, S. Foxley, C. Wang, C. Scott, A. Smart, O. Ansorge, M. Pallebage-Gamarallage, K. L. Miller, and A. F. Howard. An automated pipeline for extracting histological stain area fraction for voxelwise quantitative MRI-histology comparisons. *NeuroImage*, 264: 119726, 12 2022. ISSN 10538119. doi: 10.1016/j.neuroimage.2022.119726. URL https://linkinghub.elsevier.com/retrieve/pii/S1053811922008473.

U. Köthe. Edge and Junction Detection with an Improved Structure Tensor. In B. Michaelis and G. Krell, editors, *Pattern Recognition*, pages 25–32. Springer, Berlin, Heidelberg, 2003. doi: 10.1007/978-3-540-45243-0{_}4. URL http://link.springer.com/10.1007/978-3-540-45243-0_4.

N. Kovačević, J. Henderson, E. Chan, N. Lifshitz, J. Bishop, A. Evans, R. Henkelman, and X. Chen. A Three-dimensional MRI Atlas of the Mouse Brain with Estimates of the Average and Variability. *Cerebral Cortex*, 15(5):639–645, 5

2005. ISSN 1460-2199. doi: 10.1093/cercor/bhh165.

T. Ku, J. Swaney, J.-Y. Park, A. Albanese, E. Murray, J. H. Cho, Y.-G. Park, V. Mangena, J. Chen, and K. Chung. Multiplexed and scalable super-resolution imaging of three-dimensional protein localization in size-adjustable tissues. *Nature Biotechnology*, 34(9):973–981, 9 2016. ISSN 1087-0156. doi: 10.1038/nbt.3641.

T. Kumamoto and T. Tsurugizawa. Potential of Multiscale Astrocyte Imaging for Revealing Mechanisms Underlying Neurodevelopmental Disorders. *International Journal of Molecular Sciences*, 22(19):10312, 9 2021. ISSN 1422-0067. doi: 10.3390/ijms221910312.

T. Kuwajima, A. A. Sitko, P. Bhansali, C. Jurgens, W. Guido, and C. Mason. ¡i¿ClearT¡/i¿ : a detergent- and solvent-free clearing method for neuronal and non-neuronal tissue. *Development*, 140(6):1364–1368, 3 2013. ISSN 1477-9129. doi: 10.1242/dev.091844.

H. M. Lai, A. K. L. Liu, H. H. M. Ng, M. H. Goldfinger, T. W. Chau, J. DeFelice, B. S. Tilley, W. M. Wong, W. Wu, and S. M. Gentleman. Next generation histology methods for three-dimensional imaging of fresh and archival human brain tissues. *Nature Communications*, 9(1):1066, 3 2018. ISSN 2041-1723. doi: 10.1038/s41467-018-03359-w.

B. Lampinen, F. Szczepankiewicz, J. Lätt, L. Knutsson, J. Mårtensson, I. M. Björkman-Burtscher, D. van Westen, P. C. Sundgren, F. Ståhlberg, and M. Nilsson. Probing brain tissue microstructure with MRI: principles, challenges, and the role of multidimensional diffusion-relaxation encoding. *NeuroImage*, page 120338, 8 2023. ISSN 10538119. doi: 10.1016/j.neuroimage.2023.120338. URL https://linkinghub.elsevier.com/retrieve/pii/S1053811923004895.

F. J. Lange, J. Ashburner, S. M. Smith, and J. L. Andersson. A Symmetric Prior for the Regularisation of Elastic Deformations: Improved anatomical plausibility in nonlinear image registration. *NeuroImage*, 219:116962, 10 2020. ISSN 10538119. doi: 10.1016/j.neuroimage.2020.116962. URL https://linkinghub.elsevier.com/retrieve/pii/S1053811920304481.

S. Latifi and S. T. Carmichael. The emergence of multiscale connectomics-based approaches in stroke recovery. *Trends in Neurosciences*, 2 2024. ISSN 01662236. doi: 10.1016/j.tins.2024.01.003.

A. Lazari and I. Lipp. Can MRI measure myelin? Systematic review, qualitative assessment, and meta-analysis of studies validating microstructural imaging with myelin histology. *NeuroImage*, 230, 4 2021. ISSN 10538119. doi: 10.1016/j.neuroimage.2021.117744.

D. Le Bihan. IVIM method measures diffusion and perfusion. *Diagnostic Imaging*, 12(6):133–136, 6 1990.

S. Lee, Y. Chen, W. Ban, G. A. Devenyi, J. Fouquet, L. Concha, J. S. Dumas, M. Hanke, J. Grandjean, and R. Rios. BrkRaw/brkraw: BrkRaw v0.3.8 (0.3.8)., 2023. URL https://doi.org/10.5281/zenodo.8118170.

J. P. Lerch, A. J. W. van der Kouwe, A. Raznahan, T. Paus, H. Johansen-Berg, K. L. Miller, S. M. Smith, B. Fischl, and S. N. Sotiropoulos. Studying neuroanatomy using MRI. *Nature Neuroscience*, 20(3), 3 2017. ISSN 1097-6256. doi: 10.1038/nn.4501.

K. K. Leung, J. Barnes, M. Modat, G. R. Ridgway, J. W. Bartlett, N. C. Fox, and S. Ourselin. Brain MAPS: An automated, accurate and robust brain extraction technique using a template library. *NeuroImage*, 55(3):1091–1108, 4 2011. ISSN 10538119. doi: 10.1016/j.neuroimage.2010.12.067. URL https://linkinghub.elsevier.com/retrieve/pii/S1053811910016708.

C. Leuze, M. Goubran, M. Barakovic, M. Aswendt, Q. Tian, B. Hsueh, A. Crow, E. Weber, G. Steinberg, M. Zeineh, E. Plowey, A. Daducci, G. Innocenti, J.-P. Thiran, K. Deisseroth, and J. McNab. Comparison of diffusion MRI and CLARITY fiber orientation estimates in both gray and white matter regions of human and primate brain. *NeuroImage*, 228:117692, 3 2021. ISSN 10538119. doi: 10.1016/j.neuroimage.2020.117692. URL https://linkinghub.elsevier.com/retrieve/pii/S1053811920311770.

C. W. U. Leuze, A. Anwander, P.-L. Bazin, B. Dhital, C. Stuber, K. Reimann, S. Geyer, and R. Turner. Layer-Specific Intracortical Connectivity Revealed

with Diffusion MRI. *Cerebral Cortex*, 24(2), 2 2014. ISSN 1047-3211. doi: 10.1093/cercor/bhs311.

J. Li, X. Liu, J. Zhuo, R. P. Gullapalli, and J. M. Zara. An automatic rat brain extraction method based on a deformable surface model. *Journal of Neuroscience Methods*, 218(1):72–82, 8 2013. ISSN 01650270. doi: 10.1016/j.jneumeth.2013.04.011. URL https://linkinghub.elsevier.com/retrieve/pii/S0165027013001490.

X. Liang, Y. Zang, D. Dong, L. Zhang, M. Fang, X. Yang, A. Arranz, J. Ripoll, H. Hui, and J. Tian. Stripe artifact elimination based on nonsubsampled contourlet transform for light sheet fluorescence microscopy. *Journal of Biomedical Optics*, 21(10):106005, 10 2016. ISSN 1083-3668. doi: 10.1117/1.JBO.21.10.106005. URL http://biomedicaloptics.spiedigitallibrary.org/article.aspx?doi=10.1117/1.JBO.21.10.106005.

Y. Liu, B. R. Sajja, H. E. Gendelman, and M. D. Boska. Mouse brain fixation to preserve In vivo manganese enhancement for ex vivo manganese-enhanced MRI. *Journal of Magnetic Resonance Imaging*, 38(2):482–487, 8 2013. ISSN 1053-1807. doi: 10.1002/jmri.24005.

Y. Liu, H. S. Unsal, Y. Tao, and N. Zhang. Automatic Brain Extraction for Rodent MRI Images. *Neuroinformatics*, 18(3):395–406, 6 2020. ISSN 1539-2791. doi: 10.1007/s12021-020-09453-z. URL http://link.springer.com/10.1007/s12021-020-09453-z.

J. Lohmeier, T. Kaneko, B. Hamm, M. R. Makowski, and H. Okano. atlasBREX: Automated template-derived brain extraction in animal MRI. *Scientific Reports*, 9(1):12219, 8 2019. ISSN 2045-2322. doi: 10.1038/s41598-019-48489-3.

G. D. Luker and K. E. Luker. Optical Imaging: Current Applications and Future Directions. *Journal of Nuclear Medicine*, 49(1), 1 2008. ISSN 0161-5505. doi: 10.2967/jnumed.107.045799.

H. Mai, J. Luo, L. Hoeher, R. Al-Maskari, I. Horvath, Y. Chen, F. Kofler, M. Piraud, J. C. Paetzold, J. Modamio, M. Todorov, M. Elsner, F. Hellal, and A. Ertürk. Whole-body cellular mapping in mouse using standard

IgG antibodies. *Nature Biotechnology*, 7 2023. ISSN 1087-0156. doi: 10.1038/s41587-023-01846-0. URL https://www.nature.com/articles/s41587-023-01846-0.

K. H. Maier-Hein, P. F. Neher, J.-C. Houde, M.-A. Côté, E. Garyfallidis, J. Zhong, M. Chamberland, F.-C. Yeh, Y.-C. Lin, Q. Ji, W. E. Reddick, J. O. Glass, D. Q. Chen, Y. Feng, C. Gao, Y. Wu, J. Ma, R. He, Q. Li, C.-F. Westin, S. Deslauriers-Gauthier, J. O. O. González, M. Paquette, S. St-Jean, G. Girard, F. Rheault, J. Sidhu, C. M. W. Tax, F. Guo, H. Y. Mesri, S. Dávid, M. Froeling, A. M. Heemskerk, A. Leemans, A. Boré, B. Pinsard, C. Bedetti, M. Desrosiers, S. Brambati, J. Doyon, A. Sarica, R. Vasta, A. Cerasa, A. Quattrone, J. Yeatman, A. R. Khan, W. Hodges, S. Alexander, D. Romascano, M. Barakovic, A. Auría, O. Esteban, A. Lemkaddem, J.-P. Thiran, H. E. Cetingul, B. L. Odry, B. Mailhe, M. S. Nadar, F. Pizzagalli, G. Prasad, J. E. Villalon-Reina, J. Galvis, P. M. Thompson, F. D. S. Requejo, P. L. Laguna, L. M. Lacerda, R. Barrett, F. Dell'Acqua, M. Catani, L. Petit, E. Caruyer, A. Daducci, T. B. Dyrby, T. Holland-Letz, C. C. Hilgetag, B. Stieltjes, and M. Descoteaux. The challenge of mapping the human connectome based on diffusion tractography. *Nature Communications*, 8(1), 12 2017. ISSN 2041-1723. doi: 10.1038/s41467-017-01285-x.

J. Maranzano, M. Dadar, A. Bertrand-Grenier, E.-M. Frigon, J. Pellerin, S. Plante, S. Duchesne, C. L. Tardif, D. Boire, and G. Bronchti. A novel ex vivo, in situ method to study the human brain through MRI and histology. *Journal of Neuroscience Methods*, 345:108903, 11 2020. ISSN 01650270. doi: 10.1016/j.jneumeth.2020.108903. URL https://linkinghub.elsevier.com/retrieve/pii/S0165027020303265.

R. B. Mars, R. E. Passingham, and S. Jbabdi. Connectivity Fingerprints: From Areal Descriptions to Abstract Spaces. *Trends in Cognitive Sciences*, 22(11): 1026–1037, 11 2018. ISSN 13646613. doi: 10.1016/j.tics.2018.08.009. URL https://linkinghub.elsevier.com/retrieve/pii/S1364661318302092.

P. Matryba, L. Bozycki, M. Pawłowska, L. Kaczmarek, and M. Stefaniuk. Opti-

mized perfusion-based CUBIC protocol for the efficient whole-body clearing and imaging of rat organs. *Journal of Biophotonics*, 11(5), 5 2018. ISSN 1864063X. doi: 10.1002/jbio.201700248.

Q. A. Meslier, T. J. Duerr, W. Guan, B. Nguyen, J. R. Monaghan, and S. J. Shefelbine. WISHBONE: Whole-mount in situ histology, to label osteocyte mRNA and protein in 3D adult mouse bones. *The FASEB Journal*, 38(19), 10 2024. ISSN 0892-6638. doi: 10.1096/fj.202400635R.

K. L. Miller, F. Alfaro-Almagro, N. K. Bangerter, D. L. Thomas, E. Yacoub, J. Xu, A. J. Bartsch, S. Jbabdi, S. N. Sotiropoulos, J. L. R. Andersson, L. Griffanti, G. Douaud, T. W. Okell, P. Weale, I. Dragonu, S. Garratt, S. Hudson, R. Collins, M. Jenkinson, P. M. Matthews, and S. M. Smith. Multimodal population brain imaging in the UK Biobank prospective epidemiological study. *Nature Neuroscience*, 19(11):1523–1536, 11 2016. ISSN 1097-6256. doi: 10.1038/nn.4393. URL http://www.nature.com/articles/nn.4393.

M. Molbay, Z. I. Kolabas, M. I. Todorov, T. Ohn, and A. Ertürk. A guidebook for DISCO tissue clearing. *Molecular Systems Biology*, 17(3), 3 2021. ISSN 1744-4292. doi: 10.15252/msb.20209807.

J. Mollink, M. Kleinnijenhuis, A. M. v. Cappellen van Walsum, S. N. Sotiropoulos, M. Cottaar, C. Mirfin, M. P. Heinrich, M. Jenkinson, M. Pallebage-Gamarallage, O. Ansorge, S. Jbabdi, and K. L. Miller. Evaluating fibre orientation dispersion in white matter: Comparison of diffusion MRI, histology and polarized light imaging. *NeuroImage*, 157:561–574, 8 2017. ISSN 10959572. doi: 10.1016/j.neuroimage.2017.06.001.

M. Morawski, E. Kirilina, N. Scherf, C. Jäger, K. Reimann, R. Trampel, F. Gavriilidis, S. Geyer, B. Biedermann, T. Arendt, and N. Weiskopf. Developing 3D microscopy with CLARITY on human brain tissue: Towards a tool for informing and validating MRI-based histology. *NeuroImage*, 182:417–428, 11 2018. ISSN 10538119. doi: 10.1016/j.neuroimage.2017.11.060. URL https://linkinghub.elsevier.com/retrieve/pii/S1053811917310066.

P. Morell and R. Quarles. Characteristic Composition of Myelin. In G. Siegel,

B. Agranoff, and R. Albers, editors, *Basic Neurochemistry: Molecular, Cellular and Medical Aspects*. Lippincott-Raven, Philadelphia, 6 edition, 1999.

A. Moreno-García, A. Kun, O. Calero, M. Medina, and M. Calero. An Overview of the Role of Lipofuscin in Age-Related Neurodegeneration. *Frontiers in Neuroscience*, 12, 7 2018. ISSN 1662-453X. doi: 10.3389/fnins.2018.00464.

T. Morita, M. Asada, and E. Naito. Contribution of Neuroimaging Studies to Understanding Development of Human Cognitive Brain Functions. *Frontiers in Human Neuroscience*, 10, 9 2016. ISSN 1662-5161. doi: 10.3389/fnhum.2016.00464.

E. Murray, J. Cho, D. Goodwin, T. Ku, J. Swaney, S.-Y. Kim, H. Choi, Y.-G. Park, J.-Y. Park, A. Hubbert, M. McCue, S. Vassallo, N. Bakh, M. Frosch, V. Wedeen, H. Seung, and K. Chung. Simple, Scalable Proteomic Imaging for High-Dimensional Profiling of Intact Systems. *Cell*, 163(6):1500–1514, 12 2015. ISSN 00928674. doi: 10.1016/j.cell.2015.11.025. URL https://linkinghub.elsevier.com/retrieve/pii/S0092867415015056.

B. J. Nieman, N. A. Bock, J. Bishop, X. J. Chen, J. G. Sled, J. Rossant, and R. M. Henkelman. Magnetic resonance imaging for detection and analysis of mouse phenotypes. *NMR in Biomedicine*, 18(7):447–468, 11 2005. ISSN 0952-3480. doi: 10.1002/nbm.981. URL https://onlinelibrary.wiley.com/doi/10.1002/nbm.981.

B. J. Nieman, M. C. van Eede, S. Spring, J. Dazai, R. M. Henkelman, and J. P. Lerch. MRI to Assess Neurological Function. *Current Protocols in Mouse Biology*, 8(2), 6 2018. ISSN 21612617. doi: 10.1002/cpmo.44.

J. Nijs, S. Z. George, D. J. Clauw, C. Fernández-de-las Peñas, E. Kosek, K. Ickmans, J. Fernández-Carnero, A. Polli, E. Kapreli, E. Huysmans, A. I. Cuesta-Vargas, R. Mani, M. Lundberg, L. Leysen, D. Rice, M. Sterling, and M. Curatolo. Central sensitisation in chronic pain conditions: latest discoveries and their potential for precision medicine. *The Lancet Rheumatology*, 3(5):e383–e392, 5 2021. ISSN 26659913. doi: 10.1016/S2665-9913(21)00032-1.

D. S. Novikov, V. G. Kiselev, and S. N. Jespersen. On modeling. *Magnetic*

Resonance in Medicine, 79(6):3172–3193, 6 2018. ISSN 07403194. doi: 10.1002/mrm.27101. URL http://doi.wiley.com/10.1002/mrm.27101.

V. Ntziachristos. Going deeper than microscopy: the optical imaging frontier in biology. *Nature Methods*, 7(8):603–614, 8 2010. ISSN 1548-7091. doi: 10.1038/nmeth.1483. URL http://www.nature.com/articles/nmeth.1483.

I. Oguz, J. Lee, F. Budin, A. Rumple, M. McMurray, C. Ehlers, F. Crews, J. Johns, and M. Styner. Automatic skull-stripping of rat MRI/DTI scans and atlas building. In B. M. Dawant and D. R. Haynor, editors, *Proceedings SPIE 7962*, page 796225, 3 2011. doi: 10.1117/12.878405. URL http://proceedings.spiedigitallibrary.org/proceeding.aspx?doi=10.1117/12.878405.

I. Oguz, M. S. McMurray, M. Styner, and J. M. Johns. The Translational Role of Diffusion Tensor Image Analysis in Animal Models of Developmental Pathologies. *Developmental Neuroscience*, 34(1):5–19, 2012. ISSN 1421-9859. doi: 10.1159/000336825.

I. Oguz, R. Yaxley, F. Budin, M. Hoogstoel, J. Lee, E. Maltbie, W. Liu, and F. T. Crews. Comparison of Magnetic Resonance Imaging in Live vs. Post Mortem Rat Brains. *PLoS ONE*, 8(8), 8 2013. ISSN 1932-6203. doi: 10.1371/journal.pone.0071027.

I. Oguz, H. Zhang, A. Rumple, and M. Sonka. RATS: Rapid Automatic Tissue Segmentation in rodent brain MRI. *Journal of Neuroscience Methods*, 221, 1 2014. ISSN 01650270. doi: 10.1016/j.jneumeth.2013.09.021.

K. K. Osen, J. Imad, A. E. Wennberg, E. A. Papp, and T. B. Leergaard. Waxholm Space atlas of the rat brain auditory system: Three-dimensional delineations based on structural and diffusion tensor magnetic resonance imaging. *NeuroImage*, 199, 10 2019. ISSN 10538119. doi: 10.1016/j.neuroimage.2019.05.016.

M. Pagani, M. Damiano, A. Galbusera, S. A. Tsaftaris, and A. Gozzi. Semi-automated registration-based anatomical labelling, voxel based morphometry and cortical thickness mapping of the mouse brain. *Journal of Neuroscience Methods*, 267:62–73, 7 2016. ISSN 01650270. doi:

10.1016/j.jneumeth.2016.04.007. URL https://linkinghub.elsevier.com/retrieve/pii/S0165027016300450.

N. Pallast, M. Diedenhofen, S. Blaschke, F. Wieters, D. Wiedermann, M. Hoehn, G. R. Fink, and M. Aswendt. Processing Pipeline for Atlas-Based Imaging Data Analysis of Structural and Functional Mouse Brain MRI (AIDAmri). *Frontiers in Neuroinformatics*, 13, 6 2019. ISSN 1662-5196. doi: 10.3389/fninf.2019.00042.

E. Panagiotaki, T. Schneider, B. Siow, M. G. Hall, M. F. Lythgoe, and D. C. Alexander. Compartment models of the diffusion MR signal in brain white matter: A taxonomy and comparison. *NeuroImage*, 59(3):2241–2254, 2 2012. ISSN 10538119. doi: 10.1016/j.neuroimage.2011.09.081. URL https://linkinghub.elsevier.com/retrieve/pii/S1053811911011566.

E. A. Papp, T. B. Leergaard, E. Calabrese, G. A. Johnson, and J. G. Bjaalie. Waxholm Space atlas of the Sprague Dawley rat brain. *NeuroImage*, 97, 8 2014. ISSN 10538119. doi: 10.1016/j.neuroimage.2014.04.001.

C. Paquola, J. Royer, L. B. Lewis, C. Lepage, T. Glatard, K. Wagstyl, J. DeKraker, P.-J. Toussaint, S. L. Valk, L. Collins, A. R. Khan, K. Amunts, A. C. Evans, T. Dickscheid, and B. Bernhardt. The BigBrainWarp toolbox for integration of BigBrain 3D histology with multimodal neuroimaging. *eLife*, 10, 8 2021. ISSN 2050-084X. doi: 10.7554/eLife.70119.

Y.-G. Park, C. H. Sohn, R. Chen, M. McCue, D. H. Yun, G. T. Drummond, T. Ku, N. B. Evans, H. C. Oak, W. Trieu, H. Choi, X. Jin, V. Lilascharoen, J. Wang, M. C. Truttmann, H. W. Qi, H. L. Ploegh, T. R. Golub, S.-C. Chen, M. P. Frosch, H. J. Kulik, B. K. Lim, and K. Chung. Protection of tissue physicochemical properties using polyfunctional crosslinkers. *Nature Biotechnology*, 37(1):73–83, 1 2019. ISSN 1087-0156. doi: 10.1038/nbt.4281. URL https://www.nature.com/articles/nbt.4281.

A. Parra-Damas and C. A. Saura. Tissue Clearing and Expansion Methods for Imaging Brain Pathology in Neurodegeneration: From Circuits to Synapses and Beyond. *Frontiers in Neuroscience*, 14, 10 2020. ISSN 1662-453X. doi:

10.3389/fnins.2020.00914.

M. Pawłowska, M. Stefaniuk, D. Legutko, and L. Kaczmarek. Light-Sheet Microscopy for Whole-Brain Imaging. In *Advanced Optical Methods for Brain Imaging*, pages 69–81. Springer, 2019. doi: 10.1007/978-981-10-9020-2{_}3. URL http://link.springer.com/10.1007/978-981-10-9020-2_3.

J. Pichat, J. E. Iglesias, T. Yousry, S. Ourselin, and M. Modat. A Survey of Methods for 3D Histology Reconstruction. *Medical Image Analysis*, 46:73–105, 5 2018. ISSN 13618415. doi: 10.1016/j.media.2018.02.004.

C. Pierpaoli and P. J. Basser. Toward a quantitative assessment of diffusion anisotropy. *Magnetic Resonance in Medicine*, 36(6), 12 1996. ISSN 07403194. doi: 10.1002/mrm.1910360612.

A. R. Pines, B. Larsen, Z. Cui, V. J. Sydnor, M. A. Bertolero, A. Adebimpe, A. F. Alexander-Bloch, C. Davatzikos, D. A. Fair, R. C. Gur, R. E. Gur, H. Li, M. P. Milham, T. M. Moore, K. Murtha, L. Parkes, S. L. Thompson-Schill, S. Shanmugan, R. T. Shinohara, S. M. Weinstein, D. S. Bassett, Y. Fan, and T. D. Satterthwaite. Dissociable multi-scale patterns of development in personalized brain networks. *Nature Communications*, 13(1):2647, 5 2022. ISSN 2041-1723. doi: 10.1038/s41467-022-30244-4.

T. J. Pisano, A. T. Hoag, Z. M. Dhanerawala, S. R. Guariglia, C. Jung, H.-J. Boele, K. M. Seagraves, J. L. Verpeut, and S. S.-H. Wang. Automated high-throughput mouse transsynaptic viral tracing using iDISCO+ tissue clearing, light-sheet microscopy, and BrainPipe. *STAR Protocols*, 3(2):101289, 6 2022. ISSN 26661667. doi: 10.1016/j.xpro.2022.101289.

S. Pontes-Filho, A. G. Dahl, S. Nichele, and G. B. Moreno e Mello. A deep learning based tool for automatic brain extraction from functional magnetic resonance images in rodents. *arXiv*, 12 2019.

J. D. Power and B. L. Schlaggar. Neural plasticity across the lifespan. *WIREs Developmental Biology*, 6(1), 1 2017. ISSN 1759-7684. doi: 10.1002/wdev.216.

S. Preibisch, S. Saalfeld, and P. Tomancak. Globally optimal stitching of tiled 3D microscopic image acquisitions. *Bioinformatics*, 25(11):1463–1465, 6 2009.

ISSN 1367-4811. doi: 10.1093/bioinformatics/btp184.

S. Raghavan, R. I. Reid, S. A. Przybelski, T. G. Lesnick, J. Graff-Radford, C. G. Schwarz, D. S. Knopman, M. M. Mielke, M. M. Machulda, R. C. Petersen, C. R. Jack, and P. Vemuri. Diffusion models reveal white matter microstructural changes with ageing, pathology and cognition. *Brain Communications*, 3 (2), 4 2021. ISSN 2632-1297. doi: 10.1093/braincomms/fcab106.

B. X. Ren, I. Huen, Z. J. Wu, H. Wang, M. Y. Duan, I. Guenther, K. N. Bhanu Prakash, and F. R. Tang. Early postnatal irradiation-induced age-dependent changes in adult mouse brain: MRI based characterization. *BMC Neuroscience*, 22(1):28, 12 2021. ISSN 1471-2202. doi: 10.1186/s12868-021-00635-2.

N. Renier, Z. Wu, D. Simon, J. Yang, P. Ariel, and M. Tessier-Lavigne. iDISCO: A Simple, Rapid Method to Immunolabel Large Tissue Samples for Volume Imaging. *Cell*, 159(4):896–910, 11 2014. ISSN 00928674. doi: 10.1016/j.cell.2014.10.010. URL https://linkinghub.elsevier.com/retrieve/pii/S0092867414012975.

N. Renier, E. L. Adams, C. Kirst, Z. Wu, R. Azevedo, J. Kohl, A. E. Autry, L. Kadiri, K. Umadevi Venkataraju, Y. Zhou, V. X. Wang, C. Y. Tang, O. Olsen, C. Dulac, P. Osten, and M. Tessier-Lavigne. Mapping of Brain Activity by Automated Volume Analysis of Immediate Early Genes. *Cell*, 165 (7):1789–1802, 6 2016. ISSN 00928674. doi: 10.1016/j.cell.2016.05.007. URL https://linkinghub.elsevier.com/retrieve/pii/S0092867416305554.

P. Ricci, V. Gavryusev, C. Müllenbroich, L. Turrini, G. de Vito, L. Silvestri, G. Sancataldo, and F. S. Pavone. Removing striping artifacts in light-sheet fluorescence microscopy: a review. *Progress in Biophysics and Molecular Biology*, 168:52–65, 1 2022. ISSN 00796107. doi: 10.1016/j.pbiomolbio.2021.07.003. URL https://linkinghub.elsevier.com/retrieve/pii/S0079610721000821.

D. S. Richardson, W. Guan, K. Matsumoto, C. Pan, K. Chung, A. Ertürk, H. R. Ueda, and J. W. Lichtman. Tissue clearing. *Nature Reviews Methods Primers*,

1(1):84, 12 2021. ISSN 2662-8449. doi: 10.1038/s43586-021-00080-9. URL https://www.nature.com/articles/s43586-021-00080-9.

A. Roebroeck, K. L. Miller, and M. Aggarwal. Ex vivo diffusion MRI of the human brain: Technical challenges and recent advances. *NMR in Biomedicine*, 32(4):e3941, 4 2019. ISSN 0952-3480. doi: 10.1002/nbm.3941. URL https://onlinelibrary.wiley.com/doi/10.1002/nbm.3941.

S. Roy, A. Knutsen, A. Korotcov, A. Bosomtwi, B. Dardzinski, J. A. Butman, and D. L. Pham. A deep learning framework for brain extraction in humans and animals with traumatic brain injury. In *2018 IEEE 15th International Symposium on Biomedical Imaging (ISBI 2018)*, pages 687–691. IEEE, 4 2018. ISBN 978-1-5386-3636-7. doi: 10.1109/ISBI.2018.8363667. URL https://ieeexplore.ieee.org/document/8363667/.

H. Rusch, M. Brammerloh, J. Stieler, M. Sonntag, S. Mohammadi, N. Weiskopf, T. Arendt, E. Kirilina, and M. Morawski. Finding the best clearing approach - Towards 3D wide-scale multimodal imaging of aged human brain tissue. *NeuroImage*, 247:118832, 2 2022. ISSN 10538119. doi: 10.1016/j.neuroimage.2021.118832. URL https://linkinghub.elsevier.com/retrieve/pii/S1053811921011034.

C. Saleeba, B. Dempsey, S. Le, A. Goodchild, and S. McMullan. A Student's Guide to Neural Circuit Tracing. *Frontiers in Neuroscience*, 13, 8 2019. ISSN 1662-453X. doi: 10.3389/fnins.2019.00897.

P. A. Santi, S. B. Johnson, M. Hillenbrand, P. Z. Grandpre, T. J. Glass, and J. R. Leger. Thin-sheet laser imaging microscopy for optical sectioning of thick tissues. *BioTechniques*, 46(4):287–294, 4 2009. ISSN 0736-6205. doi: 10.2144/000113087. URL https://www.future-science.com/doi/10.2144/000113087.

K. Schilling, V. Janve, Y. Gao, I. Stepniewska, B. A. Landman, and A. W. Anderson. Comparison of 3D orientation distribution functions measured with confocal microscopy and diffusion MRI. *NeuroImage*, 129:185–197, 4 2016. ISSN 10538119. doi: 10.1016/j.neuroimage.2016.01.022. URL

https://linkinghub.elsevier.com/retrieve/pii/S1053811916000288.

K. G. Schilling, V. Janve, Y. Gao, I. Stepniewska, B. A. Landman, and A. W. Anderson. Histological validation of diffusion MRI fiber orientation distributions and dispersion. *NeuroImage*, 165, 1 2018. ISSN 10538119. doi: 10.1016/j.neuroimage.2017.10.046.

K. G. Schilling, Y. Gao, I. Stepniewska, V. Janve, B. A. Landman, and A. W. Anderson. Histologically derived fiber response functions for diffusion MRI vary across white matter fibers—An ex vivo validation study in the squirrel monkey brain. *NMR in Biomedicine*, 32(6):e4090, 6 2019a. ISSN 0952-3480. doi: 10.1002/nbm.4090.

K. G. Schilling, V. Nath, C. Hansen, P. Parvathaneni, J. Blaber, Y. Gao, P. Neher, D. B. Aydogan, Y. Shi, M. Ocampo-Pineda, S. Schiavi, A. Daducci, G. Girard, M. Barakovic, J. Rafael-Patino, D. Romascano, G. Rensonnet, M. Pizzolato, A. Bates, E. Fischi, J.-P. Thiran, E. J. Canales-Rodríguez, C. Huang, H. Zhu, L. Zhong, R. Cabeen, A. W. Toga, F. Rheault, G. Theaud, J.-C. Houde, J. Sidhu, M. Chamberland, C.-F. Westin, T. B. Dyrby, R. Verma, Y. Rathi, M. O. Irfanoglu, C. Thomas, C. Pierpaoli, M. Descoteaux, A. W. Anderson, and B. A. Landman. Limits to anatomical accuracy of diffusion tractography using modern approaches. *NeuroImage*, 185:1–11, 1 2019b. ISSN 10538119. doi: 10.1016/j.neuroimage.2018.10.029. URL https://linkinghub.elsevier.com/retrieve/pii/S1053811918319888.

K. G. Schilling, F. Grussu, A. Ianus, B. Hansen, M. Aggarwal, S. Michielse, F. Nasrallah, W. Syeda, N. Wang, J. Veraart, A. Roebroeck, A. F. Bagdasarian, C. Eichner, F. Sepehrband, J. Zimmermann, B. Jeurissen, L. Frydman, Y. van de Looij, D. Hike, J. F. Dunn, K. L. Miller, B. A. Landman, N. Shemesh, A. Anderson, E. McKinnon, S. Farquharson, F. D. Acqua, C. Pierpaoli, I. Drobnjak, A. Leemans, K. D. Harkins, M. Descoteaux, D. Xu, M. D. Santin, S. Grant, A. Obenaus, G. S. Kim, D. Wu, D. L. Bihan, S. J. Blackband, L. Ciobanu, E. Fieremans, R. Bai, T. Leergaard, J. Zhang, T. B. Dyrby, G. A. Johnson, J. Cohen-Adad, M. D. Budde, and I. O. Jelescu.

Recommendations and guidelines from the ISMRM Diffusion Study Group for preclinical diffusion MRI: Part 2 - Ex vivo imaging. *arXiv*, 9 2022.

R. Schurr and A. A. Mezer. The glial framework reveals white-matter fiber architecture in human and primate brains. *Science*, 10 2021.

S. B. Sébille, A.-S. Rolland, M.-L. Welter, E. Bardinet, and M. D. Santin. Post mortem high resolution diffusion MRI for large specimen imaging at 11.7 T with 3D segmented echo-planar imaging. *Journal of Neuroscience Methods*, 311:222–234, 1 2019. ISSN 01650270. doi: 10.1016/j.jneumeth.2018.10.010.

A. Seehaus, A. Roebroeck, M. Bastiani, L. Fonseca, H. Bratzke, N. Lori, A. Vilanova, R. Goebel, and R. Galuske. Histological validation of high-resolution DTI in human post mortem tissue. *Frontiers in Neuroanatomy*, 9, 7 2015. ISSN 1662-5129. doi: 10.3389/fnana.2015.00098.

K. K. Seunarine and D. C. Alexander. Multiple Fibers: Beyond the Diffusion Tensor. In *Diffusion MRI*. Elsevier, 2014. doi: 10.1016/B978-0-12-396460-1.00006-8.

A. A. Sharief and G. A. Johnson. Enhanced T2 contrast for MR histology of the mouse brain. *Magnetic Resonance in Medicine*, 56(4), 10 2006. ISSN 0740-3194. doi: 10.1002/mrm.21026.

T. M. Shepherd, J. J. Flint, P. E. Thelwall, G. J. Stanisz, T. H. Mareci, A. T. Yachnis, and S. J. Blackband. Postmortem interval alters the water relaxation and diffusion properties of rat nervous tissue — Implications for MRI studies of human autopsy samples. *NeuroImage*, 44(3):820–826, 2 2009a. ISSN 10538119. doi: 10.1016/j.neuroimage.2008.09.054. URL https://linkinghub.elsevier.com/retrieve/pii/S1053811908010628.

T. M. Shepherd, P. E. Thelwall, G. J. Stanisz, and S. J. Blackband. Aldehyde fixative solutions alter the water relaxation and diffusion properties of nervous tissue. *Magnetic Resonance in Medicine*, 62(1):26–34, 7 2009b. ISSN 07403194. doi: 10.1002/mrm.21977. URL https://onlinelibrary.wiley.com/doi/10.1002/mrm.21977.

G. Silasi and T. Murphy. Stroke and the Connectome: How Connectivity Guides

Therapeutic Intervention. *Neuron*, 83(6):1354–1368, 9 2014. ISSN 08966273. doi: 10.1016/j.neuron.2014.08.052. URL https://linkinghub.elsevier.com/retrieve/pii/S089662731400782X.

L. Silvestri, I. Costantini, L. Sacconi, and F. S. Pavone. Clearing of fixed tissue: a review from a microscopist's perspective. *Journal of Biomedical Optics*, 21 (8), 3 2016. ISSN 1083-3668. doi: 10.1117/1.JBO.21.8.081205.

S. M. Smith. Fast robust automated brain extraction. *Human Brain Mapping*, 17(3), 11 2002. ISSN 1065-9471. doi: 10.1002/hbm.10062.

S. M. Smith, G. Douaud, W. Chen, T. Hanayik, F. Alfaro-Almagro, K. Sharp, and L. T. Elliott. An expanded set of genome-wide association studies of brain imaging phenotypes in UK Biobank. *Nature Neuroscience*, 24(5):737–745, 5 2021. ISSN 1097-6256. doi: 10.1038/s41593-021-00826-4.

J. D. Sokolowski, S. Soldozy, K. A. Sharifi, P. Norat, K. N. Kearns, L. Liu, A. M. Williams, K. Yağmurlu, P. Mastorakos, G. W. Miller, M. Y. S. Kalani, M. S. Park, R. T. Kellogg, and P. Tvrdik. Preclinical models of middle cerebral artery occlusion: new imaging approaches to a classic technique. *Frontiers in Neurology*, 14, 6 2023. ISSN 1664-2295. doi: 10.3389/fneur.2023.1170675.

S. N. Sotiropoulos and A. Zalesky. Building connectomes using diffusion MRI: why, how and but. *NMR in Biomedicine*, 32(4):e3752, 4 2019. ISSN 0952-3480. doi: 10.1002/nbm.3752. URL https://onlinelibrary.wiley.com/doi/abs/10.1002/nbm.3752.

S. N. Sotiropoulos, M. Hernández-Fernández, A. T. Vu, J. L. Andersson, S. Moeller, E. Yacoub, C. Lenglet, K. Ugurbil, T. E. Behrens, and S. Jbabdi. Fusion in diffusion MRI for improved fibre orientation estimation: An application to the 3T and 7T data of the Human Connectome Project. *NeuroImage*, 134:396–409, 7 2016. ISSN 10538119. doi: 10.1016/j.neuroimage.2016.04.014.

R. G. Spencer, K. W. Fishbein, A. Cheng, and M. P. Mattson. Compatibility of Gd-DTPA perfusion and histologic studies of the brain. *Magnetic Resonance Imaging*, 24(1):27–31, 1 2006. ISSN 0730725X. doi: 10.1016/j.mri.2005.10.017.

O. Sporns, G. Tononi, and R. Kötter. The Human Connectome: A Structural

Description of the Human Brain. *PLoS Computational Biology*, 1(4), 2005. ISSN 1553-734X. doi: 10.1371/journal.pcbi.0010042.

M. Stefaniuk, E. J. Gualda, M. Pawlowska, D. Legutko, P. Matryba, P. Koza, W. Konopka, D. Owczarek, M. Wawrzyniak, P. Loza-Alvarez, and L. Kaczmarek. Light-sheet microscopy imaging of a whole cleared rat brain with Thy1-GFP transgene. *Scientific Reports*, 6(1):28209, 9 2016. ISSN 2045-2322. doi: 10.1038/srep28209.

H. B. Stolp, G. Ball, P.-W. So, J.-D. Tournier, M. Jones, C. Thornton, and A. D. Edwards. Voxel-wise comparisons of cellular microstructure and diffusion-MRI in mouse hippocampus using 3D Bridging of Optically-clear histology with Neuroimaging Data (3D-BOND). *Scientific Reports*, 8(1): 4011, 12 2018. ISSN 2045-2322. doi: 10.1038/s41598-018-22295-9. URL http://www.nature.com/articles/s41598-018-22295-9.

E. Susaki, K. Tainaka, D. Perrin, F. Kishino, T. Tawara, T. Watanabe, C. Yokoyama, H. Onoe, M. Eguchi, S. Yamaguchi, T. Abe, H. Kiyonari, Y. Shimizu, A. Miyawaki, H. Yokota, and H. Ueda. Whole-Brain Imaging with Single-Cell Resolution Using Chemical Cocktails and Computational Analysis. *Cell*, 157(3):726–739, 4 2014. ISSN 00928674. doi: 10.1016/j.cell.2014.03.042. URL https://linkinghub.elsevier.com/retrieve/pii/S0092867414004188.

E. A. Susaki, K. Tainaka, D. Perrin, H. Yukinaga, A. Kuno, and H. R. Ueda. Advanced CUBIC protocols for whole-brain and whole-body clearing and imaging. *Nature Protocols*, 10(11):1709–1727, 11 2015. ISSN 1754-2189. doi: 10.1038/nprot.2015.085. URL http://www.nature.com/articles/nprot.2015.085.

E. A. Susaki, C. Shimizu, A. Kuno, K. Tainaka, X. Li, K. Nishi, K. Morishima, H. Ono, K. L. Ode, Y. Saeki, K. Miyamichi, K. Isa, C. Yokoyama, H. Kitaura, M. Ikemura, T. Ushiku, Y. Shimizu, T. Saito, T. C. Saido, M. Fukayama, H. Onoe, K. Touhara, T. Isa, A. Kakita, M. Shibayama, and H. R. Ueda. Versatile whole-organ/body staining and imaging based on electrolyte-gel

properties of biological tissues. *Nature Communications*, 11(1):1982, 4 2020. ISSN 2041-1723. doi: 10.1038/s41467-020-15906-5.

S. Taqi, S. Sami, L. Sami, and S. Zaki. A review of artifacts in histopathology. *Journal of Oral and Maxillofacial Pathology*, 22(2), 2018. ISSN 0973-029X. doi: 10.4103/jomfp.JOMFP{_}125{_}15.

B. C. Tendler, T. Hanayik, O. Ansorge, S. Bangerter-Christensen, G. S. Berns, M. F. Bertelsen, K. L. Bryant, S. Foxley, M. P. van den Heuvel, A. F. Howard, I. N. Huszar, A. A. Khrapitchev, A. Leonte, P. R. Manger, R. A. Menke, J. Mollink, D. Mortimer, M. Pallebage-Gamarallage, L. Roumazeilles, J. Sallet, L. H. Scholtens, C. Scott, A. Smart, M. R. Turner, C. Wang, S. Jbabdi, R. B. Mars, and K. L. Miller. The Digital Brain Bank, an open access platform for post-mortem imaging datasets. *eLife*, 11, 3 2022. ISSN 2050-084X. doi: 10.7554/eLife.73153.

M. Thiebaut de Schotten and S. J. Forkel. The emergent properties of the connected brain. *Science*, 378(6619):505–510, 11 2022. ISSN 0036-8075. doi: 10.1126/science.abq2591.

C. Thomas, F. Q. Ye, M. O. Irfanoglu, P. Modi, K. S. Saleem, D. A. Leopold, and C. Pierpaoli. Anatomical accuracy of brain connections derived from diffusion MRI tractography is inherently limited. *Proceedings of the National Academy of Sciences*, 111(46), 11 2014. ISSN 0027-8424. doi: 10.1073/pnas.1405672111.

T. Tian, Z. Yang, and X. Li. Tissue clearing technique: Recent progress and biomedical applications. *Journal of Anatomy*, 238(2), 2 2021. ISSN 0021-8782. doi: 10.1111/joa.13309.

R. Tomer, L. Ye, B. Hsueh, and K. Deisseroth. Advanced CLARITY for rapid and high-resolution imaging of intact tissues. *Nature Protocols*, 9(7), 7 2014. ISSN 1754-2189. doi: 10.1038/nprot.2014.123.

N. J. Tustison and B. B. Avants. Explicit B-spline regularization in diffeomorphic image registration. *Frontiers in Neuroinformatics*, 7, 2013. ISSN 1662-5196. doi: 10.3389/fninf.2013.00039.

N. J. Tustison, B. B. Avants, P. A. Cook, Yuanjie Zheng, A. Egan, P. A.

Yushkevich, and J. C. Gee. N4ITK: Improved N3 Bias Correction. *IEEE Transactions on Medical Imaging*, 29(6):1310–1320, 6 2010. ISSN 0278-0062. doi: 10.1109/TMI.2010.2046908.

H. R. Ueda, A. Ertürk, K. Chung, V. Gradinaru, A. Chédotal, P. Tomancak, and P. J. Keller. Tissue clearing and its applications in neuroscience. *Nature Reviews Neuroscience*, 21(2):61–79, 2 2020. ISSN 1471-003X. doi: 10.1038/s41583-019-0250-1. URL http://www.nature.com/articles/s41583-019-0250-1.

A. Valcourt Caron, A. Shmuel, Z. Hao, and M. Descoteaux. versaFlow: a versatile pipeline for resolution adapted diffusion MRI processing and its application to studying the variability of the PRIME-DE database. *Frontiers in Neuroinformatics*, 17, 8 2023. ISSN 1662-5196. doi: 10.3389/fninf.2023.1191200.

D. C. Van Essen, S. M. Smith, D. M. Barch, T. E. Behrens, E. Yacoub, and K. Ugurbil. The WU-Minn Human Connectome Project: An overview. *NeuroImage*, 80, 10 2013. ISSN 10538119. doi: 10.1016/j.neuroimage.2013.05.041.

R. J. Vigouroux, M. Belle, and A. Chédotal. Neuroscience in the third dimension: shedding new light on the brain with tissue clearing. *Molecular Brain*, 10(1):33, 12 2017. ISSN 1756-6606. doi: 10.1186/s13041-017-0314-y.

J. W. Vogel, N. Corriveau-Lecavalier, N. Franzmeier, J. B. Pereira, J. A. Brown, A. Maass, H. Botha, W. W. Seeley, D. S. Bassett, D. T. Jones, and M. Ewers. Connectome-based modelling of neurodegenerative diseases: towards precision medicine and mechanistic insight. *Nature Reviews Neuroscience*, 24(10):620–639, 10 2023. ISSN 1471-003X. doi: 10.1038/s41583-023-00731-8.

O. Vogt and C. Vogt. Zur anatomischen gliederung des cortex cerebri. *Journal of Psychology and Neuroscience*, 2(4):160–180, 1903.

K. Walhovd, H. Johansen-Berg, and R. Káradóttir. Unraveling the secrets of white matter – Bridging the gap between cellular, animal and human imaging studies. *Neuroscience*, 276:2–13, 9 2014. ISSN 03064522. doi:

10.1016/j.neuroscience.2014.06.058. URL https://linkinghub.elsevier.com/retrieve/pii/S0306452214005430.

H. Wang, C. Lenglet, and T. Akkin. Structure tensor analysis of serial optical coherence scanner images for mapping fiber orientations and tractography in the brain. *Journal of Biomedical Optics*, 20 (3):036003, 3 2015. ISSN 1083-3668. doi: 10.1117/1.JBO.20.3.036003. URL http://biomedicaloptics.spiedigitallibrary.org/article.aspx?doi=10.1117/1.JBO.20.3.036003.

H. Wang, C. Magnain, R. Wang, J. Dubb, A. Varjabedian, L. S. Tirrell, A. Stevens, J. C. Augustinack, E. Konukoglu, I. Aganj, M. P. Frosch, J. D. Schmahmann, B. Fischl, and D. A. Boas. as-PSOCT: Volumetric microscopic imaging of human brain architecture and connectivity. *NeuroImage*, 165:56–68, 1 2018a. ISSN 10538119. doi: 10.1016/j.neuroimage.2017.10.012.

N. Wang, R. J. Anderson, D. G. Ashbrook, V. Gopalakrishnan, Y. Park, C. E. Priebe, Y. Qi, R. Laoprasert, J. T. Vogelstein, R. W. Williams, and G. A. Johnson. Variability and heritability of mouse brain structure: Microscopic MRI atlases and connectomes for diverse strains. *NeuroImage*, 222, 11 2020a. ISSN 10538119. doi: 10.1016/j.neuroimage.2020.117274.

Q. Wang, S.-L. Ding, Y. Li, J. Royall, D. Feng, P. Lesnar, N. Graddis, M. Naeemi, B. Facer, A. Ho, T. Dolbeare, B. Blanchard, N. Dee, W. Wakeman, K. E. Hirokawa, A. Szafer, S. M. Sunkin, S. W. Oh, A. Bernard, J. W. Phillips, M. Hawrylycz, C. Koch, H. Zeng, J. A. Harris, and L. Ng. The Allen Mouse Brain Common Coordinate Framework: A 3D Reference Atlas. *Cell*, 181(4): 936–953, 5 2020b. ISSN 00928674. doi: 10.1016/j.cell.2020.04.007.

S. Wang, I. V. Larina, and K. V. Larin. Label-free optical imaging in developmental biology [Invited]. *Biomedical Optics Express*, 11(4):2017, 4 2020c. ISSN 2156-7085. doi: 10.1364/BOE.381359.

X. Wang, W. E. Allen, M. A. Wright, E. L. Sylwestrak, N. Samusik, S. Vesuna, K. Evans, C. Liu, C. Ramakrishnan, J. Liu, G. P. Nolan, F.-A. Bava, and K. Deisseroth. Three-dimensional intact-tissue sequencing of single-cell

transcriptional states. *Science*, 361(6400), 7 2018b. ISSN 0036-8075. doi: 10.1126/science.aat5691.

S. Warrington, E. Thompson, M. Bastiani, J. Dubois, L. Baxter, R. Slater, S. Jbabdi, R. B. Mars, and S. N. Sotiropoulos. Concurrent mapping of brain ontogeny and phylogeny within a common space: Standardized tractography and applications. *Science Advances*, 8(42), 10 2022. ISSN 2375-2548. doi: 10.1126/sciadv.abq2022.

N. Weiskopf, L. J. Edwards, G. Helms, S. Mohammadi, and E. Kirilina. Quantitative magnetic resonance imaging of brain anatomy and in vivo histology. *Nature Reviews Physics*, 3(8):570–588, 6 2021. ISSN 2522-5820. doi: 10.1038/s42254-021-00326-1.

K. R. Weiss, F. F. Voigt, D. P. Shepherd, and J. Huisken. Tutorial: practical considerations for tissue clearing and imaging. *Nature Protocols*, 16(6):2732–2748, 6 2021. ISSN 1754-2189. doi: 10.1038/s41596-021-00502-8. URL https://www.nature.com/articles/s41596-021-00502-8.

M. Welniak–Kaminska, M. Fiedorowicz, J. Orzel, P. Bogorodzki, K. Modlinska, R. Stryjek, A. Chrzanowska, W. Pisula, and P. Grieb. Volumes of brain structures in captive wild-type and laboratory rats: 7T magnetic resonance in vivo automatic atlas-based study. *PLOS ONE*, 14(4):e0215348, 4 2019. ISSN 1932-6203. doi: 10.1371/journal.pone.0215348.

C. A. Wheeler-Kingshott and M. Cercignani. About "axial" and "radial" diffusivities. *Magnetic Resonance in Medicine*, 61(5), 5 2009. ISSN 07403194. doi: 10.1002/mrm.21965.

T. Wood, , , D. Lythgoe, and S. Williams. rBET: Making BET work for Rodent Brains. In *Proceedings of the International Society for Magnetic Resonance in Medicine*, pages 2706–2706. ISMRM, 2013.

D. Wu and J. Zhang. Recent Progress in Magnetic Resonance Imaging of the Embryonic and Neonatal Mouse Brain. *Frontiers in Neuroanatomy*, 10, 3 2016. ISSN 1662-5129. doi: 10.3389/fnana.2016.00018.

Y. Xiao, J. C. Lau, T. Anderson, J. DeKraker, D. L. Collins, T. Peters, and

A. R. Khan. An accurate registration of the BigBrain dataset with the MNI PD25 and ICBM152 atlases. *Scientific Data*, 6(1), 12 2019. ISSN 2052-4463. doi: 10.1038/s41597-019-0217-0.

A. Yendiki, M. Aggarwal, M. Axer, A. F. Howard, A.-M. v. C. van Walsum, and S. N. Haber. Post mortem mapping of connectional anatomy for the validation of diffusion MRI. *NeuroImage*, 256:119146, 8 2022. ISSN 10538119. doi: 10.1016/j.neuroimage.2022.119146. URL https://linkinghub.elsevier.com/retrieve/pii/S1053811922002737.

T. Yu, J. Zhu, D. Li, and D. Zhu. Physical and chemical mechanisms of tissue optical clearing. *iScience*, 24(3):102178, 3 2021. ISSN 25890042. doi: 10.1016/j.isci.2021.102178. URL https://linkinghub.elsevier.com/retrieve/pii/S2589004221001462.

D. H. Yun, Y.-G. Park, J. H. Cho, L. Kamentsky, N. B. Evans, A. Albanese, K. Xie, J. Swaney, C. H. Sohn, Y. Tian, Q. Zhang, G. Drummond, W. Guan, N. DiNapoli, H. Choi, H.-Y. Jung, L. Ruelas, G. Feng, and K. Chung. Ultrafast immunostaining of organ-scale tissues for scalable proteomic phenotyping. *bioRiv*, 2019.

F. Zhang, A. Daducci, Y. He, S. Schiavi, C. Seguin, R. E. Smith, C.-H. Yeh, T. Zhao, and L. J. O'Donnell. Quantitative mapping of the brain's structural connectivity using diffusion MRI tractography: A review. *NeuroImage*, 249: 118870, 4 2022. ISSN 10538119. doi: 10.1016/j.neuroimage.2021.118870. URL https://linkinghub.elsevier.com/retrieve/pii/S1053811921011411.

H. Zhang, T. Schneider, C. A. Wheeler-Kingshott, and D. C. Alexander. NODDI: Practical in vivo neurite orientation dispersion and density imaging of the human brain. *NeuroImage*, 61(4):1000–1016, 7 2012. ISSN 10538119. doi: 10.1016/j.neuroimage.2012.03.072. URL https://linkinghub.elsevier.com/retrieve/pii/S1053811912003539.

Y. Zhang, M. Brady, and S. Smith. Segmentation of brain MR images through a hidden Markov random field model and the expectation-maximization algorithm. *IEEE Transactions on Medical Imaging*, 20(1):45–57, 2001. ISSN

02780062. doi: 10.1109/42.906424.

H. Zheng and L. Rinaman. Simplified CLARITY for visualizing immunofluorescence labeling in the developing rat brain. *Brain Structure and Function*, 221 (4):2375–2383, 5 2016. ISSN 1863-2653. doi: 10.1007/s00429-015-1020-0.

S. Zhu, I. N. Huszar, M. Cottaar, G. Daubney, N. Eichert, T. Hanayik, A. A. Khrapitchev, R. B. Mars, J. Mollink, J. Sallet, C. Scott, A. Smart, S. Jbabdi, K. L. Miller, and A. F. Howard. Imaging the structural connectome with hybrid diffusion MRI-microscopy tractography. *bioRxiv*, 1 2024.

X. Zhu, Y. Xia, X. Wang, K. Si, and W. Gong. Optical Brain Imaging: A Powerful Tool for Neuroscience. *Neuroscience Bulletin*, 33(1):95–102, 2 2017. ISSN 1673-7067. doi: 10.1007/s12264-016-0053-6. URL http://link.springer.com/10.1007/s12264-016-0053-6.

G. K. H. Zupanc. Mapping brain structure and function: cellular resolution, global perspective. *Journal of Comparative Physiology A*, 203(4):245–264, 4 2017. ISSN 0340-7594. doi: 10.1007/s00359-017-1163-y.